KAUNO TECHNOLOGIJOS UNIVERSITETAS

ŠARŪNAS JANKAUSKAS

TIESIOGINĖ GRAFENO SINTEZĖ: STRUKTŪRINIAI TYRIMAI IR TAIKYMO PRIETAISUOSE GALIMYBĖS

Daktaro disertacija
Technologijos mokslai, medžiagų inžinerija (T 008)

Kaunas, 2026

Disertacija rengta 2021–2025 metais Kauno technologijos universiteto Medžiagų mokslo institute. Mokslinius tyrimus rėmė Lietuvos mokslo taryba.

Mokslinis vadovas:
vyr. m. d. dr. Šarūnas MEŠKINIS (Kauno technologijos universitetas, technologijos mokslai, medžiagų inžinerija, T 008).

Mokslinis konsultantas:
vyresn. m. d. dr. Rimantas GUDAITIS (Kauno technologijos universitetas, technologijos mokslai, medžiagų inžinerija, T 008).

Redagavo: anglų kalbos redaktorius dr. Armandas Rumšas (leidykla „Technologija“), lietuvių kalbos redaktorė Aurelija Gražina Rukšaitė (leidykla „Technologija“).

Medžiagų inžinerijos mokslo krypties disertacijos gynimo taryba:
prof. habil. dr. Arvaidas GALDIKAS (Kauno technologijos universitetas, technologijos mokslai, medžiagų inžinerija, T 008) – **pirmininkas**;
prof. dr. Eva KOVACEVIC (Orleano universitetas, Prancūzija, technologijos mokslai, medžiagų inžinerija, T 008);
prof. dr. Giedrius LAUKAITIS (Kauno technologijos universitetas, technologijos mokslai, medžiagų inžinerija, T 008);
prof. dr. Alvydas LISAUSKAS (Vilniaus universitetas, gamtos mokslai, fizika, N 002);
prof. dr. Liutauras MARCINAUSKAS (Kauno technologijos universitetas, technologijos mokslai, medžiagų inžinerija, T 008).

Disertacija bus ginama viešame Medžiagų inžinerijos mokslo krypties disertacijos gynimo tarybos posėdyje 2026 m. rugpjūčio 27 d. 10 val. Kauno technologijos universiteto Rektorato salėje.

Adresas: K. Donelaičio g. 73-402, LT-44249 Kaunas, Lietuva.
Tel: +370 608 28 527; el. paštas doktorantura@ktu.lt

Disertacija išsiųsta 2026 m. liepos 27 d.
Su disertacija galima susipažinti interneto svetainėje http://ktu.edu ir Kauno technologijos universiteto bibliotekoje (Gedimino g. 50, Kaunas).

© Š. Jankauskas, 2026

KAUNAS UNIVERSITY OF TECHNOLOGY

ŠARŪNAS JANKAUSKAS

DIRECT SYNTHESIS OF GRAPHENE: STRUCTURAL CHARACTERIZATION AND POTENTIAL FOR DEVICE APPLICATIONS

Doctoral dissertation
Technological Sciences, Materials Engineering (T 008)

2026, Kaunas

The dissertation has been prepared at the Institute of Materials Science of Kaunas University of Technology in 2021-2025. The research has been sponsored by the Research Council of Lithuania.

Research supervisor:
Chief Researcher Dr. Šarūnas MEŠKINIS (Kaunas University of Technology, Technological Sciences, Materials Engineering, T 008).

Research consultant:
Senior Researcher Dr. Rimantas GUDAITIS (Kaunas University of Technology, Technological Sciences, Materials Engineering, T 008).

Edited by: English language editor Dr. Armandas Rumšas (Publishing House *Technologija*), Lithuanian language editor Aurelija Gražina Rukšaitė (Publishing House *Technologija*).

Dissertation Defence Board of Materials Engineering Science Field:
Prof. Dr. Hab. Arvaidas GALDIKAS (Kaunas University of Technology, Technological Sciences, Materials Engineering, T 008) – **chairperson**;
Prof. Dr. Eva KOVACEVIC (University of Orléans, France, Technological Sciences, Materials Engineering, T 008);
Prof. Dr. Giedrius LAUKAITIS (Kaunas University of Technology, Technological Sciences, Materials Engineering, T 008);
Prof. Dr. Alvydas LISAUSKAS (Vilnius University, Natural Sciences, Physics, N 002);
Prof. Dr. Liutauras MARCINAUSKAS (Kaunas University of Technology, Technological Sciences, Materials Engineering, T 008).

The dissertation defence will be held on 27 August 2026, at 10 a. m. at the Rectorate Hall of Kaunas University of Technology in the meeting of the Dissertation Defence Board of the Materials Engineering Science Field.

Address: K. Donelaičio 73-402, LT-44249 Kaunas, Lithuania.
Phone: +370 608 28 527; e-mail doktorantura@ktu.lt

The dissertation was sent out on 27 July 2026.
The dissertation is available on http://ktu.edu and at the library of Kaunas University of Technology (Gedimino 50, Kaunas).

© Š. Jankauskas, 2026

TURINYS

LENTELIŲ SĄRAŠAS 6
PAVEIKSLŲ SĄRAŠAS 7
SANTRUMPŲ IR TERMINŲ SĄRAŠAS 8
ĮVADAS 9
1. LITERATŪROS APŽVALGA 14
1.1. Grafenas 14
1.2. Grafeno sintezė 18
1.3. Grafeno analizės metodai 20
1.4. Grafeno taikymas elektronikoje 21
2. MEDŽIAGOS IR TYRIMŲ METODAI 24
2.1. Plonų sluoksnių sintezė 24
2.2. AJM analizė 26
2.3. Ramano sklaidos spektroskopijos analizė 27
2.4. Elektrinių prietaisų formavimas ir tyrimas 29
2.5. Elektriniai matavimai 31
3. REZULTATŲ APŽVALGA IR APTARIMAS 32
3.1. Grafeno sintezės optimizavimas 32
3.2. Fotodiodų ir lauko tranzistoriaus principu veikiančio biologinio jutiklio, suformuoto taikant grafeno plėveles, funkcinės savybės 45
IŠVADOS 50
ABSTRACT 52
LITERATŪROS SĄRAŠAS 61
MOKSLO STRAIPSNIŲ KOPIJOS 68
GYVENIMO, MOKSLINĖS IR KŪRYBINĖS VEIKLOS APRAŠYMAS (CV) 152
MOKSLO STRAIPSNIŲ IR MOKSLO KONFERENCIJŲ SĄRAŠAS 153
PADĖKA 156

LENTELIŲ SĄRAŠAS

1 lentelė. H-BN sintezės ant Si(100), naudojant didelės galios impulsinį magnetroninį dulkinimą, auginimo parametrai 26
2 lentelė. Grafeno/Si(100) charakteringų Ramano sklaidos spektrų smailių parametrai 35

PAVEIKSLŲ SĄRAŠAS

1 pav. Pagrindinės galimos keliasluoksnio grafeno konfigūracijos 15
2 pav. Grafene vyraujančių defektų pavyzdžiai 16
3 pav. Skystosios užtūros (angl. *liquid-gated*) G-FET schema 25
4 pav. Grafeno sintezės schema taikant MW-PECVD 24
5 pav. Pavyzdiniai MW-PECVD sintezės etapai auginant grafeną ant C-safyro pagrindų 25
6 pav. Paviršiaus elektrinio laidumo matavimų schema, naudojant kontaktinį laidų atominių jėgų mikroskopijos metodą 27
7 pav**.** Grafenui charakteringų Ramano sklaidos spektro sričių aproksimavimo pavyzdys 28
8 pav. Grafeno/Si(100) fotodiodo prototipo schema 29
9 pav. Biologinio jutiklio prototipo matavimo schema 30
10 pav. Šviesos diodų valdymo bloko schema 31
11 pav. Grafeno plėvelių, sintetintų ant Si(100) pagrindų MW-PECVD būdu, AJM vaizdai 34
12 pav. Grafeno plėvelių, sintetintų ant SiO_2/Si(100) pagrindų MW-PECVD būdu, AJM (kairėje) ir laidumo AJM (dešinėje) vaizdai 36
13 pav. Grafeno, sintetinto ant C-safyro pagrindų MW-PECVD būdu, Ramano sklaidos spektrų analizė 38
14 pav. Grafeno, sintetinto naudojant CH_4/H_2 – 35/65 srautų santykį bei 10 mBar slėgį, morfologija 39
15 pav. Tipiniai h-BN plėvelių Ramano sklaidos spektrai 40
16 pav. Grafeno, sintetinto ant skirtingo storio h-BN plėvelių, struktūros tyrimai Ramano sklaidos spektroskopija 41
17 pav. Įvairūs grafenui būdingų smailių parametrai ir jų santykiai 42
18 pav. Grafeno, sintetinto ant skirtingo storio h-BN plėvelių, morfologijos tyrimai taikant AJM bei laidumo AJM 43
19 pav. Skirtingais sintezės parametrais (dujų srautų santykiu, temperatūra bei slėgiu) augintų grafeno plėvelių Ramano sklaidos spektrų palyginimas 44
20 pav. Grafeno/Si(100) fotodiodų VACh 47
21 pav. T-G-FET biologinių jutiklių ir MW-PECVD-G-FET biologinių jutiklių perdavimo charakteristikos 49

SANTRUMPŲ IR TERMINŲ SĄRAŠAS

Santrumpos:

ACE2 – angiotenziną konvertuojantis fermentas II

AJM **–** atominių jėgų mikroskopija

BSA – jaučio serumo albumino tirpalas

CVD – cheminis nusodinimas iš garų fazės

FET – lauko tranzistorius

G-FET – grafeno lauko tranzistorius

GO – grafeno oksidas

H-BN – heksagoninis boro nitridas

HG – hidrogenizuotas grafenas

MW-PECVD – mikrobangų plazma aktyvuotas cheminis nusodinimas iš garų fazės

MW-PECVD-G-FET – mikrobangų plazma aktyvuoto cheminio nusodinimo iš garų fazės būdu suformuoti grafeno lauko tranzistoriai

PBASE – 1-pirenbutano rūgšties sukcinimidilo esteris

PBS – fosfatu buferizuotas fiziologinis tirpalas

PDMS – polidimetilsiloksanas

PMMA – polimetilmetakrilatas

T-G-FET – grafeno perkėlimo sintezės būdu suformuoti grafeno lauko tranzistoriai

VACh – voltamperinės charakteristikos

Terminai:

Lateralinis – šoninis, nutolęs nuo kūno vidurinės plokštumos

ĮVADAS

Dvimatės nanomedžiagos – vis didėjanti medžiagų šeima, pasižyminti stabiliomis struktūromis, kai atomų išsidėstymas vyrauja vienoje plokštumoje. Pirmoji tokia atrasta medžiaga – tai anglies alotropinė atmaina grafenas. Nepaisant įvairių gamtoje randamų anglies alotropų – deimanto, amorfinės anglies, grafito, būtent grafenas pasižymi vienomis įdomiausių savybių, tinkamų taikyti mechanikos, biotechnologijų, elektronikos bei optikos srityse. Plonas dangos sluoksnis yra optiškai pralaidus, be to, kovalentiniai ryšiai suteikia nepaprastą stiprumą. Šios savybės kartu su dideliu laidumu, kuriuo medžiaga pasižymi dėl delokalizuotų elektronų, leidžia grafeną naudoti kaip skaidrų laidininką optoelektronikoje bei taikyti jį Si paremtų fotoelektrinių įtaisų gamyboje. Be to, grafeną galima funkcionalizuoti įvairiais jonais arba pasitelkiant analites, o tai atveria galimybes taikyti grafeną kaip įprastą ar biologinį jutiklį.

Seniausias grafeno sintezės būdas yra eksfoliacija. Tam naudojamas grafitas, kurio sluoksniai yra atskiriami įvairiais mechaniniais ar ultragarsiniais metodais. Tokiu būdu gaunamas grafenas pasižymi savybėmis, artimomis tikrai monosluoksnei dangai. Visgi šis metodas turi svarbų trūkumą. Gaunamos medžiagos išeiga yra nedidelė, o efektyvus naudojamo grafeno plotas – mažas. Norint išgauti didesnio paviršiaus ploto grafeno dangas, reikia taikyti „iš apačios į viršų“ (angl. *bottom-up*) sintezės metodus. Pagrindinė didelio ploto grafeno auginimui taikoma technologija – tai cheminis nusodinimas iš garų fazės ant katalizinio pagrindo. Būtent varis ir nikelis yra dažniausiai naudojami padėklai, atitinkantys sėkmingo monosluoksnio augimo ir jo pasyvavimo kriterijus taikant šį metodą. Nepaisant to, grafeno sintezė ant šių pagrindų nėra lengvai pritaikoma puslaidininkių pramonėje bei optoelektronikoje dėl proceso metu reikalingų dangos pernešimų nuo metalo folijos ant norimų dielektrinių arba puslaidininkinių padėklų. Šioje stadijoje iškyla problemų – grafenas lankstosi, trūkinėja, ant jo paviršiaus lieka organinių adsorbatų, metalinio pagrindo likučių. Taip pat ant katalizinių pagrindų auginamam grafenui reikalinga aukšta proceso temperatūra.

Plazma aktyvuoto cheminio nusodinimo iš garų fazės metodas pašalina prieš tai aprašytų technologijų apribojimus. Pademonstruota, kad šiuo būdu galima atlikti tiesioginę grafeno sintezę ant pasirinktų dielektrinių bei puslaidininkių pagrindų, kaip antai Si. Taip pat proceso metu naudojama žemesnė, masinei gamybai palanki temperatūra. Pagrindiniai proceso trūkumai – tai didelis tarpkristalinių briaunų defektų tankis ir grafeno plėvelės netolygumas. Svarbu paminėti, kad metodas nėra gerai išvystytas, tad jo tobulinimas gali atnešti teigiamų rezultatų, kaip antai defektų tankio mažinimą, platesnę galimų pagrindų gamą bei dangų vientisumą.

Būtent skirtingų pagrindų naudojimas grafeno sintezėje yra vienas iš svarbesnių aspektų siekiant formuoti optoelektrinius įtaisus, susidedančius iš grafeno/Si heterodarinių. Tokių heterodarinių vaidmuo elektronikoje leistų valdyti krūvio pernašos mechanizmus ir galėtų pagerinti fotoelektrines prietaisų savybes. Šiuo atveju plazma aktyvuoto cheminio nusodinimo iš garų fazės būdas – ideali technologija, atverianti galimybes auginti grafeno struktūras ant pasirinktų paviršių be papildomų ir sudėtingų dangų perkėlimo etapų – taip formuojant grafeno/Si heterodariniais paremtus prietaisus.

Šiame baigiamajame darbe bus aptariami pagrindiniai plazma aktyvuoto cheminio nusodinimo iš garų fazės būdu sintetinto grafeno struktūros ypatumai bei analizė Ramano spektroskopija ir atominių jėgų mikroskopijos metodais. Taip pat bus tiriamos elektrinių prietaisų (fotodiodų ir lauko tranzistoriaus principu veikiančio biologinio jutiklio), suformuotų taikant grafeno plėveles, funkcinės savybes.

Tyrimo tikslas

Užauginti grafeną ant dažniausiai mikroelektronikoje naudojamų Si ir SiO_2 pagrindų, labai panašių į grafeno kristaline gardele pasižyminčio $Al_2O_3(0001)$ bei grafeno elektrines savybes gerinančio h-BN pasluoksnio, naudojant plazma aktyvuoto cheminio nusodinimo iš garų fazės metodą, bei ištirti plėvelių struktūrą ir elektrinių prietaisų, suformuotų taikant grafeno plėveles, funkcines savybes.

Tyrimo uždaviniai

1. Užauginti grafeno plėveles ant Si, SiO_2, $Al_2O_3(0001)$ bei h-BN/SiO_2 pagrindų, naudojant plazma aktyvuoto cheminio nusodinimo iš garų fazės metodą, ir ištirti jas taikant Ramano sklaidos spektroskopiją bei atominių jėgų mikroskopiją.
2. Ištirti žemos temperatūros (<600 °C) plazma aktyvuoto cheminio nusodinimo iš garų fazės metodo galimybes, formuojant grafeno sluoksnius ant SiO_2/Si(100) pagrindų.
3. Ištirti elektrinių prietaisų (fotodiodų ir lauko tranzistoriaus principu veikiančio biologinio jutiklio), suformuotų taikant grafeno plėveles, funkcines savybes.

Mokslinis naujumas

Šiame darbe atlikta grafeno sintezė naudojant tiesiogine plazma aktyvuoto cheminio nusodinimo iš garų fazės metodą, pasitelkiant plieninį dangtelį, apsaugantį nuo nepageidaujamo plazmos poveikio. Grafeno plėvelės formuotos ant mikroelektronikoje plačiai naudojamų (Si ir SiO_2), gimininga grafenui struktūra pasižyminčių ($Al_2O_3(0001)$) bei elektrines savybes gerinančių (h-BN/SiO_2) pagrindų.

Pademonstruotas tiesiogiai užauginto grafeno tinkamumas optoelektronikos ir bioelektronikos prietaisams gaminti bei nustatyti pagrindiniai dėsningumai, siejantys grafeno struktūrinę kokybę su suformuotų fotodiodų ir lauko tranzistoriaus principu veikiančių biologinių jutiklių jautriu.

Taip pat nustatytos kritinės žemos temperatūros (<600 °C) sintezės ribos, optimizuojant vandenilio ir metano dujų srautų santykį bei termodinaminį slėgį, kas atveria kelius integruoti grafeną į standartinę CMOS technologiją.

Pagrindiniai teiginiai

1. Mikrobangų plazma aktyvuotas cheminis nusodinimas iš garų fazės gali būti optimizuotas žemos temperatūros grafeno sintezei ant dielektrinių bei puslaidininkinių pagrindų, siekiant kontroliuoti medžiagos defektų lygį ir elektronines savybes.

2. Norint sumažinti nepageidaujamą tiesioginės plazmos poveikį pagrindui bei formuojamam grafenui sintezės metu, galima taikyti plieninį dangtelį, juo uždengiant pagrindą.
3. Sukurtas Ramano spektrų analizatorius tinka automatiniam įvairių tipų grafeno dangų, susintetintų mikrobangų plazma aktyvuoto cheminio nusodinimo iš garų fazės būdu, spektrams analizuoti.
4. Dielektrinio heksagoninio boro nitrido pasluoksniai dvigubai padidina grafeno/Si prietaisų trumpojo jungimo srovę ir fotosrovę dėl sumažėjusios paviršinės krūvininkų rekombinacijos.

Disertacijos struktūra

Ši disertacija paremta 5 moksliniais straipsniais, kurie atitinka autoriaus doktorantūros studijų metu atliktus tyrimus. Disertacijoje publikacijos pažymėtos raide [P] bei atitinkamai sunumeruotos ([**P1**, **P2**] ir t. t.). Moksliniame darbe pateikiama su doktorantūros tematika susijusi literatūros apžvalga, straipsniuose naudota metodologija ir straipsniuose pateiktų rezultatų, taip pat susijusių su doktorantūros užduotimi bei asmeniniu indėliu, apibendrinimas. Disertacijos turinys remiasi iškelto tikslo siekimu, taikant jau minėtiems uždaviniams spręsti. Mokslinį darbą sudaro 157 puslapiai, 21 paveikslėlis, 2 lentelės ir 142 šaltiniai.

Pirmajame disertacijos skyriuje, literatūros apžvalgoje, trumpai supažindinama su grafeno istorija, šios medžiagos struktūrinėmis ypatybėmis: konfigūracijomis, defektų tipais, galimais dariniais. Toliau trumpai apibendrinami grafeno sintezės metodai, pateikiami jų pranašumai ir trūkumai. Literatūros apžvalga užbaigiama pagrindiniais grafeno tyrimų metodais ir šios medžiagos taikymo elektronikoje pavyzdžiais.

Antrajame mokslinio darbo skyriuje apibendrinami pagrindiniai su publikacijų ir disertacijos turiniu susiję grafeno sintezės bei analizės metodai, supažindinama su spektroskopine, mikroskopine ir kita naudota įranga. Skyriuje aprašomi individualūs grafeno struktūrinės analizės algoritmai ir elektrinių matavimų schemos.

Trečiame skyriuje atskleidžiami pagrindiniai doktorantūros studijų metu gauti rezultatai, susiję su grafeno sinteze ant skirtingų pagrindų, bei apibendrinami grafeno struktūros ypatumai. Šiame skyriuje taip pat atskleidžiamos elektroninių prietaisų (fotodiodų ir lauko tranzistoriaus principu veikiančio biologinio jutiklio), suformuotų taikant tiesiogiai užaugintas grafeno plėveles, funkcinės savybės. Rezultatų skilties turinys apima iškeltus uždavinius ir pagrindžia pagrindinius teiginius.

Pabaigoje pateikiamos disertacijos išvados, susijusios su disertacijos uždaviniais, taip pat paryškinamas darbo mokslinis naujumas ir pateikiamos su tyrimo tematika susijusios rekomendacijos. Toliau pateikiama padėkų skiltis ir naudotos literatūros sąrašas, taip pat disertacijos santrauka anglų kalba. Disertacija užbaigiama autoriaus gyvenimo aprašymu bei publikacijų kopijomis, taip pat doktorantūros metu paskelbtų publikacijų ir konferencijų sąrašu.

Autorių indėlis į publikacijas

P1: Disertacijos autorius prisidėjo prie pirminio straipsnio rankraščio kūrimo bei redagavimo, atliko grafeno sintezę taikant MW-PECVD, suformavo grafeno

Ramano spektrų tyrimo metodiką, atliko Ramano spektrų analizę, išmatavo fotodiodų voltamperines charakteristikas, apdorojo Ramano sklaidos spektrų bei voltamperinių charakteristikų duomenis, parengė daugumą straipsnyje naudojamų vizualizacijų ir grafikų. R. Gudaitis prisidėjo prie idėjos konceptualizavimo, atliko grafeno sintezę taikant MW-PECVD, prisidėjo prie grafeno tyrimų taikant Ramano sklaidos spektroskopiją, parengė fotodiodų voltamperinių charakteristikų matavimo stendą. A. Vasiliauskas atliko fotodiodų elektrodų formavimą. A. Guobienė prisidėjo prie straipsnio redagavimo, atliko grafeno plėvelių morfologijos analizę AJM, prisidėjo prie straipsnyje naudojamų vizualizacijų bei grafikų kūrimo. Š. Meškinis prisidėjo prie idėjos konceptualizavimo, prisidėjo prie pirminio straipsnio rankraščio kūrimo bei redagavimo, prisidėjo prie straipsnyje naudojamų vizualizacijų bei grafikų kūrimo.

P2: Š. Meškinis prisidėjo prie idėjos konceptualizavimo, pirminio straipsnio rankraščio kūrimo bei redagavimo. R. Gudaitis prisidėjo prie tyrimų metodikos formavimo, atliko grafeno sintezę taikant MW-PECVD, prisidėjo prie grafeno tyrimų taikant Ramano sklaidos spektroskopiją. A. Vasiliauskas prisidėjo prie grafeno tyrimų taikant Ramano sklaidos spektroskopiją. A. Guobienė atliko grafeno plėvelių morfologijos analizę AJM, prisidėjo prie straipsnyje naudojamų vizualizacijų ir grafikų kūrimo. Disertacijos autorius suformavo grafeno Ramano spektrų tyrimo metodiką, atliko Ramano spektrų analizę, apdorojo Ramano sklaidos spektrų duomenis. V. Stankevič prisidėjo prie tyrimų metodikos formavimo, pirminio straipsnio rankraščio kūrimo bei redagavimo, atliko elektrinių matavimų duomenų analizę, prisidėjo prie straipsnyje naudojamų vizualizacijų bei grafikų kūrimo. S. Keršulis prisidėjo prie tyrimų metodikos formavimo, atliko elektrinių matavimų duomenų analizę, parengė dalį straipsnyje naudojamų vizualizacijų ir grafikų. A. Stirkė prisidėjo prie tyrimų metodikos formavimo, pirminio straipsnio rankraščio kūrimo ir redagavimo, prisidėjo prie tyrime naudojamų biologinių tirpalų paruošimo. E. Andriukonis prisidėjo prie G-FET kūrimo ir elektrinių savybių tyrimų, prie straipsnyje naudojamų vizualizacijų ir grafikų kūrimo. W. Melo prisidėjo prie rankraščio redagavimo, tyrime naudojamų biologinių tirpalų paruošimo, atliko duomenų analizę. V. Vertelis atliko grafeno sintezę taikant pernešimo metodą ir Ramano spektrų analizę. N. Žurauskienė prisidėjo prie idėjos konceptualizavimo, prie pirminio straipsnio rankraščio kūrimo bei redagavimo.

P3: Disertacijos autorius parengė pirminį straipsnio rankraštį ir jį redagavo, parengė grafeno sintezės metodiką ir atliko sintezės eksperimentus taikant MW-PECVD, suformavo grafeno Ramano spektrų tyrimo metodiką, atliko Ramano spektrų analizę, parengė daugumą straipsnyje naudojamų vizualizacijų ir grafikų. Š. Meškinis prisidėjo prie straipsnio rankraščio rengimo ir jo redagavimo. N. Žurauskienė prisidėjo prie idėjos konceptualizavimo, straipsnio rankraščio redagavimo. A. Guobienė prisidėjo prie idėjos konceptualizavimo, atliko grafeno plėvelių morfologijos analizę AJM, prisidėjo prie straipsnio rankraščio redagavimo.

P4: Š. Meškinis prisidėjo prie idėjos konceptualizavimo, pirminio straipsnio rankraščio kūrimo bei redagavimo, atliko dalies Ramano sklaidos spektrų analizę, prisidėjo prie straipsnyje naudojamų vizualizacijų bei grafikų kūrimo. A. Lazauskas prisidėjo prie idėjos konceptualizavimo, pirminio straipsnio rankraščio kūrimo ir

redagavimo, prisidėjo prie straipsnyje naudojamų vizualizacijų ir grafikų kūrimo. Disertacijos autorius prisidėjo straipsnio rankraščio redagavimo, suformavo grafeno Ramano spektrų tyrimo metodiką, atliko Ramano spektrų analizę, apdorojo Ramano sklaidos spektrų duomenis, prisidėjo prie straipsnyje naudojamų vizualizacijų ir grafikų kūrimo. A. Guobienė atliko grafeno plėvelių morfologijos analizę AJM. R. Gudaitis atliko grafeno sintezę MW-PECVD būdu, prisidėjo prie Ramano sklaidos spektrų analizės.

P5: Š. Meškinis prisidėjo prie idėjos konceptualizavimo, pirminio straipsnio rankraščio kūrimo ir redagavimo, prisidėjo prie straipsnyje naudojamų vizualizacijų ir grafikų kūrimo. Disertacijos autorius prisidėjo straipsnio rankraščio redagavimo, suformavo grafeno Ramano spektrų tyrimo metodiką, atliko Ramano spektrų analizę, apdorojo Ramano sklaidos spektrų duomenis prisidėjo prie straipsnyje naudojamų vizualizacijų ir grafikų kūrimo. A. Vasiliauskas prisidėjo prie h-BN sintezės taikant HIPIMS, atliko fotodiodų elektrodų formavimą. V. Stankus prisidėjo prie h-BN sintezės taikant HIPIMS. A. Guobienė atliko grafeno plėvelių morfologijos analizę AJM, prisidėjo prie straipsnyje naudojamų vizualizacijų ir grafikų kūrimo. K. Lukoševičius išmatavo fotodiodų voltamperines charakteristikas. A. Jasutis išmatavo fotodiodų voltamperines charakteristikas. R. Gudaitis atliko grafeno sintezę MW-PECVD būdu, prisidėjo prie Ramano sklaidos spektrų analizės.

Visi autoriaus paskelbtų disertacijoje naudotų straipsnių leidėjai ir bendraautoriai sutinka su straipsnių kopijų naudojimu šioje disertacijoje.

1. LITERATŪROS APŽVALGA

Ilgą laiką buvo manyta, kad medžiagos gali egzistuoti tik tūrinės konfigūracijos. XX a. kvantinių taškų atradimas įrodė, kad medžiagos gali turėti mažiau nei tris laisvės laipsnius (angl. *degrees of freedom*), tačiau jų struktūros išlieka trimatės [1]. Nors mokslininkai tyrė grafito sandarą [2] ir skaičiavimais įrodė, kad atskiri jo sluoksniai gali egzistuoti [3], tai tebuvo užuomina, kad netrukus bus atrasta pirmoji dvimatė medžiaga. Didžiausias proveržis pasiektas prasidėjus XXI a., kai Andre Geim'o ir Konstantin'o Novoselov'o mokslinė grupė atrado atomiškai plonus grafito sluoksnius [4], dabar žinomus kaip grafenas. Už šiuos nuopelnus 2010 m. mokslininkai buvo apdovanoti Nobelio premija. Šiuo metu grafenas tiriamas įvairiose mokslinėse šakose: mechanikos, biologijos, elektronikos bei optikos. Mokslinės bendruomenės susidomėjimas šia medžiaga auga, tačiau optimalių sintezės metodų, kai išlaikoma grafeno struktūra ir užtikrinamas didelis grafeno plėvelių paviršiaus plotas, nėra, o tai sumažina medžiagos pritaikymo galimybes [5,6].

1.1. Grafenas

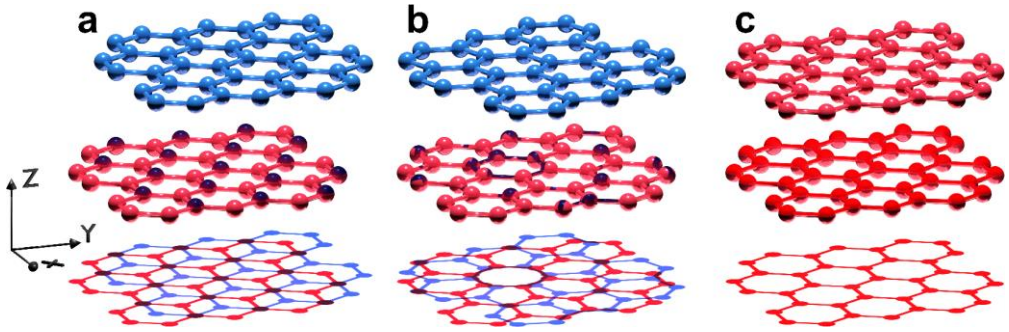
1.1.1. Monosluoksnis ir keliasluoksnis grafenas

Grafenas – šešiakampiu anglies atomų išsidėstymu pasižymintis grafito monosluoksnis. Matematiniu požiūriu, tokia heksagoninė struktūra yra pati efektyviausia dėl didelio perimetro ir ploto santykio. Būtent 1999 m. įrodyta bičių korio konjektūra (angl. *Honeycomb Conjecture*) atspindi šia geometrine figūra paremtų struktūrų unikalumą [7]. Grafenas sudarytas iš sp^2 hibridizacijos anglies atomų. Plokštumoje tarp anglies atomų vyrauja stiprūs kovalentiniai ryšiai, o keliasluoksniame grafene jas jungia silpnos elektrostatinės Van der Valso jėgos. Šie sluoksniai yra atskirti 0,335 nm atstumu, kaip patvirtinta atspindžio bei kontrasto spektroskopijos metodais [8], o tai atitinka grafito tarpsluoksnį atstumą [9]. Monosluoksnio grafeno elementarusis narvelis susideda iš dviejų anglies atomų, kurie formuoja trikampio formos tinklą, o tarpusavyje atomai atskirti 0,142 nm atstumu [10]. Dėl šios unikalios struktūros vienas grafeno sluoksnis yra optiškai skaidrus (pralaidumas siekia ~97,7 % regimame diapazone [11]), turi didžiulį krūvininkų judrį (200,000 $cm^2\ V^{-1}\ s^{-1}$ [12]), išsiskiria mechaninėmis savybėmis (Jungo modulis 1 TPa [13]) ir pasižymi dideliu šiluminiu laidumu (3000–5000 Wm/K [14]). Dėl šių savybių grafeno reikšmė technologijų raidai neabejotina, tačiau ji labiausiai juntama optoelektronikoje, kur pasireiškia šios medžiagos savybių visapusiškumas ir tarpusavio sąveika.

Grafenas, sudarytas iš daugiau nei vieno bičių korio pavidalu išsidėsčiusių anglies atomų sluoksnio (<10 sluoksnių [15]), vadinamas daugiasluoksniu grafenu. Nepaisant dvimatės struktūros, medžiaga pasižymi panašiomis fizikinėmis savybėmis net ir tuomet, kai ją sudaro keli grafeno sluoksniai. Pagrindinis kelių vienas ant kito esančių grafeno lakštų išsidėstymas yra vadinamas Bernalio išsidėstymu, kai sluoksniai yra pastumti vienas kito atžvilgiu taip, kad vieno sluoksnio anglies atomai persidengtų su kito sluoksnio anglies atomų šešiakampio žiedo centru [10] (**1 pav., a**). Nepaisant tokios sluoksnių tvarkos, galimi nuokrypiai ir neretai pastebimas šių sluoksnių tarpusavio prasiskyrimas nedideliais kampais (~10° - 30°). Dėl šios

priežasties tarp grafeno sluoksnių esantis atstumas išauga (>0,335 nm) [10]. Toks grafenas vadinamas turbostratiniu [16] (**1 pav., b**). Manoma, kad gali egzistuoti ir trečia galima keliasluoksnio grafeno konfigūracija. *Ab-initio* skaičiavimai rodo, jog lygiagrečiai, vienas po kitu sugretinti sluoksniai turėtų būti metastabilūs [17,18] (**1 pav., c**). Savo ruožtu atstumas tarp tokių sluoksnių turėtų būti gerokai mažesnis (0,156 nm [17]), tačiau realių šios būsenos stebėjimų kol kas nedaug [19,20,21,22,23,24]. Nepriklausomai nuo keliasluoksnio grafeno konfigūracijų, tokio tipo medžiagos taikymų yra apstu, pavyzdžiui, skaidriuose elektroduose, mažos varžos elektrinių takelių gamyboje ir šilumos sklaidos įrenginiuose [25,26]. Be to, galimybė kontroliuoti grafeno sluoksnių kiekį prisidėtų prie anglimi paremtų medžiagų taikymo perspektyvų.

Taigi, nepriklausomai nuo to, ar grafenas yra monosluoksnis, ar daugiasluoksnis, jis pasižymi unikaliomis cheminėmis, optinėmis, elektrinėmis bei mechaninėmis savybėmis. Pritaikius kontroliuojamą grafeno sintezę, tai leistų šią medžiagą taikyti kuriant įvairius įtaisus.

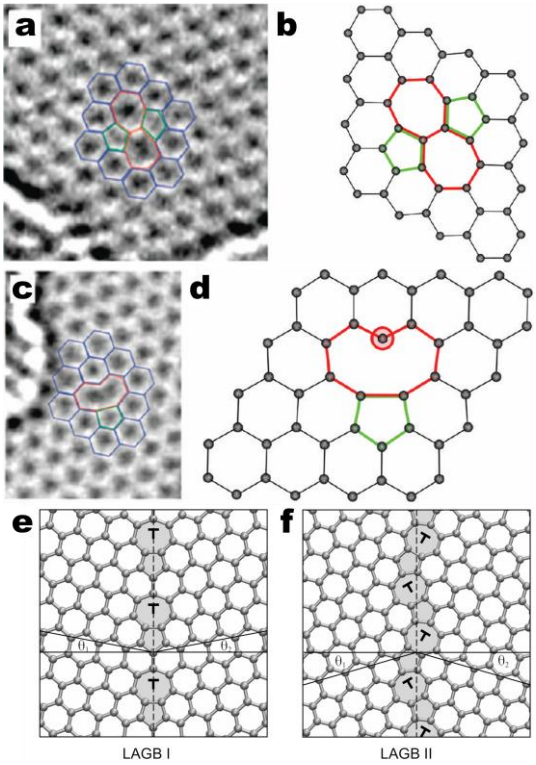


1 pav. Pagrindinės galimos keliasluoksnio grafeno konfigūracijos: Bernalio išsidėstymas (a), turbostratinis (b), metastabilus (c)

1.1.2. Grafeno defektai

Grafenas retai egzistuoja kaip vientisas anglies atomų darinys. Medžiagoje vyrauja įvairūs defektai, kurie, priklausomai nuo taikymo, yra nepageidaujami arba, atvirkščiai, leidžiantys grafeną derinti su sudėtingesniais įtaisais, tarp jų ir puslaidininkiais. Pagrindiniai defektų tipai matomi 2 paveiksle. Vienas unikaliausių grafene pastebimų defektų yra Stone-Waleso defektas (**2 pav., a, b**), kuris nereikalauja jokių atimtų ar pridėtų atomų [27]. Šis defektas apsiriboja dviejų atomų poros pasisukimu 90° kampu. Jis buvo atrastas tyrinėjant grafitą [28]. Nors iš pirmo žvilgsnio šio tipo defektui formuoti reikalingas energingas atomų judėjimas (defekto susidarymo energija – E_f = ~5 eV), jo susiformavimas galimas vykstant įvairiems elektronų susidūrimams su gardele [29]. Antrasis defektų tipas ir bene dažniausiai pasitaikantis defektas visose kristalinėse struktūrose – tai atomų vakansijos. Šio tipo defektai grafene formuoja dvi atomų žiedų poras, kurių viena susideda iš 5 atomų, kita – 9 atomų (**2 pav., c, d**). Vakansijų susidarymo energija yra aukšta, siekianti 7,5 eV [27]. Joninis arba elektroninis švitinimas yra pagrindiniai veiksniai, kurie lemia vakansijų atsiradimą grafene [30]. Žinoma, šie reiškiniai turi turėti pakankamos energijos, kad išjudintų anglies atomus gardelėje, savo ruožtu struktūroje sukurdami

skyles. Atitinkamai, didinant terpės temperatūrą, šis procesas paspartinamas ir gaunamas didesnis šio tipo defektų tankis [30]. Svarbu paminėti, kad grafene egzistuoja ne tik lokalūs defektai, kaip Stone-Waleso ir įprastiniai įterptiniai atomai bei vakansijos. Dėl dvimatės medžiagos prigimties ir sluoksnių lygumo grafeno struktūra neišvengiamai užsibaigia plėvelės kraštuose. Šiose srityse įprastinio, laisvai stovinčio (angl. *free-standing*) grafeno atveju kraštiniai atomai yra pasyvuojami vandenilio atomais dėl mažos aktyvacijos energijos [31]. Tačiau kai grafenas formuojamas cheminiu nusodinimu iš garų fazės, galimas kelių augimo užuomazgų susidarymas [27]. Taip vienoje plokštumoje augantys keli atskiri medžiagos domenai pradeda jungtis. Galutiniame sintezės etape, suformavus bendrą medžiagos plėvelę, galima matyti grūdelių ribos defektus (**2 pav., e, f**). Apskaičiavus energijos juostų sandaras, pastebėta, kad skirtingi grūdelio ribos defektai turi didžiulę įtaką medžiagos elektrinėms savybėms [32]. Siekiant to išvengti, svarbu mažinti augimo užuomazgų tankį. Taip pat dėl išvardintų defektų bei didelio kiekio užuomazgų grafenas gali glamžytis ir formuoti nanokristalus. Ši grafeno savybė dažnai nėra pageidautina, tačiau neišvengiama taikant žemos temperatūros sintezės metodus, kurie nepajėgūs formuoti vakansijų ar priemaišų atomų dėl didelio defektų susidarymo energijos poreikio [27].



2 pav. Grafene vyraujančių defektų pavyzdžiai: (a, b) Stone-Waleso defektas, (c, d) vakansija, (e, f) grūdelių ribos defektai [32]. (a, c) pralaidumo elektroninės mikroskopijos vaizdai [33], (b, d) atominės struktūros, apskaičiuotos taikant tankio funkcionalo teoriją [27]

Dėl įvairių defektų iškraipoma grafeno geometrija, o tai keičia medžiagos mechanines, chemines, optines ir elektrines savybes. Idealiam grafeno atvejui išvestos Dirako lygties taikyti negalima, tad fizikinių ir cheminių savybių skaičiavimo metodai tampa sudėtingesni. Tačiau aišku, kad defektai nulemia elektronų bangų sklaidą, keičia elektronų sklidimo kryptis, sustiprinami rehibridizacijos reiškiniai. Dėl to, pavyzdžiui, vakansijos ir Stone-Waleso defektai atveria draustinę juostą, skatina lokalių magnetinių momentų atsiradimą ir mažina Jungo modulį, o grūdelių ribos defektai gali sukelti tobulą ar dalinį krūvininkų atspindį arba pralaidumą [27].

Taigi, nors ir grafenas pasižymi neįprasta dvimate struktūra bei sluoksnių išsidėstymu, įvairiausi medžiagoje vyraujantys defektai kelia iššūkių unikalių grafeno savybių eksploatacijai, pavyzdžiui kuriant stiprų ir skaidrų laidininką. Nors įvairūs defektai daro neigiamą įtaką grafeno fizikinėms savybėms, gebėjimas juos kontroliuoti atvertų plačias šios medžiagos taikymo galimybes.

1.1.3. Grafeno dariniai

Grafenas, nepaisant medžiagos apibrėžimo, dėl pakankamai mažų susidarymo energijų gali ne tik turėti daug defektų, bet ir sudaryti įvairius darinius. Nors daugiausia dėmesio sulaukia šios medžiagos monosluoksnis, tokio tipo grafeno formavimas yra sudėtingas. Iš tiesų, daugeliu atvejų pastebimi įvairios konfigūracijos grafeno nanodariniai. Pavyzdžiui, 2002 m., prieš grafeno atradimą, pastebėta, kad MW-PECVD būdu iš anglies turinčių dujų vykdytose sintezėse susidaro anglies nanosienos [34,35]. Tokio tipo dariniai buvo prilyginami anglies nanovamzdeliams, kurie tuo metu jau buvo plačiai tyrinėjami. Neilgai truko, kol vertikalias anglies struktūras pradėjo sieti su grafenu, anglies atomų monosluoksniu. Tokioms nanosienoms formuoti reikalingas kryptingas augimas, statmenas naudojamam pagrindui. Būtent dėl šios priežasties plazma aktyvuota medžiagų sintezė padeda sukurti kryptingą krūvininkų judėjimą ir pakankamą plazmos tankį, kurio reikia formuojant vertikalias grafeno dangas [35].

Vertikalios grafeno dangos nėra vieninteliai grafenu paremti dariniai. Iš tiesų, grafeno funkcionalizavimas leidžia sukurti skirtingo tipo grafeno darinius. Vienas labiausiai paplitusių darinių – grafeno oksidas (GO). Tokio tipo medžiaga gaunama oksiduojant grafitą [36,37]. GO pasižymi išskirtinėmis savybėmis, kurios labiausiai atsiskleidžia jutikliuose (aptinka milijardines, cheminiuose ginkluose naudojamų junginių dalis [36]). GO gali būti funkcionalizuotas dar labiau, taip išnaudojant medžiagos potencialą elektrocheminių bei biomedicininių taikymų atveju [38]. Kita paplitusi funkcionalizuoto grafeno forma – hidrogenizuotas grafenas (HG). Tokio tipo grafenas lengvai formuojamas pasitelkiant vandenilio plazmą [39]. Parodyta, jog sp^3 (C-H) ryšiai neardo anglies atomų korio struktūros, tačiau užpildymas vandenilio atomais įsisotina ties 25% [39]. Iš tiesų, tokios struktūros nėra griežtai dviejų dimensijų, nes papildomi vandenilio atomai paveikia grafeno gardelę. Atlikti tyrimai rodo, kad galimos net trys tokio tipo grafeno konfigūracijos: C-grafanas, B-grafanas bei W-grafanas [40,41]. Hidrogenizuoto grafeno tyrimams taip pat taikoma Ramano sklaidos spektroskopija, tačiau ji negali tiksliai nusakyti hidrogenizacijos laipsnio [41].

1.2. Grafeno sintezė

Grafenas atrastas taikant labai supaprastintą sintezės metodą, mikromechaninį skalumą, kai keli viršutiniai grafito sluoksniai atplėšiami naudojant lipnią juostą [42]. Tačiau šiuo metu yra išvystyta daug skirtingų metodų, iš kurių vieni pranašiau užtikrina grafeno kokybę, o kiti – grafeno išeigą. Nepriklausomai nuo to, kad grafenas pasižymi unikaliomis savybėmis ir struktūra, šios medžiagos sintezė gali būti įvairi, tiek taikant iš viršaus į apačią (angl. *Top down*), tiek ir iš apačios į viršų (angl. *Bottom up*) metodus.

1.2.1. Grafeno sintezė iš viršaus į apačią

Būtent mechaninis ir cheminiai sluoksnių atskyrimo metodai yra vieni iš pagrindinių grynojo grafeno gavimo būdų [5]. Tokio tipo grafenas pasižymi dideliais grafeno kristalais, kurie neturi daug defektų, tačiau mechaninio atskyrimo (angl. *Scotch tape*) metodas yra labai lėtas ir netikslus. Tokiu būdu gauti grafeno kristalai dažniausiai naudojami grafeno fizikinių savybių tyrimuose, elektrinių įrenginių prototipavime, bet ne pramoninėje gamyboje, kur šių sluoksnių pritaikymas yra labai sudėtingas [43]. Be mechaninio grafeno sluoksnių atskyrimo, naudojamas ir elektrocheminis įvairių formų grafito skalumas, kuris, nepaisant sudėtingumo, geba sintetinti grafeną didesne išeiga [44]. Pirmojoje elektrocheminėje grafeno sintezėje buvo naudojami grafito elektrodai ir dejonizuotame vandenyje ištirpintas poli(natrio-4-stirensulfonato) elektrolitas [45]. Šiuo metu tai vis dar vienas iš pagrindinių grafeno masinės gamybos metodų. Elektrocheminiu būdu gauto grafeno dispersija yra labai stabili. Nepaisant didelės išeigos ir metodo patikimumo, grafeno lateralinis dydis yra mažas, apie 1–40 μm. Būtent todėl tokios grafeno dangos pramonėje netinkamos. Iš viršaus į apačią metodų šeimai priklauso ir ultragarsu paremtas grafeno lakštų atskyrimas, tačiau tokio tipo sintezė neužtikrina didelės grafeno išeigos ir lateralinio medžiagos dydžio [43].

1.2.2. Grafeno sintezė iš apačios į viršų

Grafeno sintezė galima naudojant ir iš apačios į viršų metodus. Vienas jų – pirolizė. Šis metodas remiasi anglies atomus turinčių cheminių medžiagų skaidymu. Tarkime, SiC pirolizės 1280 °C temperatūroje metu Si desorbuoja, taip palikdamas anglies atomą [43]. Savo ruožtu anglies atomai formuoja grafeno kristalus ant 6H-SiC(0001) paviršiaus [46]. Tokios sintezės trūkumai – mažas grafeno kristalitų dydis ir prasta grafeno kokybė [46]. Parodyta, kad, naudojant metalo tarpsluoksnius, galima gauti kokybiškas kelių grafeno sluoksnių dangas, kurių storį galima kontroliuoti keičiant atkaitinimo temperatūrą [46]. Pavyzdžiui, grafeno sintezę atliekant ant deimanto nanokristalitų, kai naudojamas Ni tarpsluoksnis, galima gauti pakankamai aukštos kokybės grafeno dangas [47], tačiau tokių dangų dydis taip pat nepritaikomas pramoninėje gamyboje.

Vienas iš perspektyviausių grafeno sintezės metodų yra cheminis nusodinimas iš garų fazės (CVD) [6]. Taikant CVD sintezę, paprastai grafenas auginamas ant katalizinių pagrindų, naudojant organinių dujų pirmtakus. Šiuo atveju sintezė remiasi dujinių reagentų aktyvacija bei cheminėmis reakcijomis, vykstančiomis aukštoje temperatūroje, po kurių formuojami grafeno sluoksniai ant pasirinktų pagrindų [6].

Būtent vario plėvelės plačiai naudojamos auginant grafeną, nes anglies tirpumas varyje yra mažas [48]. Taip pat pademonstruota, kad grafeno sintezė ant vario pagrindų yra kontroliuojama paviršinių reiškinių ir iš dalies save ribojanti [6]. Dėl išvardintų priežasčių grafeno kokybė yra itin aukšta, formuojamos dangos yra vieno atomo storio ir užima didelį paviršiaus plotą. Kita vertus, grafeno dangas, užaugintas ant vario plėvelių, galima pritaikyti tik keliose srityse, daugiausia saugant varines vielas nuo korozijos ir išnaudojant grafeno šiluminį laidumą lustų technologijose [49,50]. Norint išlaikyti ant vario užauginto grafeno struktūrą, tačiau naudoti katalizinėmis savybėmis nepasižyminčius pagrindus (dielektrikų, puslaidininkių), galima taikyti CVD sintezę ant jau minėto vario plėvelių, o ją atlikus papildomai vykdyti grafeno perkėlimo procedūrą [51]. Tokiu atveju grafeno pusėje padengiamas polimetilmetakrilatas (PMMA) centrifuginio dengimo būdu. Tuomet apačioje esantis vario pagrindas ėsdinamas merkiant PMMA/grafeno/Cu dangas geležies nitrato tirpale, kol PMMA/grafeno plėvelė pradeda laisvai plūduriuoti. Pasirinktas pagrindas uždedamas ant grafeno dangos, o PMMA pašalinamas acetono vonelėje [51]. Viena vertus, tokiu būdu perkeltas grafenas išlaiko savo atominę struktūrą ir sluoksnių storį [51], kita vertus – perkėlimo procedūra yra gana sudėtinga, pasižymi prastu pasikartojamumu, gali įnešti papildomų organinių junginių perkėlimo metu [52] ir suglamžyti grafeno dangas, jas perkeliant ant kitų pagrindų [53]. Iš pirmo žvilgsnio nuostabus grafeno sintezės metodas CVD susiduria su sunkumais, kai stengiamasi išlaikyti grafeno kokybę ir visapusį medžiagos suderinamumą su įvairiais pagrindais.

1.2.3. Mikrobangų plazma aktyvuotas cheminis nusodinimas iš garų fazės

Siekiant išvengti CVD metodui privalomų katalizinių pagrindų naudojimo ir norint sumažinti proceso temperatūrą, galima taikyti plazma aktyvuotą cheminį nusodinimą iš garų fazės (PECVD). Šiuo atveju dujų pirmtakai skaidomi nenaudojant aukštos ~1000 °C temperatūros, nes trūkstama energija gaunama iš plazmoje esančių didelės energijos elektronų [54]. Procesas yra labai panašus kaip įprastinis CVD, tačiau efektyviam molekulių skilimui užtikrinti svarbu atsižvelgti į naudojamą plazmos generatoriaus galią [54]. Dažniausiai naudojama nuotolinė plazma, tokiu būdu grafeno užuomazgų susidarymas ir augimas bei dujų molekulių skilimo reiškiniai yra atskiriami [55]. Vis dėlto tokia PECVD konfigūracija nėra praktiška ir užima daug vietos. Norint sumažinti įrangos gabaritus, neišvengiamai susiduriama su tiesioginės plazmos problemomis. Esant artimam plazmos poveikiui, pagrindas, ant kurio vykdoma grafeno sintezė, ardomas veikiant jonams, todėl būtinas augimo mechanizmo atskyrimas nuo tiesioginio plazmos poveikio [56]. Tam tikslui gali būti naudojami plieniniai dangteliai, apsaugantys bandinius nuo greito ėsdinimo [**P1**]. Nors tyrimų, kuriuose PECVD sintezei taikomas papildomas apsauginis dangtelis, yra nemažai, daugelyje jų naudojami sudėtingi dujų mišiniai [56], anksčiau minėti kataliziniai pagrindai [57,58], taip pat atliekamos papildomos pagrindų paruošimo procedūros, skatinančios užuomazgų susidarymą [58]. Bandymų tiesiogiai sintetinti grafeno plėveles ant puslaidininkių ir dielektrinių pagrindų PECVD metodais nėra daug.

1.3. Grafeno analizės metodai

1.3.1. Atominių jėgų mikroskopija

Plonoms dangoms labai aktualūs paviršiaus morfologijos tyrimai, leidžiantys suprasti sintezės dinamiką, auginamos dangos ir pagrindo sąlyčio paviršiuje vykstančius reiškinius. Ypatingas dėmesys skiriamas vieno ar kelių atomų storio dangoms, kai įprastiniai metodai, tokie kaip optinė mikroskopija (dėl per mažos plonų dangų įtakos šviesai) ir peršviečiamoji elektroninė mikroskopija (dėl sunkiai pasireiškiančių dvimačių kristalų požymių), nėra priimtini. Ne išimtis ir grafeno plėvelės. Parodyta, kad grafeno dangų morfologijos [59,60] storio [61,62] bei adhezijos [63] tyrimams lengvai taikoma atominių jėgų mikroskopija (AJM). Nors metodas labiausiai patikimas, kai analizuojamas vieno ar kelių sluoksnių, mažai defektų turintis grafenas [59,62,64], jį galima taikyti ir dideliu paviršiaus šiurkštumu pasižyminčioms dangoms [65,66], tačiau tai įmanoma naudojant pusiau kontaktinį virpančio zondo režimą. Svarbu paminėti, kad dažnai dėl didelio lankstumo grafenas atkartoja pagrindo, ant kurio yra suformuotas, paviršiaus morfologiją, o į tai atsižvelgti yra ganėtinai sunku, ypač kai taikomi pagrindo paviršių modifikuojantys sintezės metodai, tokie kaip CVD ir PECVD. Taip pat šiais metodais formuojamas grafenas retai pasižymi itin lygiais paviršiais, todėl pusiau kontaktinio virpančio zondo režimas yra būtinas [67].

1.3.2. Ramano sklaidos spektroskopija

Atsižvelgiant į įvairias grafeno konfigūracijas, medžiagoje minimus defektus bei sluoksnių kiekį, reikalingas patikimas struktūros analizės metodas, gebantis identifikuoti skirtingo tipo grafeno plėveles. Dėl stiprios fononinės sąveikos įvairiose grafeno plėvelėse pastebimi aiškūs akustinių ir optinių virpesių pokyčiai [68]. Tam įtakos turi π elektronų dispersija, kur elektronai tampa delokalizuoti, todėl rezonansiniai reiškiniai yra itin stiprūs [10,68,69]. Elastinius virpesius lengva sukelti pasinaudojant šviesa, o atspindėtos šviesos bangos ilgio pokyčius nesunku priskirti skirtingoms modoms. Būtent dėl šių priežasčių Ramano sklaidos spektroskopija yra nepamainomas įrankis vertinant grafeno kokybę, net jei ir danga tėra sudaryta iš vieno anglies atomų sluoksnio [68].

Skirtingos vibracijos grafeno gardelėje turi būdingus atsakus Ramano spektruose, todėl gardelės iškraipymai ir storio informacija lengvai registruojama [10,68,69]. Trys smailės yra pagrindinės ir pastebimos daugelyje grafeno Ramano spektrų. Dvi iš jų, D ir G smailės, priskiriamos visiems poli-aromatiniams angliavandeniliams. G smailė susijusi su įtempiais esančiais sp^2 atomų porose, o D smailė – tai sp^2 atomų žiedų „kvėpavimo“ moda, atsirandanti dėl fononų sąveikos su defektais [10,69]. Trečioji, 2D smailė yra susijusi su antros eilės Ramano sklaida – procese dalyvauja ne vienas, o du fononai [10]. Nors ši moda yra dvigubai didesnė už D modą ($\omega_{2D} \sim 2\omega_D$), jos atsiradimas galimas ir tuomet, kai defektai neegzistuoja [10]. Bendrame Ramano spektrų fone visos šios smailės yra labai intensyvios regimoje šviesoje, būtent dėl vyraujančių sp^2 ryšių [69]. Kai naudojamas 2,41 eV (~514,5 nm) šviesos šaltinis, D smailė matoma ties 1350 cm^{-1}, G smailė ties ~1582 cm^{-1}, o 2D smailė ties ~2700 cm^{-1} [10]. Taip pat pastebima ir papildoma smailė, esanti ties

~1620 cm^{-1}, kuri taip pat susijusi su grafene esančiais defektais, jų tankiu bei tipu [10]. Grafeno Ramano sklaidos spektruose taip pat matomos ir kiek mažiau ryškios smailės (ties ~2450 cm^{-1}, ~2900 cm^{-1}, ~3240 cm^{-1}), tačiau dėl smailių prigimties bei intensyvumo jų analizė nesuteikia daug informacijos apie grafeno struktūrą [68].

Ramano spektre matomų smailių aptikimas leidžia kokybiškai įvertinti grafeno plėveles, tačiau to neužtenka medžiagos struktūrai nuodugniau paaiškinti. Norint nustatyti grafeno kokybę, reikalinga smailių intensyvumų (I) santykių, padėčių (Pos) bei puspločių (FWHM) analizė [10,68,69]. Būtent dėl to Ramano sklaidos spektroskopijoje didžiąją dalį sudaro duomenų interpretavimas. Vienas iš pagrindinių parametrų, į kurį verta atkreipti dėmesį, tai 2D bei G smailių intensyvumų santykis (I_{2D}/I_G), kuris nurodo grafeno storį. Jei $I_{2D}/I_G \geq 2$, toks grafenas laikomas vieno sluoksnio, jei $I_{2D}/I_G \sim 2$, tuomet grafenas yra poros sluoksnių, o kai $I_{2D}/I_G \sim 0{,}5$, tai grafenas yra keleto sluoksnių [70]. Pirmasis šią priklausomybę aprašė A. C. Ferrari's [15], tačiau neilgai truko, kol šis dėsningumas buvo patvirtintas eksperimentiškai [71]. Atitinkamai D ir G smailių santykis (I_D/I_G) nurodo defektų tankį, kur vertės >1 yra būdingos daug defektų pasižyminčioms grafeno plėvelėms [72]. Norint įvertinti ne tik defektų kiekį, bet ir dominuojančių defektų tipą, naudojamas $I_D/I_{D'}$ parametras [73]. Nustatyta, kad $I_D/I_{D'}$ gali aptikti sp^3 hibridizacijos defektus ($I_D/I_{D'} \simeq 13$), vakansijas ($I_D/I_{D'} \simeq 7$) bei grūdelių ribos defektus ($I_D/I_{D'} \simeq 3{,}5$) [73]. Smailių padėtys ir puspločiai yra papildomi parametrai, indikuojantys medžiagoje aptinkamus įtempius, legiravimo įtaką bei struktūros iškraipymus, kurie nebūtinai susiję su defektais [70,74,75]. Pavyzdžiui, 2D smailės padėties (Pos_{2D}) pokytis didesnių banginių skaičių link rodo grafeno sluoksnių kiekio didėjimą, o 2D smailės puspločio ($FWHM_{2D}$) mažėjimas iki 30 cm^{-1} priskiriamas sluoksnių kiekio artėjimui prie 1 [70]. G smailės pozicija taip pat susijusi su sluoksnių skaičiumi – smailės centrui slenkantis į mažesnių banginių skaičių pusę, matomas sluoksnių skaičiaus padidėjimas, tačiau G smailės pusplotis aiškios priklausomybės nuo sluoksnių skaičiaus nerodo [70].

Taigi, atsižvelgiant į Ramano sklaidos spektroskopijos suteikiamą informaciją apie grafeno struktūrą, natūralu, kad šis bandinio neardantis metodas yra nepamainomas įrankis skirtingų tipų grafeno kokybei vertinti. Derinant šį analizės metodą su mikroskopija, galima analizuoti tiek grafeno morfologiją, elektrines savybes, tiek ir grafene esančius defektus, priemaišas.

1.4. Grafeno taikymas elektronikoje

Nors grafeno taikymo sričių apstu, visgi medžiagos išskirtinės fizikinės savybės geriausiai atsiskleidžia elektronikoje dėl mažos paviršinės varžos, mechaninio lankstumo, jau minėto elektrinio laidumo bei regimosios šviesos pralaidumo [76,77,78]. Potencialios elektronikos kryptys, kuriose galima atskleisti grafeno savybes, tai aukšto dažnio tranzistoriai, saulės elementai, biologiniai jutikliai ir kt. Būtent šiose srityse grafenas gali būti naudojamas kaip skaidrus ir laidus elektrodas [77]. Sujungus šias fizikines savybes su dideliu grafeno lankstumu, galima suformuoti daugiafunkcines elektrines sistemas.

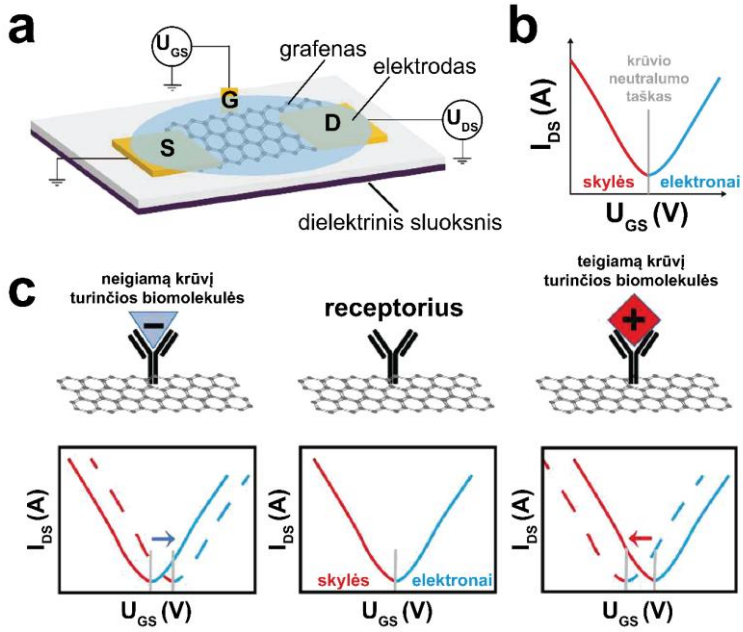
1.4.1. Fotodiodai

Grafeno kaip skaidraus ir laidaus elektrodo savybės labiausiai išryškėja fotodioduose [79,80]. Pagrindiniai fotodiodo parametrai, nusakantys įrenginio efektyvumą, – atsakas, kvantinis efektyvumas, atsako trukmė bei fotodetektoriaus talpa. Iš šių su fotodetektoriaus gebėjimu generuoti srovės stiprį (fotosrovę) susiję atsakas, kvantinis efektyvumas, šviesos konversijos efektyvumas. Atsakas apibūdina srovės stiprio fotodiode santykį su krintančios šviesos kiekiu, o kvantinis efektyvumas parodo pirminių elektrono ir skylės porų skaičiaus santykį su tuo pat metu kritusių fotonų skaičiumi. Siekiant nustatyti, ar sukurtas įtaisas pasižymi fotodiodams būdingu veikimu, nebūtina remtis atsaku ir kvantiniu efektyvumu, kuriuos skaičiuojant yra svarbi fotodiodo aktyvioji sritis ir užpildymo faktorius. Kvantinis efektyvumas yra tiesiogiai susijęs su dar vienu parametru – trumpojo jungimo srove (I_{tj}), kuri nurodo maksimalią fotodiodo srovę, kai įtampa yra lygi nuliui [81]. Fotodiodo sandūroje esančiam potencialui nustatyti yra naudojama atvirosios grandinės įtampa (U_{ag}). Šiuo atveju srovės stipris ir sandūros įtampa generuojama tik šviesos šaltiniu. Būtent U_{ag} bei I_{tj} vertės leidžia nustatyti sukurto fotodiodo ar saulės elemento veikimą. Atitinkamai trumpojo jungimo srovę gali papildyti fotosrovė (I_f), kuri apskaičiuojama iš fotodiodo veikos srities nustatytos srovės atėmus prie tos pačios įtampos esančią tamsinę srovę (susijusią su triukšmais, sandūros metališkumu). Šie išvardinti parametrai leidžia nustatyti prototipinių fotodiodų / saulės elementų efektyvumą, tačiau, norint tiksliai įvertinti sukurtų įtaisų kvantinį efektyvumą bei atsaką, reikalingas tikslus fotodiodų paviršiaus geometrijos projektavimas, siekiant įvertinti šviesą blokuojančias elektrodų sritis ir kitus susijusius reiškinius.

1.4.2. Biojutikliai

Biojutiklių, paremtų grafeno lauko tranzistoriaus (G-FET) principu, veikimas pagrįstas elektrinio laidžio (varžos) arba jutikliu tekančios elektros srovės pokyčiu, kurį sukelia aplinkos pokyčiai ir sąveika su analitėmis (DNR, bakterijomis, virusais, vaistais ir kt.) [82,83,84]. G-FET elektrinį našumą lemia grafeno cheminis modifikavimas (kitų medžiagų prijungimas) – kadangi grafenas yra atominio storio, šios pridėtinės medžiagos tiesiogiai ir stipriai veikia jo laidumą. Tai užtikrina aukštą jautrumą ir padidina aptikimo ribą iki mažesnių nei femtomolių koncentracijų [85,86]. Skysčiu valdomo (angl. *liquid-gated*), G-FET veikimo schema matoma **3 pav., a**. Tokio tipo biojutiklio veikimui bei jautrumui nustatyti naudojama G-FET perdavimo charakteristika (santakos (D) – ištakos (S) srovės I_{DS} priklausomybė nuo užtūros (G) įtampos U_{GS}, išlaikant pastovų priešįtampį U_{DS}) (**3 pav., b**). Tokios priklausomybės turi minimumo tašką esant tam tikrai užtūros įtampai $U_{GS} = U_D$ ir vadinamos Dirako tašku arba krūvio neutralumo tašku. Šios perdavimo charakteristikos kairioji ir dešinioji šakos, tolstančios nuo neutralumo taško, atitinkamai vadinamos p tipo šaka ir n tipo šaka. Jos yra susijusios su didėjančiu teigiamųjų krūvininkų (skylių) arba neigiamųjų krūvininkų (elektronų) tankiu. Dėl grafeno nulinės draustinės juostos struktūros, didinant ambipolinę užtūros įtampą, krūvininkai (elektronai ir skylės) Dirako taške gali virsti vieni kitais, o tai lemia dvipolės G-FET perdavimo charakteristikos susiformavimą [42]. Krūvio neutralumo taške srovė pasiekia minimumą, nurodantį vienodą skylių ir elektronų tankį. Geros kokybės (pavyzdžiui,

turinčio mažai defektų ir adsorbatų) grafeno U_D bus artimas U_{GS} = 0, esant žemam priešįtampiui U_{DS}. Tačiau realiais atvejais šis taškas pasislenka link teigiamų užtūros įtampų, jei grafenas yra p-tipo priemaišinis, arba link neigiamų įtampų, jei jis yra n-tipo. Priemaišinis laidumas priklauso nuo įvairių veiksnių, tokių kaip pagrindas, ant kurio yra grafenas, elektrodų metalas, grafeno plėvelėje vyraujantys defektai, raukšlėjimasis ir kt. [85,87]. Taip pat jau minėta, kad reikšmingas U_D poslinkis nuo pradinės vertės atsiranda dėl funkcionalizuoto grafeno paviršiaus sąveikos su analite, todėl tai gali būti analitės molekulių koncentracijos matas (**3 pav., c**). Taigi, geros kokybės grafeno sluoksnių paruošimas ir proceso pakartojamumas yra esminiai veiksniai kuriant itin jautrius G-FET biojutiklius.



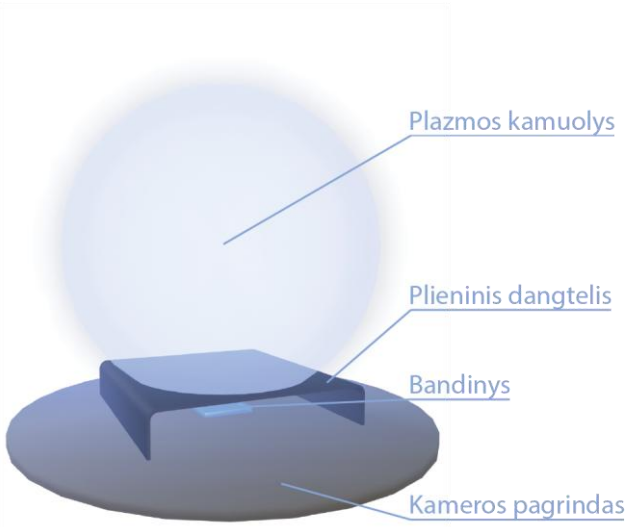
3 pav. (a) Skystosios užtūros (angl. *liquid-gated*) G-FET schema. Įrenginį sudaro ištaka (S), santaka (D), užtūra (G), grafeno kanalas, dielektriko sluoksnis ir padėklas. Įtampa tiekiama viršutiniam elektrodui, kuris su grafeno kanalo paviršiumi yra sujungtas per elektrolito tirpalą. Taip pasiekiamas kanalo potencialo ir laidumo moduliavimas. (b) Tipinė G-FET perdavimo charakteristika (I_{DS} priklausomybė nuo U_{GS}). (c) Jutiklio veikimo principas ant G-FET grafeno paviršiaus: teigiamą (neigiamą) krūvį turinčių analičių prisijungimas sukelia neigiamą (teigiamą) krūvio neutralumo taško poslinkį [88]

2. MEDŽIAGOS IR TYRIMŲ METODAI

2.1. Plonų sluoksnių sintezė

2.1.1. Grafeno sintezė

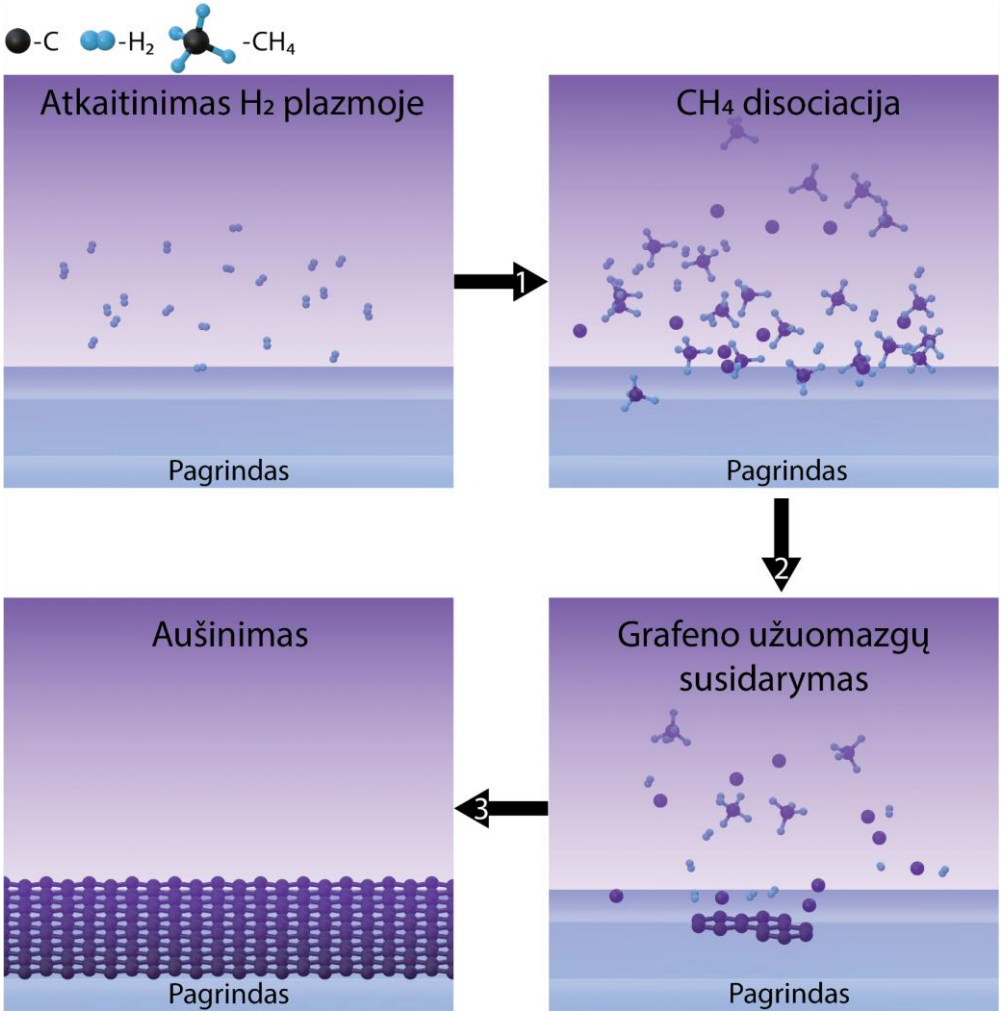
Grafeno bandiniai buvo formuojami ant skirtingų pagrindų, naudojant MW-PECVD sistemą Cyrannus („Innovative Plasma Systems (Iplas) GmbH“, Troisdorfas, Vokietija). Siekiant apsaugoti bandinius nuo tiesioginio plazmos poveikio, naudotas stačiakampio formos diamagnetinis plieninis dangtelis, kurio trumposios kraštinės užlenktos į vidų. MW-PECVD proceso schema ir naudojamas plieninis dangtelis matomi **4 pav.** Grafeno sintezėje buvo naudojami keturi skirtingi padėklai. Vienu atveju naudotas monokristalinis, iš abiejų pusių poliruotas, 1×1 cm n-tipo Si(100) („Sil'tronix Silicon Technologies“, Archamps, Prancūzija) pagrindas. Antru atveju naudotas tokio pat tipo 1,5×1,5 cm silicis, tačiau su papildomai padengtu 300 nm SiO_2 sluoksniu, suformuotu taikant terminę oksidaciją. Trečiu atveju naudotas monokristalinis, iš abiejų pusių poliruotas 1×1 cm Al_2O_3(0001) (C-safyro) („AdValue Technology“, JAV) pagrindas. Ketvirtas naudotas pagrindas – 1×1 cm h-BN plėvelės, susintetintos taikant didelės galios impulsinį magnetroninį dulkinimą ant Si(100) (2.1.2. h-BN/Si(100) bandinių sintezė). Grafeno plėvelėms formuoti naudotas vandenilio ir metano dujų mišinys.



4 pav. Grafeno sintezės schema taikant MW-PECVD

Visais atvejais procesas buvo pradedamas įvadinių dujų vamzdelių valymu. Vėliau buvo atliekamas bandinių atkaitinimas vandenilio dujų plazmoje. Atkaitinimo etapo metu buvo naudota 1 kW plazmos generatoriaus galia, 700 °C temperatūra (grafeno/Si(100) fotodiodų formavimo atveju temperatūra buvo 700–900 °C), 200 sccm H_2 srautas, 10 mBar kameros slėgis bei 10 min. trukmė. Vėliau keičiama plazmos generatoriaus galia (0,7 kW) ir sintezės temperatūra (jei reikia), o jai nusistovėjus, mažinamas H_2 srautas ir į kamerą pridedamas metanas bei nustatomas kameros slėgis (jei reikia) pagal pasirinktus sintezės parametrus. Dėl bandinių gausos

tikslius sintezės parametrus skirtingiems bandiniams galima rasti atitinkamuose straipsniuose [**P1-P3**, **P5**]. Pavyzdiniai grafeno sintezės etapai matomi **5 pav.**



5 pav. Pavyzdiniai MW-PECVD sintezės etapai auginant grafeną ant C-safyro pagrindų

2.1.2. H-BN/Si(100) sintezė

H-BN sluoksniai buvo nusodinti naudojant didelės galios impulsinį magnetroninį dulkinimą 800 °C temperatūroje. Pagrindui buvo naudojamas monokristalinis, iš abiejų pusių poliruotas, 1×1 cm n-tipo Si(100) („Sil'tronix Silicon Technologies", Archamps, Prancūzija). Naudoti impulsiniai parametrai: t_{ij} = 17 µs, $t_{iš}$ = 150 µs, impulsinė srovė – 1,2 A, vidutinė srovė ~0,12 A, vidutinė įtampa ~930 V, atstumas tarp padėklo ir katodo – 15 cm. Suformuoti h-BN sluoksnių storiai ištirti lazeriniu elipsometru „Gaertner L-115", naudojančiu He–Ne lazerį (λ = 632,8 nm). Boro nitrido plėvelių, plonesnių už 20 nm, storis buvo ekstrapoliuojamas iš gautų

duomenų storesnėms plėvelėms. N_2 dujų srautai, auginimo laikas bei h-BN storio vertės matomos **1 lentelėje**.

1 lentelė. H-BN sintezės ant Si(100), naudojant didelės galios impulsinį magnetroninį dulkinimą, auginimo parametrai [**P5**]

Bandinio nr.	N_2 srautas (sccm)	h-BN augimo laikas (s)	h-BN storis (nm)
3	152	36	1
4		108	3
5		180	5
6		360	10
7		540	15
8		720	20
9		3600	100
10		10800	300
11	197	33	1
12		99	3
13		165	5
14		330	10
15		495	15
16		660	20
17		3600	110
18		10800	330

2.1.3. Žemos temperatūros tiesioginė grafeno sintezė

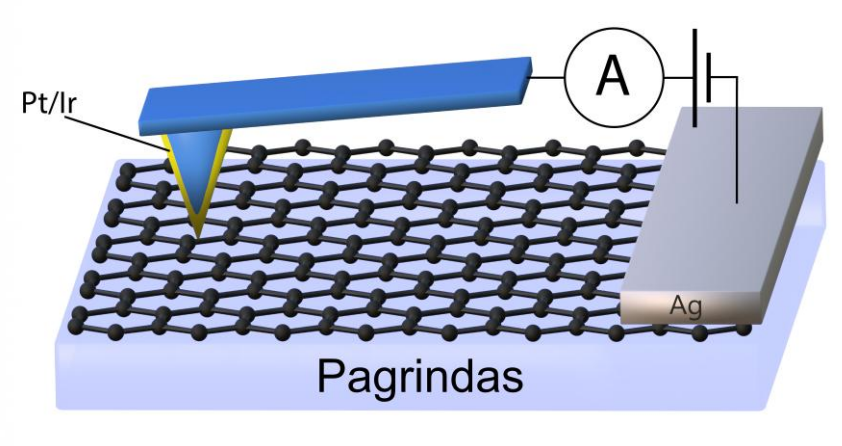
Žemos temperatūros MW-PECVD sintezėje grafeno sluoksniai buvo tiesiogiai susintetinti ant 1×1 cm n-tipo Si(100) („Sil'tronix Silicon Technologies“, Archamps, Prancūzija) padėklų. Ant šių padėklų paviršiaus terminės oksidacijos būdu suformuoti 300 nm SiO_2 sluoksniai, o sintezės parametrai aprašyti šaltinyje [**P4**]. Grafeno sintezės metu kameros slėgis buvo stebimas ir reguliuojamas taikant grįžtamojo ryšio sistemą, prijungtą prie dujų srautų valdiklio. Realaus laiko matavimams ir tiksliam slėgio valdymui buvo naudojamas kalibruotas slėgio matuoklis.

2.2. AJM analizė

Paviršių morfologijai bei topografijai įvertinti buvo naudota AJM. Matavimai atlikti kambario temperatūroje, įprastinėmis aplinkos sąlygomis, naudojant „NanoWizard III AJM“ mikroskopą („JPK Instruments“, Bruker Nano GmbH, Vokietija). Tyrimas buvo vykdomas pusiau kontaktiniu režimu (angl. *tapping mode*), naudojant silicio zondus („CS Instrument“, Vokietija), padengtus plonu (25±5 nm) platinos / iridžio sluoksniu iš abiejų pusių. Zondai pasižymi 2,7 N/m standumo

konstanta, 60 kHz rezonansiniu dažniu, 30 nm galiuko kreivumo spinduliu ir piramidės formos struktūra. Surinkti 2×2 µm vaizdai buvo apdoroti naudojant JPKSPM Data Processing programą (versija spm-4.3.13, „JPK Instruments“, Berlynas, Vokietija).

Be įprastinių paviršiaus morfologijos tyrimų, su grafeno/SiO_2/Si(100) ir grafeno / C-safyro bandiniais atlikti paviršiaus elektrinio laidžio tyrimai, nustatyti kontaktiniu laidžiuoju atominių jėgų mikroskopijos metodu. Tam naudotas Pt/Ir padengtas ANSCM-PT zondas (25 ± 5 nm danga), turintis 30 nm kreivumo spindulio tetraedrinį galiuką ir 61 kHz rezonansinį dažnį. Matavimai atlikti kambario temperatūroje ore, taikant ±10 mV įtampą. Matavimo schema matoma **6 pav.**



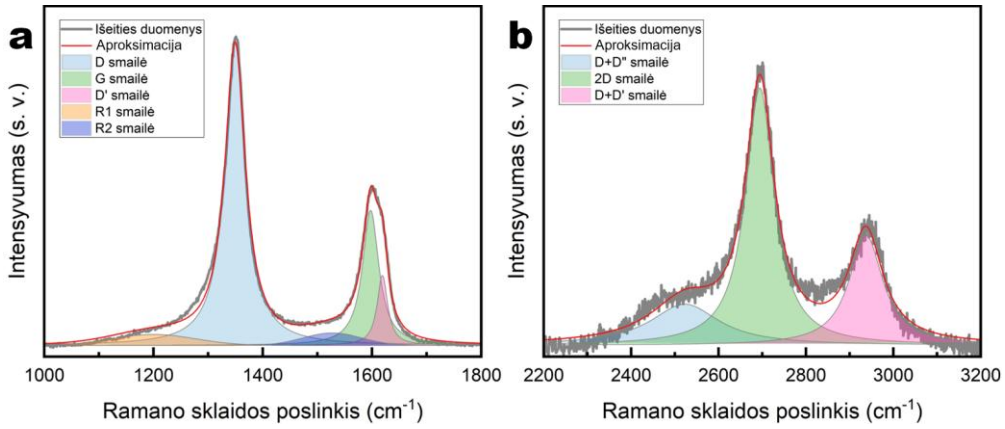
6 pav. Paviršiaus elektrinio laidumo matavimų schema, naudojant kontaktinį laidų atominių jėgų mikroskopijos metodą [**P3**]

2.3. Ramano sklaidos spektroskopijos analizė

Grafeno sluoksnių storio ir defektų tankio analizė buvo atlikta taikant Ramano sklaidos spektroskopiją („Renishaw InVia“, JK) naudojant 532 nm lazerį. Matavimams atlikti naudota 10–100 s ekspozicija (spektrų analizei ši įtaka buvo nykstamai maža), 1,5 mW galia ir 50 kartų didinantis objektyvas. Matavimai buvo atlikti iškart po grafeno sintezės (prieš pradedant prototipinių įrenginių gamybą). Matuota bent trijose vietose kiekviename bandinyje, siekiant įvertinti struktūros netolygumą. Išsamiai analizuotos D, G, 2D ir D‘ smailės – jų padėtys (Pos), intensyvumo santykiai (I_D/I_G, I_{2D}/I_G, $I_D/I_{D'}$) ir puspločiai (FWHM), leidžiantys įvertinti medžiagoje esančius defektus, kristalitų dydį, įtempius bei padedantys atskleisti grafeno sintezės dinamiką (žr. 1.3.2. Ramano sklaidos spektroskopija).

Dėl vieningos Ramano sklaidos spektrų analizės sistemos trūkumo buvo sukurtas spektrų analizatorius MATLAB aplinkoje, skirtas nuodugniam grafenui charakteringų sričių aproksimavimui. Grafeno Ramano sklaidos spektrai padalinti į dvi sritis, kurios apibrėžtos kaip DG (~1000-1800 cm^{-1}) ir 2D (~2200-3200 cm^{-1}). Prieš kiekvieną aproksimaciją buvo atliekamas interpoliuotos (kai interpoliavimo mazgus apibrėžia splainai) fono linijos, einančios per sritis, nepatenkančias į DG bei 2D sritį, panaikinimas. Aproksimacijų kokybei vertinti naudotas apibrėžtumo

koeficientas R^2 (šios vertės nepateiktos, tačiau naudotos tobulinant spektro analizatorių) [89]. Aproksimacijos pavyzdys pateiktas **7 pav.**



7 pav. Grafenui charakteringų Ramano sklaidos spektro sričių aproksimavimo pavyzdys: (a) DG sritis, (b) 2D sritis

Pagrindinės Ramano sklaidos smailės D, G, D‘ ir 2D aprašytos naudojant Lorenco funkcijos išraišką, pavaizduotą lygtyje (1) [90]:

$$L(x) = \frac{I_0}{1+\frac{4(x-x_0)^2}{w^2}}, \tag{1}$$

čia $L(x)$ yra Lorenco funkcija, I_0 – smailės intensyvumas ties centrine smailės padėtimi, x_0 – centrinė smailės padėtis, w^2 – smailės pusplotis.

Pagalbinėms smailėms, neanalizuotoms šiame darbe, tačiau įtrauktoms į DG (smailės R1 ir R2) ir 2D (smailės D+D’ bei D+D”) sričių aproksimaciją, taikyta koreguota Gauso ir Lorenco smailių sumos išraiška (2) [90]:

$$GLS(x) = I_0(1-F_L)e^{-4\cdot ln\,2\cdot\frac{(x-x_0)^2}{w^2}} + \frac{I_0F_L}{1+\frac{4(x-x_0)^2}{w^2}}, \tag{2}$$

čia $GLS(x)$ yra Gauso bei Lorenco smailių sumos funkcija, F_L – Lorenco faktorius ($0 \geq F_L \geq 1$), aprašantis Gauso ir Lorenco funkcijų dedamųjų santykį, I_0 – smailės intensyvumas ties centrine smailės padėtimi, x_0 – centrinė smailės padėtis, w^2 – smailės pusplotis.

Abi charakteringos spektrinės sritys aprašytos jose aptinkamų smailių suma. DG sritis aprašyta 5-ių smailių (D, G, D‘, R1 ir R2) suma (3), o 2D sritis aprašyta 3-jų smailių (D+D”, 2D ir D+D’) suma (4):

$$S_{DG}(x) = L_D(x) + L_G(x) + L_{D'}(x) + GLS_{R1}(x) + GLS_{R2}(x); \tag{3}$$

$$S_{2D}(x) = GLS_{D+D"}(x) + L_{2D}(x) + GLS_{D+D'}(x), \tag{4}$$

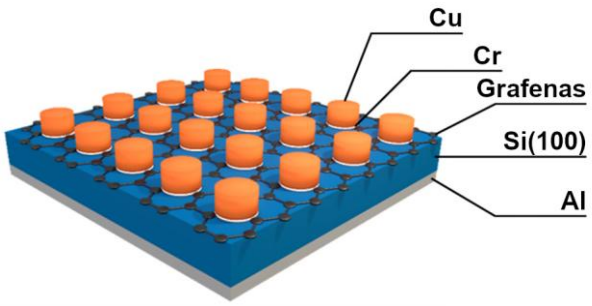
čia $S_{DG}(x)$ ir $S_{2D}(x)$ yra atitinkamai DG ir 2D sritims taikomos aproksimacijos išraiškos, $L_D(x)$, $L_G(x)$, $L_{D'}(x)$, $L_{2D}(x)$ – D, G, D‘ ir 2D smailėms aprašyti skirtos

atitinkamos išraiškos, o $GLS_{R1}(x)$, $GLS_{R2}(x)$, $GLS_{D+D''}(x)$, $GLS_{D+D'}(x)$ – R1, R2, D+D“ ir D+D‘ smailėms aprašyti skirtos atitinkamos išraiškos.

2.4. Elektrinių prietaisų formavimas ir tyrimas

2.4.1. Fotodiodai

Siekiant išsiaiškinti suformuotų grafeno plėvelių, kaip skaidraus laidininko, galimybes, buvo sukurti fotodiodų prototipai ir ištirtos jų fotoelektrinės savybės. Fotodiodų prototipai buvo kurti grafeno/Si(100) bei grafeno/h-BN/Si(100) pagrindu (žr. 2.1.1. Grafeno sintezė ir 2.1.2 h-BN/Si(100) bandinių sintezė). Iš pradžių po grafeno sintezės atlikti bandinių valymo etapai: virinimas dimetilformamide ir acetono mišinyje, $NH_4OH + H_2O_2 + H_2O$, atitinkamai santykiu 1:1:5, priemaišoms šalinti naudotas $HF + H_2O$, santykiu 1:50, ir $HCl + H_2O_2 + H_2O$, atitinkamai santykiu 1:1:6. Vėliau suformuotas nugarinis Al kontaktas ant grafenu nepadengtos Si pusės naudojant elektronų pluošto technologiją. Tuomet ant grafeno nusodinti Cr/Cu elektrodai per kaukę su 500 µm skersmens skylėmis; Cr tarpsluoksnio storis – 20 nm, o Cu – 200 nm. Suformuotų fotodiodų elektrodų geometrija nebuvo optimizuota. Pavyzdinė grafeno/n-Si(100) fotodiodų schema matoma **8 pav.** (grafeno/h-BN/Si(100) prototipo schema yra analogiška).



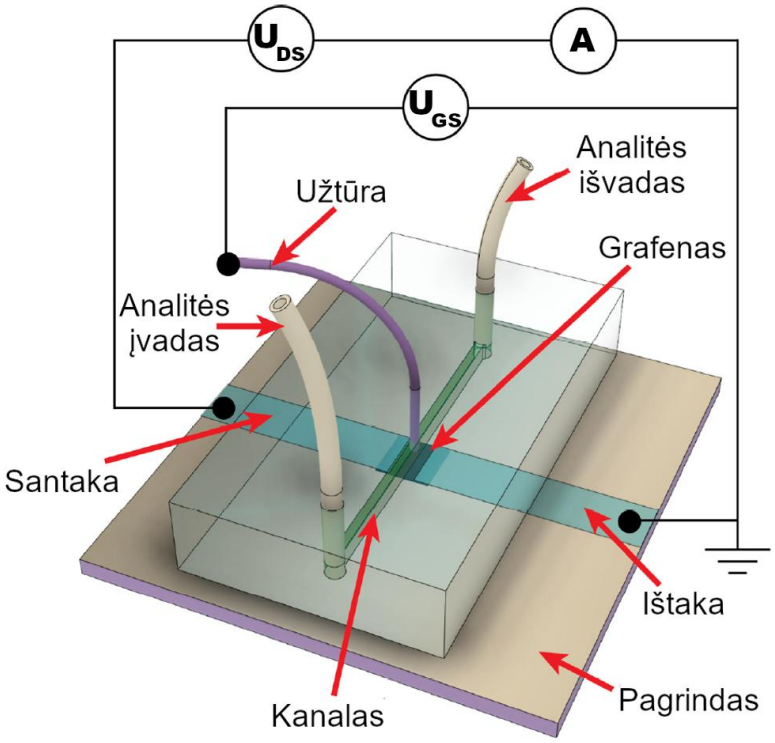
8 pav. Grafeno/Si(100) fotodiodo prototipo schema [**P1**]

2.4.2. Lauko tranzistoriai

Siekiant ištirti tiesiogiai sintetinto MW-PECVD grafeno bei pernešto grafeno biologinio jutimo savybių skirtumą, buvo sukurti FET principu veikiantys biologinio jutiklio prototipai. Plintant COVID-19 virusui, buvo sukurti grafeno biologiniai jutikliai, jautrūs SARS-CoV-2 spyglio (S) baltymui. Grafeno sluoksniai buvo tiesiogiai susintetinti ant SiO_2/Si padėklo MW-PECVD būdu (žr. 2.1.1. Grafeno sintezė). Taip pat palyginimui buvo naudojamas komercinis CVD-grafenas, perneštas ant stiklo pagrindo. Grafeno paviršius buvo funkcionalizuotas 1 mM PBASE („Cayman Chemical“, Ann Arboras, Minesota, JAV) ir metanolio („VWR International“, Prancūzija) tirpale, valandą kambario temperatūroje. Procedūra atlikta remiantis šaltiniu [91]. Po to bandinys paliktas 60 °C krosnyje pernakt. Paruošti PBASE/grafeno bandiniai buvo naudojami mikroskystinėje sistemoje, siekiant sukurti FET su skystąja užtūra.

PBASE/grafeno bandiniai buvo uždengti polidimetilsiloksano (PDMS) („Sylgard™ 184 Silicone Elastomer“, DOW Europe, Vokietija) lustu su mikroskystiniais kanalais (0,5×3 mm). Prieš uždengiant PBASE/grafeno bandinius luste buvo suformuotos skylės, prie kurių buvo prijungti lankstūs vamzdeliai. Nerūdijančio plieno 200 µm skersmens viela buvo naudojama siekiant suformuoti skystąją užtūrą. Grafeno FET schema matoma **9 pav.**

Pradžioje 4 val. kambario temperatūroje PBASE/grafeno FET įtaisas buvo paveiktas skirtingų koncentracijų (nuo 10 ag/ml iki 10 µg/ml) angiotenziną konvertuojančio fermento II (ACE2) (UAB „Baltymas“, Vilnius, Lietuva) baltymu, paruoštu 0,1× fosfatu buferizuotame fiziologiniame tirpale (PBS) (turinčiame 0,0137 M NaCl („VWR International“, Villers-lès-Nancy, Prancūzija), 0,00027 M KCl („VWR International“, Villers-lès-Nancy, Prancūzija), 0,001 M Na_2HPO_4 („Sigma Aldrich“, Sent Luisas, JAV) ir 0,00018 mM KH_2PO_4 („Merck“, Darmštatas, Vokietija)). ACE2 perteklius buvo pašalintas praplaunant analitės įvadą, kanalą ir išvadą su 1 ml PBS ir polisorbatu 20 (0,05%), o vėliau tik su 2 ml PBS. Tuomet mikroskystinė sistema pripildyta 1 ml PBS ir 0,1% koncentracijos jaučio serumo albumino tirpalo (BSA) („Sigma Aldrich“, Sent Luisas, JAV), norint išvalyti likusias ACE2 nepaliestas sritis. Baigiant tyrimai atlikti su SARS-CoV-2 spyglio glikoproteinais (S) (UAB „Baltymas“, Vilnius, Lietuva), paruoštais 0,1× PBS tirpaluose, naudojant skirtingas baltymų koncentracijas (nuo 10 ag/ml iki 10 µg/ml).

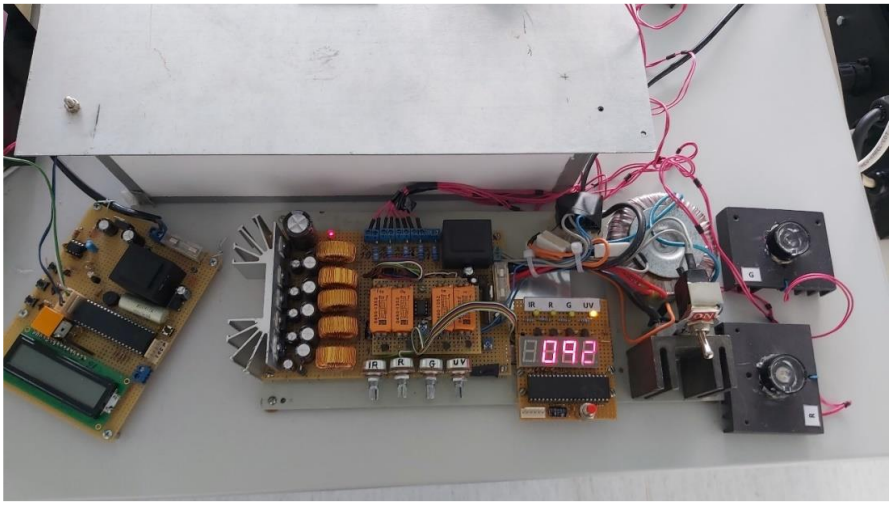


9 pav. Biologinio jutiklio prototipo matavimo schema [**P2**]

2.5. Elektriniai matavimai

2.5.1. Fotodiodų voltamperinių charakteristikų tyrimai

Sukurtų grafeno fotodiodų fotoelektrinėms savybėms ištirti atlikta voltamperinių charakteristikų analizė. „Keithley 6487“ („Tektronix Inc“, Beavertonas, JAV) pikoampermetras / įtampos šaltinis buvo naudojamas voltamperinių charakteristikų matavimams. Fotodiodų voltamperinės charakteristikos matuotos trimis atvejais. Tamsoje (fotodiodų neapšviečiant), apšviečiant UV (406 nm) bei apšviečiant IR (730 nm) šviesos diodais. Naudota ±2 V įtampa, kintanti 0,1 V žingsniu. Siekiant išlaikyti pastovią šviesos diodų optinę galią (5,2 mW), parinkti skirtingi diodu tekančios srovės stipriai (UV atveju – 92 mA, IR atveju – 200 mA). Šviestukų valdymo bloko schema matoma **10 pav.** Gautos voltamperinės charakteristikos buvo naudojamos trumpojo jungimo srovei I_{tj} (kai U = 0 V) ir atviros grandinės įtampai (kai I = 0 A) nustatyti, naudojant tiek UV, tiek IR šviestukus. Diodui būdingo veikimo analizei buvo nustatoma tamsinė atbulinė srovė I_{ta} (kai U = -0,5 V). Taip pat tiek UV, tiek ir IR apšvietimo atveju buvo skaičiuojama fotosrovė – tamsinės atbulinės srovės ir šviesa paveiktų fotodiodų atbulinės srovės santykis (kai U = -0,5 V).



10 pav. Šviesos diodų valdymo bloko schema

2.5.2. Lauko tranzistoriaus elektriniai matavimai

Grafeno FET elektriniai matavimai buvo atlikti naudojant GS610 („Yokogawa“, Tokijas, Japonija) įtampos / srovės šaltinį, matavimo įrenginį ir IT6123 („ITECH electronic Co.“, Ltd., Kinija) nuolatinės įtampos / srovės šaltinį, matavimo įrenginį. Lauko tranzistoriaus priklausomybės tarp santakos ir ištakos srovės I_{DS} ir užtūros bei ištakos įtampos U_{GS} matavimai atlikti išlaikant pastovų priešįtampį U_{DS} = 50 mV. Po kiekvieno grafeno paviršiaus funkcionalizavimo proceso matavimai atlikti po 30 min. pertraukos. Šis laikas buvo pakankamas tranzistoriaus varžos įsisotinimo vertei pasiekti. Tyrimo metu, naudojant I_{DS}–U_{GS} charakteristikas, buvo nustatoma Dirako įtampa U_D (kai min{I_{DS}}). Naudota U_{GS} įtampa ±0,8 V.

3. REZULTATŲ APŽVALGA IR APTARIMAS

3.1. Grafeno sintezės optimizavimas

Siekiant optimizuoti MW-PECVD grafeno sintezę, tirtos grafeno paviršiaus morfologija bei struktūra, atitinkamai remiantis AJM ir Ramano sklaidos spektrais. Ši metodika pasirinkta siekiant išvengti sudėtingos ir nepatikimos plazmos procesų analizės MW-PECVD kameroje. Proceso metu vykstant įvairiems fizikiniams reiškiniams tarp elektronų, jonų, radikalų bei neutralių CH_4 molekulių, sunku nuspėti skirtingų dalelių ir atmainių pasiskirstymą reakcijos kameroje, taip pat ir elektrinio lauko pasiskirstymą dėl per didelio laisvės laipsnių skaičiaus [58]. Situacija tampa sudėtingesnė, kai naudojamos santykinai žemos plazmos generatoriaus galios (< 1 kW) [58]. Mūsų atveju sintezės metu buvo naudota žema mikrobangų plazmos generatoriaus galia, siekiant išlaikyti sluoksnių horizontalumą, atsižvelgiant į tai, kad didesnės plazmos galios skatina vertikalaus grafeno augimą [92,93]. Būtent dėl to visais atvejais naudota 0,7 kW plazmos generatoriaus galia. Kiti pirminio proceso parametrai buvo pasirenkami atsitiktiniu būdu, siekiant rasti optimalų grafeno sintezės parametrų rinkinį (CH_4/H_2 santykį, kameros slėgį, temperatūrą bei sintezės laiką). Empiriškai nustatyta, jog, keičiant abiejų dujų srautų absoliutines vertes, tenka koreguoti ir kameroje esantį slėgį, siekiant išlaikyti plazmos stabilumą [94].

3.1.1. Dujų srautų bei sintezės laiko įtaka ant Si(100) nusodintam grafenui

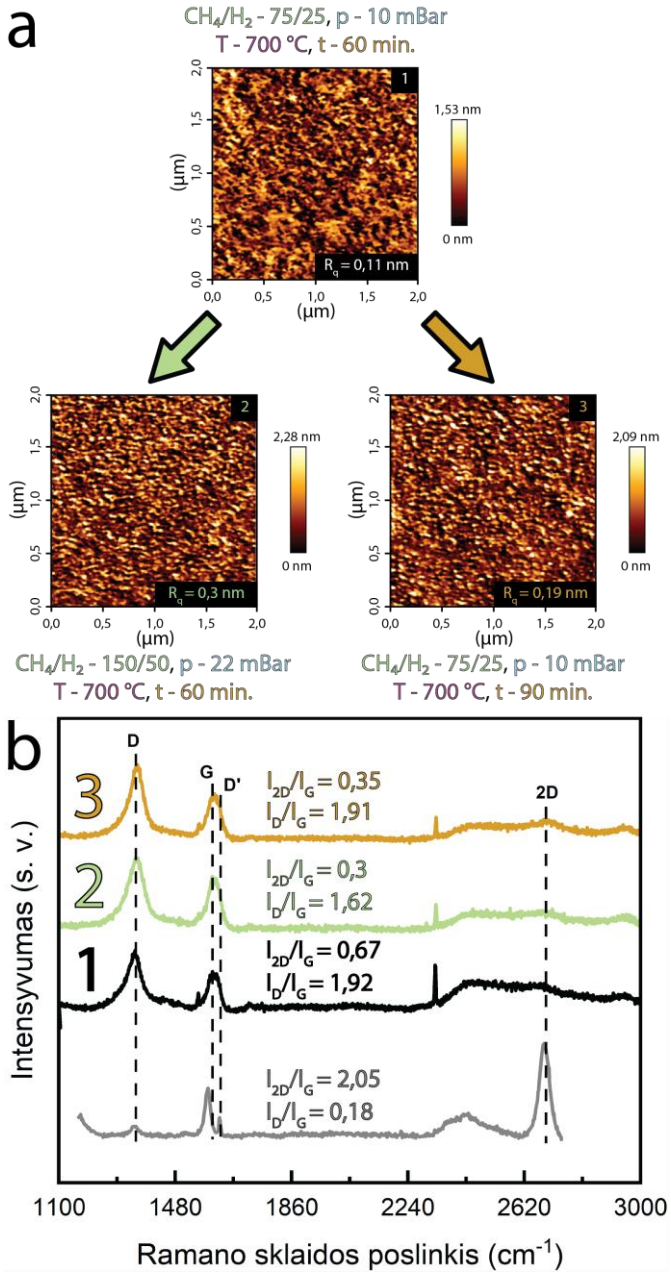
Pirmieji grafeno sintezės eksperimentai pradėti naudojant Si(100) pagrindus, atsižvelgiant į milžinišką grafeno/Si(100) fotodiodų potencialą. Remiantis ankstesniais tiesioginės grafeno sintezės taikant MW-PECVD tyrimais [94] nuspręsta nagrinėti CH_4/H_2 bei sintezės trukmės įtaką grafeno morfologijai ir struktūrai. CH_4/H_2 ir sintezės trukmės įtaka grafeno plėvelėms matoma **11 pav., a**. Pastebėta, kad mažiausiu vidutiniu kvadratiniu šiurkštumu (R_q = 0,11 nm) pasižymi bandinys, sintetintas naudojant CH_4/H_2 – 75/25, p – 10 mBar, T – 700 °C ir t – 60 min. Šiame bandinyje matomi grafeno dariniai yra smulkūs, o jų aukštis 1–1,3 nm. Atsižvelgiant į vieno sluoksnio grafeno storį (~0,4 nm) galima manyti, kad individualių kristalitų aukštis viršija 3 grafeno sluoksnius. Didinant mažiausiu vidutiniu kvadratiniu šiurkštumu pasižyminčio bandinio CH_4 ir H_2 srautus ir ilginant proceso trukmę, bandinių paviršius ima šiurkštėti. Svarbu paminėti, kad pagrindo šiurkštumas atsispindi AJM vaizduose matomoje grafeno morfologijoje, tad tikrasis grafeno kristalitų aukštis gali būti mažesnis [67]. Siekiant ištirti bandinių struktūrą ir grafeno kokybę, atitinkamai analizuoti šių bandinių Ramano sklaidos spektrai (**11 pav., b**). Palyginimui analizuotas ant stiklo perkelto grafeno atvejis[1]. Nustatyta, kad bandinys su mažiausiu R_q pasižymėjo didžiausia I_{2D}/I_G verte (0,67), o tai rodo mažiausią grafeno kristalitų storį šioje bandinių imtyje ir patvirtina storį, nustatytą taikant AJM. Atitinkamai didinant įleidžiamų dujų srautus, pastebėtas kristalitų storio padidėjimas. Šis storio didėjimas siejamas su prastu auginimo parametrų deriniu (H_2 srauto bei didelio slėgio), kuris neleidžia grafeno kristalams tinkamai atsipalaiduoti ir mažina

[1] Grafeno, perkelto ant stiklo, bandiniai paruošti Fizinių ir technologijos mokslų centre, Funkcinių medžiagų ir elektronikos skyriuje.

užuomazgų susidarymą, taip skatindamas defektų tankio didėjimą [95]. Sintezės trukmės ilgėjimas pastebimai mažina 2D bei G smailių intensyvumų santykį (grafeno storis didėja), taip nurodydamas sp^3 ryšių kiekio didėjimą dėl tirpios anglies kiekio didėjimo Si(100) pagrinde [96]. Nagrinėjant I_D/I_G vertes nustatyta, kad ploniausia polikristaline grafeno plėvele pasižymintis bandinys turi didžiausią defektų tankį (I_D/I_G = 1,92). Nustatyta, kad perkeltas grafenas yra vieno sluoksnio storio ir beveik neturi defektų (I_{2D}/I_G ~ 2, I_D/I_G = 0,18), atitinka CVD būdu ant katalizinių pagrindų sintetintą grafeną [70].

Taip pat analizuoti ir kiti grafenui charakteringų Ramano sklaidos spektre esančių smailių parametrai (**2 lentelė**). Pavyzdžiui, defektų tipą nusakantis $I_D/I_{D'}$ santykis rodo grūdelių ribos defektų tipo dominavimą visuose tiesiogiai MW-PECVD būdu sintetinto grafeno bandiniuose ($I_D/I_{D'}$ = 2,98 1-ojo bandinio atveju, $I_D/I_{D'}$ = 2,76 2-ojo bandinio atveju, $I_D/I_{D'}$ = 3,29 3-iojo bandinio atveju) [73]. Tai sutampa su pastebimais grafeno polikristalais, nustatytais AJM. Atitinkamai perkeltas grafenas pasižymi labai žemomis $I_D/I_{D'}$ vertėmis (<1,3), kurios būdingos beveik defektų neturinčiam grafenui [97]. Palyginti su perkelto grafeno Ramano sklaidos spektrais, tiesiogiai sintetinto grafeno G smailių padėtys buvo šiek tiek pasislinkusios aukštesnių bangos skaičių link, o $FWHM_G$ padidėjęs apie du kartus (nuo 15,7 cm^{-1} iki ~34 cm^{-1}). Toks G smailės parametrų skirtumas, kartu su padidėjusiu I_D/I_G rodo gerokai padidėjusį defektų tankį [98]. Bene didžiausias verčių skirtumas pastebimas $FWHM_{2D}$ atveju. $FWHM_{2D}$ didėjimas daugiau nei 30 cm^{-1} susijęs su grafeno sluoksnių kiekio didėjimu, tačiau tai būdinga dideliu kristalitų dydžiu pasižyminčiam grafenui [70]. Polikristalinėse tiesiogiai sintetintose grafeno plėvelėse tai gali nusakyti gniuždomo grafeno atvejį [99,100]. Papildomai Pos_G ir Pos_{2D} smailių padėčių slinkimas aukštesnių verčių link būdingas legiruotam grafenui [101,102,103], nors $FWHM_G$ turėtų mažėti. Manoma, kad defektų tankis grafene neleidžia tiksliai įvertinti grafeno savaiminio legiravimo atvejo. Didelį defektų kiekį bei grafeno polikristališkumą galima paaiškinti aiškiu šiluminio plėtimosi koeficiento skirtumu tarp grafeno ir Si(100) pagrindų [104,105].

Išanalizavus Ramano sklaidos spektrus buvo pasirinktas grafeno sintezės parametrų (CH_4/H_2, p, T) atramos taškas, naudotas tolesniems tiesioginės grafeno sintezės ant SiO_2/Si(100), C-safyro bei h-BN padėklų tyrimams. Nepaisant didelio defektų tankio ir pakankamai storų polikristalinių grafeno plėvelių, atsižvelgiant į proceso parametrų praktiškumą, grafeno struktūrinių parametrų analizę ir grafeno horizontalumą, skirtingiems padėklams taikyti šiek tiek pakoreguoti, tačiau 1-ojo bandinio sintezei artimi grafeno auginimo parametrai (CH_4/H_2 – 75/25, p – 10 mBar, T – 700 °C).



11 pav. (a) grafeno plėvelių, sintetintų ant Si(100) pagrindų MW-PECVD būdu, AJM vaizdai. Paveiksle pavaizduotos skirtingomis sąlygomis sintetintų bandinių paviršiaus morfologijos. CH_4/H_2 kitimas pavaizduotas žalia rodykle, o sintezės laiko kitimas pavaizduotas geltona rodykle. Bandiniai sunumeruoti 1, 2, 3 dėl aiškumo; **(b)** Ramano sklaidos spektrai ir pagrindiniai charakteringų smailių intensyvumų santykiai (spektrų numeracija atitinka **(a)** dalyje pavaizduotus bandinius). Perkelto grafeno spektras (pilkos spalvos) pateiktas palyginimo tikslu

2 lentelė. Grafeno/Si(100) charakteringų Ramano sklaidos spektrų smailių parametrai

Bandinio nr.	Grafeno tipas	$I_D/I_{D'}$	Pos_G (cm^{-1})	Pos_{2D} (cm^{-1})	$FWHM_G$ (cm^{-1})	$FWHM_{2D}$ (cm^{-1})
1	Tiesiogiai sintetintas grafenas	2,98	1597	2661,9	34,1	228,3
2	Tiesiogiai sintetintas grafenas	2,76	1600	2660,3	36	200
3	Tiesiogiai sintetintas grafenas	3,29	1599,6	2683,8	35,7	148,8
	Perkeltas grafenas	0,55	1586	2685,6	15,7	32,8

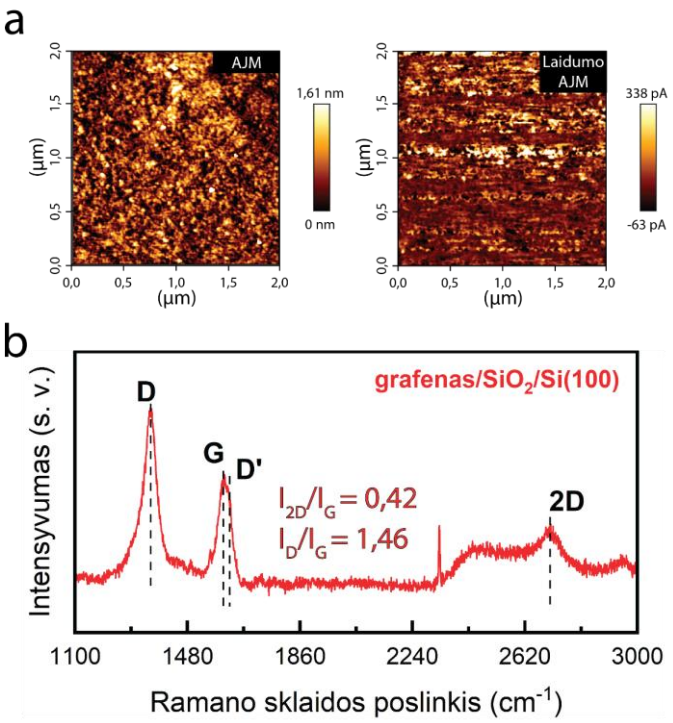
3.1.2. Grafeno sintezė ant stabilaus SiO_2

Atlikus grafeno sintezės ant Si(100) pagrindų tyrimą, atsižvelgta į grafeno plėvelių formavimo galimybes ant dielektrinio SiO_2 padėklo. Dėl cheminio inertiškumo, atsparumo aukštoms temperatūroms ir stiprių cheminių ryšių stokos SiO_2/Si(100) (kai SiO_2 sluoksnio storis yra artimas 300 nm) pagrindas yra tobulas kandidatas lygaus, horizontalaus grafeno sintezei [106], tačiau kol kas tokio tipo PECVD sintezės eksperimentų nedaug. Remiantis ankstesniais grafeno sintezės ant SiO_2 bei Si(100) tyrimais [93,94, **P1**] naudoti šie grafeno sintezės parametrai – CH_4/H_2 – 75/25, p – 10 mBar, T – 700 °C ir t – 120 min. Svarbu paminėti ir priminti, kad visuose procesuose naudota galia yra 0,7 kW, norint užtikrinti horizontalaus grafeno struktūrą [93].

Grafeno/SiO_2/Si(100) bandinių tirta paviršiaus morfologija, taikant AJM. Išanalizavus AJM vaizdus matyti, kad grafenas yra sudarytas iš 20–25 nm dydžio darinių (**12 pav., a**). Darinių aukštis ~1–1,3 nm. Dariniai yra panašūs į tuos, kurie matomi grafeno/Si(100) bandiniuose. Papildomai dėl dielektrinės SiO_2 prigimties išnaudota grafeno laidumo AJM matavimų galimybė. Vaizduose matyti skirtingos grafeno laidumo sritys, pasireiškiančios dėl grafeno nanokristališkumo bei grūdelių ribose pasireiškiančio mažesnio laidumo [107]. Ramano sklaidos spektrų informacija (**12 pav., b**) atitinka AJM vaizduose matomus paviršiaus netolygumus. Atlikus spektrų analizę nustatyta, kad I_{2D}/I_G ~ 0,42, o tai rodo kelių sluoksnių grafeną. Atsižvelgiant į tai, kad sintezė vykdyta ilgiau nei 1-ojo grafeno/Si(100) bandinio atveju (vietoje 60 min. naudota 120 min. trukmė), nenuostabu, kad I_{2D}/I_G vertė mažesnė, o grafeno storis – didesnis. Svarbu paminėti, kad grafeno plėvelės, sintetintos ant SiO_2 pagrindų, pasižymi mažesniu defektų kiekiu nei ant Si(100). Tai rodo I_D/I_G ~ 1,46. $I_D/I_{D'}$ santykis (3,26) rodo, kad vyrauja grūdelių ribos defektai.

Panašu, kad grafenas, sintetintas tiek ant SiO_2, tiek ant Si(100) pagrindų, pasižymi panašia struktūra ir morfologija. Abiem atvejais grafeno sąveika su

pagrindais yra silpna, SiO_2 atveju dėl stiprių cheminių ryšių stokos, o Si(100) – dėl šiluminio plėtimosi koeficiento nesuderinamumo.



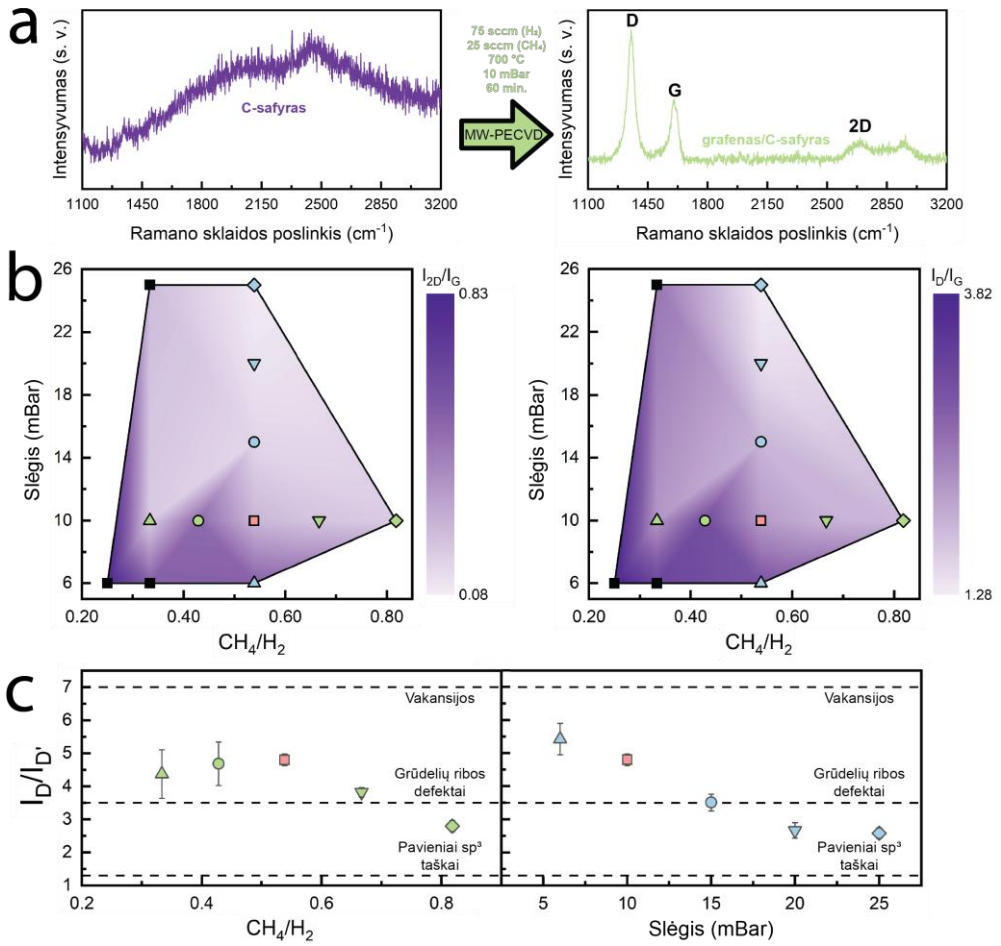
12 pav. (a) grafeno plėvelių, sintetintų ant SiO_2/Si(100) pagrindų MW-PECVD būdu, AJM (kairėje) bei laidumo AJM (dešinėje) vaizdai; **(b)** Ramano sklaidos spektrai ir pagrindiniai charakteringų smailių intensyvumų santykiai

3.1.3. Grafeno/C-safyro sintezės dinamika

Katalizinė C-safyro prigimtis dėl natūraliai derančios šešiakampės Al_2O_3(0001) bei grafeno struktūros padeda sumažinti grūdelių ribos defektus, padidinti kristalitų dydį ir užtikrina stabilų grafeno sintezės procesą [108]. Remiantis C-safyro pagrindo suderinamumu su grafeno plėvelėmis, grafeno/C-safyro perspektyvos tirtos ir MW-PECVD sintezės metodu, analizuojant CH_4 ir H_2 dujų srautų santykius (išlaikant vienodą 100 sccm dujų srautų sumą) bei nagrinėjant slėgio įtaką grafeno sintezei. Atsižvelgiant į sintezės trukmės įtaką grafeno storiui (didinant trukmę, storis didėja), C-safyro pagrindų atveju šis parametras nenagrinėtas.

Grafeno sintezė ant C-safyro pagrindų buvo vykdyta dviem etapais: pirmiausia atlikta grafeno sintezė taikant standartines sąlygas (3.1.1 ir 3.1.2). Atlikus gautų grafeno plėvelių Ramano sklaidos spektroskopijos bei morfologijos analizę, pasirinkta didinti CH_4 dujų srautą, išlaikant bendrą srautų sumą (Q_{CH_4} + Q_{H_2} = 100 sccm). Sintezės taikant skirtingus srautus metu buvo palaikomas toks pat 10 mBar slėgis, nes didinant slėgį skatinama daugiasluoksnio grafeno sintezė, procesas greitinamas, o labai žemas slėgis neleidžia formuotis grafeno grūdeliams [109,110]. C-safyro pagrindo Ramano sklaidos spektre matomas aiškus liuminescencijos fonas

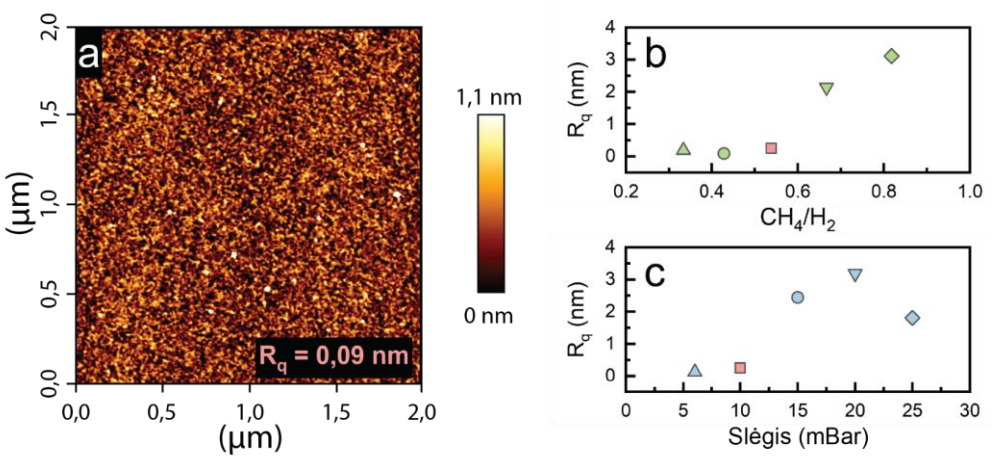
ties ~2000 cm^{-1} (**13 pav., a**). Atliekant Ramano sklaidos spektrų analizes, šis fonas buvo pašalinamas. Po MW-PECVD sintezės, Ramano sklaidos spektruose matomos tipinės grafeno smailės (**13 pav., a**). Panašūs tiesiogiai sintetinto grafeno ant C-safyro spektrai pastebėti ir kitų mokslinių grupių darbuose [56,111]. Atlikus grafeno struktūros analizę remiantis I_{2D}/I_G bei I_D/I_G priklausomybėmis nuo CH_4/H_2 (**13 pav., b**) matomi aiškūs grafeno plėvelių skirtumai. Didinant CH_4 srautą, pastebėtas tiek I_{2D}/I_G, tiek ir I_D/I_G mažėjimas. Tik vienu atveju, kai naudoti standartiniai sintezės parametrai, nustatyta didelė Ramano spektrų smailių parametrų sklaida. Šis bandinys neatitinka bendrosios tendencijos dėl sudėtingo plazmos homogeniškumo užtikrinimo. I_{2D}/I_G ir I_D/I_G abipusis mažėjimas rodo, kad bandiniuose defektų tankis priklauso nuo storio. Panašu, kad grafeno užuomazgų susidarymo metu pastebima daug grūdelių ribos defektų, tačiau, didėjant grafeno plėvelių storiui, grafeno kristalitų kiekis ima mažėti. Šis reiškinys aptariamas ir grafeno Ramano sklaidos spektroskopijos teorijoje [73,97]. Grūdelių ribos defektų dominavimą grafeno/C-safyro bandiniuose patvirtina ir $I_D/I_{D'}$ santykiai (**13 pav., c**). Nei vakansijų, nei pavienių sp^3 ryšiais paremtų defektų nepastebėta. Atlikus pagrindinių Ramano sklaidos spektrų smailių analizę buvo pradėtos slėgio kitimu paremtos sintezės. Atsižvelgiant į sintezės proceso sklandumą (parametrų palaikymo užtikrinimą) ir kameros paruošimo tolesniam sintezės procesui paprastumą, šiems eksperimentams pasirinktas CH_4/H_2 – 35/65 dujų srautų santykis. Pastebėta, kad, didinant slėgį, atitinkamai mažėja I_{2D}/I_G ir I_D/I_G vertės (**13 pav., b**). Nustatyta, kad žemas slėgis neužtikrina stabilaus augimo, dėl to didėja defektų kiekis, net jeigu ir grafeno storis mažesnis. Atitinkamai, didinant sintezės metu palaikomą kameros slėgį, matomas grafeno storio augimo greičio didėjimas, kartu mažėja ir defektų tankis. Priešingai nei $I_D/I_{D'}$ priklausomybės nuo CH_4/H_2 atveju, slėgis turi aiškią įtaką defektų tipui (**13 pav., c**). Kai nustatytas slėgis yra 5 mBar, tuomet $I_D/I_{D'} \sim 5{,}5$, o tai rodo vakansijų ir grūdelių ribos defektų mišiniu pasižyminčias grafeno plėveles [73]. Kai slėgis mažėja, pastebimas $I_D/I_{D'}$ mažėjimas, kuris nusistovi esant žemesniems nei 20 mBar slėgiams ($I_D/I_{D'} \sim 2{,}5$). Nors $I_D/I_{D'}$ vertės artėja prie 1,5, o tai būdinga lygiam, vieno sluoksnio grafenui, pasižyminčiam pavienėmis sp^3 defektų sritimis [73], tolimesnis slėgio didėjimas skatina grafeno storio augimą ir grūdelių ribos defektų susidarymą, todėl ir nepastebimas $I_D/I_{D'} < 2{,}5$.



13 pav. Grafeno, sintetinto ant C-safyro pagrindų MW-PECVD būdu, Ramano sklaidos spektrų analizė. **(a)** C-safyro pagrindo (purpurinis kairėje) Ramano spektras prieš grafeno MW-PECVD sintezę bei grafeno/C-safyro (žalias dešinėje) Ramano spektras po sintezės. Sintezės parametrai matomi virš rodyklės; **(b)** grafeno/C-safyro Ramano sklaidos smailių I_{2D}/I_G (kairėje) bei I_D/I_G (dešinėje) santykių priklausomybės nuo sintezės parametrų, spalvinės diagramos (juodi taškai žymi papildomus sintezės bandymus, šiek tiek padidinančius imtį); **(c)** Ramano sklaidos smailių $I_D/I_{D'}$ santykio priklausomybės nuo sintezėse naudojamo CH_4/H_2 (kairėje) ir slėgio (dešinėje). Punktyrinės linijos žymi defektų tipą, paremtą $I_D/I_{D'}$ analize [73, **P3**]

Grafeno/C-safyro morfologijai ištirti bandiniai taip pat analizuoti AJM. Vidutinio kvadratinio šiurkštumo vertės ir jų priklausomybės nuo sintezės parametrų matomos **14 pav**. Mažiausiu šiurkštumu pasižymėjo bandiniai, sintetinti CH_4/H_2 – ≤35/65 dujų santykiu bei ≤10 mBar slėgiu (**14 pav., b, c**). Tiek didinant CH_4/H_2 srautų santykį, tiek slėgį, vidutinis kvadratinis šiurkštumas didėja pastebimai. Panašu, kad tai patvirtina Ramano spektruose matomų charakteringų grafeno smailių analizės rezultatus. Mažas CH_4/H_2 ir slėgis neužtikrina grafeno storio augimo, sintezės metu

dominuoja paviršių ėsdinimo reiškiniai, todėl vyrauja plėvelių polikristališkumas. Viršijus slenkstines vertes, pastebimas staigus grafeno sluoksnių formavimas, ir defektų tankis ima mažėti, tačiau dėl greito plėvelių augimo matomas didelis vidutinio kvadratinio šiurkštumo padidėjimas.



14 pav. (a) Grafeno, sintetinto naudojant CH_4/H_2 – 35/65 srautų santykį bei 10 mBar slėgį, morfologija (R_q nurodo vidutinį kvadratinį šiurkštumą); **(b)** R_q priklausomybė nuo dujų srautų santykio; **(c)** R_q priklausomybė nuo sintezės metu naudojamo slėgio. Spalvos bei žymekliai atitinka 13 pav. vaizduojamus duomenis [**P3**]

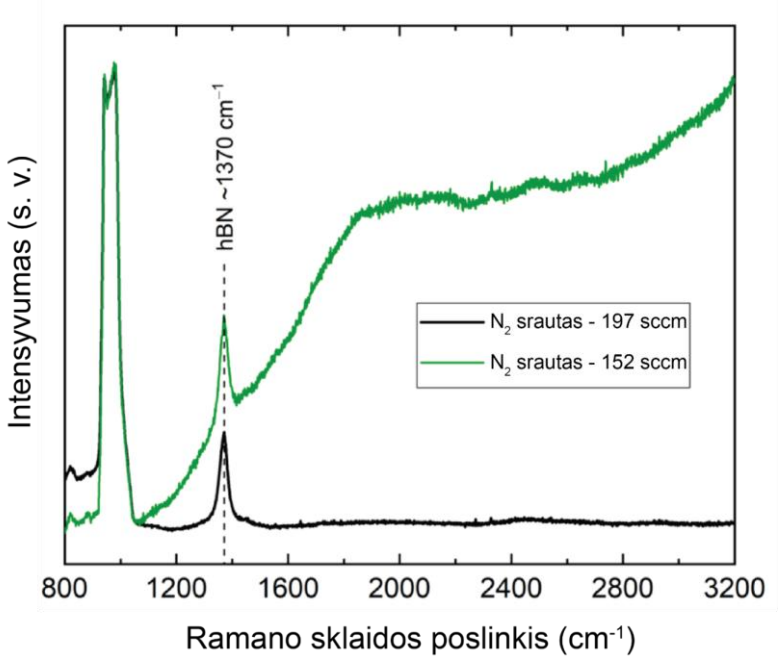
3.1.4. H-BN ir grafeno suderinamumas

Heksagoninis boro nitridas – tai dar viena medžiaga, kurios atomai išsidėstę vienoje plokštumoje. H-BN plokštumoje atomai formuoja šešiakampius žiedus, o Boro ir Azoto atomai išsidėstę taip, kad tokios pat rūšies atomai tiesiogiai nesąveikautų. Tokia struktūra ir h-BN gardelės parametrai yra artimi grafenui, todėl nenuostabu, kad kelios mokslinės grupės jau atliko sėkmingą grafeno sintezę ant šio pagrindo [112,113,114,115,116,117]. Nepaisant perspektyvaus grafeno ir h-BN suderinamumo, tiesioginės MW-PECVD grafeno sintezės tyrimų ant h-BN pagrindų nėra.

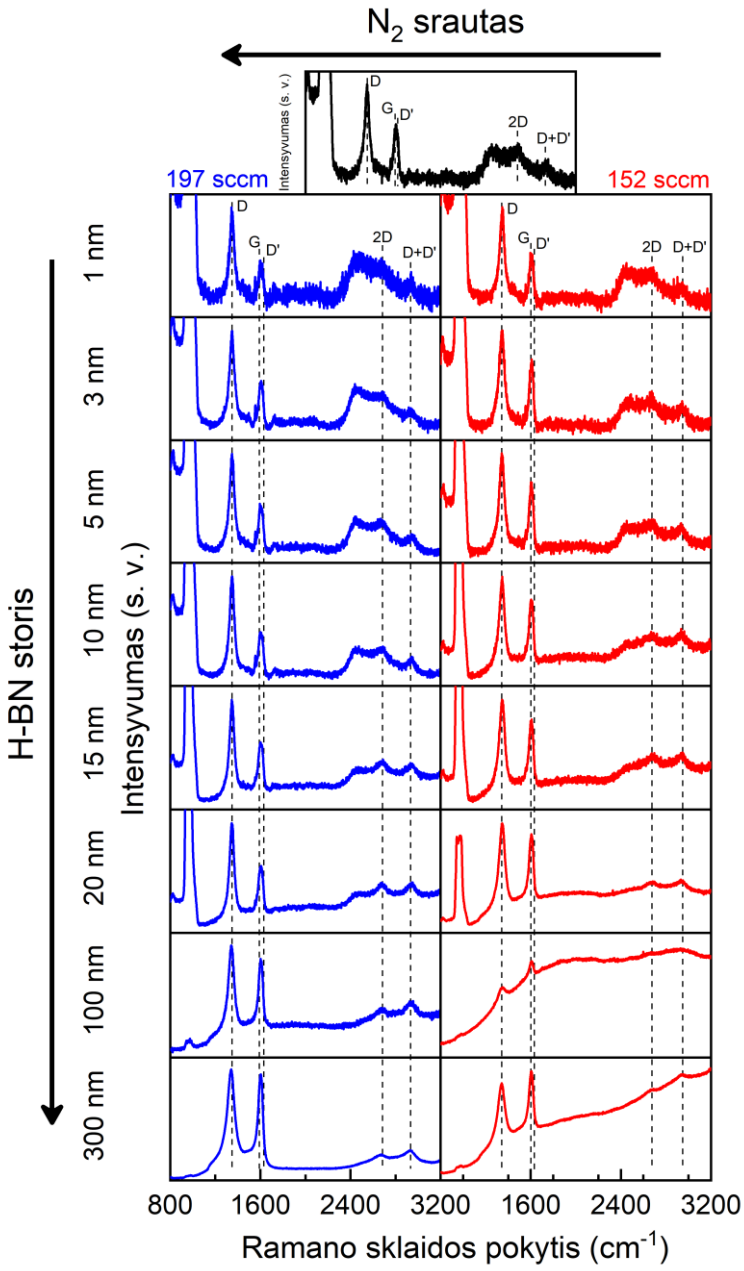
Naudojant skirtingas HIPIMS sintezės sąlygas (197 sccm bei 152 sccm N_2 srautai) buvo gautos skirtingo storio (keičiant sintezės trukmę) ir struktūros h-BN plėvelės, formuotos ant Si(100) pagrindų. Sėkmingą h-BN dangų sintezę patvirtina Ramano sklaidos spektrų analizė (**15 pav.**). Juose matyti charakteringa h-BN smailė ties ~1370 cm^{-1} [118,119,120]. Atlikus sėkmingus h-BN plėvelių auginimus, toliau vyko grafeno sintezė ant skirtingų h-BN/Si(100) pagrindų ir šių bandinių struktūros tyrimai Ramano sklaidos spektroskopijos metodu (**16 pav.**). Visais atvejais Ramano sklaidos spektruose pastebimos charakteringos grafeno smailės (2D, G). Taip pat pastebėta, kad visais atvejais matomos intensyvios D bei D‘ smailės, tad, taikant h-BN pasluoksnį, grafeno defektų tankio sumažinti nepavyko. Didinant sintezės trukmę (t. y. storį) matyti, kad liuminescencijos fonas išryškėja, kai h-BN sintezėje naudojamas 152 sccm N_2 srautas. Tai sutampa su kitų autorių gautais rezultatais ir yra

tiesiogiai susiję su B-H ir C-H ryšių formavimu [121]. Taip pat didinant h-BN plėvelių storį pastebėtas D+D' smailės intensyvumo didėjimas. Tai būdinga HG plėvelėms [122,123,124,125].

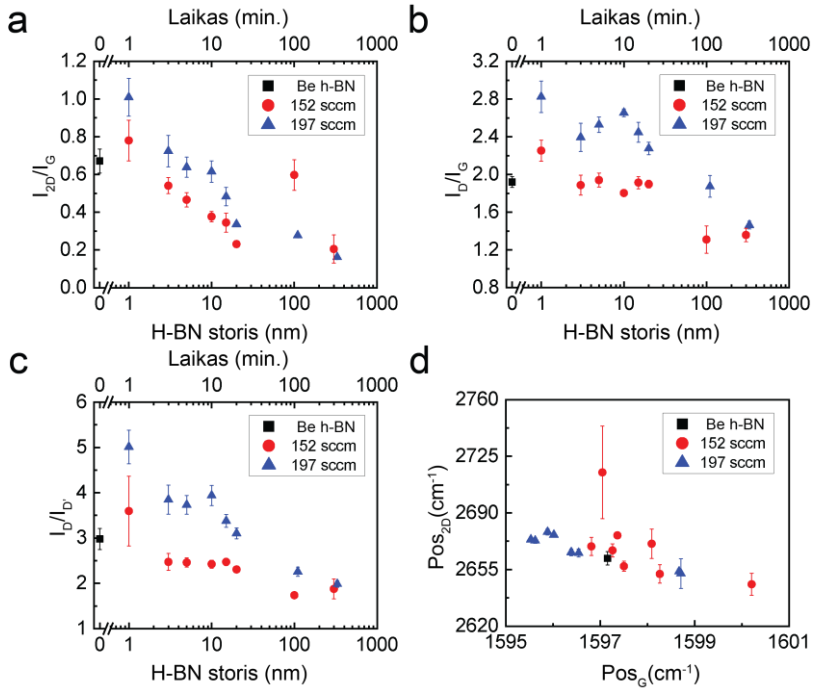
Detalesnė charakteringų Ramano sklaidos spektrų smailių analizė matoma **17 pav.** Atsižvelgiant į I_{2D}/I_G (**17 pav., a**) matyti, kad grafeno storis keitėsi drastiškai, kai naudoti skirtingo storio h-BN pasluoksniai. Įprastinės grafeno/Si(100) atveju grafenas buvo kelių sluoksnių, o grafeno sintezė ant kelių nm storio h-BN plėvelių sumažino grafeno storį iki 2–3 sluoksnių. Toliau didinant h-BN pasluoksnio storį, pastebėtas grafeno sintezės greitėjimas, todėl didėja ir I_{2D}/I_G (grafeno storis). Galima manyti, kad storesnės h-BN plėvelės paviršius yra netolygus, šiurkštus, todėl yra daugiau užuomazgų, skatinančių grafeno sintezę. Kaip ir ankstesniuose tyrimuose [**P1**,**P2**,**P3**], grafeno defektų tankis (I_D/I_G) mažėja su I_{2D}/I_G (**17 pav., b**). Vertinant $I_D/I_{D'}$ pastebėtas aiškus skirtumas tarp skirtingais N_2 srautais sintetintų h-BN plėvelių (**17 pav., c**). 152 sccm N_2 srautu sintetintoms h-BN plėvelėms būdingi sp^3 ryšiais pasižymintys pavieniai defektai. Tokio tipo defektai dažniausiai susiję su H atomų prisijungimu prie grafeno plėvelių [97]. Tai tik dar kartą patvirtina HG atvejį. Papildomai grafeno dangose tirta ir Pos_{2D} priklausomybė nuo Pos_G (**17 pav., d**). Pastebėta, kad 2D smailės pozicija slenkasi žemesnių banginių skaičių link, kai G smailė slenkasi aukštesnių banginių skaičių link. Ši tendencija pastebima n-tipo savaiminiu legiravimu pasižyminčiame grafene [98,101]. Svarbu paminėti, kad šis reiškinys matomas ir tiesiogiai sintetintame grafene ant h-BN/SiO_2 pagrindų, kai h-BN plėvelės augintos taikant CVD [126].



15 pav. Tipiniai h-BN plėvelių (sintetintų naudojant 152 sccm ir 197 sccm N_2 dujų srautus) Ramano sklaidos spektrai. Plėvelių storiai 300 nm ir 330 nm, atitinkamai naudojant 152 sccm ir 197 sccm srautą [**P5**]

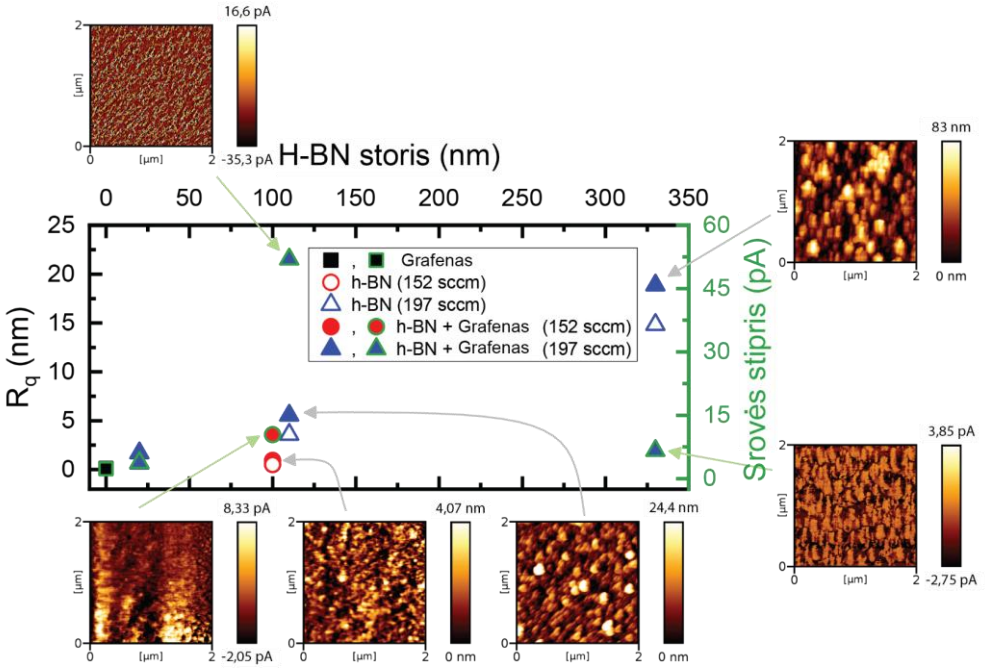


16 pav. Grafeno, sintetinto ant skirtingo storio h-BN plėvelių, struktūros tyrimai Ramano sklaidos spektroskopija. Skirtingais N_2 srautais sintetintos h-BN plėvelės pažymėtos mėlynai (197 sccm) ir raudonai (152 sccm). Tiesiogiai auginto grafeno ant Si(100) pagrindo spektras matomas viršuje (juodai) [**P5**]



17 pav. Įvairūs grafenui būdingų smailių parametrai ir jų santykiai, gauti analizuojant grafeno/h-BN/Si(100) (h-BN formuotas skirtingais N_2 srautais) ir grafeno/Si(100) Ramano spektrus. **(a)** I_{2D}/I_G priklausomybė nuo h-BN storio (sintezės laiko); **(b)** I_D/I_G priklausomybė nuo h-BN storio (sintezės laiko); **(c)** $I_D/I_{D'}$ priklausomybė nuo h-BN storio (sintezės laiko); **(d)** 2D smailės padėties priklausomybė nuo G smailės padėties [**P5**]

Taip pat tirta ir h-BN/Si(100) bei grafeno/h-BN/Si(100) bandinių paviršiaus morfologija bei paviršinio laidumo skirtumai taikant AJM ir laidumo AJM (**18 pav.**). Tiek h-BN, tiek ant jo sintetinto grafeno R_q didėjo augant h-BN sluoksnio storiui. Tai patvirtina paviršiaus netolygumo išvadas, remiantis Ramano sklaidos spektrų analize. Grafeno paviršiaus šiurkštumas akivaizdžiai didėjo didėjant padėklo paviršiaus šiurkštumui, ir visais atvejais grafeno R_q buvo šiek tiek didesnis už h-BN pasluoksnio R_q. H-BN plėvelių paviršiaus srovės vertės buvo nežymios, greičiausiai atkartojančios foninį signalą ir neviršijo 1,5–2 pA. Grafeno/h-BN/Si(100) bandiniai pasižymėjo skirtingomis paviršiaus srovės stiprio vertėmis, tačiau ryšio tarp grafeno paviršiaus laidumo ir savaiminio legiravimo nepastebėta. Paviršiaus srovės signalas pasiekia maksimalią vertę (51,9 pA) esant optimaliam 5,55 nm šiurkštumui, o šiurkštumui didėjant, srovė pradeda mažėti.



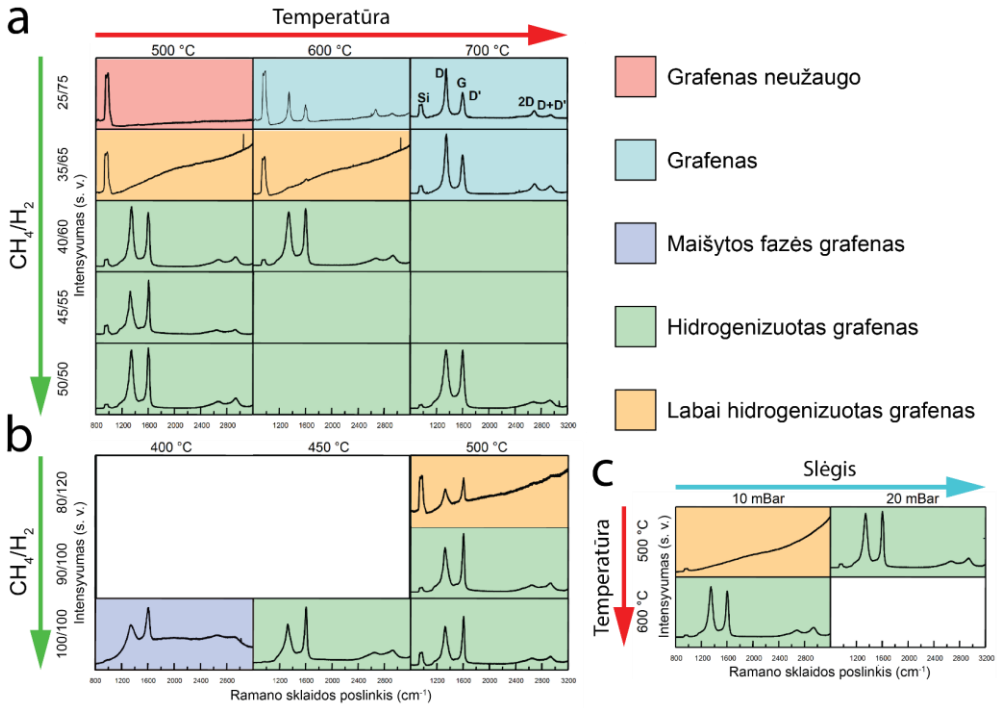
18 pav. Grafeno, sintetinto ant skirtingo storio h-BN plėvelių, morfologijos tyrimai taikant AJM bei laidumo AJM. h-BN plėvelės pažymėtos mėlynai (197 sccm) ir raudonai (152 sccm). Tiesiogiai auginto grafeno ant Si(100) duomenys pažymėti juodai [**P5**]

3.1.5. Žemos temperatūros, tiesioginės grafeno sintezės link

Atsižvelgiant į tai, kad grafeno plėvelės tiesiogiai sintetintos MW-PECVD būdu ant įvairių pagrindų (Si(100), SiO_2, C-safyras bei h-BN) bei naudojant įvairius auginimo parametrus, buvo tiriama žemos temperatūros tiesioginės grafeno sintezės galimybė. Įprastai PECVD sistemose naudojamos temperatūros yra ~700 °C. Norint dar labiau sumažinti šią temperatūrą, tenka atsižvelgti į sintezės metodo konfigūraciją. Būtent dėl to MW-PECVD sistemose, kai plazmos reiškiniai tiesiogiai veikia grafeno sintezės dinamiką, atsiranda galimybė mažinti proceso temperatūrą, optimizuojant CH_4/H_2 dujų srautus ir kameroje palaikomą slėgį.

Pirmiausia buvo naudojami jau anksčiau parinkti ir aptarti optimaliausi sintezės parametrai, siekiant palyginti šias grafeno plėveles su grafeno plėvelėmis, sintetintomis taikant begalę skirtingų CH_4/H_2 dujų srautų, įvairių slėgių ir temperatūrų kombinacijas. Siekiant dar labiau sumažinti sintezės temperatūrą, optimizuojant sintezės parametrus, pradžioje eksperimentai buvo atliekami esant 20 mbar darbiniam slėgiui ir 700 °C. Matyti, kad 700 °C temperatūroje kelių sluoksnių grafenas gali būti sintetinamas naudojant 25 sccm CH_4 ir 75 sccm H_2 dujų srautus (**19 pav., a**). Sintetinto grafeno Ramano spektrai rodo ryškias G ir 2D smailes [68,127] kartu su defektus apibūdinančiomis D [68,127] ir D+D′ smailėmis [122,123,124,125,128]. Be to, G smailės „petys“ rodo D′ smailės buvimą – tai dar vienas su defektais susijęs

požymis [68]. Ryški D smailė yra būdinga grafenui, tiesiogiai sintetintam ant dielektrinių ir puslaidininkinių pagrindų, ir ji priskiriama nanokristalinei medžiagos struktūrai, kaip ir minėta ankstesniuose skyriuose. Sumažinus sintezės temperatūrą iki 600 °C (naudojant 25 sccm metano ir 75 sccm vandenilio srautus), grafeno sintezė buvo sėkminga. I_{2D}/I_G santykis padidėjo, o tai leidžia daryti prielaidą, kad užaugo mažiau grafeno sluoksnių. Šios I_{2D}/I_G santykio vertės buvo būdingos dviejų sluoksnių grafenui [129]. Padidinus metano srautą iki 35 sccm ir sumažinus vandenilio srautą iki 65 sccm, Ramano spektruose atsirado stiprus fotoliuminescencijos fonas, būdingas stipriai hidrogenizuoto amorfinės anglies sluoksnio (~40–50 at.% vandenilio) augimui [129]. Tačiau, nustačius dujų srautus ties 40 sccm CH_4 ir 60 sccm H_2, pavyko sintetinti HG. Panašūs rezultatai buvo pastebėti ir esant 500 °C sintezės temperatūrai. Šios įžvalgos rodo, kad metano srauto didinimas ir vandenilio srauto mažinimas skatina HG augimą, kurį galima pasiekti žemesnėje temperatūroje nei „įprastą“ grynojo grafeno nusodinimą.



19 pav. Skirtingais sintezės parametrais (dujų srautų santykiu, temperatūra bei slėgiu) augintų grafeno plėvelių Ramano sklaidos spektrų palyginimas: **(a)** skirtingomis temperatūromis bei dujų srautų santykiais (kai bendras dujų srautas 100 sccm) sintetinto grafeno/SiO_2/Si(100) bandinių Ramano sklaidos spektrų palyginimas; **(b)** skirtingomis temperatūromis bei dujų srautų santykiais (kai bendras dujų srautas 200 sccm) sintetinto grafeno/SiO_2/Si(100) bandinių Ramano sklaidos spektrų palyginimas; **(c)** skirtingu slėgiu bei temperatūromis sintetinto grafeno/SiO_2/Si(100) bandinių Ramano sklaidos spektrų palyginimas. Spalvinis žymėjimas naudotas skirtingo tipo grafeno plėvelėms paryškinti [**P4**]

Esant 500 °C sintezės temperatūrai ir 200 sccm bendram dujų srautui (kai CH_4 ir H_2 dujų santykis 1:1), formuojasi HG grafenas (**19 pav., b**). Tačiau, sumažinus metano srautą iki 80 sccm ir padidinus vandenilio srautą iki 120 sccm, Ramano spektruose atsirado fotoliuminescencijos fonas, o 2D ir D+D′ smailės beveik išnyko. Nepaisant to, D ir G smailės išliko ryškios. Pažymėtina, kad HG sluoksnis buvo sėkmingai užaugintas 450 °C temperatūroje, naudojant 50 sccm CH_4 ir 50 sccm H_2 srautus. 400 °C temperatūroje Ramano spektrai pasižymėjo HG būdingomis savybėmis, įskaitant 2D ir D+D′ smailės ir platų fotoliuminescencijos foną. Šie stebėjimai leidžia manyti, kad 400 °C temperatūroje sintetintas bandinys buvo pereinamosios būsenos – hidrogenizuoto grafeno ir stipriai hidrogenizuoto anglies sluoksnio mišinys. Visgi šiuo atveju Ramano spektrų liuminescencijos pobūdis skiriasi nuo kitų šiame tyrime stebėtų stipriai hidrogenizuotų anglies sluoksnių. Tikėtina, kad tam įtakos turi defektiniai policiklinių aromatinių angliavandenilių ryšiai [130].

Sumažinus sintezės slėgį nuo 20 mbar iki 10 mbar, grafeno augimas išliko tiek taikant 700 °C, tiek ir 600 °C temperatūrą (**19 pav., c**). I_{2D}/I_G santykis grafene, augintame 600 °C temperatūroje ir esant 10 mbar slėgiui, buvo didesnis nei 20 mbar sintezės atveju – tai rodo lėtesnį grafeno augimo procesą. Be to, 500 °C temperatūroje HG nesiformavo, kai buvo naudojamas 10 mbar darbinis slėgis. Vietoje to Ramano spektruose atsirado fotoliuminescencijos fonas ir su padėklu susijusi smailė. Šiomis sąlygomis HG sintezė buvo pastebėta tik esant 600 °C temperatūrai (**19 pav., c**). Esant 500 °C temperatūrai ir 10 mbar slėgiui, keičiant bendrą dujų srautą, atsirado papildomų įžvalgų. Sumažinus bendrą srautą iki 100 sccm, susiformavo stipriai hidrogenizuotos anglies plėvelės, o padidinus bendrą srautą iki 200 sccm, Ramano spektruose pasirodė D ir G smailės, kartu pastebėtas fotoliuminescencijos fono sumažėjimas. Naudojant 20 mbar slėgį 500 °C temperatūroje, visais atvejais užaugo HG, nepriklausomai nuo naudojamo bendro dujų srauto.

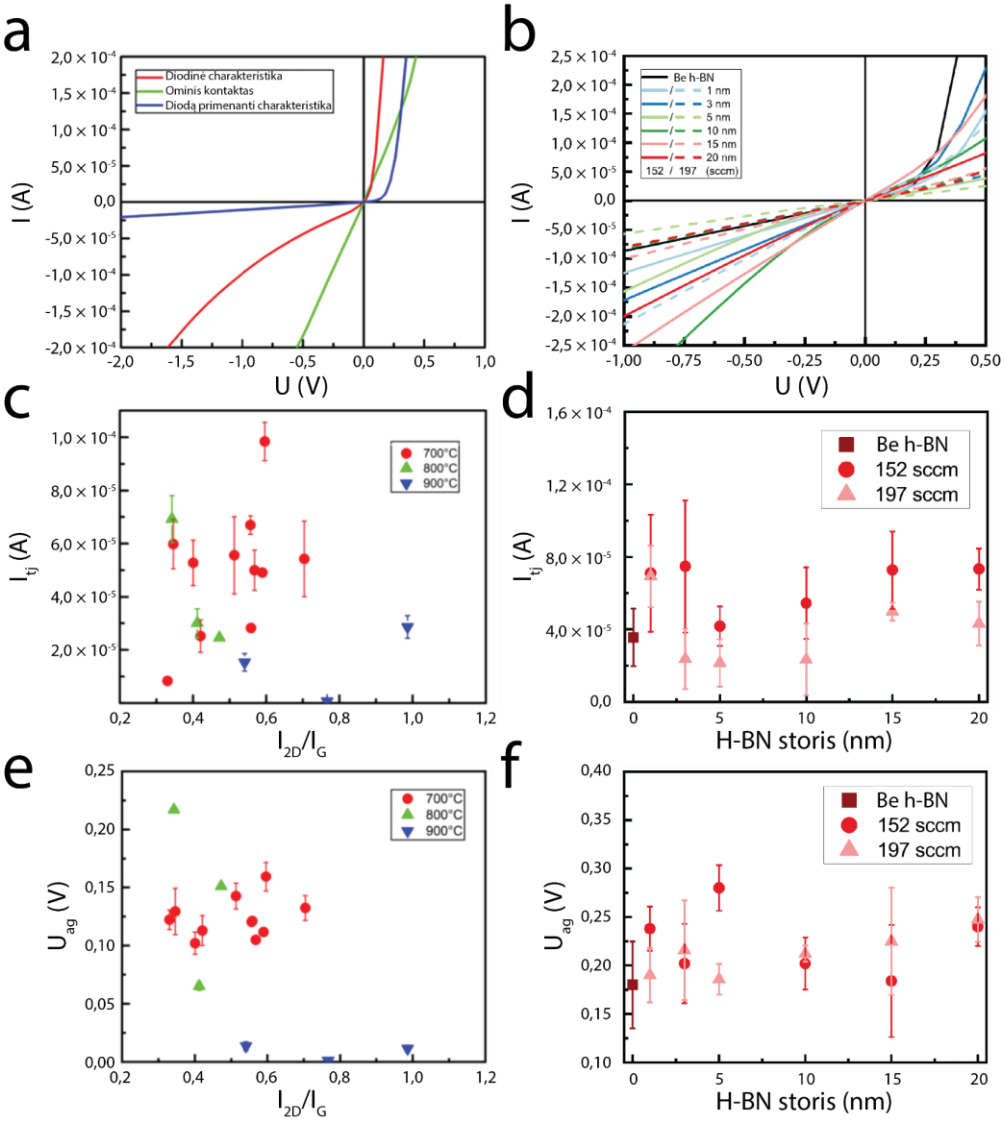
3.2. Fotodiodų ir lauko tranzistoriaus principu veikiančio biologinio jutiklio, suformuoto taikant grafeno plėveles, funkcinės savybės

3.2.1. Grafeno struktūros ir h-BN pasluoksnio įtaka fotodiodų charakteristikoms

Išmatavus grafeno/Si(100) ir grafeno/h-BN/Si(100) fotodiodų, suformuotų taikant skirtingomis sintezės sąlygomis sintetintą grafeną, VACh nustatyti trys šių prietaisų veikimo režimai, kuriuos galima suskirstyti į tris kategorijas: diodinį, ominio kontakto ir į diodinį panašų režimą (**20 pav., a, b**). Išmatuotos tiek UV, tiek ir IR spinduliuote apšviestų fotodiodų charakteristikos, tačiau pateikiami fotoelektrinių savybių duomenys, kai taikytas IR šviesos šaltinis dėl pranašesnio fotoatsako. Tiek grafeno/Si(100), tiek ir grafeno/h-BN/Si(100) fotodiodų atveju buvo matuojamos trumpojo jungimo srovė (**20 pav., c, d**) ir atviros grandinės įtampa (**20 pav., e, f**) fotodiodus apšvietus infraraudonąja spinduliuote ir atitinkamai skaičiuotos šių parametrų priklausomybės nuo grafeno bei h-BN storio. Pastebėta, kad grafeno/Si(100) prietaisų fotovoltiniai parametrai beveik nekoreliuoja su I_{2D}/I_G. Tik bandiniai, atkaitinti 700 °C temperatūroje, rodė tam tikrą I_{tj} ir U_{ag} padidėjimą didėjant I_{2D}/I_G santykiui (mažėjant sluoksnių skaičiui) (**20 pav., c, e**). Bandiniai, atkaitinti 900

°C temperatūroje, pasižymėjo mažomis I_{tj} vertėmis bei mažiausiomis U_{ag} vertėmis. Taigi, paviršiaus paruošimo sąlygos fotovoltiniams parametrams yra svarbesnės nei grafeno sluoksnių skaičius. O h-BN pasluoksnio įterpimas patvirtina, kad h-BN tarpinis sluoksnis gali būti naudojamas diodo trumpojo jungimo srovei padidinti. Šis efektas buvo kur kas ryškesnis, kai tarpinis sluoksnis buvo auginamas esant 152 sccm N_2 dujų srautui. Pastebėta, kad fotosrovė ir trumpojo jungimo srovė nuo storio priklausė nemonotoniškai: mažiausia trumpojo jungimo srovė nustatyta bandiniuose, suformuotuose taikant 5–15 nm storio h-BN tarpinį sluoksnį. Svarbu paminėti, kad vidutinė grafeno/h-BN/Si(100) diodo atviros grandinės įtampa beveik visada buvo didesnė nei grafeno/Si(100) diodo.

Taigi, matyti, kad h-BN pasluoksnis pagerina fotoelektrines fotodiodo, suformuoto taikant tiesiogiai sintetintą grafeną, savybes. Pažymėtina, kad grafeno/Si heterosandūros fotodiodų, pagamintų taikant perneštą grafeną, atveju h-BN pasluoksnio įterpimas dar reikšmingiau padidina atviros grandinės įtampą ir trumpojo jungimo srovę [131,132,133,134,135,136,137].



20 pav. (a) grafeno/Si(100) fotodiodų VACh; **(b)** grafeno/h-BN/Si(100) fotodiodų VACh; **(c)** grafeno/Si(100) fotodiodų trumpojo jungimo srovės priklausomybė nuo I_{2D}/I_G (grafeno storio); **(d)** grafeno/h-BN/Si(100) fotodiodų trumpojo jungimo srovės priklausomybė nuo h-BN pasluoksnio storio; **(e)** grafeno/Si(100) fotodiodų atviros grandinės įtampos priklausomybė nuo I_{2D}/I_G (grafeno storio); **(f)** grafeno/h-BN/Si(100) fotodiodų atviros grandinės įtampos priklausomybė nuo h-BN pasluoksnio storio [**P1**, **P5**]

3.2.2. FET principu paremti biologiniai jutikliai

Remdamiesi PBASE/grafeno imobilizavimo su ACE2 receptoriumi tyrimais, padarėme išvadą, kad T-G-FET jutikliams reikalinga optimali 10 µg/mL ACE2

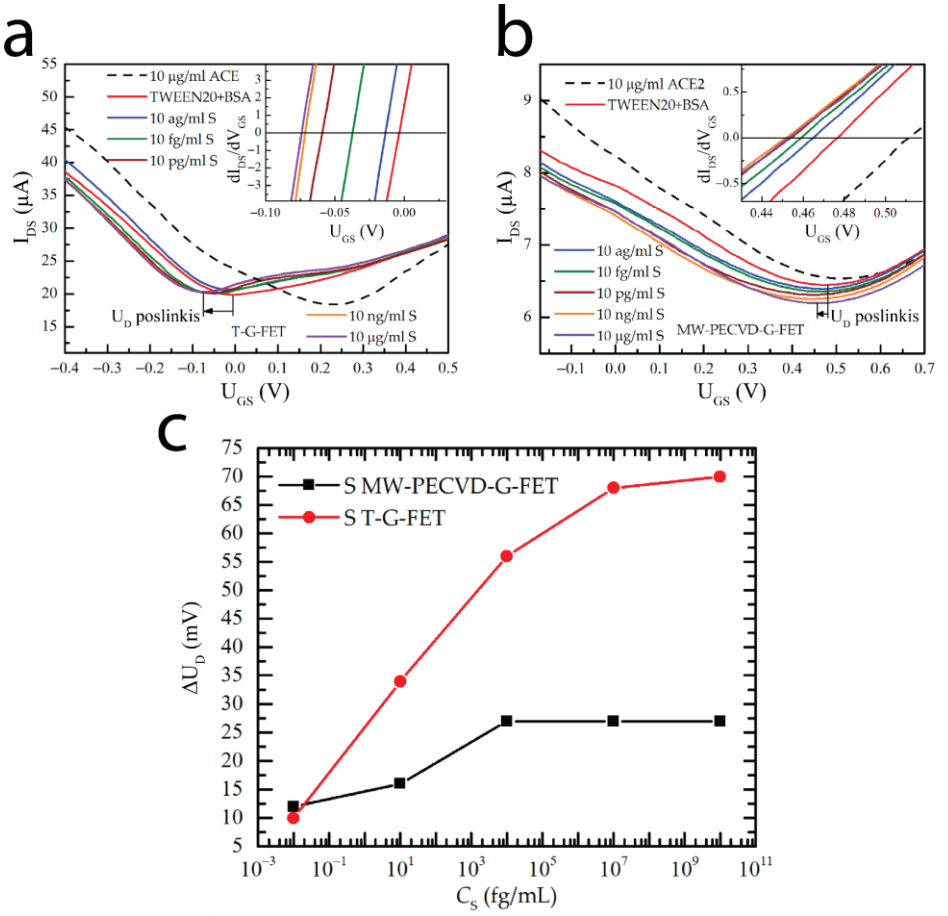
koncentracija, o MW-PECVD-G-FET jutikliams pakaktų ir 10 ng/mL ACE2 koncentracijos. Todėl tolimesnių tyrimų metu abiejų tipų G-FET biologiniams jutikliams paruošti buvo naudojama 10 µg/mL ACE2 koncentracija, siekiant užtikrinti gautų rezultatų palyginamumą. Kitame etape grafeno jutiklio paviršius buvo nuplautas 1 mL PBS tirpalo su „Tween-20“, po to – 2 mL PBS tirpalo, siekiant pašalinti ACE2 perteklių ir pasyvuoti nepadengtą grafeno paviršių. Vėliau į mikroskysčių sistemą buvo įšvirkšta 1 mL PBS tirpalo su 0,1 % BSA, kad būtų blokuotos visos ACE2 nepadengtos sritys. Po šių veiksmų biologiniai jutikliai buvo paruošti ir panaudoti S baltymo detekcijai naudojant G-FET.

21 pav. pateikiamos abiejų G-FET jutiklių būdingosios perdavimo kreivės (I_{DS} priklausomybė nuo U_{GS}), nustatytos esant skirtingoms S baltymo koncentracijoms PBS tirpale. Palyginimui pateikiami grafeno elementų, imobilizuotų naudojant 10 µg/mL koncentracijos ACE2 (juoda brūkšninė linija), ir tų pačių elementų po plovimo „Tween-20“ ir vėlesnio apdorojimo BSA (raudona linija) perėjimo charakteristikų matavimai. Galima matyti, kad skalavimo procedūra sukėlė reikšmingus minimumo padėties pokyčius perdavimo kreivėse. Tai ypač išryškėjo pernešto grafeno T-G-FET bandiniuose (**21 pav., a**), kur Dirako įtampa pasislinko iš U_{GS} = 270 mV į mažesnes užtūros / ištakos įtampas U_{GS} = –3 mV. MW-PECVD G-FET atveju poslinkis buvo daug mažesnis: nuo 510 mV iki 475 mV (**21 pav., b**). Vėliau, užpildant mikroskystinį sistemos kanalą didesnės koncentracijos spyglio (S) baltymu, buvo pastebimas tolesnis Dirako taško poslinkis į mažesnių U_{GS} pusę. Tačiau, didėjant S baltymo koncentracijai, šis poslinkis mažėja ir pastebima sotis.

21 pav., c, apibendrinami **21 pav., a, b,** pateikti duomenys. Matyti, kad abu G-FET prietaisai pasižymėjo puikiu jautrumu ir sugebėjo aptikti S baltymą, kurio koncentracija siekė vos 10^{-2} fg/mL. Esant šiai koncentracijai, Dirako įtampa pasislinko apie 10 mV. Didėjant S baltymo koncentracijai (C_S), Dirako įtampos poslinkis pradėjo sotintis. Visgi MW-PECVD G-FET biologinių jutiklių ΔV_D pradėjo sotintis esant 10^4 fg/mL S baltymo koncentracijai, o maksimalus Dirako įtampos pokytis siekė 27 mV. Kita vertus, T-G-FET biologiniai jutikliai gali veikti platesniame S baltymo koncentracijų diapazone, o užtūros įtampos poslinkis pradeda sotintis tik ties 10^7 fg/mL. Šiuo atveju bendras pasiektas Dirako įtampos poslinkis buvo ~70 mV. Iš gautų rezultatų analizės tapo akivaizdu, kad grafeno savybės ir kokybė daro didelę įtaką visiems grafeno paviršiaus modifikavimo procesams, tokiems kaip funkcionalizavimas PBASE, imobilizavimas ACE2 ir S baltymo detekcija.

Gauti rezultatai rodo, kad nors MW-PECVD būdu užauginto grafeno biologiniai jutikliai pasižymi siauresniu jautrumo diapazonu ir aukštesne aptikimo riba, palyginti su pernešto grafeno biologiniu jutikliu, jis gali būti sėkmingai naudojamas SARS-CoV-2 spyglio (S) baltymui aptikti. MW-PECVD-G-FET vis tiek geba fiksuoti dešimtis ag/mL (atogramų mililitre) siekiančias koncentracijas. Atsižvelgiant į šiuos rezultatus ir tiesioginio grafeno auginimo ant Si/SiO_2 paviršiaus suderinamumą su silicio technologija, tiesiogiai susintetinto grafeno pagrindu veikiantis FET biologinis jutiklis yra labai perspektyvus. Siekiant padidinti MW-PECVD-G-FET jautrumą ir jų darbinį koncentracijų diapazoną, būtinas tolesnis tiesiogiai susintetinto grafeno struktūros optimizavimas. Reikėtų paminėti, kad tiesiogiai susintetinto grafeno FET biologinių jutiklių jautrumo priklausomybė nuo struktūros išlieka neaiški. Grafenas,

turintis mažesnius grūdelius ir daugiau grūdelių ribų, pasižymėjo mažesniu vidutiniu judriu [138]. Dar svarbesnis pagrindo sukeltas savaiminio grafeno legiravimo valdymas. Sumažinus padėklo sukeltą savaiminį legiravimą, padidėja tiek pernešto grafeno judris [139,140], tiek pernešto grafeno FET dujų jutiklių jautrumas [141]. Pagrindo sukelto legiravimo poveikį galima sumažinti jį pasyvuojant [138]. Tačiau šis metodas netinka grafeno biologiniams jutikliams, nes pasyvuojantis sluoksnis padidina atstumą tarp grafeno ir analitės molekulių, o tai sumažina jutiklio jautrumą. Perspektyviau būtų parinkti tinkamą pagrindą [139] ir surasti optimalų pagrindo paruošimą prieš grafeno sintezę [142].



21 pav. T-G-FET biologinių jutiklių **(a)** bei MW-PECVD-G-FET biologinių jutiklių **(b)** perdavimo charakteristikos esant skirtingoms spyglio (S) baltymo koncentracijoms. **(c)** Dirako įtampos pokyčio (ΔU_D) priklausomybė nuo spyglio (S) baltymo koncentracijos MW-PECVD-G-FET ir T-G-FET atvejais. Įterptiniuose grafikuose vaizduojamos perdavimo charakteristikų išvestinės šalia Dirako taško, kuriame išvestinė yra lygi nuliui [**P2**]

IŠVADOS

1. Grafeno plėvelės buvo sėkmingai tiesiogiai užaugintos ant Si, SiO_2, Al_2O_3(0001) ir h-BN/SiO_2 pagrindų, taip išvengiant sudėtingų sintezės žingsnių ir perkėlimo procedūrų. Atlikti Ramano sklaidos spektroskopijos ir atominių jėgų mikroskopijos tyrimai, kuriais remiantis nustatyta, kad šio tipo plėvelių struktūra bei paviršiaus šiurkštumas labiausiai priklauso nuo sintezėje naudojamų dujų srautų santykio ir jos metu palaikomo kameros slėgio:

   a. Naudojant mikrobangų plazma aktyvuoto cheminio nusodinimo iš garų fazės (MW-PECVD) metodą tiesiogiai ant dielektrinių (SiO_2, Al_2O_3(0001), h-BN) ir puslaidininkinių (pagrindų Si(100)) sėkmingai suformuotos horizontalaus grafeno plėvelės;

   b. Atominių jėgų mikroskopijos (AJM) tyrimai parodė, kad ant dielektrinio SiO_2 padėklo susidaro grafeno dariniai, kurių vidutinis aukštis siekia 1,0–1,3 nm, o tai atitinka kelių sluoksnių grafeno struktūrą;

   c. Ramano sklaidos spektroskopijos analizė patvirtino grafeno nanokristališkumą: nustatyta, kad vidutinis I_{2D}/I_G intensyvumų santykis yra ~0,4, patvirtinantis keliasluoksnio grafeno augimą, o vidutinis defektų tankio rodiklis I_D/I_G siekia ~1,46–1,84, nurodant dominuojančius grūdelių ribų defektus. Remiantis $I_D/I_{D'}$ duomenimis, beveik visais atvejais grafenas pasižymi grūdelių ribos defektais.

2. Atlikta žemos temperatūros (<600 °C) grafeno sintezė, taikant MW-PECVD ant SiO_2/Si(100) pagrindų, ištirta skirtingų sintezės parametrų įtaka gautų grafeno plėvelių struktūrai ir išanalizuota šių struktūrų įvairovė:

   a. Eksperimentiškai pagrįsta, kad, taikant optimizuotus sintezės parametrus (CH_4/H_2 srautų santykį, stabilų 10 mBar slėgį bei 0,7 kW galią), grafeno sluoksnius galima formuoti žemesnėje nei 600 °C temperatūroje, o hidrogenizuotą grafeną – net esant 400 °C;

   b. Nustatyta, kad sintezės metu naudojamas plieninis dangtelis efektyviai apsaugo padėklą nuo tiesioginio ardančio plazmos poveikio, o slėgio reguliavimas leidžia kontroliuoti defektų tipą: mažinant slėgį žemiau 20 mBar, $I_D/I_{D'}$ santykis nusistovi ties ~2,5 verte.

3. Pademonstruoti naudojant MW-PECVD metodą tiesiogiai sintetinto grafeno taikymo elektriniuose prietaisuose pavyzdžiai. Ant h-BN bei Si(100) pagrindų suformuoti grafeno fotodiodai ir ištirtos jų voltamperinės charakteristikos. Išmatuotos trumpojo jungimo srovės bei atviros grandinės įtampos vertės ir atliktas šių verčių priklausomybių nuo pagrindo storių palyginimas, esant skirtingiems pagrindams. Taip pat suformuotas ir biologiniam jutikliui pritaikytas grafeno lauko tranzistorius. Ištirtas šio jutiklio jautrumas SARS-CoV-2 spyglio (S) baltymui:

a. Nustatyta, kad h-BN tarpinis sluoksnis efektyviai pagerina prietaisų fotoelektrines savybes: padidina atviros grandinės įtampą (U_{aq}) ir trumpojo jungimo srovę (I_{tj}), nors pastaroji nuo h-BN storio priklauso nemonotoniškai;

b. Pademonstruota, kad tiesiogiai sintetintas grafenas pasižymi itin dideliu jautrumu SARS-CoV-2 spyglio (S) baltymui: pasiekta aptikimo riba siekia vos 10^{-2} fg/mL.

ABSTRACT

Introduction

Two-dimensional nanomaterials are an ever-growing family of materials characterized by stable structures where the atomic arrangement predominates in a single plane. The first such material to be discovered was graphene, an allotrope of carbon. Despite the various carbon allotropes found in nature – such as diamond, amorphous carbon, and graphite – it is graphene that possesses some of the most interesting properties suitable for applications in mechanics, biotechnology, electronics, and optics. A thin layer of such material is optically transparent; furthermore, covalent bonds provide extraordinary strength. A combination of these properties, along with high conductivity resulting from delocalized electrons, allows graphene to be used as a transparent conductor in optoelectronics and in the production of Si-based photoelectric devices. Furthermore, graphene can be functionalized in numerous ways; thus, it may be highly sensitive to various analytes, which enables it to be used for sensing or biosensing applications.

The oldest method of graphene synthesis is exfoliation. This method involves using graphite, whose layers are separated by using various mechanical or ultrasonic methods. Graphene, when obtained this way, exhibits properties close to a true monolayer coating. However, this method suffers from a significant drawback: the yield of the resulting material is low, and the effective area of the graphene used is small. To produce graphene coatings with a larger surface area, 'bottom-up' synthesis methods must be applied. The primary technology for growing large-area graphene is *Chemical Vapor Deposition* (CVD) on a catalytic substrate. Copper and nickel are the most commonly used substrates, as they meet the criteria for successful monolayer growth and passivation when using this method. Nevertheless, graphene synthesis on these substrates is not easily adaptable to the semiconductor industry and optoelectronics due to the required transfer of the coating from the metal foil onto the desired dielectric or semiconductor substrates. At this stage, problems arise: graphene folds, cracks, and organic adsorbates or residues of the metal substrate remain on its surface. Additionally, graphene grown on catalytic substrates requires high process temperatures.

Plasma-Enhanced Chemical Vapor Deposition (PECVD) eliminates the limitations of the previously described technologies. It has already been demonstrated that this method allows for direct synthesis of graphene on selected dielectric and semiconductor substrates, such as Si. Furthermore, the process requires lower temperatures, which is favorable for mass production. The main drawbacks of the process include a high density of intercrystalline grain boundary defects, and the non-uniformity of the graphene film. It is of importance to note that the method is not yet fully developed; therefore, its improvement could yield positive results, such as a reduced defect density, a wider range of possible substrates, and coating integrity.

The use of different substrates in graphene synthesis is one of the key aspects for forming optoelectronic devices consisting of graphene/Si heterostructures. The role of such heterostructures in electronics would allow for the control of charge transport mechanisms and could improve the photoelectric properties of the devices.

In this case, PECVD is an ideal technology which opens up possibilities to grow graphene structures on selected surfaces without additional and complex coating transfer stages, thereby forming devices based on graphene/Si heterostructures.

In this doctoral thesis, the main structural features of graphene synthesized by Plasma-Enhanced Chemical Vapor Deposition shall be discussed and analyzed on the basis of using Raman spectroscopy and *Atomic Force Microscopy* (AFM) methods. Additionally, the functional properties of electrical devices (photodiodes and a biological sensor operating on the field-effect transistor principle) formed by using graphene films shall be investigated.

Aim of the research

To grow graphene on Si and SiO_2 substrates commonly used in microelectronics, on an Al_2O_3(0001) substrate featuring a crystal lattice very similar to that of graphene, and on an h-BN underlayer, which improves the electrical properties of graphene, by using the plasma-enhanced chemical vapor deposition method, and to investigate the structure of the films as well as the functional properties of electrical devices formed by using the graphene films.

Objectives of the research

1. Grow graphene on Si, SiO2, Al_2O_3(0001) and h-BN/SiO_2 substrates by using the plasma-enhanced chemical vapor deposition method, and to investigate them by using Raman scattering spectroscopy and atomic force microscopy.
2. Investigate the feasibility of low-temperature (<600 °C) plasma-enhanced chemical vapor deposition for forming graphene layers on SiO_2/Si(100) substrates.
3. Analyze the functional properties of electrical devices (photodiodes and a biological sensor operating on the field-effect transistor principle) formed by using graphene films.

Scientific novelty

In this work, the synthesis of graphene has been performed by using the direct *Plasma-Enhanced Chemical Vapor Deposition* (PECVD) method, employing a steel cap to protect against undesirable plasma effects. Graphene films were formed on substrates that are widely used in microelectronics (Si and SiO_2), possess a structure akin to graphene (Al_2O_3(0001)), and improve the electrical properties (h-BN/SiO_2).

The suitability of directly grown graphene for the fabrication of optoelectronic and bioelectronic devices has been demonstrated, and the key regularities linking the structural quality of graphene with the sensitivity of the fabricated photodiodes and field-effect transistor-based biosensors have been established.

Furthermore, the critical limits of low-temperature (<600 °C) synthesis have been determined by optimizing the hydrogen-to-methane gas flow ratio and thermodynamic pressure, which paves the way for the integration of graphene into standard CMOS technology.

Methods and Materials

Graphene samples were formed on various substrates, including n-type Si(100), thermal SiO_2, Al_2O_3(0001) and h-BN films, while using a microwave plasma-enhanced chemical vapor deposition (MW-PECVD) system. To protect the samples from direct plasma exposure, a diamagnetic steel cover was utilized during the synthesis. The process involved a cleaning stage, followed by hydrogen plasma annealing at temperatures ranging from 700 °C to 900 °C, and, finally, the growth of graphene layers using a mixture of hydrogen and methane gases. For the development of h-BN buffer layers, *High-Power Impulse Magnetron Sputtering* (HiPIMS) was employed at 800 °C, with the resulting thicknesses verified via laser ellipsometry. Additionally, low-temperature synthesis (below 600 °C) was investigated on SiO_2/Si substrates by optimizing gas flow rates and chamber pressure through a feedback-controlled monitoring system. The surface morphology and topography of the synthesized films were evaluated by using *Atomic Force Microscopy* (AFM) in the tapping mode, while local electrical conductivity was mapped using conductive AFM with Pt/Ir-coated probes. To analyze the structural quality and the layer count of the graphene, Raman scattering spectroscopy was performed by using a 532 nm laser. A specialized spectrum analyzer was developed in the MATLAB environment to provide consistent peak fitting for the D, G, D' and 2D bands while using Lorentzian and Lorentzian-Gaussian functions. This methodology allowed for a precise assessment of the defect density, crystallite size and growth dynamics by calculating the peak positions, intensity ratios and *Full Width at Half Maximum* (FWHM) values. For the investigation of functional properties, graphene-based photodiode prototypes and biological sensors were fabricated. The photodiodes, based on graphene/Si and graphene/h-BN/Si heterostructures, were characterized by measuring I-V curves under dark conditions and illumination from UV (406 nm) and IR (730 nm) LEDs so that to determine photosensitivity and reverse current behavior. Simultaneously, *Graphene Field-Effect Transistor* (G-FET) biosensors were developed for the detection of the SARS-CoV-2 (S) spike protein. These devices were functionalized with PBASE and ACE2 proteins and integrated into a microfluidic system with a liquid-gate configuration. The sensing performance was evaluated by monitoring shifts in the Dirac voltage (V_D) through transfer characteristic (I_{DS} vs. V_{GS}) measurements.

Results

Influence of gas flow rates and synthesis time on graphene deposited on Si(100)

Initial experiments on Si(100) substrates focused on the influence of CH_4/H_2 ratios and synthesis duration on graphene morphology and structure [94]. The highest quality sample, characterized by the lowest root mean square roughness (R_q = 0.11 nm) and a thickness exceeding 3 layers, was achieved by using a CH_4/H_2 ratio of 75/25 at 700 °C [67]. Raman spectroscopy confirmed these findings, by showing that an increase in the gas flows or process duration led to a greater crystallite thickness and defect density [1,95]. This trend is attributed to suboptimal growth conditions that

hinder crystal relaxation and increase sp^3 bonding due to rising carbon solubility in the Si(100) substrate [96].

Detailed analysis of Raman spectral parameters revealed a dominance of grain boundary defects in all directly synthesized films, with $I_D/I_{D'}$ ratios ranging from 2.76 to 3.29 [73]. Compared to defect-free transferred graphene [70,97], the MW-PECVD samples exhibited blue-shifted G-peaks and significantly broader $FWHM_G$ and $FWHM_{2D}$ values [98]. These variations suggest a high defect density and a potential compressive strain caused by the significant mismatch in thermal expansion coefficients between graphene and the Si(100) substrate [99,100,104,105]. Despite the polycrystalline nature and high defect density of the films, the parameters from the most successful sample were established as a baseline for subsequent synthesis on SiO_2/Si(100), C-sapphire and h-BN substrates [101,102,103].

Graphene synthesis on stable SiO_2

Following the study on Si(100), direct synthesis of graphene on dielectric SiO_2/Si(100) substrates was investigated due to their chemical inertness and suitability for smooth, horizontal graphene formation [106]. Based on previous research [93,94,**P1**], synthesis was performed at 700 °C, 10 mBar and 0.7 kW for 120 minutes. AFM analysis revealed that graphene consists of 20–25 nm crystallites with a height of ~1–1.3 nm, similar to those observed on Si(100). Conductive AFM measurements highlighted variations in local conductivity, which are attributed to the nanocrystalline nature of the film and an increased resistance at grain boundaries [107].

Raman scattering analysis yielded an I_{2D}/I_G ratio of ~0.42, thus indicating multilayer graphene formation, which is consistent with the extended synthesis duration. Notably, graphene grown on SiO_2 exhibited a lower defect density (I_D/I_G ~ 1.46) compared to Si(100) samples. The $I_D/I_{D'}$ ratio (3.26) indicates that grain boundary defects remain predominant. Overall, graphene synthesized on both SiO_2 and Si(100) shows a similar morphology and structure, characterized by weak substrate interaction due to a lack of strong chemical bonding in the case of SiO_2 and a thermal expansion coefficient mismatch in the case of Si(100).

Graphene/C-sapphire synthesis dynamics

The catalytic nature of C-sapphire and its hexagonal Al2O3(0001) structure facilitate a stable graphene synthesis process while reducing grain boundary defects [108]. In this study, MW-PECVD synthesis on C-sapphire was optimized by analyzing the CH_4/H_2 gas flow ratio and chamber pressure. Graphene was successfully formed under various conditions, as evidenced by typical Raman peaks after removing the characteristic luminescence background of the sapphire substrate [56,111].

Structural analysis based on I_{2D}/I_G and I_D/I_G ratios revealed that an increase in the CH_4 flow leads to a simultaneous decrease in both ratios, which indicates that defect density is thickness-dependent. In the initial growth stages, grain boundary defects are numerous, but their density decreases as the film thickens [73,97]. The predominance of grain boundary defects was further confirmed by $I_D/I_{D'}$ ratios. Pressure also played a critical role; lower pressures resulted in unstable growth and a

higher defect density, whereas an increase in the pressure promoted faster thickness growth and lower defect density. Specifically, at 5 mBar, the $I_D/I_{D'}$ ratio of ~5.5 suggested a mix of vacancies and grain boundary defects, while, at pressures above 20 mBar, the ratio stabilized at around 2.5 [73].

AFM analysis showed that the lowest level of surface roughness was achieved with CH_4/H_2 ratios ≤35/65 and pressures ≤10 mBar. Beyond these threshold values, rapid formation of graphene layers occurred, which decreased the defect density but significantly increased the root mean square roughness (R_q). These findings align with the Raman results, suggesting that while higher pressure and methane concentrations accelerate the film growth and improve crystallinity, they also lead to an increased surface roughness due to the rapid accumulation of graphene layers.

Compatibility of h-BN and graphene

Hexagonal boron nitride (h-BN) is another material with atoms arranged in a single plane, forming hexagonal rings where boron and nitrogen atoms alternate to avoid direct interaction between the same species. Due to its structural similarity and lattice parameters being close to graphene, it is considered a promising substrate [112,113,114,115,116,117]. In this study, h-BN films of varying thickness and structure were first formed on Si(100) while using HIPIMS with different N_2 flow rates (197 sccm and 152 sccm), confirmed by the characteristic h-BN Raman peak at ~1370 cm^{-1} [118,119,120].

The subsequent graphene synthesis on these h-BN/Si(100) templates yielded characteristic 2D and G Raman peaks in all cases. However, intense D and D' peaks were observed, indicating that the h-BN buffer layer did not reduce the graphene defect density. For h-BN films synthesized at 152 sccm N_2, an emerging luminescence background was observed with an increasing thickness, which is linked to the formation of B-H and C-H bonds [121]. Additionally, the increasing intensity of the D+D' peak in thicker films suggests the presence of hydrogenated graphene (HG) [122,123,124,125].

Detailed analysis of the Raman peaks showed that the h-BN thickness significantly influences graphene growth. While graphene on Si(100) was multilayered, synthesis on thin h-BN layers (specifically, a few nm-thick) reduced the thickness to 2–3 layers. Conversely, thicker h-BN layers accelerated graphene growth, likely due to an increased surface roughness and a higher number of nucleation sites. As well as in previous studies, the defect density (I_D/I_G) decreased as the film thickness (I_{2D}/I_G) increased [P1,P2,P3].

The $I_D/I_{D'}$ ratios revealed a clear difference between the two N_2 flow rates; films grown on h-BN synthesized at 152 sccm N_2 exhibited individual sp^3 defects, which is typical of hydrogen atom attachment to graphene [97]. Furthermore, the relationship between Pos_{2D} and Pos_G showed a trend where the 2D peak red-shifts while the G peak blue-shifts. This behavior is characteristic of n-type self-doping in graphene [98,101], which is a phenomenon also observed in graphene directly synthesized on h-BN/SiO_2 substrates where h-BN was grown via CVD [126].

Towards low-temperature direct graphene synthesis

The feasibility of low-temperature direct graphene synthesis was investigated by optimizing CH_4/H_2 gas flows and chamber pressure within the MW-PECVD system. While conventional PECVD temperatures are typically ~700 °C, the direct influence of plasma dynamics enables a significant reduction in the process temperature.

Experiments at 20 mbar and 700 °C yielded multilayer graphene with distinct G and 2D peaks, alongside defect-related D, D', and D+D' peaks [68,122,123,124,125,127,128]. Reducing the temperature to 600 °C (25 sccm CH_4 and 75 sccm H_2) successfully produced bilayer graphene, as indicated by an increased I_{2D}/I_G ratio [129]. Further adjustments revealed that an increase in the methane flow (40 sccm CH_4 and 60 sccm H_2) promotes the growth of *Hydrogenated Graphene* (HG) at 600 °C and 500 °C, a state reachable at lower temperatures than standard pure graphene deposition.

At 500 °C and 20 mbar, a 1:1 CH_4/H_2 ratio consistently produced HG. Conversely, decreasing the methane flow (80 sccm) and increasing hydrogen (120 sccm) suppressed the 2D and D+D' peaks while introducing a strong photoluminescence background which is characteristic of highly hydrogenated amorphous carbon [129]. HG layers were successfully grown at temperatures as low as 450 °C. At 400 °C, the material appeared to be in a transitional state – a mixture of HG and hydrogenated amorphous carbon – influenced by defective polycyclic aromatic hydrocarbon bonds [130].

Chamber pressure also played a critical role in growth kinetics. Reducing the pressure from 20 mbar to 10 mbar slowed the growth process, resulting in higher I_{2D}/I_G ratios at 600 °C. At 10 mbar, HG synthesis failed at 500 °C regardless of the total gas flow, leading instead to amorphous carbon films. In contrast, the 20-mbar setting enabled consistent HG growth at 500 °C across all tested flow rates, thereby demonstrating that a higher pressure is essential for maintaining stable synthesis at reduced temperatures.

Influence of graphene structure and h-BN buffer layer on photodiode characteristics

Based on the I-V characteristics of graphene/Si(100) and graphene/h-BN/Si(100) photodiodes fabricated under different synthesis conditions, three operating regimes were identified: diode, ohmic contact, and diode-like. Although the characteristics were measured under both UV and IR radiation, data for IR illumination were selected to be presented due to a superior photoresponse. Short-circuit current (I_{SC}) and open-circuit voltage (V_{OC}) were measured for both photodiode types, and their dependence on graphene and h-BN thickness was analyzed.

For graphene/Si(100) devices, photovoltaic parameters showed almost no correlation with the I_{2D}/I_G ratio. Only samples annealed at 700 °C exhibited a slight increase in I_{SC} and V_{OC} with an increasing I_{2D}/I_G ratio (decreasing layer count). Whereas, samples annealed at 900 °C showed low I_{SC} and the lowest V_{OC} values, thus indicating that surface preparation conditions are more critical for photovoltaic performance than the sheer number of graphene layers.

In contrast, the inclusion of an h-BN buffer layer confirmed that such an intermediate layer can enhance the short-circuit current of the diode. This effect was significantly more pronounced when the buffer layer was grown at an N_2 flow rate of 152 sccm. Both photocurrent and short-circuit current exhibited a non-monotonic dependence on thickness, with the lowest I_{SC} values observed in samples utilizing a 5 – 15 nm thick h-BN layer. Notably, the average open-circuit voltage for graphene/h-BN/Si(100) diodes was consistently higher than that of graphene/Si(100) diodes.

Thus, the h-BN buffer layer improves the photoelectric properties of photodiodes based on directly synthesized graphene. It is worth noting that, in graphene/Si heterojunction solar cells made with transferred graphene, the insertion of an h-BN layer leads to an even more significant increase in both open-circuit voltage and short-circuit current [131,132,133,134,135,136,137].

FET-based biosensors

Based on the ACE2 immobilization studies using PBASE/graphene, it has been determined that T-G-FET sensors require an optimal ACE2 concentration of 10 μg/mL, while 10 ng/mL is sufficient for MW-PECVD-G-FET sensors. For comparability, 10 μg/mL was used for both types during bio-FET preparation. Following immobilization, the sensors were washed with PBS/Tween-20 and passivated with 0.1% BSA to block non-specific binding sites before SARS-CoV-2 spike (S) protein detection.

Transfer curves showed a significant shift in the Dirac voltage following the rinsing and BSA treatment. This shift was particularly pronounced in the transferred graphene (T-G-FET), where V_D moved from 270 mV to -3 mV, compared to a smaller shift (510 mV to 475 mV) in the MW-PECVD G-FET. Subsequent exposure to increasing concentrations of the S protein caused a further shift of the Dirac point toward lower gate voltages until saturation was reached.

Summary data demonstrate that both devices exhibit excellent sensitivity, detecting the S protein at concentrations as low as 10^{-2} fg/mL with a corresponding V_D shift of approximately 10 mV. MW-PECVD G-FET reached saturation at 10^4 fg/mL with a maximum V_D shift of 27 mV, whereas T-G-FET operated over a broader range, saturating at 10^7 fg/mL with a total shift of ~70 mV. These results highlight that graphene quality significantly influences the surface modification and sensing performance.

Although MW-PECVD graphene biosensors have a narrower sensitivity range and a higher detection limit than the transferred graphene sensors, they successfully detect concentrations in the ag/mL range. Given the compatibility of direct MW-PECVD growth on Si/SiO_2 with standard silicon technology, these FET biosensors are highly promising. Future sensitivity improvements require an optimization of the graphene structure and the management of substrate-induced self-doping. While surface passivation can reduce doping, it may decrease sensitivity by increasing the distance between graphene and the analyte; therefore, selection of appropriate substrates and optimizing pre-synthesis preparation remains the most viable path forward [138,139,140,141,142].

Conclusions

1. Graphene films have been successfully grown on Si, SiO_2, Al_2O_3(0001) and h-BN/SiO_2 substrates by using a direct synthesis method, thus effectively bypassing complex multi-step synthesis and transfer procedures. Raman spectroscopy and atomic force microscopy analysis determined that the structural properties and surface roughness of these films are primarily governed by the gas flow ratio and the chamber pressure maintained during synthesis.

   a. By using the microwave plasma-enhanced chemical vapor deposition (MW-PECVD) method, horizontal graphene films have been successfully formed directly on dielectric (SiO_2, Al_2O_3(0001), h-BN) and semiconductor (Si(100)) substrates.

   b. Atomic force microscopy (AFM) studies showed that graphene structures with an average height of 1.0–1.3 nm form on the dielectric SiO_2 substrate, which corresponds to a multilayer graphene structure.

   c. Raman scattering spectroscopy analysis confirmed the nanocrystallinity of the graphene: the average I_{2D}/I_G intensity ratio was found to be ~0.4, confirming the growth of multilayer graphene, while the average defect density index I_D/I_G reached ~1.46–1.84, thereby indicating dominant grain boundary defects. Based on the $I_D/I_{D'}$ data, graphene exhibits grain boundary defects in almost all cases.

2. Low-temperature (<600 °C) graphene synthesis was performed while using MW-PECVD on SiO_2/Si(100) substrates, and the influence of different synthesis parameters on the structure of the resulting graphene films has been investigated, along with an analysis of the diversity of these structures.

   a. It has been experimentally demonstrated that, by applying optimized synthesis parameters (CH_4/H_2 flow ratio, stable 10 mBar pressure, and 0.7 kW power), graphene layers can be formed at temperatures below 600 °C, and hydrogenated graphene can be formed even at 400 °C.

   b. It has been determined that the steel cover used during synthesis effectively protects the substrate from the direct destructive effects of the plasma, while pressure regulation allows for the control of defect types: by reducing the pressure below 20 mBar, the $I_D/I_{D'}$ ratio stabilizes at a value of ~2.5.

3. Examples of the application of directly synthesized graphene using the MW-PECVD method in electronic devices have been demonstrated. Graphene photodiodes were formed on h-BN and Si(100) substrates, and their current-voltage characteristics have been investigated. Short-circuit current and open-circuit voltage values have been measured, and a comparison of the dependence of these values on substrate thicknesses has been performed for different substrates. Additionally, a graphene field-effect transistor has been formed and adapted for a biological sensor. The sensitivity of this sensor to the SARS-CoV-2 spike (S) protein has been investigated.

a. An H-BN buffer layer effectively improves the photoelectric properties of the devices: it increases the open-circuit voltage (V_{OC}) and the short-circuit current (I_{SC}), although the latter depends non-monotonically on the h-BN thickness.

b. It has been demonstrated that directly synthesized graphene exhibits extremely high sensitivity to the SARS-CoV-2 spike (S) protein: the achieved detection limit is as low as 10^{-2} fg/mL.

LITERATŪROS SĄRAŠAS

1. REED, M. A. ir kt. Spatial quantization in GaAs–AlGaAs multiple quantum dots. *Journal of Vacuum Science & Technology B: Microelectronics Processing and Phenomena*, 4 (1986), 1, 358–360.
2. BERNAL, J. D. The structure of graphite. *Proceedings of the Royal Society of London. Series A, Containing Papers of a Mathematical and Physical Character*, 106 (1924), 740, 749–773.
3. WALLACE, P. R. The Band Theory of Graphite. *Physical Review*, 71 (1947), 9, 622–634.
4. NOVOSELOV, K. S. ir kt. Electric Field Effect in Atomically Thin Carbon Films. *Science*, 306 (2004), 5696, 666–669.
5. BHUYAN, Md. S. A. ir kt. Synthesis of graphene. *International Nano Letters*, 6 (2016), 2, 65–83.
6. MUÑOZ, R. ir C. GÓMEZ-ALEIXANDRE. Review of CVD Synthesis of Graphene. *Chemical Vapor Deposition*, 19 (2013), 10-11–12, 297–322.
7. HALES, T. C. *The Honeycomb Conjecture*. [interaktyvus], 1999. Prieiga per internetą: https://arxiv.org/abs/math/9906042 [žiūrėta 2026-04-08].
8. NI, Z. H. ir kt. Graphene Thickness Determination Using Reflection and Contrast Spectroscopy. *Nano Letters*, 7 (2007), 9, 2758–2763.
9. KELLY, B. T. *Physics of graphite*. London: Applied Science Publ, 1981. ISBN 978-0-85334-960-0.
10. MALARD, L. M. ir kt. Raman spectroscopy in graphene. *Physics Reports*, 473 (2009), 5–6, 51–87.
11. NAIR, R. R. ir kt. Fine Structure Constant Defines Visual Transparency of Graphene. *Science*, 320 (2008), 5881, 1308–1308.
12. MOROZOV, S. V. ir kt. Giant Intrinsic Carrier Mobilities in Graphene and Its Bilayer. *Physical Review Letters*, 100 (2008), 1, 016602.
13. LEE, C. ir kt. Measurement of the Elastic Properties and Intrinsic Strength of Monolayer Graphene. *Science*, 321 (2008), 5887, 385–388.
14. BALANDIN, A. A. ir kt. Superior Thermal Conductivity of Single-Layer Graphene. *Nano Letters*, 8 (2008), 3, 902–907.
15. FERRARI, A. C. ir kt. Raman Spectrum of Graphene and Graphene Layers. *Physical Review Letters*, 97 (2006), 18, 187401.
16. SHALLCROSS, S. ir kt. Electronic structure of turbostratic graphene. *Physical Review B*, 81 (2010), 16, 165105.
17. DE ANDRES, P. L. ir kt. Strong covalent bonding between two graphene layers. *Physical Review B*, 77 (2008), 4, 045403.
18. GRUBIŠIĆ-ČABO, A. ir kt. Quasi-freestanding AA-stacked bilayer graphene induced by calcium intercalation of the graphene-silicon carbide interface. *Frontiers in Nanotechnology*, 5 (2024), 1333127.
19. KIM, K. S. ir kt. Coexisting massive and massless Dirac fermions in symmetry-broken bilayer graphene. *Nature Materials*, 12 (2013), 10, 887–892.
20. LIU, Z. ir kt. Open and Closed Edges of Graphene Layers. *Physical Review Letters*, 102 (2009), 1, 015501.
21. CAFFREY, N. M. ir kt. Structural and electronic properties of Li-intercalated graphene on SiC(0001). *Physical Review B*, 93 (2016), 19, 195421.
22. ENDO, Y. ir kt. Weak localization in bilayer graphene with Li-intercalation/desorption. *Journal of Physics: Condensed Matter*, 30 (2018), 30, 305701.
23. DE JONG, T. A. ir kt. Intrinsic stacking domains in graphene on silicon carbide: A pathway for intercalation. *Physical Review Materials*, 2 (2018), 10, 104005.

24. DE JONG, T. A. ir kt. Stacking domain morphology in epitaxial graphene on silicon carbide. *Physical Review Materials*, 7 (2023), 3, 034001.
25. MURATA, H. ir kt. High-Electrical-Conductivity Multilayer Graphene Formed by Layer Exchange with Controlled Thickness and Interlayer. *Scientific Reports*, 9 (2019), 1, 4068.
26. SHAHIL, K. M. F. ir A. A. BALANDIN. Thermal properties of graphene and multilayer graphene: Applications in thermal interface materials. *Solid State Communications*, 152 (2012), 15, 1331–1340.
27. BANHART, F. ir kt. Structural Defects in Graphene. *ACS Nano*, 5 (2011), 1, 26–41.
28. STONE, A. J. ir D. J. WALES. Theoretical studies of icosahedral C60 and some related species. *Chemical Physics Letters*, 128 (1986), 5–6, 501–503.
29. KOTAKOSKI, J. ir kt. Stone-Wales-type transformations in carbon nanostructures driven by electron irradiation. *Physical Review B*, 83 (2011), 24, 245420.
30. SMITH, B. W. ir D. E. LUZZI. Electron irradiation effects in single wall carbon nanotubes. *Journal of Applied Physics*, 90 (2001), 7, 3509–3515.
31. KOSKINEN, P. ir kt. Self-Passivating Edge Reconstructions of Graphene. *Physical Review Letters*, 101 (2008), 11, 115502.
32. YAZYEV, O. V. ir LOUIE, S. G. Topological defects in graphene: Dislocations and grain boundaries. *Physical Review B*, 81 (2010), 19, 195420.
33. MEYER, J. C. ir kt. Direct Imaging of Lattice Atoms and Topological Defects in Graphene Membranes. *Nano Letters*, 8 (2008), 11, 3582–3586.
34. WU, Y. ir kt. Carbon Nanowalls Grown by Microwave Plasma Enhanced Chemical Vapor Deposition. *Advanced Materials*, 14 (2002), 1, 64–67.
35. ZHENG, W. ir kt. Review of Vertical Graphene and its Applications. *ACS Applied Materials & Interfaces*, 13 (2021),8, 9561–9579.
36. ZHU, Y. ir kt. Graphene and Graphene Oxide: Synthesis, Properties, and Applications. *Advanced Materials*, 22 (2010), 35, 3906–3924.
37. HUMMERS, W. S. ir OFFEMAN, R. E. Preparation of Graphitic Oxide. *Journal of the American Chemical Society*, 80 (1958), 6, 1339–1339.
38. CHUNG, C. ir kt. Biomedical Applications of Graphene and Graphene Oxide. In *Accounts of Chemical Research*, 46 (2013), 10, 2211–2224.
39. SON, J. ir kt. Hydrogenated monolayer graphene with reversible and tunable wide band gap and its field-effect transistor. *Nature Communications*, 7 (2016), 1, 13261.
40. CADELANO, E. ir kt. Elastic properties of hydrogenated graphene. *Physical Review B*, 82 (2010), 23, 235414.
41. PUMERA, M. ir C. H. A WONG. Graphane and hydrogenated graphene. *Chemical Society Reviews*, 42 (2013), 14, 5987.
42. GEIM, A. K. ir K. S. NOVOSELOV. The rise of graphene. *Nature Materials*, 6 (2007), 3, 183–191.
43. MBAYACHI, V. B. ir kt. Graphene synthesis, characterization and its applications: A review. *Results in Chemistry*, 3 (2021), 100163.
44. SU, C.-Y. ir kt. High-Quality Thin Graphene Films from Fast Electrochemical Exfoliation. *ACS Nano*, 5 (2011), 3, 2332–2339.
45. LUHENG, W. ir kt. Influence of carbon black concentration on piezoresistivity for carbon-black-filled silicone rubber composite. *Carbon*, 47 (2009), 14, 3151–3157.
46. MISHRA, N. ir kt. Graphene growth on silicon carbide: A review. *Physica status solidi (a)*, 213 (2016), 9, 2277–2289.
47. BERMAN, D. ir kt. Metal-induced rapid transformation of diamond into single and multilayer graphene on wafer scale. *Nature Communications*, 7 (2016), 1, 12099.

48. LI, X. ir kt. Large-Area Synthesis of High-Quality and Uniform Graphene Films on Copper Foils. *Science*, 324 (2009), 5932, 1312–1314.
49. ZHAO, Z. ir kt. Polycrystalline Few-Layer Graphene as a Durable Anticorrosion Film for Copper. *Nano Letters*, 21 (2021), 2, 1161–1168.
50. MEHTA, R. ir kt. Enhanced Electrical and Thermal Conduction in Graphene-Encapsulated Copper Nanowires. *Nano Letters*, 15 (2015), 3, 2024–2030.
51. SUK, J. W. ir kt. Transfer of CVD-Grown Monolayer Graphene onto Arbitrary Substrates. *ACS Nano*, 5 (2011), 9, 6916–6924.
52. HAIGH, S. J. ir kt. Cross-sectional imaging of individual layers and buried interfaces of graphene-based heterostructures and superlattices. *Nature Materials*, 11 (2012), 9, 764–767.
53. LIANG, X. ir kt. Toward Clean and Crackless Transfer of Graphene. *ACS Nano*, 5 (2011), 11, 9144–9153.
54. CHUGH, S. ir kt. Comparison of graphene growth on arbitrary non-catalytic substrates using low-temperature PECVD. *Carbon*, 93 (2015), 393–399.
55. NANDAMURI, G. ir kt. Remote plasma assisted growth of graphene films. In *Applied Physics Letters*, 96 (2010), 15, 154101.
56. ZHENG, S. ir kt. Metal-catalyst-free growth of graphene on insulating substrates by ammonia-assisted microwave plasma-enhanced chemical vapor deposition. *RSC Advances*, 7 (2017), 53, 33185–33193.
57. ZHAN, H. ir kt. Direct fabrication of 3D graphene on nanoporous anodic alumina by plasma-enhanced chemical vapor deposition. *Scientific Reports*, 6 (2016), 1, 19822.
58. LI, M. ir kt. Controllable Synthesis of Graphene by Plasma-Enhanced Chemical Vapor Deposition and Its Related Applications. *Advanced Science*, 3 (2016), 11, 1600003.
59. LUI, C. H. ir kt. Ultraflat graphene. *Nature*, 462 (2009), 7271, 339–341.
60. NOVOSELOV, K. S. ir kt. Two-dimensional atomic crystals. *Proceedings of the National Academy of Sciences*, 102 (2005), 30, 10451–10453.
61. SHEARER, C. J. ir kt. Accurate thickness measurement of graphene. *Nanotechnology*, 27 (2016), 12, 125704.
62. OBRAZTSOVA, E. A. ir kt. Statistical analysis of atomic force microscopy and Raman spectroscopy data for estimation of graphene layer numbers. *Physica status solidi (b)*, 245 (2008), 10, 2055–2059.
63. JIANG, T. ir Y. ZHU. Measuring graphene adhesion using atomic force microscopy with a microsphere ti *Nanoscale*, 7 (2015), 24, 10760–10766.
64. BONESCHANSCHER, M. P. ir kt. Quantitative Atomic Resolution Force Imaging on Epitaxial Graphene with Reactive and Nonreactive AFM Probes. *ACS Nano*, 6 (2012), 11, 10216–10221.
65. PAREDES, J. I. ir kt. Atomic Force and Scanning Tunneling Microscopy Imaging of Graphene Nanosheets Derived from Graphite Oxide. *Langmuir*, 25 (2009), 10, 5957–5968.
66. DENG, S. ir BERRY, V. Wrinkled, rippled and crumpled graphene: an overview of formation mechanism, electronic properties, and applications. *Materials Today*, 19 (2016), 4, 197–212.
67. NEMES-INCZE, P. ir kt. Anomalies in thickness measurements of graphene and few layer graphite crystals by tapping mode atomic force microscopy. *Carbon*, 46 (2008), 11, 1435–1442.
68. FERRARI, A. C. ir D. M. BASKORaman spectroscopy as a versatile tool for studying the properties of graphene. *Nature Nanotechnology*, 8 (2013), 4, 235–246.

69. FERRARI, A. C. Raman spectroscopy of graphene and graphite: Disorder, electron–phonon coupling, doping and nonadiabatic effects. *Solid State Communications*, 143 (2007), 1–2, 47–57.
70. HWANG, J.-S. ir kt. Imaging layer number and stacking order through formulating Raman fingerprints obtained from hexagonal single crystals of few layer graphene. *Nanotechnology*, 24 (2013), 1, 015702.
71. GRAF, D. ir kt. Spatially Resolved Raman Spectroscopy of Single- and Few-Layer Graphene. *Nano Letters*, 7 (2007), 2, 238–242.
72. CANÇADO, L. G. ir kt. Quantifying Defects in Graphene via Raman Spectroscopy at Different Excitation Energies. *Nano Letters*, 11 (2011), 8, 3190–3196.
73. ECKMANN, A. ir kt. Probing the Nature of Defects in Graphene by Raman Spectroscopy. *Nano Letters*, 12 (2012), 8, 3925–3930.
74. WU, J.-B. ir kt. Raman spectroscopy of graphene-based materials and its applications in related devices. *Chemical Society Reviews*, 47 (2018), 5, 1822–1873.
75. HAO, Y. ir kt. Probing Layer Number and Stacking Order of Few-Layer Graphene by Raman Spectroscopy. *Small*, 6 (2010), 2, 195–200.
76. BAE, S. ir kt. Roll-to-roll production of 30-inch graphene films for transparent electrodes. *Nature Nanotechnology*, 5 (2010), 8, 574–578.
77. NOVOSELOV, K. S. ir kt. A roadmap for graphene. *Nature*, 490 (2012), 7419, 192–200.
78. WOLF, E. L. *Applications of Graphene: An Overview* [interaktyvus]. Cham: Springer International Publishing, 2014. ISBN 978-3-319-03945-9.
79. TIELROOIJ, K. J. ir kt. Generation of photovoltage in graphene on a femtosecond timescale through efficient carrier heating. *Nature Nanotechnology*, 10 (2015), 5, 437–443.
80. DI BARTOLOMEO, A. ir kt. Hybrid graphene/silicon Schottky photodiode with intrinsic gating effect. *2D Materials*, 4 (2017), 2, 025075.
81. YAO, J. ir kt. Quantifying Losses in Open-Circuit Voltage in Solution-Processable Solar Cells. *Physical Review Applied*, 4 (2015), 1, 014020.
82. BÉRAUD, A. ir kt. Graphene field-effect transistors as bioanalytical sensors: design, operation and performance. *The Analyst*, 146 (2021), 2, 403–428.
83. FU, W. ir kt. Sensing at the Surface of Graphene Field-Effect Transistors. *Advanced Materials*, 29 (2017), 6, 1603610.
84. AFSAHI, S. ir kt. Novel graphene-based biosensor for early detection of Zika virus infection. *Biosensors and Bioelectronics*, 100 (2018), 85–88.
85. WANG, S. ir kt. Review – Recent Advances in Graphene-Based Field-Effect-Transistor Biosensors: A Review on Biosensor Designing Strategy. *Journal of The Electrochemical Society*, 169 (2022), 2, 027509.
86. KRSIHNA, B. V. ir kt. A Highly Sensitive Graphene-based Field Effect Transistor for the Detection of Myoglobin. *Silicon*, 14 (2022), 17, 11741–11748.
87. BURSON, K. M. ir kt. Direct Imaging of Charged Impurity Density in Common Graphene Substrates. *Nano Letters*, 13 (2013), 8, 3576–3580.
88. ZHAO, W. ir kt. Sensitivity-Enhancing Strategies of Graphene Field-Effect Transistor Biosensors for Biomarker Detection. *ACS Sensors*, 9 (2024), 2705–2727.
89. CORNELL, J. A. Factors that Influence the Value of the Coefficient of Determination in Simple Linear and Nonlinear Regression Models. *Phytopathology*, 77 (1987), 1, 63.
90. JAIN, V. ir kt. The Gaussian-Lorentzian Sum, Product, and Convolution (Voigt) functions in the context of peak fitting X-ray photoelectron spectroscopy (XPS) narrow scans. *Applied Surface Science*, 447 (2018), 548–553.
91. WU, G. ir kt. Graphene field-effect transistors-based biosensors for Escherichia coli detection. *2016 IEEE 16th International Conference on Nanotechnology (IEEE-NANO)*,

pp. 22–25. [interaktyvus]. Sendai: IEEE, 2016. Prieiga per internetą: https://ieeexplore.ieee.org/document/7751414 [žiūrėta 2026-04-08].
92. BO, Z. ir kt. Plasma-enhanced chemical vapor deposition synthesis of vertically oriented graphene nanosheets. *Nanoscale*, 5 (2013), 12, 5180.
93. MEŠKINIS, Š. ir kt. The direct growth of planar and vertical graphene on Si(100) *via* microwave plasma chemical vapor deposition: synthesis conditions effects. *RSC Advances*, 12 (2022), 29, 18759–18772.
94. GUDAITIS, R. ir kt. Catalyst-Less and Transfer-Less Synthesis of Graphene on Si(100) Using Direct Microwave Plasma Enhanced Chemical Vapor Deposition and Protective Enclosures. *Materials*, 13 (2020), 24, 5630.
95. WEI, D. ir kt. Critical Crystal Growth of Graphene on Dielectric Substrates at Low Temperature for Electronic Devices. *Angewandte Chemie International Edition*, 52 (2013), 52, 14121–14126.
96. PENG, K.-J. ir kt. Hydrogen-free PECVD growth of few-layer graphene on an ultra-thin nickel film at the threshold dissolution temperature. *Journal of Materials Chemistry C*, 1 (2013), 24, 3862.
97. VENEZUELA, P. ir kt. Theory of double-resonant Raman spectra in graphene: Intensity and line shape of defect-induced and two-phonon bands. *Physical Review B*, 84 (2011), 3, 035433.
98. CASIRAGHI, C. Probing disorder and charged impurities in graphene by Raman spectroscopy. *Physica status solidi (RRL) – Rapid Research Letters*, 3 (2009), 6, 175–177.
99. NEUMANN, C. ir kt. Raman spectroscopy as probe of nanometre-scale strain variations in graphene. *Nature Communications*, 6 (2015), 1, 8429.
100. BISSETT, M. A. ir kt. Mechanical Strain of Chemically Functionalized Chemical Vapor Deposition Grown Graphene. *The Journal of Physical Chemistry C*, 117 (2013), 6, 3152–3159.
101. LEE, J. E. ir kt. Optical separation of mechanical strain from charge doping in graphene. *Nature Communications*, 3 (2012), 1, 1024.
102. ARMANO, A. ir kt. Monolayer graphene doping and strain dynamics induced by thermal treatments in controlled atmosphere. *Carbon*, 127 (2018), 270–279.
103. LEE, U. ir kt. Time Evolution Studies on Strain and Doping of Graphene Grown on a Copper Substrate Using Raman Spectroscopy. *ACS Nano*, 14 (2020), 1, 919–926.
104. KHAN, A. ir kt. Direct CVD Growth of Graphene on Technologically Important Dielectric and Semiconducting Substrates. *Advanced Science*, 5 (2018), 11, 1800050.
105. CHEN, Z. ir kt. Direct CVD Growth of Graphene on Traditional Glass: Methods and Mechanisms. *Advanced Materials*, 31 (2019), 9, 1803639.
106. FAN, X. F. ir kt. Interaction between graphene and the surface of SiO_2. *Journal of Physics: Condensed Matter*, 24 (2012), 30, 305004.
107. CHEN, Y. ir kt. Growing Uniform Graphene Disks and Films on Molten Glass for Heating Devices and Cell Culture. *Advanced Materials*, 27 (2015), 47, 7839–7846.
108. WANG, G. ir kt. Lattice Selective Growth of Graphene on Sapphire Substrate. *The Journal of Physical Chemistry C*, 119 (2015), 1, 426–430.
109. ULLAH, Z. ir kt. A comparative study of graphene growth by APCVD, LPCVD and PECVD. *Materials Research Express*, 5 (2018), 3, 035606.
110. UEDA, Y. ir kt. Effect of Growth Pressure on Graphene Direct Growth on an A-Plane Sapphire Substrate: Implications for Graphene-Based Electronic Devices. *ACS Applied Nano Materials*, 4 (2021), 1, 343–351.
111. SONG, H.J. ir kt. Large scale metal-free synthesis of graphene on sapphire and transfer-free device fabrication. *Nanoscale*, 4 (2012), 10, 3050.

112. HAN, Z. ir kt. When graphene meets white graphene – recent advances in the construction of graphene and *h* -BN heterostructures. *Nanoscale*, 13 (2021), 31, 13174–13194.
113. YANG, W. ir kt. Epitaxial growth of single-domain graphene on hexagonal boron nitride. *Nature Materials*, 12 (2013), 9, 792–797.
114. WANG, M. ir kt. A Platform for Large-Scale Graphene Electronics – CVD Growth of Single-Layer Graphene on CVD-Grown Hexagonal Boron Nitride. *Advanced Materials*, 25 (2013), 19, 2746–2752.
115. SONG, X. ir kt. Graphene/h-BN Heterostructures: Recent Advances in Controllable Preparation and Functional Applications. *Advanced Energy Materials*, 6 (2016), 17, 1600541.
116. HUANG, M. ir kt. Substrate Engineering for CVD Growth of Single Crystal Graphene. *Small Methods*, 5 (2021), 5, 2001213.
117. GAO, W. ir kt. Growth of Single Crystalline 2D Materials beyond Graphene on Non-metallic Substrates. *Small*, 20 (2024), 35, 2311317.
118. GORBACHEV, R. V. ir kt. Hunting for Monolayer Boron Nitride: Optical and Raman Signatures. *Small*, 7 (2011), 4, 465–468.
119. SONG, L. ir kt. Large Scale Growth and Characterization of Atomic Hexagonal Boron Nitride Layers. *Nano Letters*, 10 (2010), 8, 3209–3215.
120. STENGER, I. ir kt. Low frequency Raman spectroscopy of few-atomic-layer thick hBN crystals. *2D Materials*, 4 (2017), 3, 031003.
121. STANKUS, V. ir kt. Synthesis and Characterization of Boron Nitride Thin Films Deposited by High-Power Impulse Reactive Magnetron Sputtering. *Molecules*, 29 (2024), 22, 5247.
122. LUO, Z. ir kt. Thickness-Dependent Reversible Hydrogenation of Graphene Layers. *ACS Nano*, 3 (2009), 7, 1781–1788.
123. ELIAS, D. C. ir kt. Control of Graphene's Properties by Reversible Hydrogenation: Evidence for Graphane. *Science*, 323 (2009), 5914, 610–613.
124. MELIOS, C. ir kt. Surface and interface structure of quasi-free standing graphene on SiC. *2D Materials*. 3 (2016), 2, 025023.
125. SHTEPLIUK, I. ir kt. Raman probing of hydrogen-intercalated graphene on Si-face 4H-SiC. *Materials Science in Semiconductor Processing*, 96 (2019), 145–152.
126. ENTANI, S. ir kt. Growth of graphene on SiO2 with hexagonal boron nitride buffer layer. In *Applied Surface Science*, 475 (2019), 6–11.
127. MERLEN, A. ir kt. A Guide to and Review of the Use of Multiwavelength Raman Spectroscopy for Characterizing Defective Aromatic Carbon Solids: from Graphene to Amorphous Carbons. *Coatings*, 7 (2017), 10, 153.
128. PIAZZA, F. ir kt. Low temperature, pressureless sp2 to sp3 transformation of ultrathin, crystalline carbon films. *Carbon*, 145 (2019), 10–22.
129. CASIRAGHI, C. ir kt. Bonding in hydrogenated diamond-like carbon by Raman spectroscopy. *Diamond and Related Materials*, 14 (2005), 3–7, 1098–1102.
130. CLOUTIS, E. ir kt. Identification and discrimination of polycyclic aromatic hydrocarbons using Raman spectroscopy. *Icarus*, 274 (2016), 211–230.
131. KONG, X. ir kt. Graphene/Si Schottky solar cells: a review of recent advances and prospects. *RSC Advances*, 9 (2019), 2, 863–877.
132. FALLAHAZAD, P. Rational and key strategies toward enhancing the performance of graphene/silicon solar cells. *Materials Advances*, 4 (2023), 8, 1876–1899.
133. BEHURA, S. K. ir kt. Graphene–semiconductor heterojunction sheds light on emerging photovoltaics. *Nature Photonics*, 13 (2019), 5, 312–318.

134. HUANG, K. ir kt. Progress of Graphene–Silicon Heterojunction Photovoltaic Devices. *Advanced Materials Interfaces*, 5 (2018), 24, 1801520.
135. BHOPAL, M. F. ir kt. Past and future of graphene/silicon heterojunction solar cells: a review. *J. Mater. Chem. C*, 5 (2017), 41, 10701–10714.
136. SONG, L. ir kt. A review on graphene-silicon Schottky junction interface. *Journal of Alloys and Compounds*, 806 (2019), 63–70.
137. MENG, J.-H. ir kt. Interface engineering for highly efficient graphene-on-silicon Schottky junction solar cells by introducing a hexagonal boron nitride interlayer. *Nano Energy*, 28 (2016), 44–50.
138. VAN VELDHOVEN, Z. A. ir kt. Electronic properties of CVD graphene: The role of grain boundaries, atmospheric doping, and encapsulation by ALD. *Physica status solidi (b)*, 253 (2016), 12, 2321–2325.
139. HU, Z. ir kt. Substrate dielectric effects on graphene field effect transistors. *Journal of Applied Physics*, 115 (2014), 19, 194507.
140. JI, E. ir kt. Substrate effect on doping and degradation of graphene. *Carbon*, 184 (2021), 651–658.
141. KIM, S. ir kt. Enhanced Gas Sensing Properties of Graphene Transistor by Reduced Doping with Hydrophobic Polymer Brush as a Surface Modification Layer. *ACS Applied Materials & Interfaces*, 12 (2020), 49, 55493–55500.
142. LEE, W. H. ir kt. Control of Graphene Field-Effect Transistors by Interfacial Hydrophobic Self-Assembled Monolayers. *Advanced Materials*, 23 (2011), 30, 3460–3464.

MOKSLO STRAIPSNIŲ KOPIJOS

1 straipsnis

Straipsnio pavadinimas	*The graphene structure's effects on the current-voltage and photovoltaic characteristics of directly synthesized graphene/n-Si(100) diodes*
Straipsnio bendraautoriai	*Šarūnas Jankauskas; Rimantas Gudaitis; Andrius Vasiliauskas; Asta Guobienė; Šarūnas Meškinis*
Leidėjas, žurnalo pavadinimas	*MDPI, Nanomaterials*
Metai	*2022*

nanomaterials

MDPI

Article

The Graphene Structure's Effects on the Current-Voltage and Photovoltaic Characteristics of Directly Synthesized Graphene/n-Si(100) Diodes

Šarūnas Jankauskas, Rimantas Gudaitis, Andrius Vasiliauskas, Asta Guobienė and Šarūnas Meškinis *

Institute of Materials Science, Kaunas University of Technology, K. Baršausko St. 59, LT-51423 Kaunas, Lithuania; sarunas.jankauskas@ktu.lt (Š.J.); rimantas.gudaitis@ktu.lt (R.G.); andrius.vasiliauskas@ktu.lt (A.V.); asta.guobiene@ktu.lt (A.G.)
* Correspondence: sarunas.meskinis@ktu.lt

Abstract: Graphene was synthesized directly on Si(100) substrates by microwave plasma-enhanced chemical vapor deposition (MW-PECVD). The effects of the graphene structure on the electrical and photovoltaic properties of graphene/n-Si(100) were studied. The samples were investigated using Raman spectroscopy, atomic force microscopy, and by measuring current–voltage (I-V) graphs. The temperature of the hydrogen plasma annealing prior to graphene synthesis was an essential parameter regarding the graphene/Si contact I-V characteristics and photovoltaic parameters. Graphene n-type self-doping was found to occur due to the native SiO_2 interlayer at the graphene/Si junction. It was the prevalent cause of the significant decrease in the reverse current and short-circuit current. No photovoltaic effect dependence on the graphene roughness and work function could be observed.

Keywords: graphene; MW-PECVD; photovoltaics

check for updates

Citation: Jankauskas, Š.; Gudaitis, R.; Vasiliauskas, A.; Guobienė, A.; Meškinis, Š. The Graphene Structure's Effects on the Current-Voltage and Photovoltaic Characteristics of Directly Synthesized Graphene/n-Si(100) Diodes. *Nanomaterials* **2022**, *12*, 1640. https://doi.org/10.3390/nano12101640

Academic Editors: Filippo Giannazzo and Ivan Shtepliuk

Received: 22 March 2022
Accepted: 6 May 2022
Published: 11 May 2022

Publisher's Note: MDPI stays neutral with regard to jurisdictional claims in published maps and institutional affiliations.

Copyright: © 2022 by the authors. Licensee MDPI, Basel, Switzerland. This article is an open access article distributed under the terms and conditions of the Creative Commons Attribution (CC BY) license (https://creativecommons.org/licenses/by/4.0/).

1. Introduction

Graphene, the carbon 2D material, was discovered recently [1]. Notably, graphene's exciting abilities, such as 97.7% optical transparency [2], the high charge carrier mobility of 200,000 $cm^2\ V^{-1}\ s^{-1}$ [3], and Young's modulus of 1 TPa [4], make it a perfect candidate material for optoelectronic device fabrication [5,6]. One of the prominent features of graphene is that it can be used instead of metal to form a Schottky junction with semiconductors, e.g., silicon [7]. This enables the use of a graphene/silicon (Gr/Si) contact as a base for solar cell production (see reviews [7–15]). Today, the highest power conversion efficiency (PCE) reported for Gr/Si solar cells is 16.61% [16]. That is a result of the 9-year development of the Gr/Si contact devices, from the 1.5% conversion efficiency reported for the first graphene/silicon Schottky contact-based solar cell [17]. It means that solar cells based on graphene can be very promising and achieve high PCE. Notably, according to the simulations, it was suggested that the conversion efficiency of the graphene/Si solar cell could potentially reach values higher than the conversion efficiency of the best fabricated solar cells (see [18] and [13], respectively). High-efficiency graphene/silicon solar cells were fabricated by combining silicon surface passivation with ultra-thin dielectric interlayers, graphene doping, and light management techniques such as Si substrate micro/nanotexturing and, especially, antireflective films [7–15,19].

Further increase of the graphene/Si solar cell conversion efficiency requires optimization of all the functional parts of the solar cell. In most studies, graphene is synthesized by chemical vapor deposition (CVD) on copper foil and then transferred to the silicon substrate [7–15]. The transfer is a prolonged process during which graphene is contaminated by different adsorbates [20], and cracks can be induced in the transferred graphene [21]. It can deteriorate the graphene/silicon junction device's properties resulting in complicated interface and solar cell property control [22,23]. It was reported that the use of the few-layer

three categories (A–C) based on the Si(100) substrate plasma pre-annealing temperature (700–900 °C). The sample size was 1 × 1 cm.

Table 1. Synthesis conditions for investigated graphene samples.

Sample No.	Power, kW	H_2, sccm	CH_4, sccm	p, mBar	T, °C	t, min	Annealing Temperature, °C
A1	0.7	75	25	10	700	60	700
A2	0.7	75	25	20	700	60	700
A3	0.7	75	35	10	700	60	700
A4	0.7	75	35	20	700	60	700
A5	0.7	75	35	20	700	60	700
A6	0.7	75	35	20	700	60	700
A7	0.7	150	50	22	700	60	700
A8	0.7	75	25	10	700	90	700
A9	0.7	75	35	20	700	90	700
A10	0.7	75	25	10	700	150	700
A11	0.7	75	25	10	700	150	700
B1	0.7	75	35	10	700	60	800
B2	0.7	75	25	10	700	90	800
B3	0.7	75	35	20	800	60	800
C1	0.7	75	35	20	700	60	900
C2	0.7	75	25	10	700	90	900
C3	0.7	150	50	22	900	20	900

After graphene synthesis was carried out, diode fabrication began with Al back contact formation (on the uncoated Si side) using e-beam technology. The DMF + acetone boiling and RCA 1 (1:1:5 solution of $NH_4OH + H_2O_2 + H_2O$), impurity removal (1:50 solution of $HF + H_2O$), and RCA 2 (1:1:6 solution of $HCl + H_2O_2 + H_2O$) treatments [43] were done prior to the deposition of the Al layer. Cr/Cu electrodes were deposited on the graphene through a mask with 500 µm circular holes. The thicknesses of the Cr interlayer and Cu layer were 20 and 200 nm, respectively. The schematic diagram is shown in Figure 1. The structure of the device is more similar to the real silicon solar cells than the usually used graphene/Si solar cells, with an active device part consisting of graphene on silicon in a hole opened in the silicon dioxide and metal electrodes on the graphene-coated SiO_2 [7–15]. It should be noted that graphene/Si solar cells of structure similar to ours were fabricated and investigated in [23,44–46]. The geometry of the device's metal electrodes was not optimized.

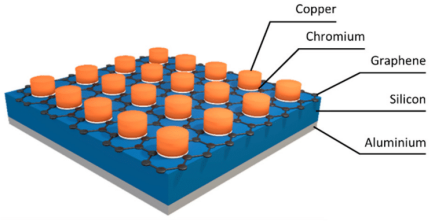


Figure 1. Schematic diagram of the graphene/n-Si(100) fabricated diodes.

Thickness and defect characterization was carried out via Raman scattering spectroscopy using a Raman spectrometer, InVia (Renishaw, Wotton-under-Edge, UK). The measurement was done just after the graphene synthesis and before the graphene/Si(100) diode fabrication. We acquired Raman spectra at several different places on each sample, considering possible differences in the graphene structure across the specimen. The beam power was set to 1.5 mW, and the excitation wavelength was 532 nm. Several peaks were

analyzed for in-depth characterization and defect estimation (D, G, and 2D). The G peak was separated into two components, with the actual G peak being at 1600 cm^{-1} and the D′ peak (which was not analyzed) being at 1620 cm^{-1}. The Lorentzian function was used for the best peak fit, considering Merlen et al. [47] who made observations to determine peak intensities, positions, and full width at half maximums (FWHM). The well-known I_D/I_G ratio was used to reveal the defectiveness of our produced samples [48]. In contrast, the I_{2D}/I_G ratio contributed to the graphene thickness evaluation [49] (smaller ratios correspond to more graphene layers). The positions and FWHM of the G and 2D peaks were analyzed to get information on graphene crystallite size, strain, and doping [50–52].

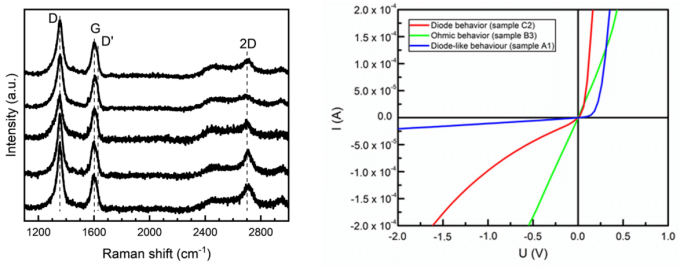
Atomic force microscopy (AFM) was employed to detect any structural peculiarities of the graphene surface. The surface morphology was investigated at room temperature and ambient air conditions using a NanoWizard III atomic force microscope (JPK Instruments, Bruker Nano GmbH, Berlin, Germany). The measurements were done in tapping mode. The silicon probes (CS Instrument, Harrislee, Germany) with a thin layer (25 ± 5 nm) of Pt/Ir coating on both re-ex and tip sides of the probes were used. The probe parameters were as follows: spring constant 2.7 N/m; 60 kHz frequency; 30 nm tip ROC; pyramidal shape. Images of 2 µm × 2 µm size were acquired from the measured data using JPKSPM Data Processing software (version spm-4.3.13, JPK Instruments, Berlin, Germany). Kelvin probe measurements were carried out using the same instrumental setup to evaluate graphene work function.

The current-voltage (I-V) characteristics were measured using a Keithley 6487 picoampere meter/voltage source. The measurements were done at several points on the sample to evaluate the possible dispersion of the characteristics. Characteristics were investigated in three different regimes to study the photovoltaic properties of the fabricated devices. These were dark mode (sample was not illuminated), UV mode (when the sample was illuminated by 406 nm wavelength light-emitting diode (LED)), and IR mode (when the sample was illuminated by 800 nm wavelength light-emitting diode). In all instances, the voltage range was from −2 to +2 V. To ensure the same optical power (5.2 mW) between different measurement modes, currents supplied to the LEDs were selected accordingly. The measurements were done at several different places on the samples to evaluate the dispersion of the results. Diode behavior was studied by examining the I-V characteristic parameters in the dark (reverse current at 0.3 V (I_R(0.3 V)), forward current vs. reverse current at ±0.1V (I_R(0.1 V)/I_F(0.1 V)), forward current vs. reverse current at ±0.3 V (I_R(0.3 V)/I_F(0.3 V))). The photovoltaic parameters (short-circuit current (I_{SC}) and open-circuit voltage (U_{OC})) were derived from current–voltage characteristics measured under illumination. The I-V characteristic's dependence on temperature was measured using a similar setup to the photovoltaic parameter measurements. The same Keithley 6487 picoampere meter/voltage source was employed, with thermal operational conditions being changed by a custom-made Peltier element configuration. The temperature varied from −20 to 40 °C. Each measurement was made after the temperature value had settled down.

3. Results

3.1. Raman Spectra, Current–Voltage Characteristics of Produced Samples and Their AFM Micrographs

The Raman fingerprints of the synthesized samples were investigated, and graphene-related peaks were confirmed (Figure 2a) [53]. The 2D peak was observed at ~2700 cm^{-1}. The G peak of our samples lay at ~1600 cm^{-1}. All synthesized samples had a prominent defect-related D peak at ~1350 cm^{-1}. The D′ band was detected at ~1620 cm^{-1} as a shoulder of the G peak. This is also a significant feature showing the presence of the defects in the graphene sample [47,54]. The defect-related peaks are due to the nanocrystalline nature of the directly synthesized graphene [29,55]. This was also confirmed by the $I_{D'}/I_D$ ratio, which was in the 2.62–4.6 range, indicating that the dominant defect source was grain boundaries [54,56]. The further analysis of the selected samples will be discussed in later sections.



(**a**) (**b**)

Figure 2. Typical Raman scattering spectra (**a**) and typical I−V characteristics (**b**) of directly synthesized graphene/Si(100) devices. The I−V characteristics of the device produced from the C2 sample exhibited diode behavior (red), ohmic contact was seen for the device produced from a sample B3 (green), and the A1 sample had diode-like I-V features (blue).

The typical current–voltage (I-V) characteristics of the produced photodiodes can be seen in Figure 2b. It is clear that even though directly synthesized graphene/n-Si(100) devices mostly showcase diode behavior (as is expected), exceptions such as ohmic device operation regimes were found.

The graphene AFM images and topography parameters were studied to supplement our Raman spectroscopy findings (Figures S2–S10, Table 2). The I_{2D}/I_G ratio values indicated the presence of few-layer graphene. The thickness of the one graphene layer was ~0.4 nm [57,58]. Thus, according to the roughness values larger than several nm, non-planar graphene was grown in some samples (Table 2, Figures S2, S5, S7–S9) [27]. Sample roughness ranged from 0.19 to 5.2 nm, indicating different surface morphologies. The work functions calculated from measured contact potential (VCPD) averaged at 4.820–4.826 eV (Table 2) despite different growth conditions. Thus, the work function variation was tiny.

Table 2. AFM parameters of the directly synthesized graphene samples.

Sample No.	Highest Surface Point, nm	RMS Roughness, nm	Φ, eV	I_{2D}/I_G
A1	~9	2.1	4.82	0.33
A7	1.3	0.295	4.824	0.42
A8	0.9	0.19	4.824	0.35
A11	3.39	0.77	-	0.6
B1	1.8	0.42	4.824	0.34
B2	~15	3.5	-	0.47
B3	~6	1.36	4.824	0.41
C2	22.9	5.2	-	0.77
C3	1.5	0.332	4.826	0.54

3.2. Raman Scattering Spectra Parameters and Synthesized Graphene Thickness, Defect Density, Doping, and Stress

In most cases, graphene Raman scattering spectra were investigated for defect-free or few-defect graphene (no Raman D peak). However, directly synthesized graphene usually contains a significant number of defects [55]. This can affect several Raman D, G, and 2D peak parameters. In addition, graphene layer number, doping, and stress can also significantly impact its Raman spectra [59,60]. Therefore, a more in-depth investigation of several aforementioned peak parameters was carried out.

Remarkably, the decreased intensity of the 2D peak is commonly observed in defected graphene, including that grown by direct synthesis [61,62]. However, no decrease in the

I_{2D}/I_G ratio with I_D/I_G ratio was found (Figure 3a). Thus, the I_{2D}/I_G ratio can still be used to evaluate graphene layer number, as suggested in [49].

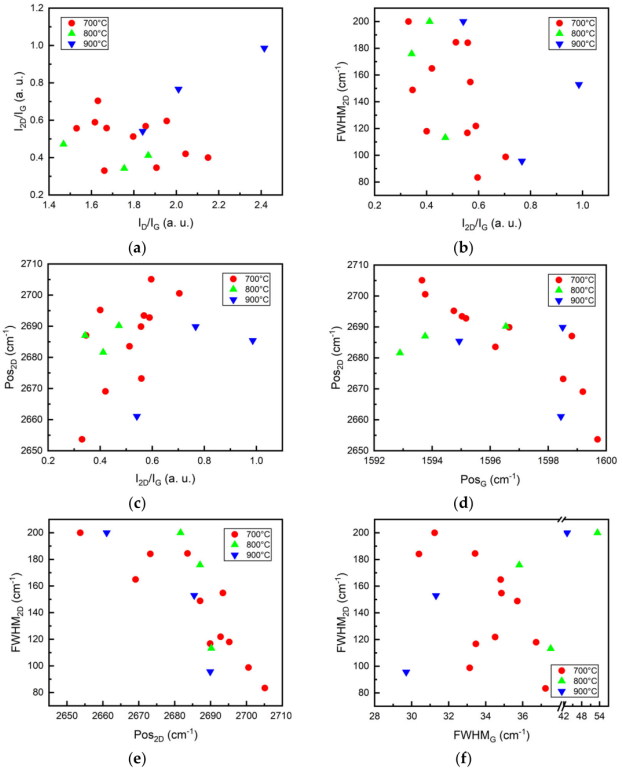


Figure 3. Relation between different Raman scattering spectra parameters: (**a**) I_{2D}/I_G vs. I_D/I_G; (**b**) $FWHM_{2D}$ vs. I_{2D}/I_G; (**c**) Pos_{2D} vs. I_{2D}/I_G; (**d**) Pos_{2D} vs. Pos_G; (**e**) $FWHM_{2D}$ vs. Pos_{2D}; (**f**) $FWHM_{2D}$ vs. $FWHM_G$. Samples were grouped according to the temperature of Si(100) substrate hydrogen plasma annealing before graphene growth: 700 °C (red), 800 °C (green), 900 °C (blue).

The width of the 2D peak increases, and the peak position upshifts with increased graphene layer number (decreased I_{2D}/I_G ratio) [49]. One can see only a weak tendency of the $FWHM_{2D}$ decrease with the I_{2D}/I_G ratio increase in Figure 3b. Very different $FWHM_{2D}$ values can be found for graphene samples of the same thickness. Thus, $FWHM_{2D}$ depends on some other factors. The Pos_{2D}, in our case, was upshifted with the I_{2D}/I_G ratio (Figure 3c). In contrast, the 2D peak should downshift with decreased layer numbers [49]. Thus, no Pos_{2D} dependence on graphene layer number was revealed. Therefore, doping or

strain effects can be the origin of the significant differences between the 2D peak position and $FWHM_{2D}$ of the different graphene samples [60,63–65].

$FWHM_G$ is related to the I_D/I_G ratio of defective graphene [66]. However, no clear $FWHM_G$ dependence on I_D/I_G ratio was found in our case (Figure S11a).

The $FWHM_G$ decreases with increased crystallite size [66–68] and graphene doping [63,69–71]. The latter case is accompanied by a Pos_G shift to the higher wavenumbers [70]. At the same time, a slight narrowing of the G peak with Pos_G upshift was seen (Figure S11b). Thus, the doping effects on G peak narrowing can be supposed. However, the influence of the crystallite size changes cannot be rejected.

The Pos_{2D} vs. Pos_G plot can be used to separate compressive and tensile stress and p-type and n-type doping effects [60,65,69,72]. The downshift of the Pos_{2D} with the upshift of the Pos_G was found (Figure 3d). It is a signature of n-type doping [60,73]. The $FWHM_{2D}$ decreased with an upshift of the Pos_{2D} (Figure 3e). This is similar to the case in [73], where such behavior was reported for n-type doped graphene. Thus, according to Figure 3d,e, the synthesized graphene samples are n-type self-doped. The 2D peak is downshifted and broadened with increased n-type dopant density [73].

It should be mentioned that the presence of the strain in graphene results in the $FWHM_{2D}$ linear increase with $FWHM_G$ [63,74]. Meanwhile, in Figure 3d, $FWHM_{2D}$ increase with $FWHM_G$ can be seen only for three samples that were grown on Si(100) pre-annealed at 900 °C. For the samples synthesized on the silicon pre-annealed at 700 °C temperature, the tendency of the $FWHM_{2D}$ to decrease with increased $FWHM_G$ was found (Figure 3f). This supports the assumption of n-type self-doping of the studied graphene [63,73]. Different sizes of the graphene crystallites can explain the significantly different $FWHM_{2D}$ values seen for samples with nearly the same $FWHM_G$ values [50]. Thus, one can suppose that the charge transfer from the Si(100) substrate to the graphene occurs during the graphene growth, resulting in the n-type self-doping of the graphene. This explanation was provided in [75], taking into account [76–78].

3.3. Current–Voltage Characteristics' Relation with Raman Parameters of Fabricated Graphene/Si Devices

The relations between the current–voltage (I-V) characteristics of the graphene/Si(100) heterojunctions and graphene structure were studied. The initial surface preparation significantly influences the Schottky and ohmic contact I-V characteristics [23,79–81]. Therefore, we separately analyzed graphene samples synthesized on the silicon substrate, with hydrogen plasma-treated at different temperatures, to discern the graphene structure and the graphene/Si interface effects. Hydrogen plasma's silicon surface treatment was widely studied and used for amorphous hydrogenated silicon and monocrystalline silicon heterojunctions. However, their mechanisms are far from the final description due to the complexity of the competing effects. That is an increase of silicon surface roughness [82], silicon etching [83] and etching rate dependence on temperature [84,85], Si surface amorphization [82], defect generation [86,87], and different silicon hydrides' creation [86].

No clear dependence of the different I-V characteristic parameters (I_R(0.3 V), I_R(0.1 V)/I_F(0.1 V), I_R(0.3 V)/I_F(0.3 V)) on the main Raman peak ratios was found (Figure S12). However, the G peak broadening influences the I-V characteristics' shape (Figure 4a–c). As $FWHM_G$ approaches higher values, indicating lowered self-doping level and, possibly, graphene crystallite size decrease [50], the reverse current rises. The reverse and forward current ratios approach 1, implying the ohmic behavior of the junction (Figure 4b,c). Differences between sample groups are not that noticeable, apart from samples annealed at 900 °C, which resulted in a smaller current ratio. We noticed a general increase of reverse current and reverse/forward current ratios, with 2D peak blueshift (ranging from 2653 to 2705 cm^{-1}), when the Si(100) substrate was hydrogen plasma pre-annealed at 700 °C (Figure 4d–f). Considering the analysis provided in the Section 3.2, the reverse current and I_R/I_F ratios decrease with increased n-type self-doping levels [59]. When looking at other sample groups, results were inconclusive, although samples annealed at 800 °C showcase a

much different trend in current ratios at 0.1 V, with the current ratio dropping when Pos_{2D} increases. When analyzing $FWHM_{2D}$ dependence on reverse current and $I_R(0.3\ V)/I_F(0.3\ V)$ ratio, it is seen that values of the reverse current and $I_R(0.3\ V)/I_F(0.3\ V)$ of the samples grown after annealing in 700 °C gradually decrease when $FWHM_{2D}$ decreases (Figure 4g–i). Thus, it supports the premise that an increased n-type self-doping level decreases the reverse current and I_R/I_F ratio [59].

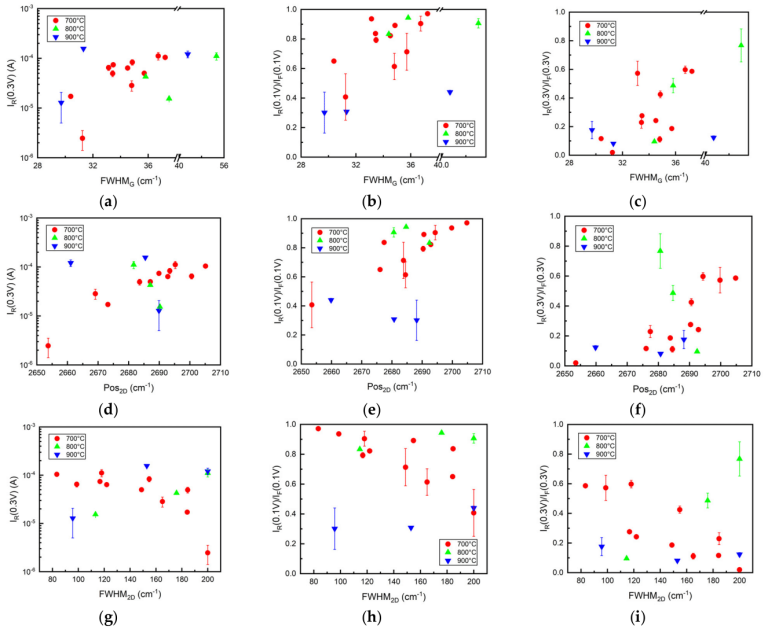


Figure 4. I−V characteristic parameters ($I_R(0.3\ V)$, $I_R(0.1\ V)/I_F(0.1\ V)$, $I_R(0.3\ V)/I_F(0.3\ V)$) in relation with: (**a**–**c**) $FWHM_G$; (**d**–**f**) Pos_{2D}; and (**g**–**i**) $FWHM_{2D}$. Samples were grouped according to the temperature of Si(100) substrate hydrogen plasma annealing before graphene growth: 700 °C (red), 800 °C (green), 900 °C (blue).

Inclusions of the non-planar graphene, such as wrinkles, can significantly influence charge transport properties [88,89]. However, results are somewhat inconsistent when analyzing I-V parameters and their relation to roughness (Figure S13). The general tendency of $I_R(0.3\ V)$ decrease ($I_R(0.3V)/I_F(0.3\ V)$ increase) with increasing surface roughness can be observed, although the plot's strange "branching out" is seen. Due to this, it is impossible to conclude whether this magnitude of roughness impacts device performance.

3.4. Photovoltaic Characteristics of Fabricated Graphene/Si Devices and Their Relation to the Raman Parameters of the Produced Graphene

Typical I-V curves of produced photovoltaic devices under illumination can be seen in Figure 4. Differences between different illumination regimes are minimal, with 800 nm

excitations, in most cases, contributing to a more significant photovoltaic effect, as presumed (Figure 5, Figure S14). The shape of the I-V characteristics in the fourth quadrant is typical for graphene/n-Si solar cells grown without the intentional graphene doping and intentionally deposited ultra-thin dielectric interlayers [24,32,44,90,91]. No S-shaped I-V characteristics reported for some graphene/Si solar cells [92–94] were found.

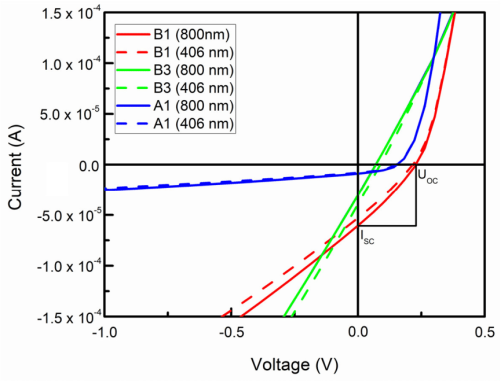


Figure 5. Typical I−V characteristics of directly synthesized graphene/Si heterojunctions measured under the illumination by 800 nm wavelength (solid) and 406 nm wavelength (dashed) LEDs.

To analyze the effects of the graphene structure on photovoltaic properties of the graphene/Si(100) samples, I_{SC} and U_{OC} were investigated concerning Raman parameters (Figure 6). Figure 5a shows an I_{SC} of our fabricated Cu/Cr/Gr/Si/Al device in relation to the I_{2D}/I_G ratio of synthesized graphene. The same investigation scheme was chosen due to the previously mentioned effects of hydrogen plasma annealing before graphene growth. Devices show little to no correlation between photovoltaic parameters and I_{2D}/I_G. Only samples that were annealed at 700 °C exhibited some increase in I_{SC} and U_{OC} when I_{2D}/I_G increased (layer number decreases) (Figure 6a,b). The samples annealed at 900 °C distinctly produced the lowest I_{SC} and U_{OC}. Thus, the surface pre-treatment conditions are more critical than the graphene layer number regarding the photovoltaic parameters. Considering the changes of the U_{OC} and I_{SC} in the samples grown using 700 °C temperature pre-treatment, the graphene layer number effects can be explained by changes in the reflectance, optical transmittance, and graphene work function [27]. In the graphene/Si solar cell, the open-circuit voltage increase was explained by the rise in the Schottky barrier height and work function [24,30]. In our case, no dependence of the graphene/Si solar cell short-circuit current and open-circuit voltage on graphene work function was found. As mentioned earlier in this article, the graphene layer number necessary for maximization of the graphene/Si solar cell photovoltaic characteristics was reported by different authors to be from two to four [24,27,28,38]. In our case, the lowest graphene layer number used, according to the I_{2D}/I_G ratio analysis, was 1–2 layers. Thus, our results are close to the data reported in [28,38], where no graphene work function influence was revealed. Noteworthily, I_{SC} exhibited a noticeable decrease with increased $FWHM_{2D}$ (Figure 6c) when samples were annealed at 700 °C. Similar results were not reproduced when looking at the U_{OC}–$FWHM_{2D}$ relation (Figure 6d), with samples occupying similar values of U_{OC} throughout the whole range of $FWHM_{2D}$.

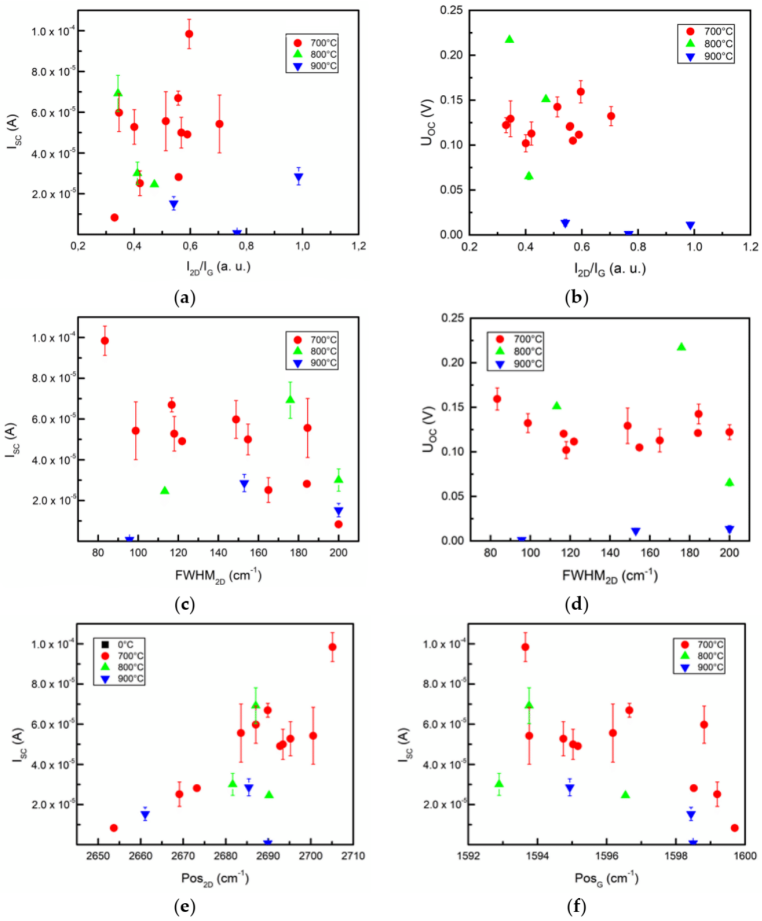


Figure 6. Structural effects on graphene/Si(100) diode's photovoltaic parameters at 800 nm illumination: (**a**) I_{SC} vs. I_{2D}/I_G plot; (**b**) U_{OC} and I_{2D}/I_G relation; (**c**) I_{SC} relation with $FWHM_{2D}$; (**d**) U_{OC} vs. $FWHM_{2D}$ plot; (**e**) I_{SC} with respect to Raman 2D peak position; and (**f**) I_{SC} and Pos_G correlation. Samples were grouped according to the temperature of Si(100) substrate hydrogen plasma annealing before graphene growth: 700 °C (red), 800 °C (green), 900 °C (blue).

We also analyzed the I_{SC} correlation with Pos_{2D} and Pos_G (Figure 6e,f). Interestingly enough, almost all analyzed samples followed an increasing I_{SC} trend with a shift of the

Pos_{2D} to the higher wavenumbers and Pos_G to the lower wavenumbers. It means that the graphene n-type self-doping could be the predominant phenomenon, affecting photovoltaic properties [75] (Table S2). Thus, the graphene n-type self-doping results in decreased short-circuit current. That is in accordance with numerous studies because graphene p-type doping is used to increase graphene/n-Si solar cell efficiency by raising the graphene/Si contact potential barrier height [10]. The same distribution could not be recorded for U_{OC} due to very dispersive data (Figure S15).

The photovoltaic properties' relation with I_D/I_G and $FWHM_G$ plots was employed to examine changes in electric properties due to defects or grain size effects (Figure S16). Relatively high dispersion can be seen when analyzing short circuit current deviation due to defects (in terms of $I_D/_G$) (Figure S16a,b), and data distribution gives no concrete answer. When observing defect influence on open-circuit voltage, higher U_{OC} values did not correlate to the aforementioned parameters (Figure S16). It should be mentioned that, in [31,39,40], graphene/Si solar cell conversion efficiency was improved by inserting a highly defective graphene interlayer. While in [30], the lowest U_{OC} and I_{SC} were found for directly synthesized graphene/Si solar cells fabricated using graphene with the lowest defect density. It is also hard to stress any presence of photovoltaic parameter variation due to grain size [50] after analyzing G band broadening (Figure S16c,d). Data points are too dispersive to conclude. When considering sample topography and its significance on photovoltaic parameters, it is essential to note that only a small I_{SC} reduction can be seen due to the increase in roughness (Figure S17). The most notable case is samples grown on the Si(100) annealed at 800 °C. In the case of the 700 °C annealing, no correlation can be observed due to predominant roughness effects. U_{OC} and RMS roughness relation indicate relatively high dispersion, thus omitting roughness as a detrimental parameter of open-circuit voltage. It should be mentioned that transferred CVD graphene/Si solar cell efficiency can be improved by inserting a graphene nanowall interlayer [38]. At the same time, the transferred graphene nanowalls and n-Si solar cell efficiency were comparable to the efficiency of the transferred CVD graphene/n-Si solar cells [40].

3.5. I-V and Photovoltaic Parameter Relation

The photovoltaic parameter's relation with $I_R(0.3V)$ was analyzed. An increase in the I_{SC} following a rise in $I_R(0.3V)$ can be seen at least in two groups of samples (Figure 7a). Curve shape investigation was carried out using reverse and forward current ratios at 0.1 V and 0.3 V, respectively, as the diode nature of samples may impact photovoltaic parameters. In samples that were annealed at 700 °C, an increase in I_{SC} can be seen when $I_R(0.1\ V)/I_F(0.1\ V)$ increases (Figure 7b), with other groups following that tendency dubiously. When $I_R(0.3\ V)/I_F(0.3\ V)$ is taken into account (Figure 7c), the dispersion of data became broad, hence limiting conclusiveness. When analyzing the aforementioned I-V parameters with respect to U_{OC}, the results were even more dispersive (Figure S18). The U_{OC} vs. $I_{SC}/I_R(0.3\ V)$ plot was employed to show that U_{OC} tends to increase with a short-circuit and reverse current ratio increase, although it branches out when the ratio reaches a value of ~1 (Figure 7d). While annealing temperatures had an impact on $I_{SC}/I_R(0.3V)$, which tends to be minimal (<0.183 V) when annealing was carried out at 900 °C, different illumination regimes show that IR irradiation yields higher U_{OC} and I_{SC}. As in many discussed relations, samples that were annealed at 700 °C also had the most significant spread of $I_{SC}/I_R(0.3\ V)$, with values situated in a range of 0.336–3.375. U_{OC} in samples that had been annealed at 800 °C before graphene growth tended to increase with $I_{SC}/I_R(0.3V)$, although moderate dispersion of values was observed.

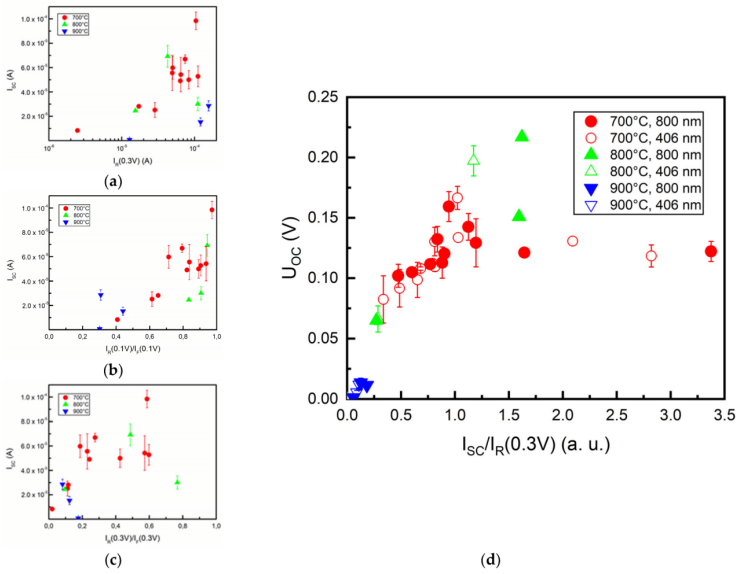


Figure 7. Diode I−V and photovoltaic parameter (at 800 nm illumination) relation: (**a**) I_{SC} vs. I_R(0.3 V) plot; I_{SC} correlation with diode's I-V curve shape estimated using reverse and forward current ratio measured at 0.1 V (**b**) and 0.3 V (**c**); U_{OC} vs. I_{SC}/I_R(0.3 V) plot (**d**) (solid and hollow markers indicate device illumination at 800 and 406 nm, respectively).

4. Discussion

The electron transfer from the n-Si(100) to the graphene should result in decreased graphene/Si contact barrier and, hence, increased reverse current [95,96]. In our case, the opposite tendency was found. However, the native oxide layer can be present at the graphene and silicon interface because silicon surface reoxidation after direct graphene synthesis was reported in [62]. Graphene placed on the silicon dioxide can be electron-doped due to the positive silanol groups on the SiO_2 surface [97,98].

The charge exchange at the graphene/SiO_2 interface results in a dipole formation, and charge redistribution imposes *n* doping in the graphene [98], although no chemical bonds form at the graphene–SiO_2 interface [99]. The graphene placed on the amorphous SiO_2 can also be n-type doped [99].

It should be mentioned that the single-layer graphene Fermi level and work function vary equally [100]. Nevertheless, in the present study, the graphene samples' work function changed in a very narrow range despite different graphene n-type doping levels found while evaluating Pos_{2D} (Figure 3d).

Graphene work-function shift with doping significantly decreased when the graphene layer number increased [101]. The main decline occurs with changing from single-layer to two-layer graphene [101]. The work function of the 4–5-layer graphene was the same as that of the pristine undoped ultra-thin graphite [101]. The work function of graphene placed on SiO_2 decrease (increase) with graphene dopant concentration is significantly suppressed by increasing the graphene layer number [102]. This is because of the charge transfer from

SiO_2 to the graphene and subsequent charge redistribution within the graphene [103]. The charge in graphene decays exponentially with distance from the substrate resulting in suppressed changes in the few-layer graphene work function [101]. Numerous defects found in the directly synthesized graphene by Raman scattering spectroscopy (Figure 2a) can also reduce the graphene's work function shift [104].

The analysis of samples' I-V characteristics measured at different temperatures revealed the flow of the tunneling and thermionic emission currents (Supplementary Materials S4). At lower measurement temperatures, the tunneling current dominated (Supplementary Materials S4, Figures S19 and S20). For I-V characteristics measured at higher temperatures of 30 and 40 °C, the current is dominated by the thermionic emission at low reverse biases, and at higher voltages, the tunneling current prevailed (Supplementary Materials S4). The tunneling current via ultra-thin dielectric grown on the n-type semiconductor can be decreased by a fixed positive charge induced in the dielectric layer [94]. The graphene Pos_{2D} should downshift and the $FWHM_{2D}$ should increase with an increase in doping and, hence, increased native oxide surface positive charge density. Thus, the reverse current and I_R/I_F ratios decrease with the graphene substrate-induced self-doping seen in Figure 3d–i is in good accordance with this assumption. In such a way, the I_{SC} increase with I_R/I_F ratio and with I_R can be explained by the flow of the tunneling photocurrent similarly to the quantum dot and superlattice solar cells where the tunneling effect was used to raise the short-circuit current [105,106]. It should be mentioned that, in the graphene/ultra-thin dielectric/Si solar cells, short-circuit current increases with tunneling current [32]. In addition, graphene/ultra-thin dielectric/Si photodiodes photoresponsivity also increases with increased tunneling current [107,108].

It was revealed that the silicon substrate hydrogen plasma pre-annealing was a very important technological parameter regarding the photovoltaic parameters. An increase in the annealing temperature to 900 °C resulted in suppression of the photovoltaic effect. The AFM study revealed no clear morphology and phase changes due to the silicon surface treatment by hydrogen plasma at both 700 and 900 °C (Table S3). Si(100) surface plasma annealing at 700 °C resulted in no work function changes. However, plasma treatment at 900 °C decreased the substrate surface work function by ~0.05 eV, indicating a silicon surface electronic structure change (Table S3). Thus, in the present study, the effects of initial substrate surface electronic structure on graphene/Si device photovoltaic properties were more significant than differences in the graphene structure.

U_{OC} did not depend on the I_{SC} and increased with I_{SC}/I_R ratio for ratios up to 1–1.5 (Figure 7). It can be explained by relatively large dark reverse currents found in studied samples [109]. That is because U_{OC}, differently from the I_{SC}, usually is decreased due to the tunneling [110]. Reduced U_{OC} with increased leakage current was reported for multi-crystalline silicon [111], organic [112,113], and graphene/GaAs [114] solar cells.

5. Conclusions

In conclusion, the graphene synthesis conditions, structure, and substrate treatment's effects on directly synthesized graphene/n-Si(100) photovoltaic devices properties were revealed.

The graphene n-type self-doping due to the charge transfer from the native SiO_2 interlayer to the graphene was the main reason for the notable reverse current (I_R) and short-circuit current (I_{SC}) decrease. Due to the tunneling photocurrent flow, the U_{OC} increased with a short-circuit current, and the reverse current ratio increased. Significant hydrogen plasma pre-treatment effects on the current-voltage characteristics and photovoltaic parameters were observed, revealing the importance of the graphene/silicon interface.

It was found that the graphene samples' work functions were nearly the same (4.820–4.826 eV), even though the graphene structure and properties of the photovoltaic devices varied dramatically. No effects of graphene surface morphology and defects on the electrical and photovoltaic characteristics were found. The short-circuit current and open-circuit voltage only slightly increased with graphene layer number.

Thus, directly synthesized graphene/n-Si solar cells can be improved by preventing n-type self-doping and optimizing the graphene/silicon interface, whereas graphene defects, layer number, work function, and morphology are much less critical.

Supplementary Materials: The following supporting information can be downloaded at https://www.mdpi.com/article/10.3390/nano12101640/s1: Figure S1: Schematic of an enclosure that was used during the MW-PECVD process to prevent direct plasma effects; Figure S2: AFM image (a), AFM phase image (b), and height profile (c) of A1 sample; Figure S3: AFM image (a), AFM phase image (b), and height profile (c) of A7 sample; Figure S4: AFM image (a), AFM phase image (b), and height profile (c) of A8 sample; Figure S5: AFM image (a), AFM phase image (b), and height profile (c) of A11 sample; Figure S6: AFM image (a), AFM phase image (b), and height profile (c) of B1 sample; Figure S7: AFM image (a), AFM phase image (b), and height profile (c) of B2 sample; Figure S8: AFM image (a), AFM phase image (b), and height profile (c) of B3 sample; Figure S9: AFM image (a), AFM phase image (b), and height profile (c) of C2 sample; Figure S10: AFM image (a), AFM phase image (b), and height profile (c) of C3 sample; Figure S11: FWHMG vs. ID/IG (a) and FWHMG vs. PosG (b) plots; Figure S12: I-V characteristic parameters: (a,d) IR(0.3 V); (b,e) IR(0.1 V)/IF(0.1 V); (c,f) IR(0.3 V)/IF(0.3 V); in relation with (a-c) I2D/IG; (d-f) ID/IG; Figure S13: I-V characteristic parameters: (a) IR(0.3 V); (b) IR(0.3 V)/IF(0.3 V) in relation with surface roughness; Figure S14: ISC vs. ID/IG (a) and UOC vs. ID/IG (b) plots showing a difference between devices measured at 800 nm illumination (solid) and 406 nm illumination (hollow); Figure S15: UOC vs. PosG plot; Figure S16: ISC (a,c) and UOC (b,d) relation with respect to ID/IG (a,b) and FWHM2D (c,d) under 800 nm illumination; Figure S17: ISC (a) and UOC (b) and sample roughness relation under 800 nm illumination; Figure S18: Diode I-V and UOC (at 800 nm illumination) relation; Figure S19: Different charge transport mechanisms estimated from typical fabricated diode I-V graphs under various thermal conditions: (a) Poole–Frenkel mechanism; (b) Image-force-induced charge transport; (c) Thermionic emission; Figure S20: Diode operating regimes in terms of temperature: (a) typical I-V characteristics measured in the dark at different temperatures (253–313 K); (b) The Arrhenius plot; (c) $\ln(\sigma/T2)$ vs. $1000/T$ plot; Table S1: Summarized benchmark showing PCE values and PCE enhancement techniques of the CVD-synthesized graphene/Si solar cells investigated by different research groups; Table S2: Probable doping and strain effects governing main graphene's Raman peak (G, 2D) positions and their FWHM; Table S3: Hydrogen plasma pre-treatment effects on Si(100) substrate surface. References [115–125] are cited in the Supplementary Materials.

Author Contributions: Conceptualization, R.G. and Š.M.; investigation, Š.J., R.G., A.V. and A.G.; writing—original draft preparation, Š.J. and Š.M.; writing—review and editing, Š.M., Š.J. and A.G.; visualization, Š.J. and A.G.; project administration, Š.M.; funding acquisition, Š.M. All authors have read and agreed to the published version of the manuscript.

Funding: The research project No. 09.3.3-LMT-K-712-01-0183 is funded under the European Social Fund measure "Strengthening the Skills and Capacities of Public Sector Researchers for Engaging in High Level R&D Activities" administered by the Research Council of Lithuania.

Institutional Review Board Statement: Not applicable.

Informed Consent Statement: Not applicable.

Data Availability Statement: Not applicable.

Acknowledgments: The research project No. 09.3.3-LMT-K-712-01-0183 is funded under the European Social Fund measure "Strengthening the Skills and Capacities of Public Sector Researchers for Engaging in High Level R&D Activities" administered by the Research Council of Lithuania. The authors acknowledge other participants of the research project No. 09.3.3-LMT-K-712-01-0183—A. Vasiliauskas, A. Guobienė, K. Šlapikas, V. Stankus, D. Peckus, E. Rajackaitė, T. Tamulevičius, A. Jurkevičiūtė, and F. Kalyk.

Conflicts of Interest: The authors declare no conflict of interest.

References

1. Novoselov, K.S. Electric Field Effect in Atomically Thin Carbon Films. *Science* **2004**, *306*, 666–669. [CrossRef] [PubMed]
2. Nair, R.R.; Blake, P.; Grigorenko, A.N.; Novoselov, K.S.; Booth, T.J.; Stauber, T.; Peres, N.M.R.; Geim, A.K. Fine Structure Constant Defines Visual Transparency of Graphene. *Science* **2008**, *320*, 1308. [CrossRef] [PubMed]
3. Morozov, S.V.; Novoselov, K.S.; Katsnelson, M.I.; Schedin, F.; Elias, D.C.; Jaszczak, J.A.; Geim, A.K. Giant Intrinsic Carrier Mobilities in Graphene and Its Bilayer. *Phys. Rev. Lett.* **2008**, *100*, 016602. [CrossRef] [PubMed]
4. Lee, C.; Wei, X.; Kysar, J.W.; Hone, J. Measurement of the Elastic Properties and Intrinsic Strength of Monolayer Graphene. *Science* **2008**, *321*, 385–388. [CrossRef]
5. Bonaccorso, F.; Sun, Z.; Hasan, T.; Ferrari, A.C. Graphene Photonics and Optoelectronics. *Nat. Photonics* **2010**, *4*, 611–622. [CrossRef]
6. Li, X.; Tao, L.; Chen, Z.; Fang, H.; Li, X.; Wang, X.; Xu, J.-B.; Zhu, H. Graphene and Related Two-Dimensional Materials: Structure-Property Relationships for Electronics and Optoelectronics. *Appl. Phys. Rev.* **2017**, *4*, 021306. [CrossRef]
7. Huang, K.; Yu, X.; Cong, J.; Yang, D. Progress of Graphene-Silicon Heterojunction Photovoltaic Devices. *Adv. Mater. Interf.* **2018**, *5*, 1801520. [CrossRef]
8. Wirth-Lima, A.J.; Alves-Sousa, P.P.; Bezerra-Fraga, W. Graphene/Silicon and 2D-MoS_2/Silicon Solar Cells: A Review. *Appl. Phys. A* **2019**, *125*, 241. [CrossRef]
9. Bhopal, M.F.; Lee, D.W.; ur Rehman, A.; Lee, S.H. Past and Future of Graphene/Silicon Heterojunction Solar Cells: A Review. *J. Mater. Chem. C* **2017**, *5*, 10701–10714. [CrossRef]
10. Kong, X.; Zhang, L.; Liu, B.; Gao, H.; Zhang, Y.; Yan, H.; Song, X. Graphene/Si Schottky Solar Cells: A Review of Recent Advances and Prospects. *RSC Adv.* **2019**, *9*, 863–877. [CrossRef]
11. Song, L.; Yu, X.; Yang, D. A Review on Graphene-Silicon Schottky Junction Interface. *J. Alloy. Compd.* **2019**, *806*, 63–70. [CrossRef]
12. Shin, D.H.; Choi, S.-H. Use of Graphene for Solar Cells. *J. Korean Phys. Soc.* **2018**, *72*, 1442–1453. [CrossRef]
13. Abdullah, M.F.; Hashim, A.M. Review and Assessment of Photovoltaic Performance of Graphene/Si Heterojunction Solar Cells. *J. Mater. Sci.* **2019**, *54*, 911–948. [CrossRef]
14. Ju, S.; Liang, B.; Wang, J.-Z.; Shi, Y.; Li, S.-L. Graphene/Silicon Schottky Solar Cells: Technical Strategies for Performance Optimization. *Opt. Commun.* **2018**, *428*, 258–268. [CrossRef]
15. Cui, K.; Maruyama, S. Multifunctional Graphene and Carbon Nanotube Films for Planar Heterojunction Solar Cells. *Prog. Energy Combust. Sci.* **2019**, *70*, 1–21. [CrossRef]
16. Shin, D.H.; Kwak, G.Y.; Kim, J.M.; Jang, C.W.; Choi, S.-H.; Kim, K.J. Remarkable Enhancement of Stability in High-Efficiency Si-Quantum-Dot Heterojunction Solar Cells by Employing Bis(Trifluoromethanesulfonyl)-Amide as a Dopant for Graphene Transparent Conductive Electrodes. *J. Alloy. Compd.* **2019**, *773*, 913–918. [CrossRef]
17. Li, X.; Zhu, H.; Wang, K.; Cao, A.; Wei, J.; Li, C.; Jia, Y.; Li, Z.; Li, X.; Wu, D. Graphene-On-Silicon Schottky Junction Solar Cells. *Adv. Mater.* **2010**, *22*, 2743–2748. [CrossRef]
18. Wirth-Lima, A.J.; Alves-Sousa, P.P.; Bezerra-Fraga, W. N-Graphene/p-Silicon-Based Schottky Junction Solar Cell, with Very High Power Conversion Efficiency. *SN Appl. Sci.* **2020**, *2*, 246. [CrossRef]
19. Badhulika, S.; Terse-Thakoor, T.; Villarreal, C.; Mulchandani, A. Graphene Hybrids: Synthesis Strategies and Applications in Sensors and Sensitized Solar Cells. *Front. Chem.* **2015**, *3*, 38. [CrossRef]
20. Haigh, S.J.; Gholinia, A.; Jalil, R.; Romani, S.; Britnell, L.; Elias, D.C.; Novoselov, K.S.; Ponomarenko, L.A.; Geim, A.K.; Gorbachev, R. Cross-Sectional Imaging of Individual Layers and Buried Interfaces of Graphene-Based Heterostructures and Superlattices. *Nat. Mater.* **2012**, *11*, 764–767. [CrossRef]
21. Liang, X.; Sperling, B.A.; Calizo, I.; Cheng, G.; Hacker, C.A.; Zhang, Q.; Obeng, Y.; Yan, K.; Peng, H.; Li, Q.; et al. Toward Clean and Crackless Transfer of Graphene. *ACS Nano* **2011**, *5*, 9144–9153. [CrossRef] [PubMed]
22. Ihm, K.; Lim, J.T.; Lee, K.-J.; Kwon, J.W.; Kang, T.-H.; Chung, S.; Bae, S.; Kim, J.H.; Hong, B.H.; Yeom, G.Y. Number of Graphene Layers as a Modulator of the Open-Circuit Voltage of Graphene-Based Solar Cell. *Appl. Phys. Lett.* **2010**, *97*, 032113. [CrossRef]
23. Suhail, A.; Pan, G.; Jenkins, D.; Islam, K. Improved Efficiency of Graphene/Si Schottky Junction Solar Cell Based on Back Contact Structure and DUV Treatment. *Carbon* **2018**, *129*, 520–526. [CrossRef]
24. Li, Y.F.; Yang, W.; Tu, Z.Q.; Liu, Z.C.; Yang, F.; Zhang, L.Q.; Hatakeyama, R. Schottky Junction Solar Cells Based on Graphene with Different Numbers of Layers. *Appl. Phys. Lett.* **2014**, *104*, 043903. [CrossRef]
25. Li, X.; Xie, D.; Park, H.; Zeng, T.H.; Wang, K.; Wei, J.; Zhong, M.; Wu, D.; Kong, J.; Zhu, H. Anomalous Behaviors of Graphene Transparent Conductors in Graphene-Silicon Heterojunction Solar Cells. *Adv. Energy Mater.* **2013**, *3*, 1029–1034. [CrossRef]
26. Das, S.; Pandey, D.; Thomas, J.; Roy, T. The Role of Graphene and Other 2D Mater. in Solar Photovoltaics. *Adv. Mater.* **2019**, *31*, 1802722. [CrossRef]
27. Shin, D.H.; Kim, J.H.; Jung, D.H.; Choi, S.-H. Graphene-Nanomesh Transparent Conductive Electrode/Porous-Si Schottky-Junction Solar Cells. *J. Alloy. Compd.* **2019**, *803*, 958–963. [CrossRef]
28. Lin, Y.-K.; Hong, Y.-T.; Shyue, J.-J.; Hsueh, C.-H. Construction of Schottky Junction Solar Cell Using Silicon Nanowires and Multi-Layered Graphene. *Superlattices Microstruct.* **2019**, *126*, 42–48. [CrossRef]
29. Chugh, S.; Mehta, R.; Lu, N.; Dios, F.D.; Kim, M.J.; Chen, Z. Comparison of Graphene Growth on Arbitrary Non-Catalytic Substrates Using Low-Temperature PECVD. *Carbon* **2015**, *93*, 393–399. [CrossRef]

30. Jiao, T.; Liu, J.; Wei, D.; Feng, Y.; Song, X.; Shi, H.; Jia, S.; Sun, W.; Du, C. Composite Transparent Electrode of Graphene Nanowalls and Silver Nanowires on Micropyramidal Si for High-Efficiency Schottky Junction Solar Cells. *ACS Appl. Mater. Interfaces* **2015**, *7*, 20179–20183. [CrossRef]
31. Liu, J.; Sun, W.; Wei, D.; Song, X.; Jiao, T.; He, S.; Zhang, W.; Du, C. Direct Growth of Graphene Nanowalls on the Crystalline Silicon for Solar Cells. *Appl. Phys. Lett.* **2015**, *106*, 043904. [CrossRef]
32. Rehman, M.A.; Akhtar, I.; Choi, W.; Akbar, K.; Farooq, A.; Hussain, S.; Shehzad, M.A.; Chun, S.-H.; Jung, J.; Seo, Y. Influence of an Al_2O_3 Interlayer in a Directly Grown Graphene-Silicon Schottky Junction Solar Cell. *Carbon* **2018**, *132*, 157–164. [CrossRef]
33. Rehman, M.A.; Roy, S.B.; Akhtar, I.; Bhopal, M.F.; Choi, W.; Nazir, G.; Khan, M.F.; Kumar, S.; Eom, J.; Chun, S.-H.; et al. Thickness-Dependent Efficiency of Directly Grown Graphene Based Solar Cells. *Carbon* **2019**, *148*, 187–195. [CrossRef]
34. Rehman, M.A.; Roy, S.B.; Gwak, D.; Akhtar, I.; Nasir, N.; Kumar, S.; Khan, M.F.; Heo, K.; Chun, S.-H.; Seo, Y. Solar Cell Based on Vertical Graphene Nano Hills Directly Grown on Silicon. *Carbon* **2020**, *164*, 235–243. [CrossRef]
35. Bhopal, M.F.; von Lee, D.; Lee, S.H.; Lee, A.R.; Kim, H.J.; Lee, S.H. Selective Nickel/Silver Front Metallization for Graphene/Silicon Solar Cells. *Mater. Lett.* **2019**, *234*, 237–240. [CrossRef]
36. Meng, J.-H.; Liu, X.; Zhang, X.-W.; Zhang, Y.; Wang, H.-L.; Yin, Z.-G.; Zhang, Y.-Z.; Liu, H.; You, J.-B.; Yan, H. Interface Engineering for Highly Efficient Graphene-on-Silicon Schottky Junction Solar Cells by Introducing a Hexagonal Boron Nitride Interlayer. *Nano Energy* **2016**, *28*, 44–50. [CrossRef]
37. Zhou, Q.; Liu, X.; Zhang, E.; Luo, S.; Shen, J.; Wang, Y.; Wei, D. The Controlled Growth of Graphene Nanowalls on Si for Schottky Photodetector. *AIP Adv.* **2017**, *7*, 125317. [CrossRef]
38. Jiao, T.; Wei, D.; Song, X.; Sun, T.; Yang, J.; Yu, L.; Feng, Y.; Sun, W.; Wei, W.; Shi, H.; et al. High-Efficiency, Stable and Non-Chemically Doped Graphene–Si Solar Cells through Interface Engineering and PMMA Antireflection. *RSC Adv.* **2016**, *6*, 10175–10179. [CrossRef]
39. Gnisci, A.; Faggio, G.; Lancellotti, L.; Messina, G.; Carotenuto, R.; Bobeico, E.; Delli Veneri, P.; Capasso, A.; Dikonimos, T.; Lisi, N. The Role of Graphene-Based Derivative as Interfacial Layer in Graphene/N-Si Schottky Barrier Solar Cells. *Phys. Status Solidi A* **2019**, *216*, 1800555. [CrossRef]
40. Zhang, L.; Huang, F.; Li, S.; He, S.; Yu, M.; Fu, J.; Yang, Q.; Huang, R.; Cheng, Q. Interface Engineering for Graphene Nanowalls/Silicon Schottky Solar Cells Prepared by Polymer-Free Transfer Method. *J. Appl. Phys.* **2020**, *128*, 025301. [CrossRef]
41. Chandramohan, S.; Janardhanam, V.; Seo, T.H.; Hong, C.-H.; Suh, E.-K. Improved Photovoltaic Effect in Graphene/Silicon Solar Cell Using $MoO_3/Ag/MoO_3$ Multilayer Coating. *Mater. Lett.* **2019**, *246*, 103–106. [CrossRef]
42. Miao, X.; Tongay, S.; Petterson, M.K.; Berke, K.; Rinzler, A.G.; Appleton, B.R.; Hebard, A.F. High Efficiency Graphene Solar Cells by Chemical Doping. *Nano Lett.* **2012**, *12*, 2745–2750. [CrossRef] [PubMed]
43. Kern, W. The Evolution of Silicon Wafer Cleaning Technology. *J. Electrochem. Soc.* **1990**, *137*, 1887–1892.
44. Pour-mohammadi, Z.; Amirmazlaghani, M. Asymmetric Finger-Shape Metallization in Graphene-on-Si Solar Cells for Enhanced Carrier Trapping. *Mater. Sci. Semicond. Process.* **2019**, *91*, 13–21. [CrossRef]
45. Kalita, G.; Wakita, K.; Umeno, M.; Tanemura, M. Fabrication and Characteristics of Solution-Processed Graphene Oxide-Silicon Heterojunction. *Phys. Status Solidi Rapid Res. Lett.* **2013**, *7*, 340–343. [CrossRef]
46. Behura, S.K.; Nayak, S.; Mukhopadhyay, I.; Jani, O. Junction Characteristics of Chemically-Derived Graphene/p-Si Heterojunction Solar Cell. *Carbon* **2014**, *67*, 766–774. [CrossRef]
47. Merlen, A.; Buijnsters, J.G.; Pardanaud, C. A Guide to and Review of the Use of Multiwavelength Raman Spectroscopy for Characterizing Defective Aromatic Carbon Solids: From Graphene to Amorphous Carbons. *Coatings* **2017**, *7*, 153. [CrossRef]
48. Childres, I.; Jauregui, L.A.; Tian, J.; Chen, Y.P. Effect of Oxygen Plasma Etching on Graphene Studied Using Raman Spectroscopy and Electronic Transport Measurements. *New J. Phys.* **2011**, *13*, 025008. [CrossRef]
49. Hwang, J.-S.; Lin, Y.-H.; Hwang, J.-Y.; Chang, R.; Chattopadhyay, S.; Chen, C.-J.; Chen, P.; Chiang, H.-P.; Tsai, T.-R.; Chen, L.-C.; et al. Imaging Layer Number and Stacking Order through Formulating Raman Fingerprints Obtained from Hexagonal Single Crystals of Few Layer Graphene. *Nanotechnology* **2013**, *24*, 015702. [CrossRef]
50. Mallet-Ladeira, P.; Puech, P.; Toulouse, C.; Cazayous, M.; Ratel-Ramond, N.; Weisbecker, P.; Vignoles, G.L.; Monthioux, M. A Raman Study to Obtain Crystallite Size of Carbon Materials: A Better Alternative to the Tuinstra–Koenig Law. *Carbon* **2014**, *80*, 629–639. [CrossRef]
51. Casiraghi, C.; Pisana, S.; Novoselov, K.S.; Geim, A.K.; Ferrari, A.C. Raman Fingerprint of Charged Impurities in Graphene. *Appl. Phys. Lett.* **2007**, *91*, 233108. [CrossRef]
52. Vinchon, P.; Glad, X.; Robert-Bigras, G.; Martel, R.; Sarkissian, A.; Stafford, L. A Combination of Plasma Diagnostics and Raman Spectroscopy to Examine Plasma-Graphene Interactions in Low-Pressure Argon Radiofrequency Plasmas. *J. Appl. Phys.* **2019**, *126*, 233302. [CrossRef]
53. Ferrari, A.C.; Meyer, J.C.; Scardaci, V.; Casiraghi, C.; Lazzeri, M.; Mauri, F.; Piscanec, S.; Jiang, D.; Novoselov, K.S.; Roth, S.; et al. Raman Spectrum of Graphene and Graphene Layers. *Phys. Rev. Lett.* **2006**, *97*, 187401. [CrossRef] [PubMed]
54. Eckmann, A.; Felten, A.; Mishchenko, A.; Britnell, L.; Krupke, R.; Novoselov, K.S.; Casiraghi, C. Probing the Nature of Defects in Graphene by Raman Spectroscopy. *Nano Lett.* **2012**, *12*, 3925–3930. [CrossRef] [PubMed]
55. Khan, A.; Islam, S.M.; Ahmed, S.; Kumar, R.R.; Habib, M.R.; Huang, K.; Hu, M.; Yu, X.; Yang, D. Direct CVD Growth of Graphene on Technologically Important Dielectric and Semiconducting Substrates. *Adv. Sci.* **2018**, *5*, 1800050. [CrossRef] [PubMed]

56. Stubrov, Y.; Nikolenko, A.; Strelchuk, V.; Nedilko, S.; Chornii, V. Structural Modification of Single-Layer Graphene Under Laser Irradiation Featured by Micro-Raman Spectroscopy. *Nanoscale Res. Lett.* **2017**, *12*, 297. [CrossRef]
57. Nemes-Incze, P.; Osváth, Z.; Kamarás, K.; Biró, L.P. Anomalies in Thickness Measurements of Graphene and Few Layer Graphite Crystals by Tapping Mode Atomic Force Microscopy. *Carbon N Y* **2008**, *46*, 1435–1442. [CrossRef]
58. Yao, Y.; Ren, L.; Gao, S.; Li, S. Histogram Method for Reliable Thickness Measurements of Graphene Films Using Atomic Force Microscopy (AFM). *J. Mater. Sci. Technol.* **2017**, *33*, 815–820. [CrossRef]
59. Kim, S.; Ryu, S. Thickness-Dependent Native Strain in Graphene Membranes Visualized by Raman Spectroscopy. *Carbon* **2016**, *100*, 283–290. [CrossRef]
60. Lee, J.E.; Ahn, G.; Shim, J.; Lee, Y.S.; Ryu, S. Optical Separation of Mechanical Strain from Charge Doping in Graphene. *Nat. Commun.* **2012**, *3*, 1024. [CrossRef]
61. Gayathri, S.; Jayabal, P.; Kottaisamy, M.; Ramakrishnan, V. Synthesis of Few Layer Graphene by Direct Exfoliation of Graphite and a Raman Spectroscopic Study. *AIP Adv.* **2014**, *4*, 027116. [CrossRef]
62. Tai, L.; Zhu, D.; Liu, X.; Yang, T.; Wang, L.; Wang, R.; Jiang, S.; Chen, Z.; Xu, Z.; Li, X. Direct Growth of Graphene on Silicon by Metal-Free Chemical Vapor Deposition. *Nano-Micro Lett.* **2018**, *10*, 20. [CrossRef] [PubMed]
63. Neumann, C.; Reichardt, S.; Venezuela, P.; Drögeler, M.; Banszerus, L.; Schmitz, M.; Watanabe, K.; Taniguchi, T.; Mauri, F.; Beschoten, B.; et al. Raman Spectroscopy as Probe of Nanometre-Scale Strain Variations in Graphene. *Nat. Commun.* **2015**, *6*, 8429. [CrossRef] [PubMed]
64. Tang, B.; Guoxin, H.; Gao, H. Raman Spectroscopic Characterization of Graphene. *Appl. Spectrosc. Rev.* **2010**, *45*, 369–407. [CrossRef]
65. Moon, J.-Y.; Kim, M.; Kim, S.-I.; Xu, S.; Choi, J.-H.; Whang, D.; Watanabe, K.; Taniguchi, T.; Park, D.S.; Seo, J.; et al. Layer-Engineered Large-Area Exfoliation of Graphene. *Sci. Adv.* **2020**, *6*, eabc6601. [CrossRef]
66. Wu, J.-B.; Lin, M.-L.; Cong, X.; Liu, H.-N.; Tan, P.-H. Raman Spectroscopy of Graphene-Based Materials and Its Applications in Related Devices. *Chem. Soc. Rev.* **2018**, *47*, 1822–1873. [CrossRef]
67. Ribeiro-Soares, J.; Oliveros, M.E.; Garin, C.; David, M.V.; Martins, L.G.P.; Almeida, C.A.; Martins-Ferreira, E.H.; Takai, K.; Enoki, T.; Magalhães-Paniago, R.; et al. Structural Analysis of Polycrystalline Graphene Systems by Raman Spectroscopy. *Carbon* **2015**, *95*, 646–652. [CrossRef]
68. Pillet, G.; Sapelkin, A.; Bacsa, W.; Monthioux, M.; Puech, P. Size-controlled Graphene-based Materials Prepared by Annealing of Pitch-based Cokes: G Band Phonon Line Broadening Effects Due to High Pressure, Crystallite Size, and Merging with D′ Band. *J. Raman Spectrosc.* **2019**, *50*, 1861–1866. [CrossRef]
69. Das, A.; Pisana, S.; Chakraborty, B.; Piscanec, S.; Saha, S.K.; Waghmare, U.V.; Novoselov, K.S.; Krishnamurthy, H.R.; Geim, A.K.; Ferrari, A.C.; et al. Monitoring Dopants by Raman Scattering in an Electrochemically Top-Gated Graphene Transistor. *Nat. Nanotechnol.* **2008**, *3*, 210–221. [CrossRef]
70. Casiraghi, C. Probing Disorder and Charged Impurities in Graphene by Raman Spectroscopy. *Phys. Status Solidi Rapid Res. Lett.* **2009**, *3*, 175–177. [CrossRef]
71. Fates, R.; Bouridah, H.; Raskin, J.-P. Probing Carrier Concentration in Gated Single, Bi- and Tri-Layer CVD Graphene Using Raman Spectroscopy. *Carbon* **2019**, *149*, 390–399. [CrossRef]
72. Lee, U.; Han, Y.; Lee, S.; Kim, J.S.; Lee, Y.H.; Kim, U.J.; Son, H. Time Evolution Studies on Strain and Doping of Graphene Grown on a Copper Substrate Using Raman Spectroscopy. *ACS Nano* **2020**, *14*, 919–926. [CrossRef] [PubMed]
73. Khalil, H.M.W.; Nam, J.T.; Kim, K.S.; Noh, H. Controlled N-Doping in Chemical Vapour Deposition Grown Graphene by Antimony. *J. Phys. D Appl. Phys.* **2015**, *48*, 015307. [CrossRef]
74. Bissett, M.A.; Tsuji, M.; Ago, H. Mechanical Strain of Chemically Functionalized Chemical Vapor Deposition Grown Graphene. *J. Phys. Chem. C* **2013**, *117*, 3152–3159. [CrossRef]
75. Gudaitis, R.; Lazauskas, A.; Jankauskas, Š.; Meškinis, Š. Catalyst-Less and Transfer-Less Synthesis of Graphene on Si(100) Using Direct Microwave Plasma Enhanced Chemical Vapor Deposition and Protective Enclosures. *Materials* **2020**, *13*, 5630. [CrossRef] [PubMed]
76. Kiraly, B.; Jacobberger, R.M.; Mannix, A.J.; Campbell, G.P.; Bedzyk, M.J.; Arnold, M.S.; Hersam, M.C.; Guisinger, N.P. Electronic and Mechanical Properties of Graphene–Germanium Interfaces Grown by Chemical Vapor Deposition. *Nano Lett.* **2015**, *15*, 7414–7420. [CrossRef]
77. Banszerus, L.; Janssen, H.; Otto, M.; Epping, A.; Taniguchi, T.; Watanabe, K.; Beschoten, B.; Neumaier, D.; Stampfer, C. Identifying Suitable Substrates for High-Quality Graphene-Based Heterostructures. *2D Mater.* **2017**, *4*, 025030. [CrossRef]
78. Kang, Y.-J.; Kang, J.; Chang, K.J. Electronic Structure of Graphene and Doping Effect on SiO_2. *Phys. Rev. B* **2008**, *78*, 115404. [CrossRef]
79. Tung, R.T. Recent Advances in Schottky Barrier Concepts. *Mater. Sci. Eng. R Rep.* **2001**, *35*, 1–138. [CrossRef]
80. Ali, M.Y.; Tao, M. Effect of Sulfur Passivation of Silicon (100) on Schottky Barrier Height: Surface States versus Surface Dipole. *J. Appl. Phys.* **2007**, *101*, 103708. [CrossRef]
81. Tao, M.; Udeshi, D.; Agarwal, S.; Maldonado, E.; Kirk, W.P. Negative Schottky Barrier between Titanium and N-Type Si(001) for Low-Resistance Ohmic Contacts. *Solid-State Electron.* **2004**, *48*, 335–338. [CrossRef]
82. Martín, I.; Vetter, M.; Orpella, A.; Voz, C.; Puigdollers, J.; Alcubilla, R.; Kharchenko, A.V.; Roca i Cabarrocas, P. Improvement of Crystalline Silicon Surface Passivation by Hydrogen Plasma Treatment. *Appl. Phys. Lett.* **2004**, *84*, 1474–1476. [CrossRef]

83. Soman, A.; Antony, A. A Critical Study on Different Hydrogen Plasma Treatment Methods of A-Si: H/c-Si Interface for Enhanced Defect Passivation. *Appl. Surf. Sci.* **2021**, *553*, 149551. [CrossRef]
84. Yamada, T.; Ohmi, H.; Okamoto, K.; Kakiuchi, H.; Yasutake, K. Effects of Surface Temperature on High-Rate Etching of Silicon by Narrow-Gap Microwave Hydrogen Plasma. *Jpn. J. Appl. Phys.* **2012**, *51*, 10NA09. [CrossRef]
85. Ishii, M. Effects of Substrate Temperature and Bias Potential on Hydrogen Plasma Etching of Silicon. *J. Vac. Sci. Technol. B Microelectron. Nanometer Struct.* **1994**, *12*, 2342. [CrossRef]
86. Schüttauf, J.W.A.; van der Werf, C.H.M.; van Sark, W.G.J.H.M.; Rath, J.K.; Schropp, R.E.I. Comparison of Surface Passivation of Crystalline Silicon by A-Si:H with and without Atomic Hydrogen Treatment Using Hot-Wire Chemical Vapor Deposition. *Thin Solid Film.* **2011**, *519*, 4476–4478. [CrossRef]
87. Lavrov, E.V.; Weber, J. Evolution of Hydrogen Platelets in Silicon Determined by Polarized Raman Spectroscopy. *Phys. Rev. Lett.* **2001**, *87*, 185502. [CrossRef]
88. Zhu, W.; Low, T.; Perebeinos, V.; Bol, A.A.; Zhu, Y.; Yan, H.; Tersoff, J.; Avouris, P. Structure and Electronic Transport in Graphene Wrinkles. *Nano Lett.* **2012**, *12*, 3431–3436. [CrossRef]
89. Zhong, H.; Liu, Z.; Shi, L.; Xu, G.; Fan, Y.; Huang, Z.; Wang, J.; Ren, G.; Xu, K. Graphene in Ohmic Contact for Both N-GaN and p-GaN. *Appl. Phys. Lett.* **2014**, *104*, 212101. [CrossRef]
90. Capasso, A.; Salamandra, L.; Faggio, G.; Dikonimos, T.; Buonocore, F.; Morandi, V.; Ortolani, L.; Lisi, N. Chemical Vapor Deposited Graphene-Based Derivative as High-Performance Hole Transport Material for Organic Photovoltaics. *ACS Appl. Mater. Interfaces* **2016**, *8*, 23844–23853. [CrossRef]
91. Yavuz, S.; Kuru, C.; Choi, D.; Kargar, A.; Jin, S.; Bandaru, P.R. Graphene Oxide as a P-Dopant and an Anti-Reflection Coating Layer, in Graphene/Silicon Solar Cells. *Nanoscale* **2016**, *8*, 6473–6478. [CrossRef] [PubMed]
92. Larsen, L.J.; Shearer, C.J.; Ellis, A.V.; Shapter, J.G. Optimization and Doping of Reduced Graphene Oxide–Silicon Solar Cells. *J. Phys. Chem. C* **2016**, *120*, 15648–15656. [CrossRef]
93. Adhikari, S.; Biswas, C.; Doan, M.-H.; Kim, S.-T.; Kulshreshtha, C.; Lee, Y.H. Minimizing Trap Charge Density towards an Ideal Diode in Graphene–Silicon Schottky Solar Cell. *ACS Appl. Mater. Interfaces* **2019**, *11*, 880–888. [CrossRef] [PubMed]
94. Song, Y.; Li, X.; Mackin, C.; Zhang, X.; Fang, W.; Palacios, T.; Zhu, H.; Kong, J. Role of Interfacial Oxide in High-Efficiency Graphene–Silicon Schottky Barrier Solar Cells. *Nano Lett.* **2015**, *15*, 2104–2110. [CrossRef] [PubMed]
95. Zhong, H.; Xu, K.; Liu, Z.; Xu, G.; Shi, L.; Fan, Y.; Wang, J.; Ren, G.; Yang, H. Charge Transport Mechanisms of Graphene/Semiconductor Schottky Barriers: A Theoretical and Experimental Study. *J. Appl. Phys.* **2014**, *115*, 013701. [CrossRef]
96. Zhang, X.; Zhang, L.; Chan, M. Doping Enhanced Barrier Lowering in Graphene-Silicon Junctions. *Appl. Phys. Lett.* **2016**, *108*, 263502. [CrossRef]
97. Wittmann, S.; Aumer, F.; Wittmann, D.; Pindl, S.; Wagner, S.; Gahoi, A.; Reato, E.; Belete, M.; Kataria, S.; Lemme, M.C. Dielectric Surface Charge Engineering for Electrostatic Doping of Graphene. *ACS Appl. Electron. Mater.* **2020**, *2*, 1235–1242. [CrossRef]
98. Shi, Y.; Dong, X.; Chen, P.; Wang, J.; Li, L.-J. Effective Doping of Single-Layer Graphene from Underlying SiO_2. *Phys. Rev. B* **2009**, *79*, 115402. [CrossRef]
99. Miwa, R.H.; Schmidt, T.M.; Scopel, W.L.; Fazzio, A. Doping of Graphene Adsorbed on the A-SiO_2 Surface. *Appl. Phys. Lett.* **2011**, *99*, 163108. [CrossRef]
100. Samaddar, S.; Coraux, J.; Martin, S.C.; Grévin, B.; Courtois, H.; Winkelmann, C.B. Equal Variations of the Fermi Level and Work Function in Graphene at the Nanoscale. *Nanoscale* **2016**, *8*, 15162–15166. [CrossRef]
101. Leenaerts, O.; Partoens, B.; Peeters, F.M.; Volodin, A.; van Haesendonck, C. The Work Function of Few-Layer Graphene. *J. Phys. Condens. Matter* **2017**, *29*, 035003. [CrossRef] [PubMed]
102. Ziegler, D.; Gava, P.; Güttinger, J.; Molitor, F.; Wirtz, L.; Lazzeri, M.; Saitta, A.M.; Stemmer, A.; Mauri, F.; Stampfer, C. Variations in the Work Function of Doped Single- and Few-Layer Graphene Assessed by Kelvin Probe Force Microscopy and Density Functional Theory. *Phys. Rev. B* **2011**, *83*, 235434. [CrossRef]
103. Renault, O.; Pascon, A.M.; Rotella, H.; Kaja, K.; Mathieu, C.; Rault, J.E.; Blaise, P.; Poiroux, T.; Barrett, N.; Fonseca, L.R.C. Charge Spill-out and Work Function of Few-Layer Graphene on SiC(0 0 0 1). *J. Phys. D Appl. Phys.* **2014**, *47*, 295303. [CrossRef]
104. Akada, K.; Terasawa, T.; Imamura, G.; Obata, S.; Saiki, K. Control of Work Function of Graphene by Plasma Assisted Nitrogen Doping. *Appl. Phys. Lett.* **2014**, *104*, 131602. [CrossRef]
105. Sugaya, T.; Numakami, O.; Furue, S.; Komaki, H.; Amano, T.; Matsubara, K.; Okano, Y.; Niki, S. Tunnel Current through a Miniband in InGaAs Quantum Dot Superlattice Solar Cells. *Sol. Energy Mater. Sol. Cells* **2011**, *95*, 2920–2923. [CrossRef]
106. Wang, Y.; Wen, Y.; Sodabanlu, H.; Watanabe, K.; Sugiyama, M.; Nakano, Y. A Superlattice Solar Cell with Enhanced Short-Circuit Current and Minimized Drop in Open-Circuit Voltage. *IEEE J. Photovolt.* **2012**, *2*, 387–392. [CrossRef]
107. Yin, J.; Liu, L.; Zang, Y.; Ying, A.; Hui, W.; Jiang, S.; Zhang, C.; Yang, T.; Chueh, Y.-L.; Li, J.; et al. Engineered Tunneling Layer with Enhanced Impact Ionization for Detection Improvement in Graphene/Silicon Heterojunction Photodetectors. *Light Sci. Appl.* **2021**, *10*, 113. [CrossRef]
108. Xu, J.; Liu, T.; Hu, H.; Zhai, Y.; Chen, K.; Chen, N.; Li, C.; Zhang, X. Design and Optimization of Tunneling Photodetectors Based on Graphene/Al2O3/Silicon Heterostructures. *Nanophotonics* **2020**, *9*, 3841–3848. [CrossRef]
109. Zhou, Y.; Khan, T.M.; Shim, J.W.; Dindar, A.; Fuentes-Hernandez, C.; Kippelen, B. All-Plastic Solar Cells with a High Photovoltaic Dynamic Range. *J. Mater. Chem. A* **2014**, *2*, 3492. [CrossRef]

110. Varghese, A.; Yakimov, M.; Tokranov, V.; Mitin, V.; Sablon, K.; Sergeev, A.; Oktyabrsky, S. Complete Voltage Recovery in Quantum Dot Solar Cells Due to Suppression of Electron Capture. *Nanoscale* **2016**, *8*, 7248–7256. [CrossRef]
111. Nishioka, K.; Sakitani, N.; Uraoka, Y.; Fuyuki, T. Analysis of Multicrystalline Silicon Solar Cells by Modified 3-Diode Equivalent Circuit Model Taking Leakage Current through Periphery into Consideration. *Sol. Energy Mater. Sol. Cells* **2007**, *91*, 1222–1227. [CrossRef]
112. Yang, W.; Luo, Y.; Guo, P.; Sun, H.; Yao, Y. Leakage Current Induced by Energetic Disorder in Organic Bulk Heterojunction Solar Cells: Comprehending the Ultrahigh Loss of Open-Circuit Voltage at Low Temperatures. *Phys. Rev. Appl.* **2017**, *7*, 044017. [CrossRef]
113. Tang, Y.; Bjuggren, J.M.; Fei, Z.; Andersson, M.R.; Heeney, M.; McNeill, C.R. Origin of Open-Circuit Voltage Turnover in Organic Solar Cells at Low Temperature. *Sol. RRL* **2020**, *4*, 2000375. [CrossRef]
114. Li, Y.; Yu, M.; Cheng, Q. Improved Performance of Graphene/n-GaAs Heterojunction Solarcells by Introducing an Electron-Blocking/Hole-Transporting Layer. *Mater. Res. Express* **2018**, *6*, 016202. [CrossRef]
115. Armano, A.; Buscarino, G.; Cannas, M.; Gelardi, F.M.; Giannazzo, F.; Schilirò, E.; Agnello, S. Monolayer Graphene Doping and Strain Dynamics Induced by Thermal Treatments in Controlled Atmosphere. *Carbon* **2018**, *127*, 270–279. [CrossRef]
116. Bissett, M.A.; Izumida, W.; Saito, R.; Ago, H. Effect of Domain Boundaries on the Raman Spectra of Mechanically Strained Graphene. *ACS Nano* **2012**, *6*, 10229–10238. [CrossRef]
117. Frank, O.; Mohr, M.; Maultzsch, J.; Thomsen, C.; Riaz, I.; Jalil, R.; Novoselov, K.S.; Tsoukleri, G.; Parthenios, J.; Papagelis, K.; et al. Raman 2D-Band Splitting in Graphene: Theory and Experiment. *ACS Nano* **2011**, *5*, 2231–2239. [CrossRef]
118. Shiwakoti, N.; Bobby, A.; Asokan, K.; Antony, B. Interface and Transport Properties of Gamma Irradiated Au/n-GaP Schottky Diode. *Mater. Sci. Semicond. Processing* **2018**, *74*, 1–6. [CrossRef]
119. Becker, J.A.; Brattain, W.H. The Thermionic Work Function and the Slope and Intercept of Richardson Plots. *Phys. Rev.* **1934**, *45*, 694–705. [CrossRef]
120. Lin, T.; Xie, J.; Ning, S.; Ma, Z.; Mu, Y.; Sun, W.; Yang, S. Effect of Annealing Process Parameters on N-GaAs Ohmic Contacts. *Microelectron. Eng.* **2022**, *258*, 111772. [CrossRef]
121. Lin, T.; Xie, J.; Ning, S.; Li, Q.; Li, B. Study on the P-Type Ohmic Contact in GaAs-Based Laser Diode. *Mater. Sci. Semicond. Processing* **2021**, *124*, 105622. [CrossRef]
122. Latreche, A. Combined Thermionic Emission and Tunneling Mechanisms for the Analysis of the Leakage Current for Ga_2O_3 Schottky Barrier Diodes. *SN Appl. Sci.* **2019**, *1*, 188. [CrossRef]
123. Arslan, E.; Çakmak, H.; Özbay, E. Forward Tunneling Current in Pt/p-InGaN and Pt/n-InGaN Schottky Barriers in a Wide Temperature Range. *Microelectron. Eng.* **2012**, *100*, 51–56. [CrossRef]
124. An, Y.; Behnam, A.; Pop, E.; Ural, A. Metal-Semiconductor-Metal Photodetectors Based on Graphene/p-Type Silicon Schottky Junctions. *Appl. Phys. Lett.* **2013**, *102*, 013110. [CrossRef]
125. Tomer, D.; Rajput, S.; Hudy, L.J.; Li, C.H.; Li, L. Carrier Transport in Reverse-Biased Graphene/Semiconductor Schottky Junctions. *Appl. Phys. Lett.* **2015**, *106*, 173510. [CrossRef]

2 straipsnis

Straipsnio pavadinimas	*Biosensor based on graphene directly grown by MW-PECVD for detection of COVID-19 spike (S) protein and its entry receptor ACE2*
Straipsnio bendraautoriai	*Šarūnas Meškinis; Rimantas Gudaitis; Andrius Vasiliauskas; Asta Guobienė; Voitech Stankevič; Skirmantas Keršulis; Arūnas Stirkė; Šarūnas Jankauskas; Eivydas Andriukonis; Wanessa Melo; Vilius Vertelis; Nerija Žurauskienė*
Leidėjas, žurnalo pavadinimas	*MDPI, Nanomaterials*
Metai	*2023*

nanomaterials

MDPI

Article

Biosensor Based on Graphene Directly Grown by MW-PECVD for Detection of COVID-19 Spike (S) Protein and Its Entry Receptor ACE2

Šarunas Meškinis [1,*], Rimantas Gudaitis [1], Andrius Vasiliauskas [1], Asta Guobienė [1], Šarūnas Jankauskas [1], Voitech Stankevič [2], Skirmantas Keršulis [2], Arūnas Stirkė [2], Eivydas Andriukonis [2], Wanessa Melo [2], Vilius Vertelis [2] and Nerija Žurauskienė [2]

[1] Institute of Materials Science, Kaunas University of Technology, K. Baršausko St. 59, LT-51423 Kaunas, Lithuania; rimantas.gudaitis@ktu.lt (R.G.); andrius.vasiliauskas@ktu.lt (A.V.); asta.guobiene@ktu.lt (A.G.); sarunas.jankauskas@ktu.lt (Š.J.)

[2] Department of Functional Materials and Electronics, Center for Physical Sciences and Technology, Saulėtekio Ave. 3, LT-10257 Vilnius, Lithuania; voitech.stankevic@ftmc.lt (V.S.); skirmantas.kersulis@ftmc.lt (S.K.); arunas.stirke@ftmc.lt (A.S.); eivydas.andriukonis@ftmc.lt (E.A.); wanessa.melo@ftmc.lt (W.M.); vilius.vertelis@ftmc.lt (V.V.); nerija.zurauskiene@ftmc.lt (N.Ž.)

* Correspondence: sarunas.meskinis@ktu.lt

Abstract: Biosensors based on graphene field-effect transistors (G-FET) for detecting COVID-19 spike S protein and its receptor ACE2 were reported. The graphene, directly synthesized on SiO_2/Si substrate by microwave plasma-enhanced chemical vapor deposition (MW-PECVD), was used for FET biosensor fabrication. The commercial graphene, CVD-grown on a copper substrate and subsequently transferred onto a glass substrate, was applied for comparison purposes. The graphene structure and surface morphology were studied by Raman scattering spectroscopy and atomic force microscope. Graphene surfaces were functionalized by an aromatic molecule PBASE (1-pyrenebutanoic acid succinimidyl ester), and subsequent immobilization of the receptor angiotensin-converting enzyme 2 (ACE2) was performed. A microfluidic system was developed, and transfer curves of liquid-gated FET were measured after each graphene surface modification procedure to investigate ACE2 immobilization by varying its concentration and subsequent spike S protein detection. The directly synthesized graphene FET sensitivity to the receptor ACE2, evaluated in terms of the Dirac voltage shift, exceeded the sensitivity of the transferred commercial graphene-based FET. The concentration of the spike S protein was detected in the range of 10 ag/mL up to 10 µg/mL by using a developed microfluidic system and measuring the transfer characteristics of the liquid-gated G-FETs. It was found that the shift of the Dirac voltage depends on the spike S concentration and was 27 mV with saturation at 10 pg/mL for directly synthesized G-FET biosensor, while for transferred G-FET, the maximal shift of 70 mV was obtained at 10 µg/mL with a tendency of saturation at 10 ng/mL. The detection limit as low as 10 ag/mL was achieved for both G-FETs. The sensitivity of the biosensors at spike S concentration of 10 pg/mL measured as relative current change at a constant gate voltage corresponding to the highest transconductance of the G-FETs was found at 5.6% and 8.8% for directly synthesized and transferred graphene biosensors, respectively. Thus, MW-PECVD-synthesized graphene-based biosensor demonstrating high sensitivity and low detection limit has excellent potential for applications in COVID-19 diagnostics.

Keywords: graphene; direct synthesis; PECVD; field-effect transistor-based biosensor; COVID-19; SARS-CoV-2 spike protein; receptor ACE2; charge neutrality point; shift of Dirac voltage

check for updates

Citation: Meškinis, Š.; Gudaitis, R.; Vasiliauskas, A.; Guobienė, A.; Jankauskas, Š.; Stankevič, V.; Keršulis, S.; Stirkė, A.; Andriukonis, E.; Melo, W.; et al. Biosensor Based on Graphene Directly Grown by MW-PECVD for Detection of COVID-19 Spike (S) Protein and Its Entry Receptor ACE2. *Nanomaterials* **2023**, *13*, 2373. https://doi.org/10.3390/nano13162373

Academic Editor: Daniela Iannazzo

Received: 24 July 2023
Revised: 9 August 2023
Accepted: 16 August 2023
Published: 18 August 2023

Copyright: © 2023 by the authors. Licensee MDPI, Basel, Switzerland. This article is an open access article distributed under the terms and conditions of the Creative Commons Attribution (CC BY) license (https://creativecommons.org/licenses/by/4.0/).

1. Introduction

COVID-19, also known as the coronavirus disease 2019, is a recently emerged infectious disease that affects humans and causes severe respiratory distress. It was first

identified in 2019 as a novel coronavirus, referred to as 2019-nCov, which was found in the bronchoalveolar lavage fluid of a patient. Subsequently, the virus was renamed severe acute respiratory syndrome coronavirus 2 (SARS-CoV-2) by the International Committee on Taxonomy of Viruses [1]. Due to its rapid spread among individuals, the World Health Organization (WHO) declared the COVID-19 outbreak as a pandemic on 12 March 2020. As of July 2023, there have been more than 767,000,000 confirmed cases of COVID-19 worldwide, resulting in almost 7 million deaths, according to the World Health Organization's official website (https://covid19.who.int, accessed on 13 July 2023). Thus, these data emphasize that the virus is still present and more research is needed. Although the specific mechanism by which SARS-CoV-2 causes the disease is not fully understood, recent research has indicated that SARS-CoV-2 utilizes angiotensin-converting enzyme II (ACE2) as a receptor to enter host cells. It is noteworthy that ACE2 also is a known cellular receptor for SARS-CoV [2]. In animal cells, SARS-CoV-2, and ACE2 are found in close proximity, and the virus's spike (S) protein exhibits a strong binding affinity for ACE2 [3,4].

The growing prevalence of diseases and their associated risks necessitates the exploration of novel sensor types for detection purposes. The recent encounter with the COVID-19 pandemic highlighted the crucial significance of virus detection methods, particularly due to the virus's rapid mutation and emergence of different variants.

Among the many diagnostic methods currently available, field-effect transistor (FET)-based biosensor devices can be used for virus detection [5–8]. These devices offer several advantages due to their small size and sensitivity, including the ability to make highly sensitive and instantaneous measurements using small amounts of analytes. Furthermore, FET-based biosensors are considered one of the perspective types of sensors to be potentially valuable for point-of-care testing, particularly for on-site detection, with the possibility to integrate on a chip using complementary metal oxide semiconductor (CMOS) technology [5–9]. Two-dimensional (2D) nanomaterials offer many unique possibilities for FET-based biosensors due to their atomically thin nature and extra-large surface-to-volume ratio [8]. Graphene, a two-dimensional carbon allotrope composed of a single layer of carbon atoms arranged in a honeycomb lattice, was the first isolated 2D nanomaterial to be studied [10]. It has garnered tremendous attention in the scientific community due to its extraordinary electronic and mechanical properties. Notably, ultra-high charge carrier mobility of 350,000 $cm^2V^{-1}s^{-1}$ [11], Young's modulus of 1 TPa [12], ease tunable electrical properties [8,13–15], large surface area and ability to sense molecules [8,13,16,17] offer significant advantages for applications. Remarkably, the large surface-to-volume ratio of the graphene provides a lot of the exposed atoms available for functional group attachment, resulting in significantly enhanced surface reactivity. Combined with easily tunable electrical properties, it opens up new possibilities for chemical sensing [18]. Therefore, graphene became a viable option for biosensing applications [8,13,16,19,20].

The operation of graphene field-effect transistors (G-FETs) designed as bioanalytical sensors are based on the change of the electrical conductance (resistance) or electrical current flowing through the sensor induced by changes in the environment and the interaction with bioanalytes (DNA sequences, bacteria, viruses, drugs, etc.) [21–23]. Due to the atomically thin graphene layer, the accumulation of bioanalytes on the surface of functionalized graphene induces a significant response of the G-FET. It thus ensures high sensitivity and increased detection limit to less than femtomolar concentrations [8,24]. One of the most investigated characteristics for the measure of biomolecules is a transfer characteristic of the FET (dependence of drain (D)—source (S) current, I_{DS}, on the gate voltage V_{GS} while keeping the bias voltage V_{DS} constant). Such dependences have a minimum at a specific gate voltage $V_{GS} = V_D$ called Dirac point or charge neutrality point (CNP). This transfer characteristic's left and right branches moving away from the CNP are called the p-branch and n-branch, respectively. They are related to the increasing density of positive charge carriers (holes) or negative charge carriers (electrons). Due to the zero-bandgap structure of graphene, carriers (electrons and holes) can be changed to each other at the Dirac point by increasing ambipolar gate voltage, which results in the formation of bipolar transfer

characteristics of G-FET [25]. At the CNP, the current reaches a minimum indicating an equal density of holes and electrons. One expects the V_D to be close to V_{GS} = 0 V for good quality (e.g., few defects and adsorbants) intrinsic graphene at low bias voltage V_{DS}. However, in real cases, it is shifted to positive gate voltages if graphene is p-doped or negative voltages if it is n-doped. The doping depends on various factors, such as substrate, metal of electrodes, defects and wrinkles of transferred graphene, nonhomogeneous distribution of charged species forming electron and hole paddles, etc. [8,26]. It is worth mentioning that a significant shift of the V_D from its initial value is obtained due to the interaction of the functionalized graphene surface with an analyte and could be a measure of the concentration of the analyte molecules. Therefore, preparing good structural quality graphene layers and process reproducibility is essential for developing highly sensitive G-FET biosensors.

The main methods used for graphene synthesis today are either exfoliation or chemical vapor deposition (CVD) on copper or nickel films with an additional transfer of graphene film to a required substrate. The exfoliation yields pristine graphene samples. However, the reproducibility of this process is complicated [27,28]. Combining the chemical vapor deposition on the catalytic metal foil with subsequent transfer to the targeted substrate produces much larger graphene samples. However, this prolonged process still needs to be improved for industrial applications [29,30]. It can even produce cracks and tears in the transferred graphene sheets [31], not to mention different organic adsorbates that accumulate on the graphene surface during the transfer [32]. The alternative is direct graphene synthesis on dielectric or semiconducting substrates via plasma-enhanced chemical vapor deposition (PECVD). This deposition method eliminates graphene transfer-related problems and keeps most of the pristine graphene properties required for biosensing applications intact [27,33]. In this case, control of the graphene flakes' orientation and growth of both planar graphene and vertical graphene nanowalls is possible [34,35]. However, direct graphene synthesis and its application for biosensor fabrication are much less studied than exfoliated or CVD-grown and transferred graphene. In some studies, graphene directly synthesized on dielectric substrates without using any catalyst was already successfully used as a FET channel [36–42]. However, only in [41], an initial study on the use of the directly synthesized graphene-based FET (G-FET) as a biosensor for adenosine tri-phosphate detection was presented. Despite that, in the recent review on graphene-based FET biosensors [8], it was pointed out that direct synthesis of the graphene on an insulating substrate is a promising technology for manufacturing G-FET-based biosensors.

This study presents the findings of examining graphene directly grown on the SiO_2 substrate through the microwave plasma-enhanced chemical vapor deposition (MW-PECVD) technique for its suitability in biosensors designed to detect the spike (S) protein of COVID-19. The results are compared with biosensors fabricated using commercially grown graphene on a copper substrate, which was subsequently wet transferred to a glass substrate.

2. Materials and Methods

2.1. Synthesis of MW-PECVD Graphene

Graphene samples were produced using a microwave plasma-enhanced chemical vapor deposition system, Cyrannus (Innovative Plasma Systems (Iplas) GmbH, Troisdorf, Germany). The Si(100) wafer coated by 300 nm thickness silicon dioxide (SiO_2) film using thermal oxidation was used as a substrate. During the fabrication process of the sensor, graphene was grown on a SiO_2/Si substrate with dimensions of 15 × 15 mm^2. The graphene synthesis conditions were based on our previous studies [35,43,44] and are outlined in Table 1.

Afterward, the graphene was patterned to obtain active area dimensions of 3 × 3 mm^2. At first, copper film was deposited through mask using electron beam evaporation. Then, unprotected graphene was etched out using oxygen plasma. Finally, the copper mask was removed by wet chemical etching. To create electrical contact, two Ag electrodes (source and drain) were deposited using unbalanced DC magnetron sputtering. The thickness of

the silver film was 250 nm. The dimensions of the electrodes were 7×3 mm^2, and the distance between them was 1.5 mm. Thus, the metal electrodes covered two 3×0.75 mm^2 areas of the graphene surface, creating a low contact resistance between the graphene and the electrodes.

Table 1. Graphene direct synthesis conditions.

Plasma Power (kW)	H_2 Gas Flow (sccm)	CH_4 Gas Flow (sccm)	Pressure (mBar)	Temperature (°C)	Time (min)
0.7	75	25	10	700	120

2.2. Preparation of Graphene by Wet Transfer Procedure

For comparison, a sensing element with graphene transferred from Cu foil was also used for biosensor fabrication. During the fabrication process, the graphene grown on a Cu foil (Graphenea Semiconductor SLU) was transferred onto a 1 mm thick glass substrate with already deposited Ag contacts using a wet chemical etching procedure. The Ag electrodes, with a Cr sublayer, were thermally deposited on the top of the glass substrate and post-annealed at 450 °C for 1 h in an Ar atmosphere for good adhesion with the substrate. The electrodes had the same configuration as in the previous case (MW-PECVD graphene). During the transfer procedure, the Cu foil with graphene was cut into pieces of 3×3 mm^2; then, the Cu was chemically dissolved using an ammonium persulfate solution from the bottom of the Cu/Graphene/PMMA structure. As a result, the single-layer graphene (SLG) with a PMMA flake was floating on the surface of the etching solution. Subsequently, rinsing with deionized water was performed, and the floating flake was captured and transferred onto the glass substrate (15 mm × 15 mm) with the pre-existing Ag contacts. The PMMA layer was removed using acetone and isopropanol just before the functionalization of the graphene film. To ensure good contact between the electrodes and graphene, an additional deposition of Ag electrodes with the same configuration was applied on the top of the graphene. As a result, at the point of contact, the electrodes covered both sides of the graphene layer.

2.3. Characterization of Graphene Sensing Elements

Transferred and directly grown graphene samples were characterized using Raman spectroscopy. Raman spectroscopy measurements of graphene were carried out using the InVia Raman microscope (Renishaw, Wotton-under-Edge, UK) equipped with a thermo-electrically cooled (–70 °C) CCD detector and 532 nm laser radiation source. The step size was 30×35 µm in x- and y-directions; each map consisted of 50 measurements with 20 s acquisition time at 0.23 mW laser power focused on a sample using 50×/0.75 NA objective lens (Leica). 2D and G intensity ratio (2D/G) was plotted using Wire 5.5 (Renishaw, Wotton-under-Edge, UK).

The directly synthesized graphene surface conductivity and morphology of graphene sheets were analyzed by atomic force microscopy (NanoWizard®3, JPK Instruments, Bruker Nano GmbH, Berlin, Germany). The morphology and phase images were collected using an ACTA (Applied NanoStructures, Inc., Mountain View, CA, USA) probe operating in tapping mode. The probe tip radius of curvature was 6 nm. More details regarding these measurements can be found in [35,45]. To investigate the surface electrical conductance, the special Ag electrodes were formed over the graphene layer (see Figure 1). The conductivity was measured using contact-mode conductive atomic force microscopy (C-AFM) with a metal-coated tip ANSCM-PT (AppNano, Mountain View, CA, USA) silicon probe with a thin layer of Pt/Ir coating (thickness (nm) -25 ± 5) on both reflex and tip sides of the probe. ANSCM probes with a 1.6 spring constant are ideal for use in C-AFM mode. Tip Shape-Tetrahedral; Tip ROC (nm)—30, Height (µm), 14–16, Frequency (kHz)—61. The electrical current was measured as a function of the applied bias voltage (−10–10 mV). All the measurements were performed at room temperature in the air.

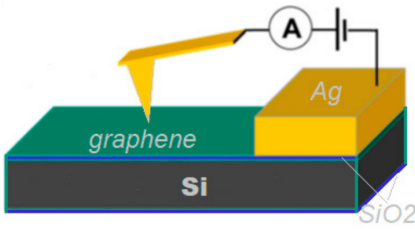


Figure 1. The schematic of C-AFM used for measurements of the graphene surface conductivity.

2.4. Preparation of Graphene Biosensor

In order to make a graphene-based sensor sensitive to the spike (S) protein of COVID-19, the surface of graphene was functionalized. For this purpose, the fabricated graphene-based elements underwent a soaking process in a solution of 1 mM 2.5-dioxopyrrolidin-1-yl 4-(pyrene-1-y) butanoate (PBASE) (Cayman Chemical, Ann Arbor, MI, USA) in methanol (VWR International, France) at room temperature for one hour. This procedure was performed based on a reference [46] with certain adjustments. After that, the graphene-based element was left overnight in the oven at 60 °C. The prepared PBASE/graphene samples were used in the microfluidic system in order to create a liquid-gated field effect transistor (FET) structure for the subsequent experiments. The microfluidic system (see Figure 2) was created by covering the graphene-based sensing element by specially prepared polydimethylsiloxane (PDMS) chips with microfluidic channels with a width of 0.5 mm and a length of 3 mm. So, only the graphene under the channel (0.5 mm × 3 mm) was exposed to the liquid analyte. The microfluidic channel was prepared using master mold casting technics. The cast PDMS (Sylgard^{TM} 184 Silicone Elastomer, DOW Europe, Germany) mold was cured at 60 °C overnight. Then, de-molded PDMS was punctured using a biopsy puncher to obtain inlets to which two flexible tubes were connected. The liquid gate was formed by inserting a stainless steel wire with a 200 µm diameter through the PDMS chips, positioning the end of the wire at the center of the channel directly over the graphene, and protruding from the channel to be submerged in the liquid by approximately 0.1 mm (0.4 mm away from the surface of graphene). A gate voltage was then connected to the opposite end of the wire. To ensure sealing between the elastomer and the surface of the graphene-based device, a custom 3D-printed holder was used (not shown in the figure). Moreover, this holder had a set of connectors for easy connecting of measurement devices.

First, the PBASE functionalized device was exposed to several concentrations (from 10 ag/mL to 10µg/mL) of the recombinant angiotensin-converting enzyme 2 (ACE2) (Baltymas UAB, Vilnius, Lithuania) protein prepared in 0.1× phosphate-buffered saline (PBS) (contains 0.0137 M of NaCl (VWR International, Villers-lès-Nancy, France), 0.00027 M of KCl (VWR International, Villers-lès-Nancy, France), 0.001 M of Na_2HPO_4: (Sigma Aldrich (St. Louis, MO, USA), and KH_2PO_4: 0.00018 mM (Merck, Darmstadt, Germany)) at least for 4 h at room temperature. The excess ACE2 was removed by rinsing 1 mL of PBS with Tween-20 (0.05%) and then with 2 mL of PBS only. Then, 1 mL of PBS with 0.1% concentration of Bovine Serum Albumin (BSA) (Sigma Aldrich (St. Louis, MO, USA) was injected into the microfluidic system to block ACE2 uncovered places. Finally, the experiments with a different recombinant SARS-CoV-2 Spike glycoprotein trimeric ectodomain (S) (Baltymas UAB, Vilnius, Lithuania) of protein concentrations ranging from 10 ag/mL to 10 µg/mL prepared in 0.1× PBS (chemical composition of PBS described above) were performed.

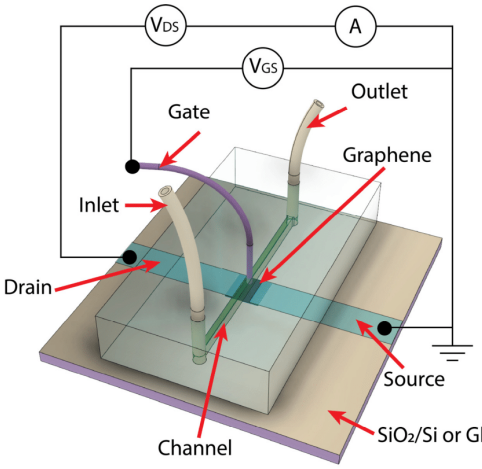


Figure 2. Graphene-sensing element with microfluidic system and measurement scheme.

2.5. Electrical Measurements

The schematic of the measurement circuit for liquid-gated G-FET biosensors is shown in Figure 2. The electrical performance was evaluated using a YOKOGAWA GS610 source measurement unit from Japan and an ITECH IT6123 DC source meter from the US. The G-FET transfer characteristics, i.e., dependences of a drain (D)-source (S) current I_{DS} vs. gate voltage V_{GS} were measured while maintaining constant bias voltage V_{DS} of 50 mV. Prior to conducting transfer characteristic measurements, real-time (kinetics) resistance measurements of the graphene channel were carried out. Following each process of the functionalization of the graphene surface, a waiting period of 30 min was implemented. This duration proved adequate for relaxation processes to occur and for the resistance saturation value to be attained.

During the experiments, the voltage of the Dirac point V_D was determined as the gate voltage at a minimum current value in the I_{DS}-V_{GS} characteristics of the liquid-gated G-FET. The voltage applied to the gate (V_{GS}) was swept within the range of ±0.8 V.

3. Results and Discussion

3.1. Graphene Structure and Properties

The Raman scattering spectra are presented in Figure 3. The spectrum of CVD-grown and transferred graphene is typical for pristine graphene [15,47,48]. Two prominent peaks, namely the G and 2D peaks, were observed. The G peak corresponds to lattice vibrations, while the 2D peak originates from second-order Raman scattering [47]. Notably, the average I_{2D}/I_G ratio of CVD graphene was approximately 1.94 (Table 2), indicating that it is single-layer graphene [49]. Weak defect-related D and D′ peaks [47,50] can be seen, too. In the case of the transferred graphene, the $I_D/I_{D'}$ ratio was 0.55 (Table 2). Thus, the presence of the on-site defects induced by transfer-related adsorbants can be supposed [50]. The same main peaks were found in Raman scattering spectra of the graphene directly synthesized by MW-PECVD. However, in this case, the D peak was much stronger, resulting in a significantly larger I_D/I_G ratio, indicating a much larger defect density. Another defect-related peak, D′ peak, was merged with the G peak and

was seen as a shoulder. An analysis of the $I_D/I_{D'}$ ratio (Table 2) revealed the prevalence of the boundary defects in the directly synthesized graphene. That can be explained by the nanocrystalline nature of the graphene directly synthesized by MW-PECVD. In our case, the average nanocrystal size was below 10 nm. The average nanocrystal size (L_a), estimated using the equation of the Tuinstra and Koenig $L_a = 4.4/(I_D/I_G)$ nm [51,52], was ~3 nm. While the average nanocrystal size calculated using the equation proposed by P. Mallet-Ladeira et al. [53] L_a = (68-FWHM(G))/5.2 nm was ~5.8 nm. According to the [49], the I_{2D}/I_G ratio of the directly synthesized graphene indicates the formation of the three-layer and four-layer graphene. G-band peak position (Pos(G)) of the Raman spectra of directly synthesized graphene was upshifted compared to the Raman spectra of transferred graphene, and FWHM(G) was much increased. Along with the increased I_D/I_G ratio, it indicates increased defects density [54]. That can be explained by a large number of boundary defects due to the directly synthesized graphene nanocrystalline nature. The increase in the FWHM(2D) can indicate the presence of compressive stress in the directly synthesized graphene [55,56]. The upshift of the 2D peak position (Pos(2D)) and Pos(G) was in good accordance with this assumption [48,57–59]. The upshift of the Pos(2D) and Pos(G) can also be related to graphene doping [48,58,59]. However, FWHM(G) should decrease with graphene doping [54,55]. In contrast, we observed an opposite trend. Thus, if there was an effect of possible doping of graphene, it was overshadowed by the impact of defects.

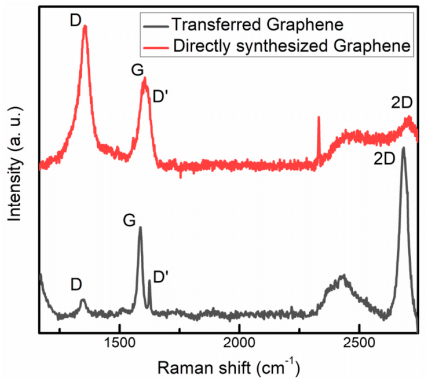


Figure 3. Typical Raman spectra of CVD grown and transferred graphene and graphene directly synthesized by MW−PECVD.

Table 2. Graphene Raman scattering spectra parameters.

Graphene Type	I_D/I_G	I_{2D}/I_G	$I_D/I_{D'}$	Pos(G) (cm^{-1})	Pos(2D) (cm^{-1})	FWHM(G) (cm^{-1})	FWHM(2D) (cm^{-1})
Directly synthesized graphene	1.46	0.42	3.26	1595.8	2703.3	37.6	75
Transferred graphene	0.18	2.05	0.55	1586	2685.6	15.7	32.8

The morphology and conductivity of the directly synthesized graphene were additionally studied by atomic force microscopy. The graphene consisted of the 20–25 nm size features (Figure 4). The height of those grains was 1–1.3 nm (Figure 4). Taking into account that graphene monolayer thickness is ~0.4 nm [60], the abovementioned feature height was in good accordance with the directly synthesized graphene layer number estimated by Raman scattering spectroscopy. The phase image was very similar to the 2D morphology image, confirming the observation of the graphene nanograins or nanoflakes. Considering average graphene nanocrystallite size evaluated using Raman scattering spectroscopy, in our case, 20–25 nm nanocrystalline graphene flakes consisted of the 3–6 nm average size nanocrystallites.

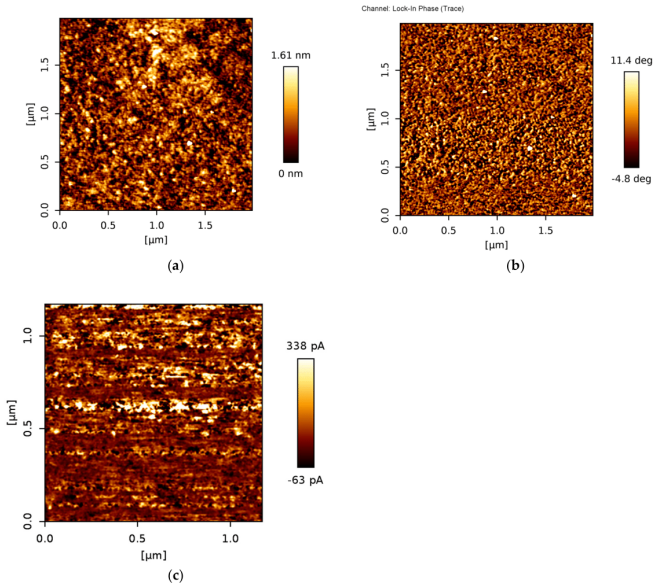


Figure 4. Directly synthesized graphene 2D morphology (**a**), phase (**b**) and conductivity (**c**) images.

The conductivity image revealed the presence of very different conductivity areas (Figure 4c). This can be explained by the nanocrystalline nature of the directly synthesized graphene due to the much lower conductivity of the grain boundaries [61]. The average current measured by CAFM was 440 pA, and the maximum current was 1.6 nA.

3.2. Immobilization of G-FET Sensing Elements by Receptor ACE2

Before performing the experiments with a recombinant SARS-CoV-2 Spike (S), the ACE2 receptors were immobilized on PBASE/graphene. To enhance the immobilization of ACE2 on the PBASE, the variations in ACE2 concentration were examined.

Figure 5 presents the characteristic transfer curves (I_{DS} vs. V_{GS}) of both G-FETs for different concentrations of ACE2 in the PBS solution. All curves had the characteristic minimum, which corresponded to the Dirac point (charge neutrality point, CNP). For

a more accurate determination of the position of the minimum, the derivatives of these curves are shown in the inset. The voltages at which $dI_{DS}/dV_{GS} = 0$ corresponded to the Dirac point.

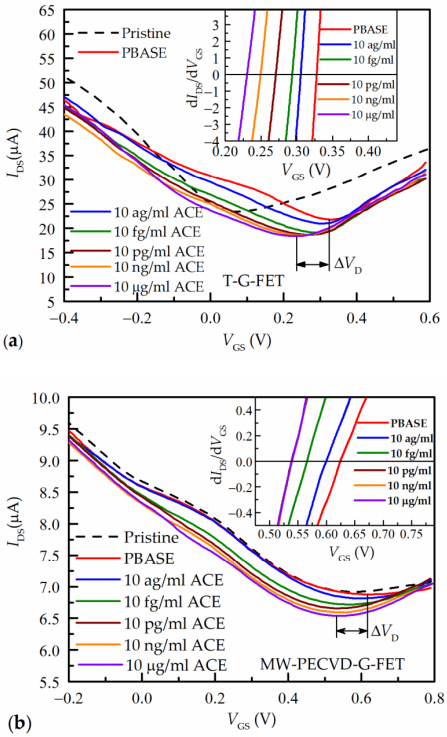


Figure 5. G-FET transfer characteristics at different ACE2 concentrations for T-G-FET (**a**) and MW-PECVD G-FET (**b**) sensors. Insets: the derivatives of transfer characteristics close to Dirac point at which derivative is equal to zero.

For comparison, the measurements of G-FET transfer characteristics of pristine graphene elements before the functionalization by PBASE are also shown (dashed black curve). In general, for detecting biomolecules, the key parameter of significance is the magnitude of the shift in the Dirac voltage. However, it should be noted that for graphene, the surface of which is functionalized, the primary transfer characteristic corresponding to pristine graphene (exhibiting a Dirac voltage closer to zero) is also very critical. This is because contaminants on the graphene surface not only affect its doping but also diminish carrier mobility and restrict surface functionalization [62]. One can see from the graphs in Figure 5a that for transferred graphene T-G-FET the Dirac voltage of pristine graphene is equal to $V_D = 74$ mV, meanwhile for MW-PECVD-G-FET (see Figure 5b), it is shifted up to $V_D = 580$ mV. In general

case, the doping level of pristine graphene is influenced by various factors, which include the interaction of the interface between graphene and other materials (such as substrate, electrodes, and media) and the distribution of charged species or impurities within these materials [63]. The results obtained for pristine graphene in MW-PECVD-G-FET can be explained based on the results of previous works: a similar positive shift of the Dirac voltage was reported for graphene directly synthesized on the SiO_2 film without the use of any dopants in [37,39,42]. However, no shift was found for graphene directly synthesized on the molten glass and afterward transferred onto the SiO_2 film [64]. Therefore, substrate-induced p-type doping of the directly synthesized graphene can be supposed. It should be mentioned that substrate-induced graphene self-doping was reported in numerous studies [65–71]. Notably, p-type self-doping can be induced in the graphene transferred onto the SiO_2 substrate due to the different surface treatments and residual charges created on the substrate [65]. It was found that the presence or absence of the graphene self-doping phenomena and graphene self-doping type (p-type or n-type) can be controlled by selecting the appropriate substrate [68]. The modeling revealed that the electronic structure of the graphene placed onto the SiO_2 significantly depends on the interface geometry and surface polarity [69]. O-polar SiO_2 surface with dangling bonds induces p-type doping in the graphene [69]. Using the Si-polar surface with dangling bonds results in the graphene n-type self-doping [69]. Thus, one can suppose that substrate treatment before graphene growth and/or the direct graphene synthesis process itself resulted in changes in the substrate surface or interface composition and the resultant transfer of the induced positive charge to the graphene.

Nevertheless, for transferred graphene T-G-FET, the quality of the fabrication process can also be associated with the level of doping, as it can indicate the amount of impurities present between graphene and the substrate after the transfer process [41,72]. Although during the transfer of graphene on the surface of the glass, the effort to reduce contaminants in the transfer process was made by chemical cleaning and treatment in oxygen plasma, the Dirac voltage of pristine graphene was shifted from 0 V: V_D = 74 mV.

As was mentioned before, the pristine graphene sensing elements were functionalized by PBASE. One can see that for transferred graphene T-G-FET (Figure 5a), a shift of minimum (V_D) to higher gate voltages V_{GS} of the transfer curve after the covering of the graphene by PBASE was much larger in comparison to ME-PECVD-G-FET (Figure 5b): from 74 mV up to 327 mV (ΔV_D = 253 mV) and from 580 mV up to 624 mV (ΔV_D = 44 mV), respectively. The shift in the positive direction by PBASE can be explained by its p-doping effect through the charge transfer between the pyrene group and graphene [73]. This shift confirms the successive surface functionalization by the PBASE. However, for the MW-PECVD-G-FET, the small shift of the minimum indicates that a smaller area of the graphene channel was functionalized by PBASE. This can be caused by numerous grain boundary defects in the directly grown graphene, which is nano-crystalline with a large number of grain boundaries (see Figure 4). It should be noted that the defects and contaminations over the graphene surface induce electrical characteristics that vary from sample to sample and lead to the increase in the Dirac point of the pristine graphene. This is consistent with the result of Raman spectroscopy studies of the MW-PECVD-grown graphene on SiO_2/Si substrates. Moreover, as was mentioned before, the Dirac point shifted only by several tens of millivolts after the functionalizing of the surface of the MW-PECVD graphene, indicating the smaller active area of graphene in this case.

For the immobilization of receptor ACE2 on the PBASE, the microfluidic channel was filled by ACE2, and transfer characteristics of both G-FETs were measured for each concentration. The concentration of ACE2 in the microfluidic system was increased step by step from the lowest (10 ag/mL) to the highest (10 mg/mL). The results of these measurements are shown in Figure 5. The immobilization of ACE2 caused the shift of V_D to the lower voltage depending on the concentration—the higher the concentration of ACE2, the larger shift of V_D takes place. The reason for the shift in the Dirac point in the negative direction is related to a negative charge induced by ACE2 on the PBASE/graphene surface.

Figure 6 summarizes the data presented in Figure 5. As shown in Figure 6, the Dirac voltage shift (ΔV_D) was observed as a response to ACE2 concentration C_{ACE2} for both G-FETs. First, MW-PECVD-G-FET showed quite good sensitivity at the lowest ACE2 concentrations. Even at 10 ag/mL (or 10^{-2} fg/mL) of ACE2 protein, it was possible to detect measurable signals. Then, at higher concentrations, it tended to saturate when it reached 10^4 fg/mL, which corresponded to the maximal ΔV_D =86 mV. The saturation at lower concentration in comparison to transferred graphene (red curve) may be due to the specific features of the graphene layer nanostructure of MW-PECVD-G-FET described above: due to a large number of grain boundaries and small size nanocrystallites, the relative area of perfect graphene which could be functionalized was smaller in comparison to transferred graphene. Therefore, for the T-G-FET, the saturation of the ΔV_D value occurred at much higher concentrations. One can see that the shift of the Dirac voltage tended to saturate at 10^7 fg/mL. However, in all cases, the ΔV_D of the MW-PECVD-G-FET was larger than the ΔV_D of the T-G-FET, revealing good functionalization possibilities of directly synthesized graphene.

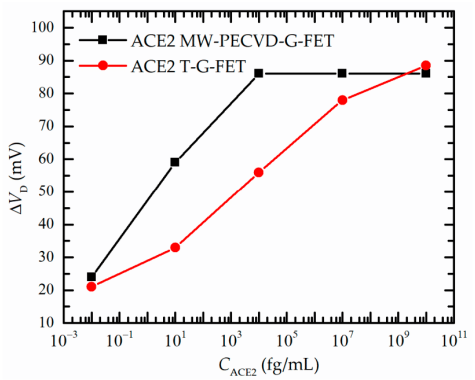


Figure 6. Change of V_D vs. ACE2 receptor concentrations for PECVD-G-FET and T-G-FET.

3.3. Detection of SARS-CoV-2 Spike S Protein

To demonstrate and to compare G-FETs biosensing properties, recombinant SARS-CoV-2 spike (S) and recombinant angiotensin-converting enzyme 2 (ACE2) proteins were selected as a model. It is known that ACE2 is recognized as the entry receptor for SARS-CoV-2 [74]. This fact was explained through structural studies, which showed that SARS-CoV-2 spike (S) glycoproteins exhibit a stronger binding affinity to ACE2 [75,76]. Additionally, the overall structure of SARS-CoV-2 S closely resembles that of SARS-CoV S, with the spike receptor-binding domain (RBD) making contact with the extracellular region of ACE2 [77].

Based on the studies conducted on the immobilization of PBASE/graphene with the ACE2 receptor, we concluded that an optimal concentration of 10 µg/mL of ACE2 is required for T-G-FET, while an ACE2 concentration of 10 ng/mL could be sufficient for MW-PECVD-G-FET. Therefore, during the subsequent research, the concentration of 10 µg/mL of ACE2 was used for the preparation of both G-FET biosensors to ensure further comparison of obtained results.

In the next step, the surface of the graphene sensor was rinsed with 1 mL of PBS with Tween-20 and then with 2 mL of PBS to remove the excess ACE2 and to passivate the uncoated surface of the graphene. Subsequently, 1 mL of PBS with 0.1% Bovine Serum

Albumin (BSA) (Sigma Aldrich, St. Louis, MO, USA) was injected into the microfluidic system to block any ACE2-uncovered areas. Following this, biosensors were prepared and utilized to examine the detection of the recombinant S protein by G-FETs.

Figure 7 presents the characteristic transfer curves (I_{DS} vs. V_{GS}) of both G-FETs for different concentrations of S protein in a PBS solution. For comparison, the measurements of the G-FET transfer characteristics of graphene elements immobilized by ACE2 with a concentration of 10 µg/mL (black dashed line) and after rinsing with Tween-20 and subsequent treatment with BSA (red line) are shown.

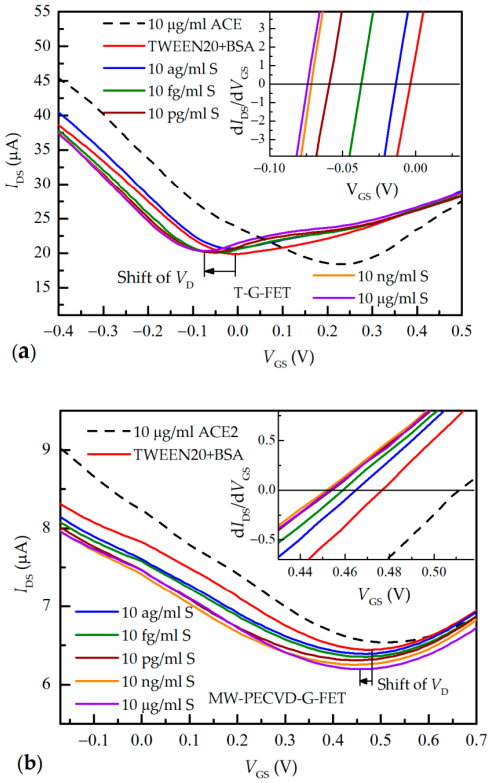


Figure 7. G-FET transfer characteristics at different spike S protein concentrations for T-G-FET sensors (**a**) and MW-PECVD G-FET (**b**). Insets: the derivatives of transfer characteristics close to the Dirac point at which the derivative is equal to zero.

It can be observed that the rinsing procedure induced significant changes in the position of the minimum on the transfer curves. This was particularly evident in the samples of transferred graphene T-G-FET (see Figure 7a), where the minimum (V_D) shifted

from V_{GS} = 270 mV to lower gate voltages of V_{GS} = −3 mV. However, for the MW-PECVD G-FET, the shift was much smaller: from 510 mV to 475 mV (see Figure 7b).

Subsequently, by filling the channel of the microfluidic system with higher spike S protein concentration, the shift of the Dirac point to the lower voltages was further observed. However, this shift becomes smaller with an increase in spike S protein concentration, and saturation is seen.

Figure 8 summarizes the data presented in Figure 7. One can see that both G-FET devices showed remarkable sensitivity and were capable to detect the S spike protein with a concentration as low as 10^{-2} fg/mL. At this concentration, the Dirac voltage was shifted by ~10 mV. With an increase in the spike S protein concentration C_S, the shift of the Dirac voltage ΔV_D increased with the tendency of saturation. However, for MW-PECVD-G-FET biosensors, the ΔV_D started saturating at a spike S concentration of 10^4 fg/mL (shown as black squares in Figure 8), with the maximum Dirac voltage change being ΔV_D = 27 mV. On the other hand, the T-G-FET biosensor can operate across a broader range of the spike S concentrations, and the gate voltage shift tended to saturate only at 10^7 fg/mL (depicted as red dots). In this case, the total shift of the Dirac voltage achieved approximately ΔV_D = 70 mV. From the analysis of the obtained results, it became evident that the characteristics and quality of pristine graphene have a significant influence on all modification processes of graphene surface, such as functionalization by PBASE, immobilization by ACE2, and S protein detection.

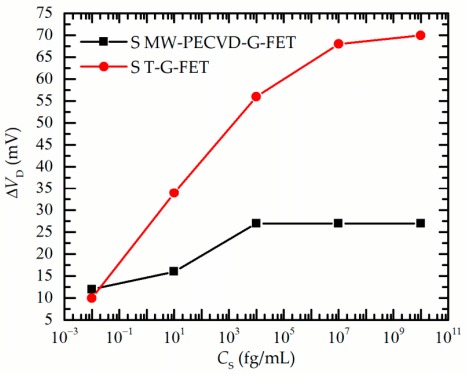


Figure 8. Change of V_D vs. spike S protein concentrations for PECVD and transferred graphene sensors.

Furthermore, it should be highlighted that the detection of biomolecules using FET devices could be performed not only by measuring the change in the Dirac voltage. Other measurable parameters of the transfer curves that could change during the detection of analytes are the change in the transconductance $g_m = dI_{DS}/dV_{GS}$ (the slope of the transfer curves) and the relative change in current $\Delta I_{DS}/I_{0DS}$ (or conductance) at a constant gate voltage, which is frequently measured at the CNP or in the p- or n- branches at a constant V_{GS}. This method allows fast and easier measurement, which could be performed in real-time. It is crucial to carefully select the gate voltage at which the current exhibits the most significant change in the concentration of the analyzed biomolecules to achieve maximum sensitivity. By calculating the derivatives of the transfer curves shown in Figure 8, it was determined that for MW-PECVD-G-FET biosensors, the largest slope was at $V_{GS} \approx 200$ mV, while for T-G-FET biosensors, it was ≈ -200 mV. Therefore, the relative change in current

$\Delta I_{DS}/I_{0DS}$ was calculated at these gate voltages. It was found $\Delta I_{DS}/I_{0DS} \approx 5.6\%$ for the MW-PECVD-G-FET and ≈8.8% for T-G-FET for a concentration of spike S protein equal to C_S = 10 pg/mL and 6% and 10%, respectively, for C_S = 10 μg/mL. However, it is worth mentioning that this method has accuracy limitations because when biological analytes interact with the sensor, two distinct effects can occur. These effects are a shift of the Dirac point due to a change in the charge carrier density and a decrease in transconductance (slope of the transfer curve) in one or both branches of the characteristic due to an increase in charge carrier scattering [21]. Therefore, the measurement of the relative change of the current at a specific constant gate voltage is the simplest approach and could be used in real-time measurements. However, its interpretation becomes challenging, as it may involve contributions from both mentioned mechanisms, making it difficult to evaluate the individual contribution.

The obtained results demonstrate that although the MW-PECVD-grown graphene biosensor has a narrower range of sensitivity and a higher level of detection in comparison to the transferred graphene biosensor, it can be successfully used to detect SARS-CoV-2 spike S protein. MW-PECVD-G-FET can still sense tens of ag/mL concentration. Despite much larger defect density, a relative change in current $\Delta I_{DS}/I_{0DS}$ because of the spike S protein action for directly grown graphene biosensor was comparable with the transferred graphene (5.6% and 8.8%, respectively), while MW-PECVD-G-FET sensitivity to the receptor ACE2 even exceeded the sensitivity of the T-G-FET. Considering these results and the compatibility of the graphene direct growth on the Si/SiO_2 surface with Si technology, the directly synthesized graphene-based FET biosensor is very promising for integration into the lab-on-chip devices. Further optimization of the directly synthesized graphene structure is necessary to increase the sensitivity of the MW-PECVD-G-FET and their operating concentration range. It should be mentioned that the dependence of the directly synthesized graphene-based FET biosensor sensitivity on the structure remains unclear. Particularly, the graphene containing smaller grains and more grain boundaries exhibited lower average mobility [78]. However, the line defects and grain boundaries increased the sensitivity of the polycrystalline graphene-based chemoresistors [79]. Polycrystalline graphene-based resistor sensitivity to the adsorbed gas molecules was substantially higher than the sensitivity of the grain boundary-free graphene. However, the sensitivity depended on the grain boundary number, too [80]. Even more important seems to be the control of the substrate-induced self-doping of the graphene. A reduction in the substrate-induced self-doping resulted in both increased mobility of the transferred graphene [81,82] and increased sensitivity of the transferred graphene-based FET gas sensors [83]. The effects of substrate-induced doping can be reduced by passivation overlayer deposition [78]. However, this method is unsuitable for graphene-based biosensors because the passivation layer increases the distance between the graphene and analyte molecules and, as a result, reduces the sensitivity of the sensor. More perspective seems to be a selection of the appropriate substrate [81] and finding the optimal substrate pre-treatment before the graphene synthesis [84].

4. Conclusions

In conclusion, the graphene-based Field-Effect Transistor (G-FET) biosensors for the detection of SARS-CoV-2 spike S protein were developed. The G-FETs biosensors were fabricated using graphene directly synthesized on SiO_2/Si substrate by MW-PECVD. Their sensitivity was comparable with the sensitivity of the FETs based on commercial CVD-grown graphene transferred on glass.

For the investigations of the detectivity and sensitivity of graphene biosensors, a microfluidic system with a liquid-gated FET circuit was developed. It was found that the functionalization of graphene by PBASE led to a shift of the Dirac voltage (V_D) (charge neutrality point) to higher values, while immobilization by receptor ACE2 led to the shift of V_D to lower voltages. It can be explained by graphene p-doping and n-type doping effects, respectively. For G-FET with directly synthesized graphene, the PBASE adsorption-induced

shift was significantly smaller, indicating the influence of the structure and properties of the pristine graphene layer. However, directly synthesized graphene FET sensitivity to the receptor ACE2, evaluated in terms of the Dirac voltage shift, exceeded the sensitivity of the transferred commercial graphene-based FET. Moreover, the shift in the Dirac voltage upon ACE2 immobilization could be attributed to charge transfer and changes in the doping level of the graphene.

Testing of the fabricated sensors for detecting SARS-CoV-2 spike S protein demonstrated that both types of G-FETs exhibited remarkable sensitivity and low detection limit and could detect S spike even at concentrations as low as 10^{-2} fg/mL. However, directly synthesized graphene exhibited slightly lower sensitivity compared to transferred graphene but sufficient for detection at low concentrations. Moreover, MW-PECVD G-FET biosensor showed saturation tendency at 10^4 fg/mL, while T-G-FET based on transferred graphene could detect up to 10^7 fg/mL spike S protein. The sensitivity estimation was also performed at a constant gate voltage corresponding to the largest transconductance values of both G-FETs. The relative source-drain current change for S protein concentration of 10 pg/mL was found to be 5.6% and 8.8% for directly synthesized and transferred graphene biosensors, respectively. Thus, it was comparable for both FET-based biosensors, despite the much larger defect density and nanocrystalline nature of the directly synthesized graphene.

The choice of graphene type, the structural quality of the graphene, and the functionalization process significantly affected the sensitivity and detection range of the G-FET biosensors. Overall, the results indicate that graphene-based G-FET biosensors have promising potential for sensitive detection of SARS-CoV-2 spike S protein, with further optimization of graphene quality and device fabrication, potentially enhancing their performance.

Author Contributions: Conceptualization, Š.M. and N.Ž.; methodology, V.S., S.K., A.S. and R.G.; software, V.V. and E.A.; validation, A.S., V.S. and W.M.; formal analysis, A.S. and Š.M.; investigation, S.K., W.M., R.G., A.V., A.G., V.V., E.A. and Š.J.; resources, Š.M. and N.Ž.; data curation, A.S. and V.S; writing—original draft preparation, N.Ž., Š.M., V.S. and A.S.; writing—review and editing, N.Ž., Š.M., V.S., A.S. and W.M.; visualization, E.A., V.S., S.K. and A.G.; supervision, N.Ž. and Š.M.; project administration, N.Ž.; funding acquisition, N.Ž. All authors have read and agreed to the published version of the manuscript.

Funding: This research has received funding from European Regional Development Fund (project No. 13.1.1-LMT-K-718-05-0015) under grant agreement with the Research Council of Lithuania (LMTLT). Funded as European Union's measure in response to Cov-19 pandemic.

Data Availability Statement: Not applicable.

Conflicts of Interest: The authors declare no conflict of interest.

References

1. Gorbalenya, A.E.; Baker, S.C.; Baric, R.S.; de Groot, R.J.; Drosten, C.; Gulyaeva, A.A.; Haagmans, B.L.; Lauber, C.; Leontovich, A.M.; Neuman, B.W.; et al. The Species Severe Acute Respiratory Syndrome-Related Coronavirus: Classifying 2019-NCoV and Naming It SARS-CoV-2. *Nat. Microbiol.* **2020**, *5*, 536–544. [CrossRef]
2. Li, W.; Moore, M.J.; Vasilieva, N.; Sui, J.; Wong, S.K.; Berne, M.A.; Somasundaran, M.; Sullivan, J.L.; Luzuriaga, K.; Greenough, T.C.; et al. Angiotensin-Converting Enzyme 2 Is a Functional Receptor for the SARS Coronavirus. *Nature* **2003**, *426*, 450–454. [CrossRef] [PubMed]
3. Wrapp, D.; Wang, N.; Corbett, K.S.; Goldsmith, J.A.; Hsieh, C.-L.; Abiona, O.; Graham, B.S.; McLellan, J.S. Cryo-EM Structure of the 2019-NCoV Spike in the Prefusion Conformation. *Science* **2020**, *367*, 1260–1263. [CrossRef] [PubMed]
4. Seo, G.; Lee, G.; Kim, M.J.; Baek, S.-H.; Choi, M.; Ku, K.B.; Lee, C.-S.; Jun, S.; Park, D.; Kim, H.G.; et al. Rapid Detection of COVID-19 Causative Virus (SARS-CoV-2) in Human Nasopharyngeal Swab Specimens Using Field-Effect Transistor-Based Biosensor. *ACS Nano* **2020**, *14*, 5135–5142. [CrossRef]
5. Panahi, A.; Sadighbayan, D.; Forouhi, S.; Ghafar-Zadeh, E. Recent Advances of Field-Effect Transistor Technology for Infectious Diseases. *Biosensors* **2021**, *11*, 103. [CrossRef]
6. Hao, R.; Liu, L.; Yuan, J.; Wu, L.; Lei, S. Recent Advances in Field Effect Transistor Biosensors: Designing Strategies and Applications for Sensitive Assay. *Biosensors* **2023**, *13*, 426. [CrossRef]
7. Aftab, S.; Iqbal, M.W.; Hussain, S.; Hegazy, H.H. Recent Advances in Nanomaterials-Based FETs for SARS-CoV-2 (COVID-19 Virus) Diagnosis. *Adv. Funct. Mater.* **2023**, *33*, 2301007. [CrossRef]

8. Wang, S.; Qi, X.; Hao, D.; Moro, R.; Ma, Y.; Ma, L. Review—Recent Advances in Graphene-Based Field-Effect-Transistor Biosensors: A Review on Biosensor Designing Strategy. *J. Electrochem. Soc.* **2022**, *169*, 027509. [CrossRef]
9. Xu, L.; Ramadan, S.; Rosa, B.G.; Zhang, Y.; Yin, T.; Torres, E.; Shaforost, O.; Panagiotopoulos, A.; Li, B.; Kerherve, G.; et al. On-Chip Integrated Graphene Aptasensor with Portable Readout for Fast and Label-Free COVID-19 Detection in Virus Transport Medium. *Sens. Diagn.* **2022**, *1*, 719–730. [CrossRef]
10. Castro Neto, A.H.; Guinea, F.; Peres, N.M.R.; Novoselov, K.S.; Geim, A.K. The electronic properties of graphene. *Rev. Mod. Phys.* **2009**, *81*, 109. [CrossRef]
11. Banszerus, L.; Schmitz, M.; Engels, S.; Dauber, J.; Oellers, M.; Haupt, F.; Stampfer, C. Ultrahigh-mobility graphene devices from chemical vapor deposition on reusable copper. *Sci. Adv.* **2015**, *1*, e1500222. [CrossRef]
12. Lee, C.; Wei, X.; Kysar, J.W.; Hone, J. Measurement of the Elastic Properties and Intrinsic Strength of Monolayer Graphene. *Science* **2008**, *321*, 385–388. [CrossRef] [PubMed]
13. Lee, J.-H.; Park, S.-J.; Choi, J.-W. Electrical Property of Graphene and Its Application to Electrochemical Biosensing. *Nanomaterials* **2019**, *9*, 297. [CrossRef] [PubMed]
14. Craciun, M.F.; Russo, S.; Yamamoto, M.; Tarucha, S. Tuneable Electronic Properties in Graphene. *Nano Today* **2011**, *6*, 42–60. [CrossRef]
15. Urade, A.R.; Lahiri, I.; Suresh, K.S. Graphene Properties, Synthesis and Applications: A Review. *JOM* **2022**, *75*, 614–630. [CrossRef]
16. Han, Q.; Pang, J.; Li, Y.; Sun, B.; Ibarlucea, B.; Liu, X.; Gemming, T.; Cheng, Q.; Zhang, S.; Liu, H.; et al. Graphene Biodevices for Early Disease Diagnosis Based on Biomarker Detection. *ACS Sens.* **2021**, *6*, 3841–3881. [CrossRef]
17. Rao, C.N.R.; Sood, A.K.; Subrahmanyam, K.S.; Govindaraj, A. Graphene: The New Two-Dimensional Nanomaterial. *Angew. Chem. Int. Ed.* **2009**, *48*, 7752–7777. [CrossRef]
18. Marconcini, P.; Macucci, M. Approximate Calculation of the Potential Profile in a Graphene-based Device. *IET Circuits Devices Syst.* **2015**, *9*, 30–38. [CrossRef]
19. Peña-Bahamonde, J.; Nguyen, H.N.; Fanourakis, S.K.; Rodrigues, D.F. Recent Advances in Graphene-Based Biosensor Technology with Applications in Life Sciences. *J. Nanobiotechnol* **2018**, *16*, 75. [CrossRef]
20. Hwang, M.T.; Heiranian, M.; Kim, Y.; You, S.; Leem, J.; Taqieddin, A.; Faramarzi, V.; Jing, Y.; Park, I.; van der Zande, A.M.; et al. Ultrasensitive Detection of Nucleic Acids Using Deformed Graphene Channel Field Effect Biosensors. *Nat. Commun.* **2020**, *11*, 1543. [CrossRef]
21. Béraud, A.; Sauvage, M.; Bazán, C.M.; Tie, M.; Bencherif, A.; Bouilly, D. Graphene Field-Effect Transistors as Bioanalytical Sensors: Design, Operation and Performance. *Analyst* **2021**, *146*, 403–428. [CrossRef] [PubMed]
22. Fu, W.; Jiang, L.; van Geest, E.P.; Lima, L.M.C.; Schneider, G.F. Sensing at the Surface of Graphene Field-Effect Transistors. *Adv. Mater.* **2016**, *29*, 1603610. [CrossRef] [PubMed]
23. Afsahi, S.; Lerner, M.B.; Goldstein, J.M.; Lee, J.; Tang, X.; Bagarozzi, D.A.; Pan, D.; Locascio, L.; Walker, A.; Barron, F.; et al. Novel Graphene-Based Biosensor for Early Detection of Zika Virus Infection. *Biosens. Bioelectron.* **2018**, *100*, 85–88. [CrossRef] [PubMed]
24. Vamsi Krsihna, B.; Gangadhar, A.; Ravi, S.; Mohan, D.; Panigrahy, A.K.; Rajeswari, V.R.; Prakash, M.D. A Highly Sensitive Graphene-Based Field Effect Transistor for the Detection of Myoglobin. *Silicon* **2022**, *14*, 11741–11748. [CrossRef]
25. Geim, A.K.; Novoselov, K.S. The Rise of Graphene. *Nat. Mater.* **2007**, *6*, 183–191. [CrossRef] [PubMed]
26. Burson, K.M.; Cullen, W.R.; Adam, S.; Dean, C.; Watanabe, K.; Taniguchi, T.; Kim, P.; Fuhrer, M.S. Direct Imaging of Charged Impurity Density in Common Graphene Substrates. *Nano Lett.* **2013**, *13*, 3576–3580. [CrossRef] [PubMed]
27. Li, M.; Liu, D.; Wei, D.; Song, X.; Wei, D.; Wee, A.T.S. Controllable Synthesis of Graphene by Plasma-Enhanced Chemical Vapor Deposition and Its Related Applications. *Adv. Sci.* **2016**, *3*, 1600003. [CrossRef]
28. McCreary, A.; Kazakova, O.; Jariwala, D.; Al Balushi, Z.Y. An Outlook into the Flat Land of 2D Materials beyond Graphene: Synthesis, Properties and Device Applications. *2D Mater.* **2020**, *8*, 013001. [CrossRef]
29. Whitener, K.E.; Sheehan, P.E. Graphene Synthesis. *Diam. Relat. Mater.* **2014**, *46*, 25–34. [CrossRef]
30. Muñoz, R.; Gómez-Aleixandre, C. Review of CVD Synthesis of Graphene. *Chem. Vap. Depos.* **2013**, *19*, 297–322. [CrossRef]
31. Liang, X.; Sperling, B.A.; Calizo, I.; Cheng, G.; Hacker, C.A.; Zhang, Q.; Obeng, Y.; Yan, K.; Peng, H.; Li, Q.; et al. Toward Clean and Crackless Transfer of Graphene. *ACS Nano* **2011**, *5*, 9144–9153. [CrossRef] [PubMed]
32. Haigh, S.J.; Gholinia, A.; Jalil, R.; Romani, S.; Britnell, L.; Elias, D.C.; Novoselov, K.S.; Ponomarenko, L.A.; Geim, A.K.; Gorbachev, R. Cross-Sectional Imaging of Individual Layers and Buried Interfaces of Graphene-Based Heterostructures and Superlattices. *Nat. Mater.* **2012**, *11*, 764–767. [CrossRef] [PubMed]
33. Malesevic, A.; Vitchev, R.; Schouteden, K.; Volodin, A.; Zhang, L.; Tendeloo, G.V.; Vanhulsel, A.; Haesendonck, C.V. Synthesis of Few-Layer Graphene via Microwave Plasma-Enhanced Chemical Vapour Deposition. *Nanotechnology* **2008**, *19*, 305604. [CrossRef] [PubMed]
34. Qi, Y.; Deng, B.; Guo, X.; Chen, S.; Gao, J.; Li, T.; Dou, Z.; Ci, H.; Sun, J.; Chen, Z.; et al. Switching Vertical to Horizontal Graphene Growth Using Faraday Cage-Assisted PECVD Approach for High-Performance Transparent Heating Device. *Adv. Mater.* **2018**, *30*, 1704839. [CrossRef]
35. Meškinis, Š.; Vasiliauskas, A.; Guobienė, A.; Talaikis, M.; Niaura, G.; Gudaitis, R. The Direct Growth of Planar and Vertical Graphene on Si(100) via Microwave Plasma Chemical Vapor Deposition: Synthesis Conditions Effects. *RSC Adv.* **2022**, *12*, 18759–18772. [CrossRef]

36. Nguyen, P.; Behura, S.K.; Seacrist, M.R.; Berry, V. Intergrain Diffusion of Carbon Radical for Wafer-Scale, Direct Growth of Graphene on Silicon-Based Dielectrics. *ACS Appl. Mater. Interfaces* **2018**, *10*, 26517–26525. [CrossRef]
37. Chugh, S.; Mehta, R.; Lu, N.; Dios, F.D.; Kim, M.J.; Chen, Z. Comparison of Graphene Growth on Arbitrary Non-Catalytic Substrates Using Low-Temperature PECVD. *Carbon* **2015**, *93*, 393–399. [CrossRef]
38. Shin, J.H.; Kim, S.H.; Kwon, S.S.; Park, W.I. Direct CVD Growth of Graphene on Three-Dimensionally-Shaped Dielectric Substrates. *Carbon* **2018**, *129*, 785–789. [CrossRef]
39. Luo, J.; Wang, J.; Xia, F.; Huang, X. Catalyst-Free Synthesis of Few-Layer Graphene Films on Silicon Dioxide/Si Substrates Using Ethylene Glycol by Chemical Vapor Deposition. *Mater. Res. Express* **2018**, *6*, 035602. [CrossRef]
40. Du, L.; Yang, L.; Hu, Z.; Zhang, J.; Huang, C.; Sun, L.; Wang, L.; Wei, D.; Chen, G.; Lu, W. Thickness-Controlled Direct Growth of Nanographene and Nanographite Film on Non-Catalytic Substrates. *Nanotechnology* **2018**, *29*, 215711. [CrossRef]
41. Xu, S.; Man, B.; Jiang, S.; Yue, W.; Yang, C.; Liu, M.; Chen, C.; Zhang, C. Direct Growth of Graphene on Quartz Substrates for Label-Free Detection of Adenosine Triphosphate. *Nanotechnology* **2014**, *25*, 165702. [CrossRef] [PubMed]
42. Wei, D.; Peng, L.; Li, M.; Mao, H.; Niu, T.; Han, C.; Chen, W.; Thye, A. Low Temperature Critical Growth of High Quality Nitrogen Doped Graphene on Dielectrics by Plasma-Enhanced Chemical Vapor Deposition. *ACS Nano* **2015**, *9*, 164–171. [CrossRef] [PubMed]
43. Gudaitis, R.; Lazauskas, A.; Jankauskas, Š.; Meškinis, Š. Catalyst-Less and Transfer-Less Synthesis of Graphene on Si(100) Using Direct Microwave Plasma Enhanced Chemical Vapor Deposition and Protective Enclosures. *Materials* **2020**, *13*, 5630. [CrossRef] [PubMed]
44. Jankauskas, Š.; Gudaitis, R.; Vasiliauskas, A.; Guobienė, A.; Meškinis, Š. The Graphene Structure's Effects on the Current-Voltage and Photovoltaic Characteristics of Directly Synthesized Graphene/N-Si(100) Diodes. *Nanomaterials* **2022**, *12*, 1640. [CrossRef]
45. Meškinis, Š.; Vasiliauskas, A.; Gudaitis, R.; Andrulevičius, M.; Guobienė, A. Direct Graphene Synthesis on Si(100) by Inductively Coupled Plasma Beam Source. *Appl. Surf. Sci.* **2022**, *580*, 152265. [CrossRef]
46. Wu, G.; Meyyappan, M.; Wai, K. Graphene Field-Effect Transistors-Based Biosensors for Escherichia Coli Detection. In Proceedings of the 16th International Conference on Nanotechnology (IEEE-NANO), Sendai, Japan, 22–25 August 2016. [CrossRef]
47. Ferrari, A.C.; Basko, D.M. Raman Spectroscopy as a Versatile Tool for Studying the Properties of Graphene. *Nat. Nanotechnol.* **2013**, *8*, 235–246. [CrossRef]
48. Lee, J.E.; Ahn, G.; Shim, J.; Lee, Y.S.; Ryu, S. Optical Separation of Mechanical Strain from Charge Doping in Graphene. *Nat. Commun.* **2012**, *3*, 1024. [CrossRef]
49. Hwang, J.-S.; Lin, Y.-H.; Hwang, J.-Y.; Chang, R.; Chattopadhyay, S.; Chen, C.-J.; Chen, P.; Chiang, H.-P.; Tsai, T.-R.; Chen, L.-C.; et al. Imaging Layer Number and Stacking Order through Formulating Raman Fingerprints Obtained from Hexagonal Single Crystals of Few Layer Graphene. *Nanotechnology* **2012**, *24*, 015702. [CrossRef]
50. Eckmann, A.; Felten, A.; Mishchenko, A.; Britnell, L.; Krupke, R.; Novoselov, K.S.; Casiraghi, C. Probing the Nature of Defects in Graphene by Raman Spectroscopy. *Nano Lett.* **2012**, *12*, 3925–3930. [CrossRef]
51. Tuinstra, F.; Koenig, J.L. Raman Spectrum of Graphite. *J. Chem. Phys.* **1970**, *53*, 1126–1130. [CrossRef]
52. Knight, D.; White, W.B. Characterization of Diamond Films by Raman Spectroscopy. *J. Mater. Res.* **1989**, *4*, 385–393. [CrossRef]
53. Mallet-Ladeira, P.; Puech, P.; Toulouse, C.; Cazayous, M.; Ratel-Ramond, N.; Weisbecker, P.; Vignoles, G.L.; Monthioux, M. A Raman Study to Obtain Crystallite Size of Carbon Materials: A Better Alternative to the Tuinstra–Koenig Law. *Carbon* **2014**, *80*, 629–639. [CrossRef]
54. Casiraghi, C. Probing Disorder and Charged Impurities in Graphene by Raman Spectroscopy. *Phys. Status Solidi (RRL)-Rapid Res. Lett.* **2009**, *3*, 175–177. [CrossRef]
55. Neumann, C.; Reichardt, S.; Venezuela, P.; Drögeler, M.; Banszerus, L.; Schmitz, M.; Watanabe, K.; Taniguchi, T.; Mauri, F.; Beschoten, B.; et al. Raman Spectroscopy as Probe of Nanometre-Scale Strain Variations in Graphene. *Nat. Commun.* **2015**, *6*, 8429. [CrossRef]
56. Bissett, M.A.; Tsuji, M.; Ago, H. Mechanical Strain of Chemically Functionalized Chemical Vapor Deposition Grown Graphene. *J. Phys. Chem. C* **2013**, *117*, 3152–3159. [CrossRef]
57. Kim, S.; Ryu, S. Thickness-Dependent Native Strain in Graphene Membranes Visualized by Raman Spectroscopy. *Carbon* **2016**, *100*, 283–290. [CrossRef]
58. Armano, A.; Buscarino, G.; Cannas, M.; Gelardi, F.M.; Giannazzo, F.; Schilirò, E.; Agnello, S. Monolayer Graphene Doping and Strain Dynamics Induced by Thermal Treatments in Controlled Atmosphere. *Carbon* **2018**, *127*, 270–279. [CrossRef]
59. Lee, U.; Han, Y.; Lee, S.H.; Kim, J.S.; Lee, Y.H.; Kim, U.J.; Son, H. Time Evolution Studies on Strain and Doping of Graphene Grown on a Copper Substrate Using Raman Spectroscopy. *ACS Nano* **2019**, *14*, 919–926. [CrossRef]
60. Yao, Y.; Ren, L.; Sitian, G.; Li, S. Histogram Method for Reliable Thickness Measurements of Graphene Films Using Atomic Force Microscopy (AFM). *J. Mater. Sci. Technol.* **2017**, *33*, 815–820. [CrossRef]
61. Ahmad, M.; An, H.; Kim, Y.S.; Lee, J.H.; Jung, J.; Chun, S.-H.; Seo, Y. Nanoscale Investigation of Charge Transport at the Grain Boundaries and Wrinkles in Graphene Film. *Nanotechnology* **2012**, *23*, 285705. [CrossRef]
62. Kybert, N.J.; Han, G.H.; Lerner, M.B.; Dattoli, E.N.; Esfandiar, A.; Charlie Johnson, A.T. Scalable Arrays of Chemical Vapor Sensors Based on DNA-Decorated Graphene. *Nano Res.* **2013**, *7*, 95–103. [CrossRef]
63. Champlain, J.G. A First Principles Theoretical Examination of Graphene-Based Field Effect Transistors. *J. Appl. Phys.* **2011**, *109*, 084515. [CrossRef]

64. Chen, Y.; Sun, J.; Gao, J.; Du, F.; Han, Q.; Nie, Y.; Chen, Z.; Bachmatiuk, A.; Priydarshi, M.K.; Ma, D.; et al. Growing Uniform Graphene Disks and Films on Molten Glass for Heating Devices and Cell Culture. *Adv. Mater.* **2015**, *27*, 7839–7846. [CrossRef] [PubMed]
65. Goniszewski, S.; Adabi, M.; Shaforost, O.; Hanham, S.M.; Hao, L.; Klein, N. Correlation of P-Doping in CVD Graphene with Substrate Surface Charges. *Sci. Rep.* **2016**, *6*, 22858. [CrossRef]
66. Eriksson, J.; Puglisi, D.; Vasiliauskas, R.; Spetz, A.L.; Yakimova, R. Thickness Uniformity and Electron Doping in Epitaxial Graphene on SiC. *Mater. Sci. Forum* **2013**, *740–742*, 153–156. [CrossRef]
67. Jee, H.; Jin, K.-H.; Han, J.-H.; Hwang, H.-N.; Jhi, S.-H.; Kim, Y.D.; Hwang, C.-C. Controlling the Self-Doping of Epitaxial Graphene on SiC via Ar Ion Treatment. *Phys. Rev. B* **2011**, *84*, 075457. [CrossRef]
68. Banszerus, L.; Janssen, H.; Otto, M.; Epping, A.; Taniguchi, T.; Watanabe, K.; Beschoten, B.; Neumaier, D.; Stampfer, C. Identifying Suitable Substrates for High-Quality Graphene-Based Heterostructures. *2D Mater.* **2017**, *4*, 025030. [CrossRef]
69. Kang, Y.-J.; Kang, J.; Chang, K.J. Electronic structure of graphene and doping effect on SiO_2. *Phys. Rev. B* **2008**, *78*, 115404. [CrossRef]
70. Wittmann, S.; Aumer, F.; Wittmann, D.; Pindl, S.; Wagner, S.; Gahoi, A.; Reato, E.; Belete, M.; Kataria, S.; Lemme, M.C. Dielectric Surface Charge Engineering for Electrostatic Doping of Graphene. *ACS Appl. Electron. Mater.* **2020**, *2*, 1235–1242. [CrossRef]
71. Shi, Y.; Dong, X.; Chen, P.; Wang, J.; Li, L.-J. Effective Doping of Single-Layer Graphene from Underlying SiO_2. *Phys. Rev. B* **2009**, *79*, 115402. [CrossRef]
72. Kim, J.-S.; Jang, Y.; Ku, G.M.; Kim, S.-H.; Lee, E.-H.; Cho, K.; Lim, K.; Lee, W.H. Liquid Coplanar-Gate Organic/Graphene Hybrid Electronics for Label-Free Detection of Single and Double-Stranded DNA Molecules. *Org. Electron.* **2018**, *62*, 163–167. [CrossRef]
73. Zhu, Y.; Hao, Y.; Adogla, E.A.; Yan, J.; Li, D.; Xu, K.; Wang, Q.; Hone, J.; Lin, Q. A Graphene-Based Affinity Nanosensor for Detection of Low-Charge and Low-Molecular-Weight Molecules. *Nanoscale* **2016**, *8*, 5815–5819. [CrossRef] [PubMed]
74. Bao, L.; Deng, W.; Huang, B.; Gao, H.; Liu, J.; Ren, L.; Wei, Q.; Yu, P.; Xu, Y.; Qi, F.; et al. The Pathogenicity of SARS-CoV-2 in HACE2 Transgenic Mice. *Nature* **2020**, *583*, 830–833. [CrossRef] [PubMed]
75. Lan, J.; Ge, J.; Yu, J.; Shan, S.; Zhou, H.; Fan, S.; Zhang, Q.; Shi, X.; Wang, Q.; Zhang, L.; et al. Structure of the SARS-CoV-2 Spike Receptor-Binding Domain Bound to the ACE2 Receptor. *Nature* **2020**, *581*, 215–220. [CrossRef] [PubMed]
76. Shang, J.; Ye, G.; Shi, K.; Wan, Y.; Luo, C.; Aihara, H.; Geng, Q.; Auerbach, A.; Li, F. Structural Basis of Receptor Recognition by SARS-CoV-2. *Nature* **2020**, *581*, 221–224. [CrossRef] [PubMed]
77. Lu, J.; Sun, P.D. High Affinity Binding of SARS-CoV-2 Spike Protein Enhances ACE2 Carboxypeptidase Activity. *J. Biol. Chem.* **2020**, *295*, 18579–18588. [CrossRef]
78. Veldhoven, V.; Alexander-Webber, J.A.; Sagade, A.A.; Braeuninger-Weimer, P.; Hofmann, S. Electronic Properties of CVD Graphene: The Role of Grain Boundaries, Atmospheric Doping, and Encapsulation by ALD. *Basic Solid State Phys.* **2016**, *253*, 2321–2325. [CrossRef]
79. Salehi-Khojin, A.; Estrada, D.; Lin, K.Y.; Bae, M.-H.; Xiong, F.; Pop, E.; Masel, R.I. Polycrystalline Graphene Ribbons as Chemiresistors. *Adv. Mater.* **2011**, *24*, 53–57. [CrossRef]
80. Yasaei, P.; Kumar, B.; Hantehzadeh, R.; Kayyalha, M.; Baskin, A.; Repnin, N.; Wang, C.; Klie, R.F.; Chen, Y.P.; Král, P.; et al. Chemical Sensing with Switchable Transport Channels in Graphene Grain Boundaries. *Nat. Commun.* **2014**, *5*, 4911. [CrossRef]
81. Hu, Z.; Sinha, D.; Lee, J.H.; Liehr, M. Substrate Dielectric Effects on Graphene Field Effect Transistors. *J. Appl. Phys.* **2014**, *115*, 194507. [CrossRef]
82. Ji, E.; Kim, M.J.; Lee, J.-Y.; Sung, D.; Kim, N.; Park, J.-W.; Hong, S.; Lee, G.-H. Substrate Effect on Doping and Degradation of Graphene. *Carbon* **2021**, *184*, 651–658. [CrossRef]
83. Kim, S.; Kwak, D.H.; Choi, I.; Hwang, J.; Kwon, B.; Lee, E.; Ye, J.; Lim, H.; Cho, K.; Chung, H.-J.; et al. Enhanced Gas Sensing Properties of Graphene Transistor by Reduced Doping with Hydrophobic Polymer Brush as a Surface Modification Layer. *ACS Appl. Mater. Interfaces* **2020**, *12*, 55493–55500. [CrossRef] [PubMed]
84. Lee, W.H.; Park, J.; Kim, Y.; Kim, K.S.; Hong, B.H.; Cho, K. Control of Graphene Field-Effect Transistors by Interfacial Hydrophobic Self-Assembled Monolayers. *Adv. Mater.* **2011**, *23*, 3460–3464. [CrossRef] [PubMed]

Disclaimer/Publisher's Note: The statements, opinions and data contained in all publications are solely those of the individual author(s) and contributor(s) and not of MDPI and/or the editor(s). MDPI and/or the editor(s) disclaim responsibility for any injury to people or property resulting from any ideas, methods, instructions or products referred to in the content.

3 straipsnis

Straipsnio pavadinimas	*Influence of synthesis parameters on structure and characteristics of the graphene grown using PECVD on sapphire substrate*
Straipsnio bendraautoriai	*Šarūnas Jankauskas; Šarūnas Meškinis; Nerija Žurauskienė; Asta Guobienė*
Leidėjas, žurnalo pavadinimas	*MDPI, Nanomaterials*
Metai	*2024*

nanomaterials

MDPI

Article

Influence of Synthesis Parameters on Structure and Characteristics of the Graphene Grown Using PECVD on Sapphire Substrate

Šarūnas Jankauskas [1], Šarūnas Meškinis [1], Nerija Žurauskienė [2] and Asta Guobienė [1,*]

[1] Institute of Materials Science, Kaunas University of Technology, K. Baršausko St. 59, LT-51423 Kaunas, Lithuania; sarunas.jankauskas@ktu.lt (Š.J.); sarunas.meskinis@ktu.lt (Š.M.)
[2] Department of Functional Materials and Electronics, Center for Physical Sciences and Technology, Saulėtekio av. 3, LT-10257 Vilnius, Lithuania; nerija.zurauskiene@ftmc.lt
* Correspondence: asta.guobiene@ktu.lt

Abstract: The high surface area and transfer-less growth of graphene on dielectric materials is still a challenge in the production of novel sensing devices. We demonstrate a novel approach to graphene synthesis on a C-plane sapphire substrate, involving the microwave plasma-enhanced chemical vapor deposition (MW-PECVD) technique. The decomposition of methane, which is used as a precursor gas, is achieved without the need for remote plasma. Raman spectroscopy, atomic force microscopy and resistance characteristic measurements were performed to investigate the potential of graphene for use in sensing applications. We show that the thickness and quality of graphene film greatly depend on the CH_4/H_2 flow ratio, as well as on chamber pressure during the synthesis. By varying these parameters, the intensity ratio of Raman D and G bands of graphene varied between ~1 and ~4, while the 2D to G band intensity ratio was found to be 0.05–0.5. Boundary defects are the most prominent defect type in PECVD graphene, giving it a grainy texture. Despite this, the samples exhibited sheet resistance values as low as 1.87 kΩ/□. This reveals great potential for PECVD methods and could contribute toward efficient and straightforward graphene growth on various substrates.

Keywords: graphene; PECVD; sapphire; sheet resistance

check for updates

Citation: Jankauskas, Š.; Meškinis, Š.; Žurauskienė, N.; Guobienė, A. Influence of Synthesis Parameters on Structure and Characteristics of the Graphene Grown Using PECVD on Sapphire Substrate. *Nanomaterials* **2024**, *14*, 1635. https://doi.org/10.3390/nano14201635

Academic Editor: Tomonori Ohba

Received: 10 September 2024
Revised: 8 October 2024
Accepted: 10 October 2024
Published: 12 October 2024

Copyright: © 2024 by the authors. Licensee MDPI, Basel, Switzerland. This article is an open access article distributed under the terms and conditions of the Creative Commons Attribution (CC BY) license (https://creativecommons.org/licenses/by/4.0/).

1. Introduction

High charge carrier mobility, mechanical strength and optical transparency are the properties that make graphene standout from other materials developed for high-speed electronics [1], solar cell [2] and sensor [3] applications. For example, the graphene/dielectric interface shows a lot of promise for sensing devices. Temperature sensors based on the graphene/SiN configuration perform excellently and have a very fast response and mechanical stability [4]. Graphene can also be used in magnetoresistance sensors, which are optimal in the 0.1–20 T range, when grown on polycrystalline Al_2O_3 substrates [5]. The peculiar nature of graphene in humidity and carbon dioxide sensing was also investigated when SiO_2 and sapphire substrates were selected [6]. It has been shown that device performance also relies on the substrate used, not only the quality of the graphene. Despite this, most concepts utilize exfoliated graphene, due to its quality (low defect density) [3,7,8]. However, exfoliation fails when large-area deposition is required [9,10]. Chemical vapor deposition (CVD) synthesis methods are far superior when it comes to graphene scalability [11–13]. To maintain the pristine quality of graphene in terms of defect density and domain (flake) size, most CVD methods focus on synthesis that requires Cu or other types of metal catalyst films [14–16]. The extra transfer step has to be taken into account for the proper utilization of graphene on desired substrates. The transfer of graphene from catalytic surfaces onto various substrates is quite complicated [17,18] and usually results in unwanted contamination, cracking or even the destruction of the initial graphene film [19,20]. Changing the growth

parameters and experimenting with different substrates might produce better results. For example, it was shown that graphene can be grown directly on SiC, with high charge carrier mobility and the ability to tune graphene properties by varying the doping amounts [21]. Similarly, there have been attempts to synthesize graphene on a Si(100) and SiO_2 substrate directly, using plasma-enhanced chemical vapor deposition (PECVD) [22–24]. In this way, graphene synthesis temperatures were significantly reduced (below 700 °C). However, directly synthesized graphene is nanocrystalline, and boundary defects dominate such samples [25,26].

During the last decade, there have been attempts to synthesize graphene on Al_2O_3 substrates [27–31], and particular attention was given to C-plane sapphire substrates [32–34]. Having a catalytic nature, C-plane sapphire ensures a more stable growth process, eliminates the unwanted grain boundary effects and significantly increases the size of graphene crystallites, due to the naturally matched hexagonal graphene and sapphire structures [35]. Recent reports indicate the enormous potential of graphene/C-plane sapphire interface. Wafer-scale, highly oriented graphene, exhibiting high carrier mobility and low sheet resistance, was directly grown on sapphire [36]. Sapphire is also an excellent substrate for GaN remote epitaxy assisted by a graphene interlayer; in this case, directly grown graphene is more beneficial than transferred graphene [37]. It has been recently shown that graphene synthesis can also be activated using Al-enriched C-plane sapphire substrates [38]. However, high quality films have only been produced using CVD, where temperatures well above 1000 °C are required [36]. The use of the PECVD would allow us to substantially decrease the temperature of synthesis. However, only a handful of studies have been performed on direct catalyst-less graphene growth on sapphire substrate using PECVD [39–41]. The use of PECVD provides an additional opportunity to control the graphene synthesis conditions. However, in the case of graphene PECVD synthesis on sapphire, only the effects of hydrogen and acetylene gas flows on the graphene structure were studied [39].

In this research, the effects of the graphene synthesis pressure and the ratio of hydrogen to methane gas flows were investigated. We show a way to couple both substrate catalytic effects and low-temperature synthesis mechanisms to make graphene growth on C-plane sapphire substrates more efficient and cost-effective. The small chamber size and the ability to change the synthesis conditions in a wide range of parameters provide versatility for further industrial development prospects. Paired with the ability to produce fairly low-resistance graphene films, this method could be considered as a viable option for sensing applications.

2. Materials and Methods

The synthesis of graphene/C-plane sapphire samples was performed using a microwave PECVD system, Cyrannus (Innovative Plasma Systems (Iplas) GmbH, Troisdorf, Germany). Monocrystalline, double-side-polished, 10 × 10 × 0.5 mm C-plane (0001) sapphire (AdValue Technology, Tuscon, AZ, USA) was used as a substrate for all samples (Figure 1a). The synthesis was carried out in a similar way to our previous work [42,43]. A schematic of our growth stages is depicted in Figure 1d. A mixture of hydrogen and methane was used as the precursor gas in all cases. Initially, plasma was ignited using hydrogen gas until the target temperature was reached. After that, a 10 min. H_2 plasma annealing phase followed , where the flow of H_2 was set to 200 sccm. Hereinafter, the H_2 flow was reduced, and methane was introduced into the chamber according to the selected growth condition. We produced two separate sample sets. A set, named F, consisted of samples where different CH_4 gas flows were used, keeping the sum of CH_4 and H_2 gas flows at 100 sccm and leaving other parameters fixed. Another set, named P, consisted of samples where the pressure was changed for each synthesis, while maintaining the CH_4/H_2 gas-flow ratio (35/65 sccm) and keeping the other parameters fixed. Additionally, three more samples were synthesized in order to populate the gas-flow ratio and pressure-space colormaps (set named S). The synthesis conditions of all graphene/C-plane sapphire

samples can be seen in Table 1. To prevent excessive direct plasma action during each graphene synthesis process, C-plane sapphire substrates were covered with a protective steel enclosure, as seen in Figure 1a.

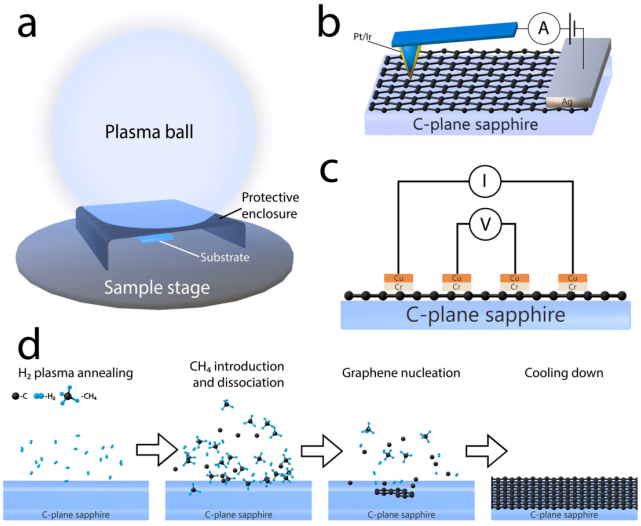


Figure 1. (**a**) Schematic of the PECVD chamber during graphene synthesis on C-sapphire substrate, (**b**) illustration of C-AFM analysis, (**c**) illustration of four-point probe analysis for sheet resistance measurement and (**d**) schematic representation of PECVD graphene synthesis stages. Atom spacing, electrode placement and dimensions are not to scale for clarity.

Table 1. Synthesis conditions for investigated graphene/C-plane sapphire samples. Note that the sample F3P2 belongs to the F and P sets.

Set	Sample No.	Power, kW	H_2, sccm	CH_4, sccm	p, mBar	T, °C	t, min.
F	F1	0.7	75	25	10	700	60
	F2	0.7	70	30	10	700	60
	F3P2	0.7	65	35	10	700	60
	F4	0.7	60	40	10	700	60
	F5	0.7	55	45	10	700	60
P	P1	0.7	65	35	6	700	60
	F3P2	0.7	65	35	10	700	60
	P3	0.7	65	35	15	700	60
	P4	0.7	65	35	20	700	60
	P5	0.7	65	35	25	700	60
S	S1	0.7	80	20	6	700	60
	S2	0.7	75	25	6	700	60
	S3	0.7	75	25	25	700	60

The graphene structure was analyzed using Raman scattering spectroscopy (Renishaw inVia microscope, Wotton-under-Edge, UK). The excitation wavelength for all measure-

ments was 532 nm, and a beam power of 1.5 mW was used. Five measurements were performed for each sample just after the synthesis of graphene films, to average the structural effects across the sample. For the detection of graphene fingerprint, the main D peak at ~1350 cm^{-1}, G peak at ~1600 cm^{-1} and 2D peak at ~2700 cm^{-1} were analyzed and fitted using a Lorentzian function [44]. Defects were analyzed using the D and G peak intensity ratio (I_D/I_G) [44–46], while the thickness of graphene was determined using the 2D and G peak intensity ratio (I_{2D}/I_G) [47]. Strain and doping were investigated using the position and full-width at half maximum (FWHM) of the peaks [46,48].

The surface conductivity and morphology of the directly synthesized graphene sheets were analyzed by atomic force microscopy (NanoWizard®3, JPK Instruments, Bruker Nano GmbH, Berlin, Germany). The morphology images of each sample were collected using an ACTA (Applied NanoStructures, Inc., Mountain View, CA, USA) probe operating in tapping mode. The probe tip radius of curvature was 6 nm. The conductivity was measured using contact-mode conductive atomic force microscopy (C-AFM) with a metal-coated tip ANSCM-PT (AppNano, Mountain View, CA, USA) silicon probe with a thin layer of Pt/Ir coating (thickness (nm) -25 ± 5) on both the reflex and tip sides of the probe. ANSCM probes with a 1.6 spring constant are ideal for use in C-AFM mode (as shown in Figure 1b). Tip shape: tetrahedral; tip ROC (nm): 30; height (μm): 14–16; frequency (kHz): 61. The electrical current was measured as a function of the applied bias voltage (−10–10 mV). All the measurements were performed at room temperature in the air [49].

To test resistive characteristics, samples F2, F5, P1, P5 were selected. A horizontal row of rectangular 2 × 1 mm contacts, which are spaced 1 mm apart, was deposited on the graphene/C-plane sapphire. Electrical contacts were made from Cr and Cu with thicknesses of 20 and 200 nm, respectively. The samples were analyzed with the GOM-805 DC Milli-Ohm Meter (GW Instek, New Taipei City, Taiwan), using the four-point probe method at ambient pressure and room temperature, as shown in Figure 1c. The acquired resistance values were corrected for the geometry and arrangement of the contacts.

3. Results

First, we compare graphene synthesized using MW-PECVD on a C-plane Al_2O_3, along with graphene grown on SiO_2. Most of the samples grown on C-plane sapphire exhibited a wide luminescence background at ~2000 cm^{-1}, which had to be subtracted. It was concluded that the substrate was the source of the background in all Raman spectra (Figure S1). The typical, baseline-corrected Raman spectra of the samples grown on C-plane sapphire can be seen in Figure 2a, along with a typical spectrum of graphene synthesized on SiO_2. Graphene fingerprints are clearly seen, with 2D (~2690 cm^{-1}), G (~1595 cm^{-1}) and D (~1350 cm^{-1}) peaks visible in all spectra. This has also been reported in similar studies, in which graphene was synthesized on Al_2O_3 [27,50,51] and SiO_2 substrates [52–54]. An apparent blueshift of the D and G peaks is visible in the graphene grown on C-plane sapphire as compared to the graphene grown on SiO_2. Furthermore, an in-depth analysis of the graphene synthesized on C-plane sapphire was performed. The thickness of the films can be discovered from the I_{2D}/I_G relation [55,56]. In our case, when the CH_4/H_2 ratio of 35/65 sccm was used and the pressure was set to 6 mBar, I_{2D}/I_G was 0.68, which indicates a few-layered graphene film as compared to the case of 25 mBar, where I_{2D}/I_G was 0.09, indicating a multilayer graphene film. A summary of I_{2D}/I_G and I_D/I_G with respect to different gas-flow ratios and chamber pressures used is shown in Figure 2b,d. The contour plot was interpolated from the points, with two cross sections indicating pressure and precursor gas-flow ratio parameter sweeps (Figure 2b,d: green and blue points, along with the red intersecting point). Increasing pressure ultimately increases I_{2D}/I_G, and a similar increase is observed with increased CH_4/H_2 gas flow. We also consider the I_D/I_G ratio, which reveals grain boundary defects [57] (Figure 2d). We show that the number of defects increases with a decrease in pressure and the CH_4/H_2 flow ratio, and it correlates linearly with I_{2D}/I_G (Figure 2c). A large increment in the growth conditions introduced a lot of variability in our reported I_D/I_G and I_{2D}/I_G values. The distribution of values across a

single sample may be associated with the inability to control certain synthesis elements, such as plasma homogeneity and substrate placement in the chamber prior to growth. This relation suggests that graphene grows more disorderly when the graphene thickness is low. As we approach thicker graphene films, the structure of samples tends to be more uniform. This might be attributed to higher amounts of boundary defects, which indicate a rather polycrystalline graphene film, as previously reported [43]. Similar conclusions can be drawn based on Raman theory [58,59]. When observing the $I_D/I_{D'}$ data with respect to the synthesis conditions used (Figure S2a,b), most of our samples exhibit boundary-like defects associated with the nanocrystalline nature of our samples, where $I_D/I_{D'}$—~3.5. Only when we drastically increase the gas-flow ratio and pressure, the value of $I_D/I_{D'}$ reduces to ~2.6, indicating a superposition of boundary and on-site defects. This could occur due to the increase in the byproducts of dissociation, when the pressure and CH_4 content are higher. When the synthesis pressure is lower, we can see vacancy and boundary defect superposition, which result from the poor nucleation of carbon atoms at the C-plane sapphire surface.

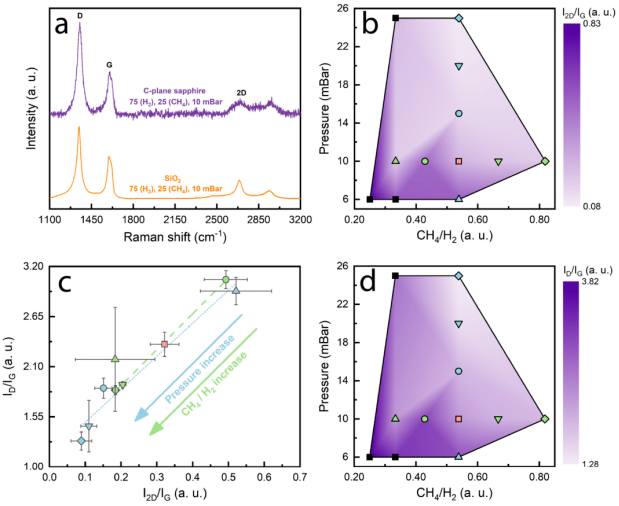


Figure 2. (**a**) Comparison of Raman spectra of PECVD graphene on C−plane sapphire (violet) and SiO_2 (orange), (**b**) colormap of I_{2D}/I_G ratio vs. synthesis parameters, (**c**) I_D/I_G ratio vs. I_{2D}/I_G ratio, (**d**) colormap of I_D/I_G ratio vs. synthesis parameters. The samples were differentiated by shapes and color, where light green represents samples that belong to the F set and light blue represents samples that belong to the P set. Sample F3P2, which belongs to both sets, is colored red. Additional samples were produced (set S) for colormap space expansion.

To assess the effects induced by strain, the 2D peak position and its full width at half maximum ($FWHM_{2D}$) were considered [38,60–62] (Figure 3). Although the distribution of the 2D peak position is broad when the CH_4/H_2 flow ratio of 25/75 is used, there is a clear decrease in the 2D peak position values (from 2702 cm^{-1} to 2694 cm^{-1}) when the precursor gas-flow ratio increases further (Figure 3a). This is in agreement with other reports from similar studies [30,34] and can be attributed to the stress induced in the graphene structure after the deposition process due to the thermal expansion coefficient mismatch [61,62].

$FWHM_{2D}$ is high in all cases, increasing from ~70 cm^{-1} to ~180 cm^{-1} when the CH_4/H_2 flow ratio is increased (Figure 3c). Multilayer graphene must be considered, and the change might be directly related to the increase in carbon species during deposition [63,64]. Ultimately, it shows a non-uniform strain distribution in all of our samples [38]. In contrast, when we increase the chamber pressure, the deviation of the 2D peak position increases, while the values remain similar (Figure 3c). There is no correlation between $FWHM_{2D}$ and changes in chamber pressure, as seen in Figure 3d.

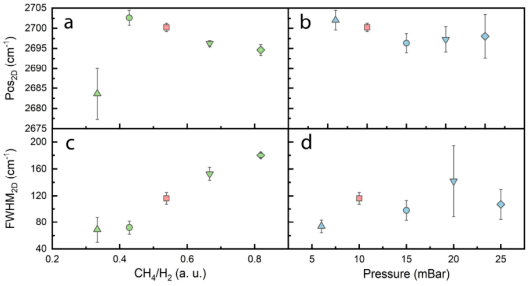


Figure 3. (**a**) Pos_{2D} vs. gas-flow ratio plot, (**b**) Pos_{2D} vs. pressure plot, (**c**) $FWHM_{2D}$ vs. gas-flow ratio plot, (**d**) $FWHM_{2D}$ vs. pressure plot of F and P samples. Conveniently, samples were given the same shapes and colors for distinction.

Furthermore, the effects of strain and doping were investigated using the Pos_{2D} vs. Pos_G plot (Figure 4) [62,65,66]. This established method suggests that most of our graphene samples are undoped or have a slight p-type doping. However, considering that most of our graphene samples are few-layered or thicker, these results may be inconclusive. Despite that, only several samples exhibit a higher Pos_G distribution. Vector decomposition analysis depicts the compressive strain present in most of our samples. Nevertheless, greater thickness might contribute to such observations, since the 2D peak position tends to blueshift with an increasing number of graphene layers [65,66].

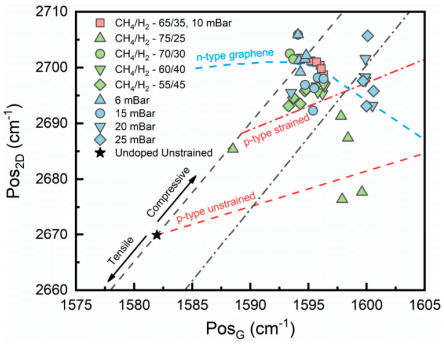


Figure 4. Pos_{2D} vs. Pos_G plot showing vector decomposition analysis of F and P sample sets. Conveniently, samples were given the same shapes and colors for distinction.

The surface morphology of graphene synthesized on C-plane sapphire was studied with atomic force microscopy. Graphene structures are grainy, albeit smooth. The root mean square roughness (R_q) of the samples was rather low, ranging from ~0.09 to 3.18 nm. The roughness of this size indicates the growth of planar graphene. The shared sample in both parameter sweeps had the lowest surface roughness (Figure 5a). It is important to note that the roughness of the pristine C-plane sapphire substrate was ~0.05 nm (Figure S3). The summarized roughness values according to CH_4/H_2 and pressure can be seen in Figure 5b,c, respectively. The produced graphene tends to become rougher with an increase in both the gas-flow ratio and pressure individually. Naturally, above certain gas-flow ratios and pressure threshold values, the surface roughness increases significantly. Low surface roughness was observed to correlate with higher I_{2D}/I_G values; however, it also increased the I_D/I_G ratio (Figure 6). Similar results have previously been observed with the synthesis of graphene performed on a Si(100) substrate [25]. It seems that the quality of graphene on the C-plane sapphire substrate is rather similar to the one that is grown on Si(100) substrate when using the MW-PECVD method. Temperatures well above 700 C might be required to achieve better quality graphene films on C-sapphire substrates, as reported by other studies [36,38]. Nevertheless, lower CH_4 flow and lower pressure favor higher quality graphene synthesis. AFM images of the produced samples can be seen in Figures S4–S12.

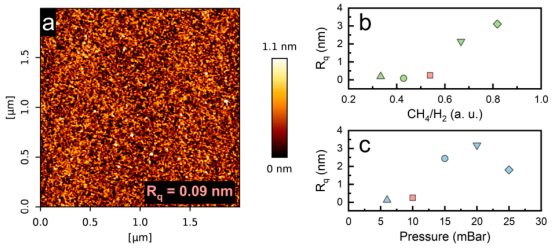


Figure 5. (**a**) Morphology of graphene synthesized using a CH_4/H_2 flow ratio of 35/65 and a pressure of 10 (R_q indicates the root mean square value of surface roughness), (**b**) R_q vs. gas-flow ratio plot, (**c**) R_q vs. pressure plot. The colors and shapes follow the same sample pattern.

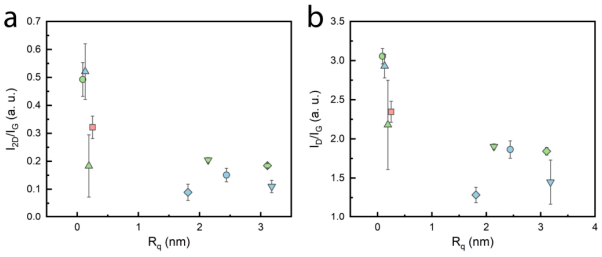


Figure 6. (**a**) Two-dimensional (2D) and G band ratio with respect to surface roughness, (**b**) plot showing correlation with surface roughness. The colors and shapes follow the same sample pattern.

Conductive atomic force microscopy measurements were performed to observe the electrical properties of the graphene films. As mentioned in the experimental section, four samples were analyzed, bearing the highest and lowest I_{2D}/I_G and I_D/I_G ratios (Figure 7).

Interestingly, most of the samples fell under the extremes of the chosen CH_4/H_2 gas-flow ratio and the experimental pressure sets. It seems that the growth conditions had a tremendous impact on the graphene current signal readouts. When the precursor gas-flow ratio was 30/70, the graphene exhibited the lowest current signals out of the four samples that were chosen, with a highest conductivity reaching 2.16 pA. When the gas-flow ratio was increased to 45/55, the current signal increased more than twentyfold, with the highest value being 51.9 pA. On the other hand, increasing the gas-flow ratio ultimately resulted in the thickest graphene sample. This would lead to the conclusion that we do not observe a monolayer, defect-free graphene effects when the thickness is low, knowing the highly conductive nature of pristine graphene [67]. The presence of graphene-like flakes or nanographene [68] could be observed and would explain the thickness-dependent increase in the current signal. We see a similar trend when pressure changes from 6 mBar to 25 mBar, where signal values change from 2.46 to 6.6 pA, respectively. It seems that the decrease in I_{2D}/I_G, seen in Figure 8a, is partly responsible for the increase in current signal. Similarly, the decrease in I_D/I_G also increases the current signal. In principle, higher amounts of intrinsic grain boundary defects should not decrease the charge carrier mobility; however, it could indicate an extrinsic grain boundary effect in our films, or low-symmetry grain boundaries, consisting of tilts and angle changes between the grains, which changes the electronic properties dramatically [69].

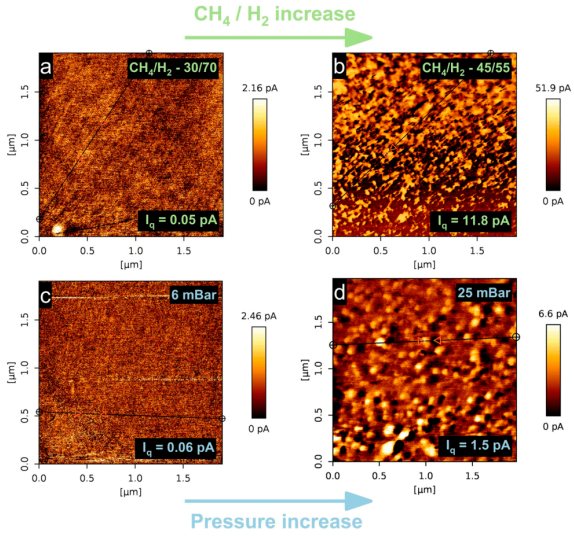


Figure 7. Conductive atomic force microscopy maps of four selected samples with varying synthesis conditions. (**a**) F2 sample, (**b**) F5 sample, (**c**) P1 sample, (**d**) P5 sample. I_q represents the root mean square of surface conductivity values.

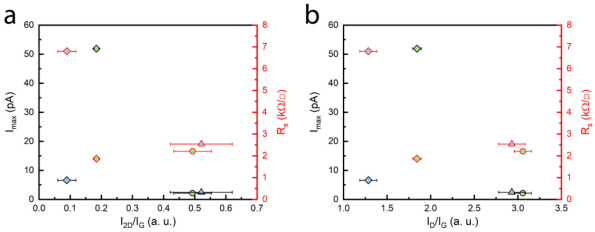


Figure 8. (**a**) Resistance characteristics vs. I_{2D}/I_G plot showing conductance and sheet resistance variation with different thicknesses of graphene, (**b**) resistance characteristics vs. I_D/I_G plot showing conductance and sheet resistance variation based on defects.

The same four samples were further modified by synthesizing four, equally spaced, contacts, as mentioned in the experimental section, to determine the sheet resistance of the graphene films, using the four-point probe method. As seen in Figure 8, we can observe high R_s values when current signals acquired from conductive atomic force microscopy are low and rather low R_s values when current signals are high. In fact, the highest and lowest sheet resistance values were 6.8 kΩ/□ and 1.87 kΩ/□, respectively. The highest R_s value of the four was reported for the sample that was synthesized using a CH_4/H_2 ratio of 35/65 and a chamber pressure of 25 mBar. The lowest sheet resistance was observed when the sample was grown with a 45/55 gas-flow ratio and a chamber pressure of 10 mBar.

Our reported sheet resistance values are similar when compared to graphene synthesis on sapphire using other methods (see Table 2). It is evident that this growth method exhibits a lot of versality with respect to structure and resistance characteristics, when considering graphene synthesis on Al_2O_3 for sensor applications. Further improvements in this synthesis method are necessary to obtain higher quality graphene films. The variability that is introduced in the structure across a film could be mitigated when plasma mechanisms occurring in the chamber are thoroughly examined. To fully understand the effects of protective enclosures, different types of enclosure materials must also be investigated.

Table 2. Sheet resistances measured for graphene on sapphire substrates.

Sample No.	Highest Surface Point, nm	Sheet Resistance, kΩ/□	Reference
A-plane sapphire	Low-pressure CVD	0.728	[29]
C-plane sapphire	Electron cyclotron resonance CVD	0.95	[39]
C-plane sapphire	High-temperature CVD	~1	[32]
Sapphire	Critical PECVD	4.1	[40]
C-plane sapphire	PECVD	1.87	This study

4. Conclusions

We have shown a novel approach to low-temperature, transfer-less graphene deposition that involves plasma-enhanced chemical vapor deposition. The quality of graphene can be varied by adjusting the pressure and the CH_4/H_2 gas-flow ratio, with I_D/I_G values ranging from ~1 to ~4. The surface roughness of graphene mimics that of a substrate when low gas-flow ratios and chamber pressures are used. There is a notable reduction in the quality of graphene as a result of boundary defects and a grainy structure. Such a deposition evolves from poor nucleation. Despite the deposition of what appears to be a grainy multilayer graphene film, the electrical properties tend to be superior when

compared to graphene synthesized using other CVD-based techniques. As a result, the sheet resistances can be as low as 1.87 kΩ/□. To further improve this synthesis method, a thorough investigation of plasma-associated effects must be considered. Naturally, plasma shielding is an important part of this synthesis technique, and the protective enclosure effect has to be investigated in more detail. By limiting the variability governed by these factors, the homogeneity of graphene films should be greatly improved, allowing for direct quality assessment based on the synthesis conditions used.

Supplementary Materials: The following supporting information can be downloaded at: https://www.mdpi.com/article/10.3390/nano14201635/s1, Figure S1: Raw Raman spectra of C-plane sapphire and SiO_2 for comparison; Figure S2: Plot showing a dominant defect type associated with graphene grown using different synthesis conditions: (a) $I_D/I_{D'}$ vs. CH_4/H_2 gas-flow ratio and (b) $I_D/I_{D'}$ vs. chamber pressure, based on fitted data using Raman theory [58,59]. Conveniently, samples were given the same shapes and colors for distinction, as in the main text.; Figure S3: AFM image of C-plane sapphire substrate; Figure S4: AFM image of F1 sample; Figure S5: AFM image of F2 sample; Figure S6: AFM image of F3P2 sample; Figure S7: AFM image of F4 sample; Figure S8: AFM image of F5 sample; Figure S9: AFM image of P1 sample; Figure S10: AFM image of P3 sample; Figure S11: AFM image of P4 sample; Figure S12: AFM image of P5 sample.

Author Contributions: Conceptualization, A.G. and N.Ž.; software, Š.J.; investigation, Š.J. and A.G.; resources, A.G. and N.Ž.; data curation, Š.J. and A.G.; writing—original draft preparation, Š.J. and Š.M.; writing—review and editing, N.Ž., Š.M. and A.G.; visualization, Š.J.; supervision, N.Ž. and A.G.; project administration, N.Ž. and A.G.; funding acquisition, N.Ž. All authors have read and agreed to the published version of the manuscript.

Funding: This research received funding from the Research Council of Lithuania (LMTLT) under Grant No. P-MIP-22-277 („Hybrid-MAGSENS“).

Data Availability Statement: No new data were created or analyzed in this study. Data sharing is not applicable to this article.

Acknowledgments: A special thanks goes to Andrius Vasiliauskas and Rimantas Gudaitis from Kaunas University of Technology for their technical assistance.

Conflicts of Interest: The authors declare no conflicts of interest.

References

1. Liao, L.; Lin, Y.-C.; Bao, M.; Cheng, R.; Bai, J.; Liu, Y.; Qu, Y.; Wang, K.L.; Huang, Y.; Duan, X. High-Speed Graphene Transistors with a Self-Aligned Nanowire Gate. *Nature* **2010**, *467*, 305–308. [CrossRef] [PubMed]
2. Miao, X.; Tongay, S.; Petterson, M.K.; Berke, K.; Rinzler, A.G.; Appleton, B.R.; Hebard, A.F. High Efficiency Graphene Solar Cells by Chemical Doping. *Nano Lett.* **2012**, *12*, 2745–2750. [CrossRef]
3. Xia, F.; Mueller, T.; Lin, Y.; Valdes-Garcia, A.; Avouris, P. Ultrafast Graphene Photodetector. *Nat. Nanotechnol.* **2009**, *4*, 839–843. [CrossRef]
4. Davaji, B.; Cho, H.D.; Malakoutian, M.; Lee, J.-K.; Panin, G.; Kang, T.W.; Lee, C.H. A Patterned Single Layer Graphene Resistance Temperature Sensor. *Sci. Rep.* **2017**, *7*, 8811. [CrossRef]
5. Zurauskiene, N.; Lukose, R.; Balevicius, S.; Stankevic, V.; Kersulis, S.; Plausinaitiene, V.; Vagner, M.; Navickas, R. Compact Manganite-Graphene Magnetoresistive Sensor. *IEEE Magn. Lett.* **2019**, *10*, 8105605. [CrossRef]
6. Elgammal, K.; Hugosson, H.W.; Smith, A.D.; Råsander, M.; Bergqvist, L.; Delin, A. Density Functional Calculations of Graphene-Based Humidity and Carbon Dioxide Sensors: Effect of Silica and Sapphire Substrates. *Surf. Sci.* **2017**, *663*, 23–30. [CrossRef]
7. Zhang, B.Y.; Liu, T.; Meng, B.; Li, X.; Liang, G.; Hu, X.; Wang, Q.J. Broadband High Photoresponse from Pure Monolayer Graphene Photodetector. *Nat. Commun.* **2013**, *4*, 1811. [CrossRef]
8. Gan, X.; Shiue, R.-J.; Gao, Y.; Meric, I.; Heinz, T.F.; Shepard, K.; Hone, J.; Assefa, S.; Englund, D. Chip-Integrated Ultrafast Graphene Photodetector with High Responsivity. *Nat. Photonics* **2013**, *7*, 883–887. [CrossRef]
9. Yi, M.; Shen, Z. A Review on Mechanical Exfoliation for the Scalable Production of Graphene. *J. Mater. Chem. A Mater.* **2015**, *3*, 11700–11715. [CrossRef]
10. Coleman, J.N. Liquid Exfoliation of Defect-Free Graphene. *Acc. Chem. Res.* **2013**, *46*, 14–22. [CrossRef]
11. Li, X.; Cai, W.; An, J.; Kim, S.; Nah, J.; Yang, D.; Piner, R.; Velamakanni, A.; Jung, I.; Tutuc, E.; et al. Large-Area Synthesis of High-Quality and Uniform Graphene Films on Copper Foils. *Science* **2009**, *324*, 1312–1314. [CrossRef] [PubMed]
12. Deokar, G.; Avila, J.; Razado-Colambo, I.; Codron, J.-L.; Boyaval, C.; Galopin, E.; Asensio, M.-C.; Vignaud, D. Towards High Quality CVD Graphene Growth and Transfer. *Carbon N. Y.* **2015**, *89*, 82–92. [CrossRef]

13. Deng, B.; Liu, Z.; Peng, H. Toward Mass Production of CVD Graphene Films. *Adv. Mater.* **2019**, *31*, e1800996. [CrossRef]
14. Zhang, Y.; Zhang, L.; Zhou, C. Review of Chemical Vapor Deposition of Graphene and Related Applications. *Acc. Chem. Res.* **2013**, *46*, 2329–2339. [CrossRef]
15. Losurdo, M.; Giangregorio, M.M.; Capezzuto, P.; Bruno, G. Graphene CVD Growth on Copper and Nickel: Role of Hydrogen in Kinetics and Structure. *Phys. Chem. Chem. Phys.* **2011**, *13*, 20836. [CrossRef] [PubMed]
16. Gao, M.; Pan, Y.; Huang, L.; Hu, H.; Zhang, L.Z.; Guo, H.M.; Du, S.X.; Gao, H.-J. Epitaxial Growth and Structural Property of Graphene on Pt(111). *Appl. Phys. Lett.* **2011**, *98*, 033101. [CrossRef]
17. Ullah, S.; Yang, X.; Ta, H.Q.; Hasan, M.; Bachmatiuk, A.; Tokarska, K.; Trzebicka, B.; Fu, L.; Rummeli, M.H. Graphene Transfer Methods: A Review. *Nano Res.* **2021**, *14*, 3756–3772. [CrossRef]
18. Leong, W.S.; Wang, H.; Yeo, J.; Martin-Martinez, F.J.; Zubair, A.; Shen, P.-C.; Mao, Y.; Palacios, T.; Buehler, M.J.; Hong, J.-Y.; et al. Paraffin-Enabled Graphene Transfer. *Nat. Commun.* **2019**, *10*, 867. [CrossRef]
19. Liang, X.; Sperling, B.A.; Calizo, I.; Cheng, G.; Hacker, C.A.; Zhang, Q.; Obeng, Y.; Yan, K.; Peng, H.; Li, Q.; et al. Toward Clean and Crackless Transfer of Graphene. *ACS Nano* **2011**, *5*, 9144–9153. [CrossRef]
20. Haigh, S.J.; Gholinia, A.; Jalil, R.; Romani, S.; Britnell, L.; Elias, D.C.; Novoselov, K.S.; Ponomarenko, L.A.; Geim, A.K.; Gorbachev, R. Cross-Sectional Imaging of Individual Layers and Buried Interfaces of Graphene-Based Heterostructures and Superlattices. *Nat. Mater.* **2012**, *11*, 764–767. [CrossRef]
21. Strupinski, W.; Grodecki, K.; Wysmolek, A.; Stepniewski, R.; Szkopek, T.; Gaskell, P.E.; Grüneis, A.; Haberer, D.; Bozek, R.; Krupka, J.; et al. Graphene Epitaxy by Chemical Vapor Deposition on SiC. *Nano Lett.* **2011**, *11*, 1786–1791. [CrossRef] [PubMed]
22. Li, M.; Liu, D.; Wei, D.; Song, X.; Wei, D.; Wee, A.T.S. Controllable Synthesis of Graphene by Plasma-Enhanced Chemical Vapor Deposition and Its Related Applications. *Adv. Sci.* **2016**, *3*, 1600003. [CrossRef] [PubMed]
23. Rehman, M.A.; Park, S.; Khan, M.F.; Bhopal, M.F.; Nazir, G.; Kim, M.; Farooq, A.; Ha, J.; Rehman, S.; Jun, S.C.; et al. Development of Directly Grown-graphene–Silicon Schottky Barrier Solar Cell Using Co-doping Technique. *Int. J. Energy Res.* **2022**, *46*, 11510–11522. [CrossRef]
24. Kadam, K.D.; Rehman, M.A.; Kim, H.; Rehman, S.; Khan, M.A.; Patil, H.; Aziz, J.; Park, S.; Abdul Basit, M.; Khan, K.; et al. Enhanced and Passivated Co-Doping Effect of Organic Molecule and Bromine on Graphene/HfO_2/Silicon Metal–Insulator–Semiconductor (MIS) Schottky Junction Solar Cells. *ACS Appl. Energy Mater.* **2022**, *5*, 10509–10517. [CrossRef]
25. Meškinis, Š.; Vasiliauskas, A.; Guobienė, A.; Talaikis, M.; Niaura, G.; Gudaitis, R. The Direct Growth of Planar and Vertical Graphene on Si(100) via Microwave Plasma Chemical Vapor Deposition: Synthesis Conditions Effects. *RSC Adv.* **2022**, *12*, 18759–18772. [CrossRef]
26. Rehman, M.A.; Roy, S.B.; Akhtar, I.; Bhopal, M.F.; Choi, W.; Nazir, G.; Khan, M.F.; Kumar, S.; Eom, J.; Chun, S.-H.; et al. Thickness-Dependent Efficiency of Directly Grown Graphene Based Solar Cells. *Carbon N. Y.* **2019**, *148*, 187–195. [CrossRef]
27. Zhan, H.; Garrett, D.J.; Apollo, N.V.; Ganesan, K.; Lau, D.; Prawer, S.; Cervenka, J. Direct Fabrication of 3D Graphene on Nanoporous Anodic Alumina by Plasma-Enhanced Chemical Vapor Deposition. *Sci. Rep.* **2016**, *6*, 19822. [CrossRef]
28. Park, J.; Lee, J.; Choi, J.-H.; Hwang, D.K.; Song, Y.-W. Growth, Quantitative Growth Analysis and Applications of Graphene on γ-Al_2O_3 Catalysts. *Sci. Rep.* **2015**, *5*, 11839. [CrossRef] [PubMed]
29. Ueda, Y.; Maruyama, T.; Naritsuka, S. Effect of Growth Pressure on Graphene Direct Growth on an A-Plane Sapphire Substrate: Implications for Graphene-Based Electronic Devices. *ACS Appl. Nano Mater.* **2021**, *4*, 343–351. [CrossRef]
30. Wördenweber, H.; Karthäuser, S.; Grundmann, A.; Wang, Z.; Aussen, S.; Kalisch, H.; Vescan, A.; Heuken, M.; Waser, R.; Hoffmann-Eifert, S. Atomically Resolved Electronic Properties in Single Layer Graphene on α-Al_2O_3 (0001) by Chemical Vapor Deposition. *Sci. Rep.* **2022**, *12*, 18743. [CrossRef]
31. Chang, C.-J.; Tsai, P.-C.; Su, W.-Y.; Huang, C.-Y.; Lee, P.-T.; Lin, S.-Y. Layered Graphene Growth Directly on Sapphire Substrates for Applications. *ACS Omega* **2022**, *7*, 13128–13133. [CrossRef] [PubMed]
32. Fanton, M.A.; Robinson, J.A.; Puls, C.; Liu, Y.; Hollander, M.J.; Weiland, B.E.; LaBella, M.; Trumbull, K.; Kasarda, R.; Howsare, C.; et al. Characterization of Graphene Films and Transistors Grown on Sapphire by Metal-Free Chemical Vapor Deposition. *ACS Nano* **2011**, *5*, 8062–8069. [CrossRef] [PubMed]
33. Hwang, J.; Kim, M.; Campbell, D.; Alsalman, H.A.; Kwak, J.Y.; Shivaraman, S.; Woll, A.R.; Singh, A.K.; Hennig, R.G.; Gorantla, S.; et al. Van Der Waals Epitaxial Growth of Graphene on Sapphire by Chemical Vapor Deposition without a Metal Catalyst. *ACS Nano* **2013**, *7*, 385–395. [CrossRef] [PubMed]
34. Li, J.; Chen, M.; Samad, A.; Dong, H.; Ray, A.; Zhang, J.; Jiang, X.; Schwingenschlögl, U.; Domke, J.; Chen, C.; et al. Wafer-Scale Single-Crystal Monolayer Graphene Grown on Sapphire Substrate. *Nat. Mater.* **2022**, *21*, 740–747. [CrossRef]
35. Wang, G.; Zhao, Y.; Deng, Y.; Huang, W.; Fan, X.; Zhang, J.; Duan, R.; Sun, L. Lattice Selective Growth of Graphene on Sapphire Substrate. *J. Phys. Chem. C* **2015**, *119*, 426–430. [CrossRef]
36. Chen, Z.; Xie, C.; Wang, W.; Zhao, J.; Liu, B.; Shan, J.; Wang, X.; Hong, M.; Lin, L.; Huang, L.; et al. Direct Growth of Wafer-Scale Highly Oriented Graphene on Sapphire. *Sci. Adv.* **2021**, *7*, eabk0115. [CrossRef]
37. Chang, C.S.; Kim, K.S.; Park, B.-I.; Choi, J.; Kim, H.; Jeong, J.; Barone, M.; Parker, N.; Lee, S.; Zhang, X.; et al. Remote Epitaxial Interaction through Graphene. *Sci. Adv.* **2023**, *9*, eadj5379. [CrossRef]
38. Mishra, N.; Forti, S.; Fabbri, F.; Martini, L.; McAleese, C.; Conran, B.R.; Whelan, P.R.; Shivayogimath, A.; Jessen, B.S.; Buß, L.; et al. Wafer-Scale Synthesis of Graphene on Sapphire: Toward Fab-Compatible Graphene. *Small* **2019**, *15*, e1904906. [CrossRef]

39. Muñoz, R.; López-Elvira, E.; Munuera, C.; Carrascoso, F.; Xie, Y.; Çakıroğlu, O.; Pucher, T.; Puebla, S.; Castellanos-Gomez, A.; García-Hernández, M. Low T Direct Plasma Assisted Growth of Graphene on Sapphire and Its Integration in Graphene/MoS_2 Heterostructure-Based Photodetectors. *NPJ 2D Mater. Appl.* **2023**, *7*, 57. [CrossRef]
40. Wei, D.; Lu, Y.; Han, C.; Niu, T.; Chen, W.; Wee, A.T.S. Critical Crystal Growth of Graphene on Dielectric Substrates at Low Temperature for Electronic Devices. *Angew. Chem. Int. Ed.* **2013**, *52*, 14121–14126. [CrossRef]
41. Lozano, M.S.; Bernat-Montoya, I.; Angelova, T.I.; Mojena, A.B.; Díaz-Fernández, F.J.; Kovylina, M.; Martínez, A.; Cienfuegos, E.P.; Gómez, V.J. Plasma-Induced Surface Modification of Sapphire and Its Influence on Graphene Grown by Plasma-Enhanced Chemical Vapour Deposition. *Nanomaterials* **2023**, *13*, 1952. [CrossRef] [PubMed]
42. Jankauskas, Š.; Gudaitis, R.; Vasiliauskas, A.; Guobienė, A.; Meškinis, Š. The Graphene Structure's Effects on the Current-Voltage and Photovoltaic Characteristics of Directly Synthesized Graphene/n-Si(100) Diodes. *Nanomaterials* **2022**, *12*, 1640. [CrossRef] [PubMed]
43. Gudaitis, R.; Lazauskas, A.; Jankauskas, Š.; Meškinis, Š. Catalyst-Less and Transfer-Less Synthesis of Graphene on Si(100) Using Direct Microwave Plasma Enhanced Chemical Vapor Deposition and Protective Enclosures. *Materials* **2020**, *13*, 5630. [CrossRef] [PubMed]
44. Merlen, A.; Buijnsters, J.; Pardanaud, C. A Guide to and Review of the Use of Multiwavelength Raman Spectroscopy for Characterizing Defective Aromatic Carbon Solids: From Graphene to Amorphous Carbons. *Coatings* **2017**, *7*, 153. [CrossRef]
45. Malard, L.M.; Pimenta, M.A.; Dresselhaus, G.; Dresselhaus, M.S. Raman Spectroscopy in Graphene. *Phys. Rep.* **2009**, *473*, 51–87. [CrossRef]
46. Childres, I.; Jauregui, L.A.; Tian, J.; Chen, Y.P. Effect of Oxygen Plasma Etching on Graphene Studied Using Raman Spectroscopy and Electronic Transport Measurements. *New J. Phys.* **2011**, *13*, 025008. [CrossRef]
47. Hwang, J.-S.; Lin, Y.-H.; Hwang, J.-Y.; Chang, R.; Chattopadhyay, S.; Chen, C.-J.; Chen, P.; Chiang, H.-P.; Tsai, T.-R.; Chen, L.-C.; et al. Imaging Layer Number and Stacking Order through Formulating Raman Fingerprints Obtained from Hexagonal Single Crystals of Few Layer Graphene. *Nanotechnology* **2013**, *24*, 015702. [CrossRef]
48. Casiraghi, C.; Pisana, S.; Novoselov, K.S.; Geim, A.K.; Ferrari, A.C. Raman Fingerprint of Charged Impurities in Graphene. *Appl. Phys. Lett.* **2007**, *91*, 233108. [CrossRef]
49. Meškinis, Š.; Gudaitis, R.; Vasiliauskas, A.; Guobienė, A.; Jankauskas, Š.; Stankevič, V.; Keršulis, S.; Stirkė, A.; Andriukonis, E.; Melo, W.; et al. Biosensor Based on Graphene Directly Grown by MW-PECVD for Detection of COVID-19 Spike (S) Protein and Its Entry Receptor ACE2. *Nanomaterials* **2023**, *13*, 2373. [CrossRef]
50. Song, H.J.; Son, M.; Park, C.; Lim, H.; Levendorf, M.P.; Tsen, A.W.; Park, J.; Choi, H.C. Large Scale Metal-Free Synthesis of Graphene on Sapphire and Transfer-Free Device Fabrication. *Nanoscale* **2012**, *4*, 3050. [CrossRef]
51. Zheng, S.; Zhong, G.; Wu, X.; D'Arsiè, L.; Robertson, J. Metal-Catalyst-Free Growth of Graphene on Insulating Substrates by Ammonia-Assisted Microwave Plasma-Enhanced Chemical Vapor Deposition. *RSC Adv.* **2017**, *7*, 33185–33193. [CrossRef]
52. Kim, Y.S.; Joo, K.; Jerng, S.-K.; Lee, J.H.; Yoon, E.; Chun, S.-H. Direct Growth of Patterned Graphene on SiO_2 Substrates without the Use of Catalysts or Lithography. *Nanoscale* **2014**, *6*, 10100–10105. [CrossRef] [PubMed]
53. Vishwakarma, R.; Rosmi, M.S.; Takahashi, K.; Wakamatsu, Y.; Yaakob, Y.; Araby, M.I.; Kalita, G.; Kitazawa, M.; Tanemura, M. Transfer Free Graphene Growth on SiO_2 Substrate at 250 °C. *Sci. Rep.* **2017**, *7*, 43756. [CrossRef] [PubMed]
54. Xu, S.C.; Man, B.Y.; Jiang, S.Z.; Chen, C.S.; Yang, C.; Liu, M.; Gao, X.G.; Sun, Z.C.; Zhang, C. Direct Synthesis of Graphene on SiO_2 Substrates by Chemical Vapor Deposition. *CrystEngComm* **2013**, *15*, 1840. [CrossRef]
55. Gupta, A.; Chen, G.; Joshi, P.; Tadigadapa, S. Eklund Raman Scattering from High-Frequency Phonons in Supported *n*-Graphene Layer Films. *Nano Lett.* **2006**, *6*, 2667–2673. [CrossRef] [PubMed]
56. Cho, J.H.; Gorman, J.J.; Na, S.R.; Cullinan, M. Growth of Monolayer Graphene on Nanoscale Copper-Nickel Alloy Thin Films. *Carbon N. Y.* **2017**, *115*, 441–448. [CrossRef]
57. Ferrari, A.C.; Basko, D.M. Raman Spectroscopy as a Versatile Tool for Studying the Properties of Graphene. *Nat. Nanotechnol.* **2013**, *8*, 235–246. [CrossRef]
58. Eckmann, A.; Felten, A.; Mishchenko, A.; Britnell, L.; Krupke, R.; Novoselov, K.S.; Casiraghi, C. Probing the Nature of Defects in Graphene by Raman Spectroscopy. *Nano Lett.* **2012**, *12*, 3925–3930. [CrossRef]
59. Venezuela, P.; Lazzeri, M.; Mauri, F. Theory of Double-Resonant Raman Spectra in Graphene: Intensity and Line Shape of Defect-Induced and Two-Phonon Bands. *Phys. Rev. B* **2011**, *84*, 035433. [CrossRef]
60. Ni, Z.H.; Yu, T.; Lu, Y.H.; Wang, Y.Y.; Feng, Y.P.; Shen, Z.X. Uniaxial Strain on Graphene: Raman Spectroscopy Study and Band-Gap Opening. *ACS Nano* **2008**, 2, 2301–2305. [CrossRef]
61. Yoon, D.; Son, Y.-W.; Cheong, H. Negative Thermal Expansion Coefficient of Graphene Measured by Raman Spectroscopy. *Nano Lett.* **2011**, *11*, 3227–3231. [CrossRef] [PubMed]
62. Neumann, C.; Reichardt, S.; Venezuela, P.; Drögeler, M.; Banszerus, L.; Schmitz, M.; Watanabe, K.; Taniguchi, T.; Mauri, F.; Beschoten, B.; et al. Raman Spectroscopy as Probe of Nanometre-Scale Strain Variations in Graphene. *Nat. Commun.* **2015**, *6*, 8429. [CrossRef]
63. Ni, Z.; Wang, Y.; Yu, T.; You, Y.; Shen, Z. Reduction of Fermi Velocity in Folded Graphene Observed by Resonance Raman Spectroscopy. *Phys. Rev. B* **2008**, *77*, 235403. [CrossRef]
64. Ferrari, A.C.; Meyer, J.C.; Scardaci, V.; Casiraghi, C.; Lazzeri, M.; Mauri, F.; Piscanec, S.; Jiang, D.; Novoselov, K.S.; Roth, S.; et al. Raman Spectrum of Graphene and Graphene Layers. *Phys. Rev. Lett.* **2006**, *97*, 187401. [CrossRef]

65. Lee, J.E.; Ahn, G.; Shim, J.; Lee, Y.S.; Ryu, S. Optical Separation of Mechanical Strain from Charge Doping in Graphene. *Nat. Commun.* **2012**, *3*, 1024. [CrossRef] [PubMed]
66. Kim, S.; Ryu, S. Thickness-Dependent Native Strain in Graphene Membranes Visualized by Raman Spectroscopy. *Carbon N. Y.* **2016**, *100*, 283–290. [CrossRef]
67. Morozov, S.V.; Novoselov, K.S.; Katsnelson, M.I.; Schedin, F.; Elias, D.C.; Jaszczak, J.A.; Geim, A.K. Giant Intrinsic Carrier Mobilities in Graphene and Its Bilayer. *Phys. Rev. Lett.* **2008**, *100*, 016602. [CrossRef]
68. Yang, W.; He, C.; Zhang, L.; Wang, Y.; Shi, Z.; Cheng, M.; Xie, G.; Wang, D.; Yang, R.; Shi, D.; et al. Growth, Characterization, and Properties of Nanographene. *Small* **2012**, *8*, 1429–1435. [CrossRef]
69. Zhang, H.; Lee, G.; Gong, C.; Colombo, L.; Cho, K. Grain Boundary Effect on Electrical Transport Properties of Graphene. *J. Phys. Chem. C* **2014**, *118*, 2338–2343. [CrossRef]

Disclaimer/Publisher's Note: The statements, opinions and data contained in all publications are solely those of the individual author(s) and contributor(s) and not of MDPI and/or the editor(s). MDPI and/or the editor(s) disclaim responsibility for any injury to people or property resulting from any ideas, methods, instructions or products referred to in the content.

4 straipsnis

Straipsnio pavadinimas	*Advancing graphene synthesis: low-temperature growth and hydrogenation mechanisms using plasma-enhanced chemical vapor deposition*
Straipsnio bendraautoriai	*Šarūnas Meškinis; Algirdas Lazauskas; Šarūnas Jankauskas; Asta Guobienė; Rimantas Gudaitis*
Leidėjas, žurnalo pavadinimas	*MDPI, Molecules*
Metai	*2024*

molecules

MDPI

Article

Advancing Graphene Synthesis: Low-Temperature Growth and Hydrogenation Mechanisms Using Plasma-Enhanced Chemical Vapor Deposition

Šarūnas Meškinis *, Algirdas Lazauskas *, Šarūnas Jankauskas, Asta Guobienė and Rimantas Gudaitis

Institute of Materials Science, Kaunas University of Technology, K. Baršausko 59, LT-51423 Kaunas, Lithuania; sarunas.jankauskas@ktu.lt (Š.J.); asta.guobiene@ktu.lt (A.G.); rimantas.gudaitis@ktu.lt (R.G.)
* Correspondence: sarunas.meskinis@ktu.lt (Š.M.); algirdas.lazauskas@ktu.edu (A.L.); Tel.: +370-61554257 (Š.M.); +370-67173375 (A.L.)

Abstract: This study explores the low-temperature synthesis of graphene using plasma-enhanced chemical vapor deposition (PECVD), emphasizing the optimization of process parameters to achieve controlled growth of pristine and hydrogenated graphene. Graphene films were synthesized at temperatures ranging from 700 °C to as low as 400 °C by varying methane (25–100 sccm) and hydrogen (25–100 sccm) gas flow rates under 10–20 mBar pressures. Raman spectroscopy revealed structural transitions: pristine graphene grown at 700 °C exhibited strong 2D peaks with an I(2D)/I(G) ratio > 2, while hydrogenated graphene synthesized at 500 °C showed increased defect density with an I(D)/I(G) ratio of ~1.5 and reduced I(2D)/I(G) (~0.8). At 400 °C, the material transitioned to a highly hydrogenated amorphous carbon film, confirmed by photoluminescence (PL) in the Raman spectra. Atomic force microscopy (AFM) showed pristine graphene with a root mean square roughness (R_q) of 0.37 nm. By carefully adjusting PECVD synthesis parameters, it was possible to tune the surface roughness of hydrogenated graphene to levels close to that of pristine graphene or to achieve even smoother surfaces. Conductive AFM measurements revealed that hydrogenation could enhance graphene's contact current under specific conditions. The findings highlight the role of PECVD parameters in tailoring graphene's structural, morphological, and electronic properties for diverse applications. This work demonstrates a scalable, low-temperature approach to graphene synthesis, offering the potential for energy storage, sensing, and electronic devices requiring customized material properties.

Keywords: PECVD; graphene synthesis; low-temperature growth; hydrogenated graphene

check for updates

Academic Editor: Yuanfu Chen

Received: 5 December 2024
Revised: 21 December 2024
Accepted: 24 December 2024
Published: 25 December 2024

Citation: Meškinis, Š.; Lazauskas, A.; Jankauskas, Š.; Guobienė, A.; Gudaitis, R. Advancing Graphene Synthesis: Low-Temperature Growth and Hydrogenation Mechanisms Using Plasma-Enhanced Chemical Vapor Deposition. *Molecules* **2025**, *30*, 33. https://doi.org/10.3390/molecules30010033

Copyright: © 2024 by the authors. Licensee MDPI, Basel, Switzerland. This article is an open access article distributed under the terms and conditions of the Creative Commons Attribution (CC BY) license (https://creativecommons.org/licenses/by/4.0/).

1. Introduction

Graphene, known for its exceptional electrical, optical, and mechanical properties, is being developed for various optoelectronic applications, ranging from solar cells to high-speed electronics [1,2]. The giant charge carrier mobility and its multiplication, optical transparency, flexibility, very high Young's modulus and failure stress, high ductility, and chemical inertness all account for the potential of emerging devices [3–6]. Although graphene is known as a planar sheet of carbon atoms arranged in a honeycomb-like pattern, it can present with many configurations that differ in structure and properties. Graphene flakes [7], vertical graphene [8], hydrogenated graphene films [9], and many more variants can be fabricated using chemical vapor deposition (CVD) [10].

For planar, in regard to high-quality graphene fabrication, graphite exfoliation is a method of choice, although it is not suitable for industrial applications because of the need for more scalability [11]. For large-area graphene production, the most promising technique is CVD, which is usually performed on catalytic metal (Cu, Ni, and Co) foils with subsequent transfer to the target substrate [12]. However, the downside of this is the complicated transfer process that involves careful handling of the graphene film, which can result in possible graphene contamination by different adsorbents [13], wrinkles, or ripple formation in the graphene [14]. Direct graphene growth on dielectric and semiconducting substrates has emerged as an effective approach to overcoming these limitations. One such technique, plasma-enhanced chemical vapor deposition (PECVD), involves the use of plasma to activate the ionization and dissociation of hydrocarbon precursors at relatively low temperatures, enabling graphene growth directly on dielectric or semiconducting substrates. PECVD provides several advantages, including reduced synthesis temperatures compared to traditional CVD (>1000 °C), lower energy consumption, and the ability to use a wider range of substrates without risking thermal damage [15,16].

In PECVD systems, remote plasma configurations are typically used to avoid radiation-induced defects or the total etching of the growing graphene film, facilitating the synthesis of high-quality planar graphene layers [17]. Direct plasma systems; however, are more challenging to control due to their higher radiation effects, but they have shown the potential to produce both planar and vertical graphene structures [17–20]. In our previous research, we demonstrated that it is possible to control the orientation of graphene flakes during direct plasma-based growth on semiconducting and dielectric substrates at temperatures ranging from 700 to 800 °C [17,19,20]. Despite this, there are relatively few studies on graphene synthesis using direct plasma systems [17–20].

In the present study, we explore the potential for reducing the direct synthesis temperature of graphene through the optimization of hydrogen and methane gas flows and process pressure. These parameters are crucial for balancing the etching and growth processes that govern the quality and properties of the synthesized graphene. By adjusting the flow rates of hydrogen and methane, we investigate how the interplay between these gasses influences the formation of both pristine and hydrogenated graphene at lower temperatures. Our findings demonstrate the feasibility of synthesizing hydrogenated graphene at significantly lower temperatures than conventional pristine graphene, which opens new avenues for low-temperature synthesis techniques and broadens the range of potential substrates that can be used in graphene-based applications.

2. Results

In our previous research, the lowest temperature achieved for the direct synthesis of graphene was 700 °C. In this study, we aimed to further reduce the synthesis temperature by optimizing the hydrogen and methane gas flow rates and the process pressure. Initially, experiments were conducted at a working pressure of 20 mBar. Figure 1 illustrates that, at 700 °C, few-layer graphene can be synthesized using gas flow rates of 75 sccm H_2 and 25 sccm CH_4. The Raman spectra of the synthesized graphene reveal prominent G and 2D peaks [21,22] alongside defect-related D [21,22] and D+D′ peaks [23–27]. Additionally, a shoulder on the G peak indicates the presence of the D′ peak, another defect-associated feature [21,22]. The pronounced D peak is characteristic of graphene directly synthesized on dielectric and semiconducting substrates, and it is attributed to the nanocrystalline structure of the material.

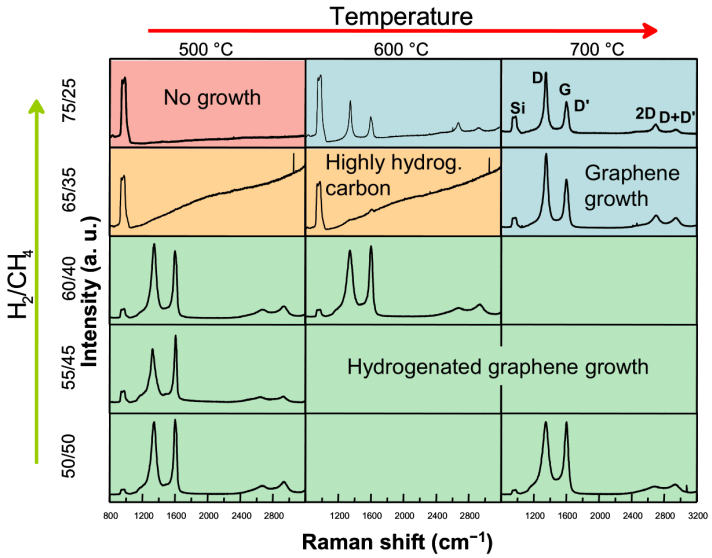


Figure 1. Characteristic Raman spectra of graphene, highly hydrogenated carbon and hydrogenated graphene films grown at different temperatures and H_2 to CH_4 gas flow ratios. The total gas flow was 100 sccm and the work pressure was 20 mBar.

Increasing the methane flow to 35 sccm while reducing the hydrogen flow to 65 sccm still resulted in graphene growth at 700 °C. Further adjustments, such as decreasing the hydrogen flow to 50 sccm and increasing the methane to 50 sccm, significantly reduced the I(D)/I(G) intensity ratio, indicating fewer defects. However, this adjustment also markedly decreased the intensity of the 2D peak, which became less prominent than the D+D′ peak. The D+D′ peak is primarily associated with on-site defects, such as hydrogen atoms covalently bonded to carbon atoms in the graphene lattice. Prior studies [23–27] and our recent work [28] support this observation. Furthermore, the hydrogenation of pristine graphene reduces the 2D band intensity while enhancing the D+D′ band, with an inverse relationship between these bands' intensities confirming that hydrogenated graphene growth occurred under these conditions.

Lowering the synthesis temperature to 600 °C, with 75 sccm hydrogen and 25 sccm methane flows, still resulted in graphene growth. However, the I(G)/I(Si) ratio was significantly lower than that of the sample grown at 700 °C, indicating a reduced suppression of the substrate's Raman signal (Table S1). The I(2D)/I(G) ratio increased, suggesting the growth of fewer graphene layers (Table S1). The I(2D)/I(G) ratio values were typical for bilayer graphene [29]. Reducing the hydrogen flow to 65 sccm while increasing the methane flow to 35 sccm led to the emergence of a strong photoluminescence (PL) background in the Raman spectra that is typical of highly hydrogenated amorphous carbon film (~40–50 at.% hydrogen) growth [29]. However, adjusting the gas flow to 60 sccm H_2 and 40 sccm of CH_4 enabled the synthesis of hydrogenated graphene. Similar results were ob-

served at a synthesis temperature of 500 °C. These findings suggest that increasing methane flow and reducing hydrogen flow promote the growth of hydrogenated graphene, which can be achieved at lower temperatures than with "conventional" pristine graphene deposition.

At 500 °C, a total gas flow of 200 sccm with a 1:1 H_2:CH_4 ratio still resulted in hydrogenated graphene growth (Figure 2). However, increasing the hydrogen flow to 120 sccm while decreasing methane to 80 sccm caused the Raman spectra to exhibit a PL background, with the 2D and D+D′ peaks nearly disappearing. Nonetheless, the D and G peaks remained prominent. Notably, a hydrogenated graphene layer was successfully grown at 450 °C with 50 sccm H_2 and 50 sccm CH_4 flows. At 400 °C, the Raman spectra featured characteristics of hydrogenated graphene, including 2D and D+D′ peaks, along with a broad PL lump. These observations suggest that the sample synthesized at 400 °C was transitioning from hydrogenated graphene to a highly hydrogenated carbon film. However, in this case, the Raman spectra luminescence feature differs from other highly hydrogenated carbon films observed in this study. The presence of defective polycyclic aromatic hydrocarbon bonds is plausible [30].

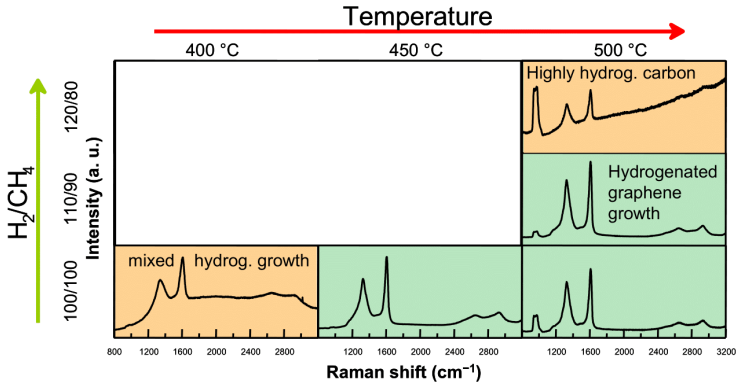


Figure 2. Characteristic Raman spectra of graphene and highly hydrogenated carbon films grown at different temperatures and H_2 to CH_4 gas flow ratios. The total gas flow was 200 sccm and the work pressure was 20 mBar.

Reducing the synthesis pressure from 20 mBar to 10 mBar maintained graphene growth at 700 and 600 °C temperatures under 75 sccm H_2 and 25 sccm CH_4 flows (Figure 3). The I(G)/I(Si) ratio was substantially lower, and the I(2D)/I(G) ratio was higher for graphene grown at 600 °C and 10 mBar pressure than for the 20 mBar sample, implying a slower graphene growth process (Table S1). In addition, at 500 °C, hydrogenated graphene did not form if 10 mBar work pressure was used (Figure 4). Instead, the Raman spectra displayed a PL background and a substrate-related peak. Under these conditions, hydrogenated graphene synthesis was observed only at 600 °C (Figure 4).

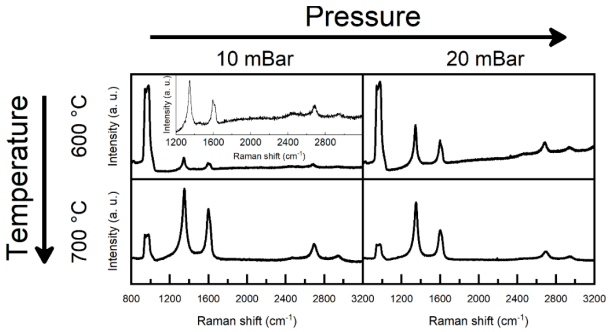


Figure 3. The Raman spectra of graphene grown under different synthesis pressures and temperatures. The hydrogen gas flow was 75 sccm and the methane gas flow was 25 sccm.

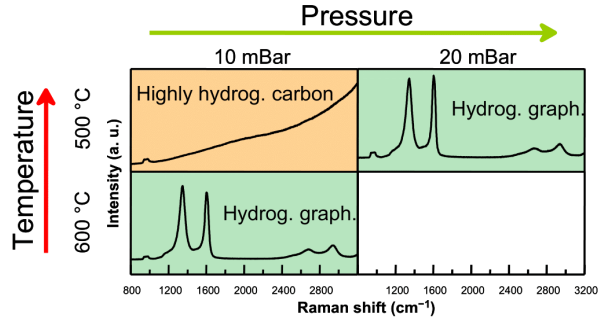


Figure 4. Raman spectra of hydrogenated graphene and highly hydrogenated carbon films grown under different temperature and synthesis pressure. The hydrogen gas flow was 50 sccm and the methane gas flow was 50 sccm.

At 500 °C and 10 mBar pressure, varying the total gas flow revealed further insights (Figure S1). Decreasing the total flow to 100 sccm resulted in highly hydrogenated carbon formation, whereas increasing the total flow to 200 sccm led to D and G peaks appearing in the Raman spectra, with a concomitant reduction being seen in the PL background (Figure 4). While using 20 mBar pressure at 500 °C temperature, in all cases, hydrogenated graphene was grown irrespectively of the total gas flow used (Figure S1).

The Raman scattering spectra parameters of the samples were further analyzed to investigate their structural characteristics. The I(2D)/I(G) ratio is commonly employed as an indicator of the number of graphene layers [31]. However, this ratio can be influenced by graphene doping and the presence of defects, both of which can reduce the I(2D)/I(G) ratio. Specifically, doping can result in a reduced I(2D)/I(G) ratio accompanied by an upshift in the Pos(G) position [32,33]. In contrast, our results exhibit different behavior (Figure 5a). Therefore, the changes in this study in the I(2D)/I(G) ratio are not attributed to the possible graphene doping.

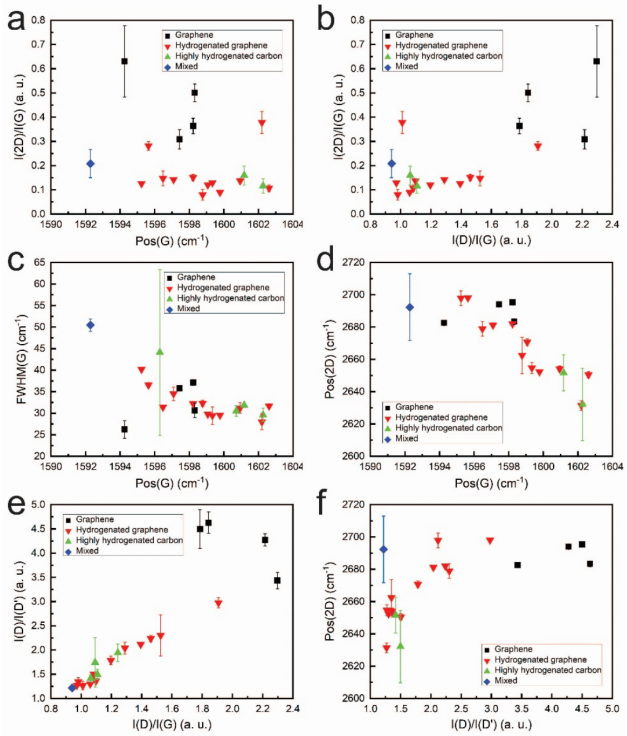


Figure 5. Plots of I(2D)/I(G) vs. Pos(G) (**a**); I(2D)/I(G) vs. I(D)/I(G) (**b**); FWHM(G) vs. Pos(G) (**c**); Pos(2D) vs. Pos(G) (**d**); I(D)/I(D′) vs. I(D)/I(G) (**e**); Pos(2D) vs. I(D)/I(D′) (**f**).

While an increase in defect density is typically associated with a decrease in the I(2D)/I(G) ratio [34,35], the hydrogenated graphene samples in this study exhibited an increase in the I(2D)/I(G) ratio with an increasing I(D)/I(G) ratio (Figure 5b). Consequently, the I(2D)/I(G) ratio was utilized to estimate the number of graphene layers. Notably, for most hydrogenated graphene samples, the I(2D)/I(G) ratio was significantly lower than that observed for pristine graphene (Figure S1), indicative of a greater number of layers.

The full width at half maximum of the G peak (FWHM(G)) decreased as Pos(G) shifted upward (Figure 5c), consistent with graphene doping effects [32,33]. Furthermore, Pos(2D) exhibited a downward shift in response to the Pos(G) upshift (Figure 5d), a behavior characteristic of n-type graphene doping [32,36]. For most hydrogenated graphene samples, Pos(2D) was less red-shifted than for conventional pristine graphene, indicating a more pronounced doping effect in hydrogenated graphene [37,38].

Consistent with our previous studies, substrate-induced graphene self-doping can be presumed [17,19,39,40]. Numerous research papers have documented this mechanism, high-

lighting the critical role of substrate interactions in graphene's electronic properties [41–47]. The type of self-doping (p-type or n-type) depends on the substrate material. For instance, studies have demonstrated that the surface orientation of SiO_2 significantly influences graphene's doping characteristics. An O-polar SiO_2 surface with dangling bonds induces p-type doping in graphene [43], whereas a Si-polar surface with dangling bonds results in n-type self-doping [43]. These findings suggest that the direct graphene synthesis process intrinsically modifies the substrate surface or interface composition, facilitating the transfer of induced charges to the graphene layer.

The I(D)/I(D′) ratio was observed to increase with the I(D)/I(G) ratio (Figure 5e). For some samples, the I(D)/I(D′) ratio was consistent with boundary defects (≈3.5). However, in most cases, the ratio suggested the co-dominance of on-site defects and boundary defects or the exclusive presence of on-site defects [48]. On-site defects in graphene are commonly attributed to adsorbed hydrogen atoms [49], corroborating the Raman scattering spectra and confirming the growth of hydrogenated graphene. Some correlation was observed between Pos(2D) and the I(D)/I(D′) ratio for hydrogenated graphene samples, indicating the graphene hydrogenation influence on graphene doping (Figure 5f). It should be noted that n-type doping of the graphene due to the hydrogenation was already reported in [50,51].

The I(G)/I(Si) peak ratio was evaluated as an additional measure of film thickness [19,31]. No dependence of the I(2D)/I(G) ratio on the I(G)/I(Si) ratio was observed for most samples (Figure S2), suggesting that I(G)/I(Si) is not directly related to the graphene layer number in hydrogenated graphene films. However, for hydrogenated graphene samples, the I(G)/I(Si) ratio was significantly smaller compared to pristine graphene, indicating the formation of thicker or less heterogeneous films.

The effects of synthesis conditions on the Raman scattering spectra parameters revealed that I(2D)/I(G) was more dependent on the graphene type (pristine or hydrogenated) than on deposition conditions for samples grown using a total gas flow of 100 sccm (Figures S3–S5). A decrease in synthesis temperature corresponded to a reduction in the I(D)/I(D′) ratio (Figures S3 and S5). Additionally, reducing the H_2/CH_4 gas flow ratio at 700 °C led to a decrease in the I(D)/I(D′) ratio and an increase in the I(G)/I(Si) ratio (Figure S3). Lowering the synthesis temperature from 700 °C to 600 °C or 500 °C enhanced graphene self-doping effects (Figure S3). However, a further temperature reduction to 400 °C diminished the self-doping effect, probably due to the changes in the nature of C-H bonds (Figure S5). It seems that decreasing the work pressure to 10 mbar promoted graphene self-doping (Figure S6).

The atomic force microscopy (AFM) topographical images depicted in Figure 6 provide detailed insights into the surface morphologies of pristine graphene and hydrogenated graphene samples synthesized via plasma-enhanced chemical vapor deposition (PECVD). The pristine graphene, shown in Figure 6a, was synthesized at a substrate temperature of 700 °C utilizing gas flow rates of 75 sccm CH_4 and 25 sccm H_2. In contrast, the hydrogenated graphene samples were fabricated at a lower substrate temperature of 500 °C, employing a 1:1 gas flow ratio. Specifically, the flow rates used were 50 sccm CH_4 and 50 sccm H_2 (Figure 6b) and 100 sccm CH_4 and 100 sccm H_2 (Figure 6c).

The AFM image of pristine graphene (Figure 6a) shows a relatively smooth surface characterized by a granular texture, indicative of a continuous and uniform graphene layer. A quantitative surface morphology analysis reveals an average height (Z_{mean}) of 0.68 nm with a root mean square roughness (R_q) of 0.37 nm. These values are consistent with those reported in earlier studies on PECVD-grown graphene [19], suggesting that the graphene layer is largely free of significant defects or discontinuities. The surface skewness (R_{sk}) of −0.06 indicates a symmetrical height distribution with slight depressions. At the same

time, the kurtosis (R_{ku}) value of 1.98 implies that the surface morphology has no extreme peaks or valleys dominating the surface features.

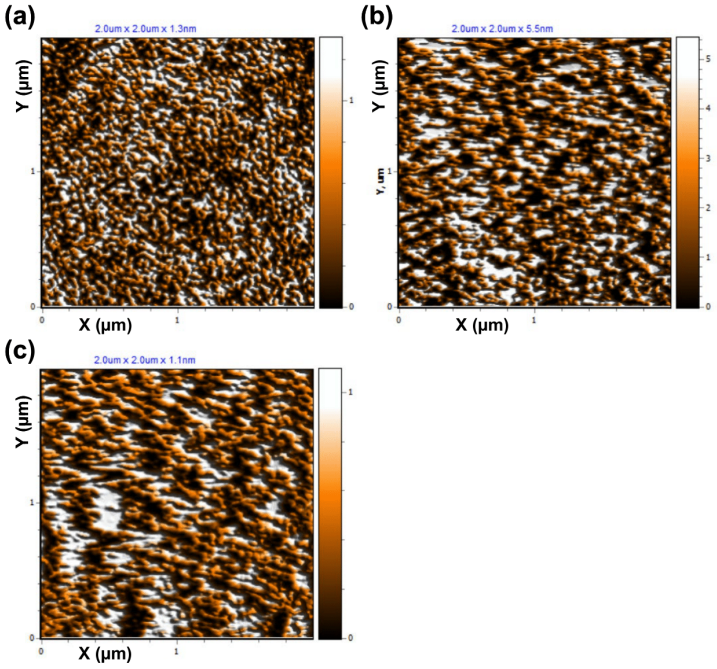


Figure 6. (AFM) topographical images of (**a**) pristine graphene, (**b**) hydrogenated graphene prepared at 50 sccm CH_4 and 50 sccm H_2 gas flow rates, and (**c**) hydrogenated graphene prepared at 100 sccm CH_4 and 100 sccm H_2 gas flow rates.

Conversely, the hydrogenated graphene samples (Figure 6b) prepared at 50 sccm CH_4 and 50 sccm H_2 gas flow rates demonstrate a markedly rougher surface morphology, reflecting significant structural changes induced by incorporating hydrogen atoms into the graphene lattice. The average height of the surface increases to 2.81 nm, with a corresponding rise in the R_q to 1.69 nm. This increase in roughness indicates surface distortions and the introduction of structural irregularities due to hydrogenation. The R_{sk} of -0.05 indicates a symmetrical distribution of surface heights similar to that of pristine graphene, but the R_{ku} value of 1.89 suggests a slightly broader distribution of height features. These changes are in line with Raman observations which suggest that the hydrogenation process disrupts the sp^2-hybridized carbon network, replacing it with localized sp^3 bonds, which lead to out-of-plane buckling and increased nanoscale surface roughness with larger, irregularly shaped grains or clusters.

The hydrogenated graphene sample (Figure 6c), prepared at 100 sccm CH_4 and 100 sccm H_2 gas flow rates, exhibits a surface morphology between pristine (Figure 6a)

and hydrogenated graphene (shown in Figure 6b). A quantitative analysis reveals a Z_{mean} of 0.57 nm and an R_q of 0.30 nm. These values suggest a surface slightly smoother than pristine graphene but with limited roughness. The R_{sk} of 0.01 indicates a nearly symmetrical height distribution, while the kurtosis R_{ku} value of 2.04 reflects a slightly sharper distribution of peaks and valleys. The surface morphology suggests smaller, more uniform grains compared to the hydrogenated graphene shown in Figure 6b.

The morphological differences between the pristine graphene and hydrogenated graphene can be attributed to the distinct synthesis conditions and the effect of hydrogen incorporation during PECVD. The pristine graphene synthesized at a higher temperature and with reduced hydrogen flow retains a planar sp^2-hybridized structure, resulting in a smoother and more uniform surface. In contrast, the hydrogenation process carried out at a lower temperature introduces localized distortions in the graphene lattice as sp^3-hybridized carbon-hydrogen bonds. These distortions disrupt the continuity of the graphene layer, leading to increased surface heterogeneity with the formation of larger grains or clusters. However, by adjusting the synthesis parameters, it is possible to tune the surface roughness to levels close to that of pristine graphene or to achieve even smoother surfaces.

These observations highlight the role of PECVD parameters in tailoring the surface morphology and structural properties of graphene. The smoother topography is suitable for electronic and optoelectronic applications requiring uniform layers, while the enhanced surface roughness can be advantageous for applications such as catalysis, sensing, or energy storage, where increased surface areas and reactive sites are desirable.

The contact current of the graphene and hydrogenated graphene samples was evaluated using Conductive Atomic Force Microscopy (CP-AFM), with the mean contact current values being plotted against various parameters, as illustrated in Figure 7. The results indicate that the contact current of hydrogenated graphene samples increased with surface roughness. The contact current of hydrogenated graphene was also found to correlate with specific Raman spectroscopy features, including a broadening of the G peak, a shift in the G peak to higher wavenumbers (Pos(G)), and a downshift in the 2D peak (Pos(2D)). This trend was consistent with the behavior observed in pristine graphene samples. Notably, the pristine graphene synthesis temperature reduction from 700 °C to 600 °C resulted in significant contact current reduction—from 9 to the 1.39 pA (Table S2). The tendencies revealed in Figure 6 mean that the reduction in contact current for both graphene and hydrogenated graphene can be attributed to self-doping phenomena. Thus, the self-doping phenomena should be suppressed to increase the contact current. Furthermore, no dependence of contact current on the I(D)/I(D') ratio was found for either hydrogenated graphene or pristine graphene, suggesting that the relationship between graphene's electrical properties, self-doping, and the type of defects, as well as hydrogenation, is not straightforward. Some competition between the substrate-induced graphene self-doping and hydrogenation-induced doping can be presumed. Interestingly, the contact current of hydrogenated graphene can exceed that of pristine graphene despite hydrogenation and the dominance of on-site defects. It indicates that hydrogenation can enhance the contact current of graphene under certain conditions that are independent of the defect type and concentration.

Summarizing, a decrease in graphene synthesis temperature and a reduction in the hydrogen/methane gas flow ratio facilitated the growth of hydrogenated graphene. Lower synthesis temperatures also enhanced the degree of graphene hydrogenation, enabling the successful synthesis of hydrogenated graphene at temperatures as low as 400–450 °C. Increasing the work pressure proved beneficial in regard t lowering the synthesis temperature required for graphene formation.

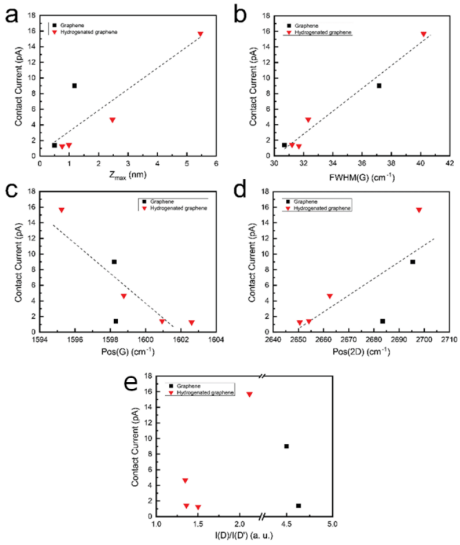


Figure 7. Mean Z(pA) values plotted against (**a**) Zmax, (**b**) FWHM(G), (**c**) Pos(G), (**d**) Pos(2D) and (**e**) I(D)/I(D′). Dashed gray lines indicate trends in the graphs.

The growth of hydrogenated graphene is likely attributed to the incomplete dissociation of methane molecules under these synthesis conditions. Self-doping effects were observed in the synthesized graphene samples. In the hydrogenated graphene, these effects were related to graphene hydrogenation, and the prevailing of the hydrogen-related on-site defects promoted n-type self-doping effects. The degree of self-doping exhibited a non-monotonic dependence on synthesis temperature, while reduced work pressure promoted self-doping.

The observed results can be explained by competition between several processes. These are methane and hydrogen molecules' dissociation and ionization, graphene/carbon film growth, and carbon etching by hydrogen. Particularly, an increase in the CH_4 gas flow and in the total gas flow results in decreased power density per methane molecule and less time for methane dissociation [52]. Decreased temperature results in suppressed molecule dissociation [53], an increased hydrogen etching rate [54], and a reduced carbon desorption rate [55]. Decreased pressure increases power density per molecule, enhancing the dissociation [56]. Lower pressure also helps to achieve higher electron mean free paths and higher electron temperatures, subsequently increasing the gas ionization rate and ion bombardment [57].

One of the challenges associated with PECVD-based graphene synthesis is achieving precise control over the number of graphene layers. While our process yielded predominantly bilayer and few-layer graphene, as evidenced by Raman spectroscopy, the scalability of the method may be influenced by factors such as substrate uniformity, plasma distribution, and gas flow dynamics. Variations in these parameters can result in localized inconsistencies in layer thickness, particularly over larger substrate areas.

Additionally, the use of a steel enclosure to shield the substrate from direct plasma exposure, while effective in minimizing excessive etching and providing a possibility to control the orientation of the graphene flakes, may inadvertently create non-uniform deposition conditions at the edges of the sample. This limitation could affect the reproducibility of the process when scaling to larger substrates.

To address these issues, further optimization of the reactor design, including uniform plasma distribution and precise substrate positioning, is necessary.

3. Materials and Methods

The graphene was synthesized directly on a 300 nm-thick silicon dioxide (SiO_2) layer thermally grown on a Si(100) substrate using a gas mixture of hydrogen (H_2) and methane (CH_4). The synthesis process was conducted in a Cyrannus microwave plasma-enhanced chemical vapor deposition (PECVD) system (Innovative Plasma Systems (Iplas) GmbH, Troisdorf, Germany). The substrate dimensions were 1×1 cm.

Prior to graphene growth, the substrate underwent a pretreatment stage involving hydrogen plasma exposure without any prior wet-chemical treatment. During this step, the plasma power was set at 1.0 kW, the process temperature was maintained at 700 °C, the hydrogen flow rate was 200 sccm, the chamber pressure was 10 mBar, and the treatment duration was 10 min.

Following the pretreatment, CH_4 gas was introduced into the reaction chamber for graphene deposition. A specially designed enclosure, fabricated from a rectangular non-magnetic steel sheet bent perpendicularly at two points, was utilized to shield the sample from direct plasma interactions. This arrangement minimized excessive etching of the growing graphene layer, ensuring controlled deposition and improved material quality. Synthesis conditions are presented in Table 1.

Table 1. Technological process synthesis conditions.

Sample No	Temperature (°C)	H_2 Flow (sccm)	CH_4 Flow (sccm)	Pressure (mBar)
1	700	75	25	20
2	700	75	25	10
3	600	75	25	20
4	600	75	25	10
5	500	75	25	20
6	700	65	35	20
7	600	65	35	20
8	500	65	35	20
9	600	60	40	20
10	500	60	40	20
11	500	55	45	20
12	700	50	50	20
13	600	50	50	10
14	500	50	50	20
15	500	50	50	10
16	500	120	80	20
17	500	110	90	20
18	500	100	100	20
19	450	100	100	20
20	400	100	100	20
21	500	100	100	10
22	500	75	75	20
23	500	80	70	20

During graphene synthesis, the chamber pressure was monitored and regulated using an automated feedback system connected to the gas flow controller. A calibrated pressure gauge was employed for real-time measurement and precise control of the chamber pressure throughout the process. Th substrate temperature was controlled using a resistive heater integrated into the PECVD system. The heater's temperature was monitored by a thermocouple positioned directly beneath the substrate, ensuring accurate temperature measurement.

The Raman scattering spectra of the synthesized samples were recorded using a Renishaw inVia Raman spectrometer (Renishaw, Wotton-under-Edge, UK). A 532 nm wavelength laser was used for excitation with a power of 3 mW. The D, G, D', and 2D peaks were fitted using the Lorentzian function. The intensity ratio of the 2D to G peaks (I(2D)/I(G)) was used to estimate the number of graphene layers [31]. The intensity ratio of the D to G peaks (I(D)/I(G)) was calculated to assess the defect density of graphene [35,58]. The intensity ratio of the D and D' peaks was analyzed to determine the dominant defect type [48,49]. The full width at half maximum (FWHM) of the G peak (FWHM(G)) [37,38,49], as well as the positions of the G and 2D peaks (Pos(G) and Pos(2D)) [32,36], were also considered as parameters sensitive to graphene doping and stress. The broad substrate-related peak at ~900 cm^{-1} (associated with SiO_2/Si) was taken into account, and the I(G)/I(Si) ratio was calculated to further estimate the thickness of the deposited film [19,31,59]. Notably, the I(G)/I(Si) ratio increases with the number of graphene layers in planar graphene [31,59] and with the total film thickness for vertical graphene and other non-planar graphene structures [19]. In this study, the substrate-related peak at ~900 cm^{-1} was used for analysis in place of the main silicon-related peak at ~520 cm^{-1} to avoid issues related to peak intensity saturation.

The surface morphology and contact current of the samples were investigated using atomic force microscopy (AFM, NanoWizard®3, JPK Instruments, Bruker Nano GmbH, Berlin, Germany). Morphological images were acquired with an ACTA probe (Applied NanoStructures, Inc., Mountain View, CA, USA) operating in tapping mode with a tip radius of curvature of 6 nm. The contact current, which serves as a measure of the samples' electrical conductivity, was examined using contact-mode conductive atomic force microscopy (C-AFM) with a Pt/Ir-coated ANSCM-PT silicon tip probe (thickness: 25 ± 5 nm; App-Nano, Mountain View, CA, USA). Both the reflex and tip sides of the probe were coated. The spring constant of the ANSCM probe was 1.6 N/m with a tetrahedral tip shape, a radius of curvature (ROC) of 30 nm, a height of 14–16 µm, and a frequency of 61 kHz. Special Ag electrodes were fabricated on the graphene layer to investigate the surface contact current. The electrical current was measured as a function of the applied bias voltage (−10 to 10 mV). All measurements were performed at room temperature in ambient air, with a bit noise of 55 fA at a current gain of 1x.

4. Conclusions

This study successfully demonstrates the potential for directly synthesizing hydrogenated graphene at significantly reduced temperatures using plasma-enhanced chemical vapor deposition (PECVD). The optimization of gas flow rates, pressure, and temperature enabled the controlled synthesis of both pristine and hydrogenated graphene, with distinct structural and electronic properties.

Few-layer graphene can be synthesized at 700 °C, and bilayer graphene can be grown at a 600 °C temperature using specific gas flow ratios (e.g., 75 sccm H_2, 25 sccm CH_4). However, the contact current of the few-layer graphene estimated by CP-AFM was much larger than that of the bilayer graphene. Increasing methane flow while reducing hydrogen flow promotes hydrogenation and decreases defect density, as evidenced by changes in Raman

spectral features, including the I(D)/I(G) and I(2D)/I(G) ratios. A 1:1 H_2:CH_4 ratio enables the synthesis of hydrogenated graphene at temperatures as low as 450 °C, suggesting the feasibility of low-temperature processes for specific graphene-based applications. At 400 °C, the material transitions to the mixture of the hydrogenated graphene and a version of the highly hydrogenated carbon, marked by significant photoluminescence (PL) backgrounds in Raman spectra. These transitions can be explained by the formation of defective polycyclic aromatic hydrocarbon bonds, particularly at extreme hydrogenation levels.

The Raman analysis indicates the co-dominance of on-site and boundary defects in hydrogenated graphene, with the presence of D and D+D′ peaks correlating to localized sp^3 hybridization due to adsorbed hydrogen atoms.

It seems that graphene hydrogenation promoted graphene n-type doping. Lower synthesis temperatures (500–600 °C) enhance self-doping effects. However, growth at 400 °C temperature results in reduced doping, probably due to the changes in the character of the C-H bonds.

Atomic force microscopy (AFM) revealed distinct surface morphologies for pristine and hydrogenated graphene. Adjusting the gas flow and temperature allowed for control over surface morphology, enabling the synthesis of graphene and hydrogenated graphene films with tailored roughness and grain sizes.

CP-AFM measurements indicate that hydrogenated graphene can exhibit enhanced electrical performance compared to pristine graphene under specific conditions. This finding highlights the potential utility of hydrogenation for tuning graphene's electronic properties.

Our findings illustrate that precise control over PECVD synthesis parameters enables the growth of graphene with desired properties, paving the way for low-temperature, scalable fabrication of functional graphene materials. The demonstrated methodologies hold promise in terms of advancing graphene integration into next-generation technologies.

Supplementary Materials: The following supporting information can be downloaded at: https://www.mdpi.com/article/10.3390/molecules30010033/s1. Table S1: Samples' Raman scattering spectra parameters. Table S2: Selected samples' average AFM feature height (Z(nm)) and contact current. Figure S1: Raman spectra of the samples grown using different total gas flow and synthesis pressure. Figure S2: Plot I(2D)/I(G) vs. I(G)/I(Si). Figure S3: H_2 and CH_4 gas flow ratios and temperature effects on samples' Raman scattering spectra parameters. The work pressure was 20 mBar and the total gas flow was 100 sccm. Figure S4: Hydrogen and methane gas flow ratio effects on samples' Raman scattering spectra parameters. The work pressure was 20 mBar, the synthesis temperature was 500 °C, and the total gas flow was 200 sccm. Figure S5: Temperature effects on samples' Raman scattering spectra parameters. The work pressure was 20 mBar, the hydrogen gas flow was 100 sccm, and the methane gas flow was 100 sccm. Figure S6: Total gas flow and work pressure effects on samples' Raman scattering spectra parameters. The synthesis temperature was 500 °C and the hydrogen and methane gas flow ratio was equal to 1.

Author Contributions: Conceptualization, Š.M. and A.L.; investigation, Š.M., A.G., Š.J. and R.G.; writing—original draft preparation, Š.M. and A.L.; writing—review and editing, Š.M., A.L. and Š.J.; visualization, Š.M., A.L. and Š.J.; project administration, Š.M.; funding acquisition, Š.M. All authors have read and agreed to the published version of the manuscript.

Funding: This study was supported by the Research Council of Lithuania (Proposal No. P-MIP-22-235; Contract No S-MIP-22-67).

Institutional Review Board Statement: Not applicable.

Informed Consent Statement: Not applicable.

Data Availability Statement: Data are contained within the article.

Conflicts of Interest: The authors declare no conflicts of interest.

References

1. Liao, L.; Lin, Y.-C.; Bao, M.; Cheng, R.; Bai, J.; Liu, Y.; Qu, Y.; Wang, K.L.; Huang, Y.; Duan, X. High-speed graphene transistors with a self-aligned nanowire gate. *Nature* **2010**, *467*, 305–308. [CrossRef] [PubMed]
2. Miao, X.; Tongay, S.; Petterson, M.K.; Berke, K.; Rinzler, A.G.; Appleton, B.R.; Hebard, A.F. High efficiency graphene solar cells by chemical doping. *Nano Lett.* **2012**, *12*, 2745–2750. [CrossRef] [PubMed]
3. Lee, C.; Wei, X.; Kysar, J.W.; Hone, J. Measurement of the elastic properties and intrinsic strength of monolayer graphene. *Science* **2008**, *321*, 385–388. [CrossRef] [PubMed]
4. Tielrooij, K.-J.; Song, J.; Jensen, S.A.; Centeno, A.; Pesquera, A.; Zurutuza Elorza, A.; Bonn, M.; Levitov, L.; Koppens, F. Photoexcitation cascade and multiple hot-carrier generation in graphene. *Nat. Phys.* **2013**, *9*, 248–252. [CrossRef]
5. Tung, T.T.; Nine, M.J.; Krebsz, M.; Pasinszki, T.; Coghlan, C.J.; Tran, D.N.; Losic, D. Recent advances in sensing applications of graphene assemblies and their composites. *Adv. Funct. Mater.* **2017**, *27*, 1702891. [CrossRef]
6. Olabi, A.G.; Abdelkareem, M.A.; Wilberforce, T.; Sayed, E.T. Application of graphene in energy storage device—A review. *Renew. Sustain. Energy Rev.* **2021**, *135*, 110026. [CrossRef]
7. Kauling, A.P.; Seefeldt, A.T.; Pisoni, D.P.; Pradeep, R.C.; Bentini, R.; Oliveira, R.V.; Novoselov, K.S.; Castro Neto, A.H. The worldwide graphene flake production. *Adv. Mater.* **2018**, *30*, 1803784. [CrossRef]
8. Zheng, W.; Zhao, X.; Fu, W. Review of vertical graphene and its applications. *ACS Appl. Mater. Interfaces* **2021**, *13*, 9561–9579. [CrossRef]
9. Pumera, M.; Wong, C.H.A. Graphane and hydrogenated graphene. *Chem. Soc. Rev.* **2013**, *42*, 5987–5995. [CrossRef]
10. Deng, B.; Liu, Z.; Peng, H. Toward mass production of CVD graphene films. *Adv. Mater.* **2019**, *31*, 1800996. [CrossRef]
11. Yi, M.; Shen, Z. A review on mechanical exfoliation for the scalable production of graphene. *J. Mater. Chem. A* **2015**, *3*, 11700–11715. [CrossRef]
12. Kuila, T.; Bose, S.; Khanra, P.; Mishra, A.K.; Kim, N.H.; Lee, J.H. Recent advances in graphene-based biosensors. *Biosens. Bioelectron.* **2011**, *26*, 4637–4648. [CrossRef] [PubMed]
13. Xu, Y.; Cheng, C.; Du, S.; Yang, J.; Yu, B.; Luo, J.; Yin, W.; Li, E.; Dong, S.; Ye, P. Contacts between two-and three-dimensional materials: Ohmic, Schottky, and p–n heterojunctions. *ACS Nano* **2016**, *10*, 4895–4919. [CrossRef] [PubMed]
14. Di Bartolomeo, A. Graphene Schottky diodes: An experimental review of the rectifying graphene/semiconductor heterojunction. *Phys. Rep.* **2016**, *606*, 1–58. [CrossRef]
15. Wei, D.; Lu, Y.; Han, C.; Niu, T.; Chen, W.; Wee, A.T.S. Critical crystal growth of graphene on dielectric substrates at low temperature for electronic devices. *Angew. Chem.* **2013**, *52*, 14121–14126. [CrossRef]
16. Li, M.; Liu, D.; Wei, D.; Song, X.; Wei, D.; Wee, A.T.S. Controllable synthesis of graphene by plasma-enhanced chemical vapor deposition and its related applications. *Adv. Sci.* **2016**, *3*, 1600003. [CrossRef]
17. Gudaitis, R.; Lazauskas, A.; Jankauskas, Š.; Meškinis, Š. Catalyst-less and transfer-less synthesis of graphene on Si (100) using direct microwave plasma enhanced chemical vapor deposition and protective enclosures. *Materials* **2020**, *13*, 5630. [CrossRef]
18. Qi, Y.; Deng, B.; Guo, X.; Chen, S.; Gao, J.; Li, T.; Dou, Z.; Ci, H.; Sun, J.; Chen, Z. Switching vertical to horizontal graphene growth using faraday cage-assisted PECVD approach for high-performance transparent heating device. *Adv. Mater.* **2018**, *30*, 1704839. [CrossRef]
19. Meškinis, Š.; Vasiliauskas, A.; Guobienė, A.; Talaikis, M.; Niaura, G.; Gudaitis, R. The direct growth of planar and vertical graphene on Si (100) via microwave plasma chemical vapor deposition: Synthesis conditions effects. *RSC Adv.* **2022**, *12*, 18759–18772. [CrossRef]
20. Meškinis, Š.; Gudaitis, R.; Vasiliauskas, A.; Tamulevičius, S.; Niaura, G. Multiwavelength Raman Scattering Spectroscopy Study of Graphene Synthesized on Si (100) and SiO_2 by Microwave Plasma-Enhanced Chemical Vapor Deposition. *Phys. Status Solidi (RRL) Rapid Res. Lett.* **2020**, *14*, 1900462. [CrossRef]
21. Ferrari, A.C.; Basko, D.M. Raman spectroscopy as a versatile tool for studying the properties of graphene. *Nat. Nanotechnol.* **2013**, *8*, 235–246. [CrossRef] [PubMed]
22. Merlen, A.; Buijnsters, J.G.; Pardanaud, C. A guide to and review of the use of multiwavelength Raman spectroscopy for characterizing defective aromatic carbon solids: From graphene to amorphous carbons. *Coatings* **2017**, *7*, 153. [CrossRef]
23. Piazza, F.; Gough, K.; Monthioux, M.; Puech, P.; Gerber, I.; Wiens, R.; Paredes, G.; Ozoria, C. Low temperature, pressureless sp2 to sp3 transformation of ultrathin, crystalline carbon films. *Carbon* **2019**, *145*, 10–22. [CrossRef]
24. Luo, Z.; Yu, T.; Kim, K.-j.; Ni, Z.; You, Y.; Lim, S.; Shen, Z.; Wang, S.; Lin, J. Thickness-dependent reversible hydrogenation of graphene layers. *ACS Nano* **2009**, *3*, 1781–1788. [CrossRef]
25. Elias, D.C.; Nair, R.R.; Mohiuddin, T.; Morozov, S.; Blake, P.; Halsall, M.; Ferrari, A.C.; Boukhvalov, D.; Katsnelson, M.; Geim, A. Control of graphene's properties by reversible hydrogenation: Evidence for graphane. *Science* **2009**, *323*, 610–613. [CrossRef]
26. Melios, C.; Spencer, S.; Shard, A.; Strupiński, W.; Silva, S.R.P.; Kazakova, O. Surface and interface structure of quasi-free standing graphene on SiC. *2D Mater.* **2016**, *3*, 025023. [CrossRef]

27. Shtepliuk, I.; Ivanov, I.G.; Iakimov, T.; Yakimova, R.; Kakanakova-Georgieva, A.; Fiorenza, P.; Giannazzo, F. Raman probing of hydrogen-intercalated graphene on Si-face 4H-SiC. *Mater. Sci. Semicond. Process.* **2019**, *96*, 145–152. [CrossRef]
28. Meškinis, Š.; Vasiliauskas, A.; Gudaitis, R.; Andrulevičius, M.; Guobienė, A. Direct graphene synthesis on Si (1 0 0) by inductively coupled plasma beam source. *Appl. Surf. Sci.* **2022**, *580*, 152265. [CrossRef]
29. Casiraghi, C.; Piazza, F.; Ferrari, A.; Grambole, D.; Robertson, J. Bonding in hydrogenated diamond-like carbon by Raman spectroscopy. *Diam. Relat. Mater.* **2005**, *14*, 1098–1102. [CrossRef]
30. Cloutis, E.; Szymanski, P.; Applin, D.; Goltz, D. Identification and discrimination of polycyclic aromatic hydrocarbons using Raman spectroscopy. *Icarus* **2016**, *274*, 211–230. [CrossRef]
31. Hwang, J.-S.; Lin, Y.-H.; Hwang, J.-Y.; Chang, R.; Chattopadhyay, S.; Chen, C.-J.; Chen, P.; Chiang, H.-P.; Tsai, T.-R.; Chen, L.-C. Imaging layer number and stacking order through formulating Raman fingerprints obtained from hexagonal single crystals of few layer graphene. *Nanotechnology* **2012**, *24*, 015702. [CrossRef] [PubMed]
32. Casiraghi, C. Probing disorder and charged impurities in graphene by Raman spectroscopy. *Phys. Status Solidi (RRL) Rapid Res. Lett.* **2009**, *3*, 175–177. [CrossRef]
33. Casiraghi, C.; Pisana, S.; Novoselov, K.; Geim, A.K.; Ferrari, A. Raman fingerprint of charged impurities in graphene. *Appl. Phys. Lett.* **2007**, *91*, 233108. [CrossRef]
34. Clapa, M.; Gaj, J. Behavior of graphene under glow discharge plasma. *Sens. Actuators A Phys.* **2021**, *332*, 113069. [CrossRef]
35. Childres, I.; Jauregui, L.A.; Tian, J.; Chen, Y.P. Effect of oxygen plasma etching on graphene studied using Raman spectroscopy and electronic transport measurements. *New J. Phys.* **2011**, *13*, 025008. [CrossRef]
36. Lee, J.E.; Ahn, G.; Shim, J.; Lee, Y.S.; Ryu, S. Optical separation of mechanical strain from charge doping in graphene. *Nat. Commun.* **2012**, *3*, 1024. [CrossRef]
37. Fates, R.; Bouridah, H.; Raskin, J.-P. Probing carrier concentration in gated single, bi-and tri-layer CVD graphene using Raman spectroscopy. *Carbon* **2019**, *149*, 390–399. [CrossRef]
38. Bong, J.H.; Sul, O.; Yoon, A.; Choi, S.-Y.; Cho, B.J. Facile graphene n-doping by wet chemical treatment for electronic applications. *Nanoscale* **2014**, *6*, 8503–8508. [CrossRef]
39. Jankauskas, Š.; Gudaitis, R.; Vasiliauskas, A.; Guobienė, A.; Meškinis, Š. The graphene structure's effects on the current-voltage and photovoltaic characteristics of directly synthesized graphene/n-Si (100) diodes. *Nanomaterials* **2022**, *12*, 1640. [CrossRef]
40. Meškinis, Š.; Gudaitis, R.; Vasiliauskas, A.; Guobienė, A.; Jankauskas, Š.; Stankevič, V.; Keršulis, S.; Stirkė, A.; Andriukonis, E.; Melo, W. Biosensor based on graphene directly grown by MW-PECVD for detection of COVID-19 spike (S) protein and its entry receptor ACE2. *Nanomaterials* **2023**, *13*, 2373. [CrossRef]
41. Shi, Y.; Dong, X.; Chen, P.; Wang, J.; Li, L.-J. Effective doping of single-layer graphene from underlying SiO_2 substrates. *Phys. Rev. B Condens. Matter Mater. Phys.* **2009**, *79*, 115402. [CrossRef]
42. Wittmann, S.; Aumer, F.; Wittmann, D.; Pindl, S.; Wagner, S.; Gahoi, A.; Reato, E.; Belete, M.; Kataria, S.; Lemme, M.C. Dielectric surface charge engineering for electrostatic doping of graphene. *ACS Appl. Electron. Mater.* **2020**, *2*, 1235–1242. [CrossRef]
43. Kang, Y.-J.; Kang, J.; Chang, K.-J. Electronic structure of graphene and doping effect on SiO_2. *Phys. Rev. B Condens. Matter Mater. Phys.* **2008**, *78*, 115404. [CrossRef]
44. Banszerus, L.; Janssen, H.; Otto, M.; Epping, A.; Taniguchi, T.; Watanabe, K.; Beschoten, B.; Neumaier, D.; Stampfer, C. Identifying suitable substrates for high-quality graphene-based heterostructures. *2D Mater.* **2017**, *4*, 025030. [CrossRef]
45. Jee, H.-g.; Jin, K.-H.; Han, J.-H.; Hwang, H.-N.; Jhi, S.-H.; Kim, Y.D.; Hwang, C.-C. Controlling the self-doping of epitaxial graphene on SiC via Ar ion treatment. *Phys. Rev. B Condens. Matter Mater. Phys.* **2011**, *84*, 075457. [CrossRef]
46. Eriksson, J.; Puglisi, D.; Vasiliauskas, R.; Lloyd Spetz, A.; Yakimova, R. Thickness uniformity and electron doping in epitaxial graphene on SiC. *Mater. Sci. Forum* **2013**, *740–742*, 153–156. [CrossRef]
47. Goniszewski, S.; Adabi, M.; Shaforost, O.; Hanham, S.; Hao, L.; Klein, N. Correlation of p-doping in CVD Graphene with Substrate Surface Charges. *Sci. Rep.* **2016**, *6*, 22858. [CrossRef]
48. Eckmann, A.; Felten, A.; Mishchenko, A.; Britnell, L.; Krupke, R.; Novoselov, K.S.; Casiraghi, C. Probing the nature of defects in graphene by Raman spectroscopy. *Nano Lett.* **2012**, *12*, 3925–3930. [CrossRef]
49. Venezuela, P.; Lazzeri, M.; Mauri, F. Theory of double-resonant Raman spectra in graphene: Intensity and line shape of defect-induced and two-phonon bands. *Phys. Rev. B Condens. Matter Mater. Phys.* **2011**, *84*, 035433. [CrossRef]
50. Whitener, K.E. Hydrogenated graphene: A user's guide. *J. Vac. Sci. Technol. A* **2018**, *36*, 05G401. [CrossRef]
51. Matis, B.R.; Burgess, J.S.; Bulat, F.A.; Friedman, A.L.; Houston, B.H.; Baldwin, J.W. Surface doping and band gap tunability in hydrogenated graphene. *ACS Nano* **2012**, *6*, 17–22. [CrossRef] [PubMed]
52. Ma, Y.; Harding, J.D.; Tu, X. Catalyst-free low temperature conversion of n-dodecane for co-generation of COx-free hydrogen and C2 hydrocarbons using a gliding arc plasma. *Int. J. Hydrog. Energy* **2019**, *44*, 26158–26168. [CrossRef]
53. Wang, S.; Wang, J.; Feng, D.; Wang, F.; Zhao, Y.; Sun, S. Plasma-induced methane catalytic cracking: Effects of experimental conditions. *Int. J. Hydrog. Energy* **2024**, *63*, 284–293. [CrossRef]

54. Muñoz, R.; Munuera, C.; Martínez, J.I.; Azpeitia, J.; Gómez-Aleixandre, C.; García-Hernández, M. Low temperature metal free growth of graphene on insulating substrates by plasma assisted chemical vapor deposition. *2D Mater.* **2016**, *4*, 015009. [CrossRef] [PubMed]
55. Chaitoglou, S.; Bertran, E. Effect of temperature on graphene grown by chemical vapor deposition. *J. Mater. Sci.* **2017**, *52*, 8348–8356. [CrossRef]
56. Klingsporn, M.; Kirner, S.; Villringer, C.; Abou-Ras, D.; Costina, I.; Lehmann, M.; Stannowski, B. Resolving the nanostructure of plasma-enhanced chemical vapor deposited nanocrystalline SiOx layers for application in solar cells. *J. Appl. Phys.* **2016**, *119*, 223104. [CrossRef]
57. Bo, Z.; Yang, Y.; Chen, J.; Yu, K.; Yan, J.; Cen, K. Plasma-enhanced chemical vapor deposition synthesis of vertically oriented graphene nanosheets. *Nanoscale* **2013**, *5*, 5180–5204. [CrossRef]
58. Dresselhaus, M.; Jorio, A.; Souza Filho, A.; Saito, R. Defect characterization in graphene and carbon nanotubes using Raman spectroscopy. *Philos. Trans. R. Soc. A Math. Phys. Eng. Sci.* **2010**, *368*, 5355–5377. [CrossRef]
59. No, Y.-S.; Choi, H.K.; Kim, J.-S.; Kim, H.; Yu, Y.-J.; Choi, C.-G.; Choi, J.S. Layer number identification of CVD-grown multilayer graphene using Si peak analysis. *Sci. Rep.* **2018**, *8*, 571. [CrossRef]

Disclaimer/Publisher's Note: The statements, opinions and data contained in all publications are solely those of the individual author(s) and contributor(s) and not of MDPI and/or the editor(s). MDPI and/or the editor(s) disclaim responsibility for any injury to people or property resulting from any ideas, methods, instructions or products referred to in the content.

5 straipsnis

Straipsnio pavadinimas	*Graphene direct growth by microwave PECVD on h-BN films deposited by reactive HIPIMS*
Straipsnio bendraautoriai	*Šarūnas Meškinis; Šarūnas Jankauskas; Andrius Vasiliauskas; Vytautas Stankus; Asta Guobienė; Kipras Lukoševičius; Augmantas Jasutis; Rimantas Gudaitis*
Leidėjas, žurnalo pavadinimas	*IOP, Nano Express*
Metai	*2025*

INCLUSIVE PUBLISHING TRUSTED SCIENCE
PURPOSE-LED PUBLISHING™

PAPER • **OPEN ACCESS**

Graphene direct growth by microwave PECVD on h-BN films deposited by reactive HIPIMS

To cite this article: Šarūnas Meškinis *et al* 2025 *Nano Ex.* **6** 025007

View the article online for updates and enhancements.

You may also like

- Bio inspired nanocontainers: intracellular delivery and controlled cargo release
Kanika Arora, Sherilraj PM and Shyam Lal Mudavath
- Synergistic pseudocapacitive behavior of Cr_2CT_x MXene and Cu-PTC MOF in CM-II: an Electroactive composite
Samika Anand, Madhushree R, Kalathiparambil Rajendra Pai Sunajadevi et al.
- Advancing the design of gold nanomaterials with machine-learned potentials
Kithma Sajini, Caroline Desgranges and Jerome Delhommelle



This content was downloaded from IP address 158.129.12.163 on 02/06/2025 at 16:05

IOP Publishing Nano Express 6 (2025) 025007 https://doi.org/10.1088/2632-959X/add6bb

NANO EXPRESS

PAPER

Graphene direct growth by microwave PECVD on h-BN films deposited by reactive HIPIMS

Šarūnas Meškinis, Šarūnas Jankauskas, Andrius Vasiliauskas, Vytautas Stankus, Asta Guobienė, Kipras Lukoševičius, Augmantas Jasutis and Rimantas Gudaitis

Institute of Materials Science, Kaunas University of Technology, K Baršausko 59, LT-51423, Kaunas, Lithuania

E-mail: sarunas.meskinis@ktu.lt **and** sarunas.jankauskas@ktu.lt

Keywords: graphene, h-BN, HIPIMS, AFM, CAFM, photoelectric properties, direct synthesis by microwave PECVD

Supplementary material for this article is available online

OPEN ACCESS

RECEIVED
10 February 2025

REVISED
30 April 2025

ACCEPTED FOR PUBLICATION
9 May 2025

PUBLISHED
20 May 2025

Original content from this work may be used under the terms of the Creative Commons Attribution 4.0 licence.

Any further distribution of this work must maintain attribution to the author(s) and the title of the work, journal citation and DOI.

Abstract

This research explores the synthesis of graphene using microwave plasma-enhanced chemical vapor deposition (PECVD) on a hexagonal boron nitride interlayer deposited by reactive high-power impulse magnetron sputtering. The effects of h-BN interlayer composition and thickness on the graphene structure, morphology, and electronic properties were investigated using Raman scattering spectroscopy, atomic force microscopy, and conductive atomic force microscopy. The electrical and photoelectrical characteristics of the graphene/Si(100) and graphene/h-BN/Si(100) diodes were studied. It was revealed that graphene self-doping effects, primarily originating from substrate-induced charge transfer, can be partially controlled, and that the dominant defect type of graphene can be changed by varying the boron interlayer thickness. The graphene layers synthesized on the SiO_2 film were substantially smoother than those grown on the boron nitride films. Graphene grown on h-BN had a substantially greater surface current than graphene synthesized on the SiO_2 layer. There was no relationship between graphene self-doping and graphene surface conductivity. Nevertheless, it should be noted that reduced graphene self-doping was achieved even though the surface roughness of the h-BN film was significantly greater than that of the SiO_2 film or Si(100), and B–H and C–H bonds were present in some h-BN films. Tunneling is the primary reverse current charge transfer mechanism, similar to graphene/Si(100) diodes, and h-BN interlayers cannot decrease the reverse dark current. Despite these circumstances, the insertion of the h-BN interlayer resulted in a significant increase in the photocurrent, short-circuit current, and open-circuit voltage compared to those of the graphene/Si(100) heterojunction. The observed effects of the h-BN interlayer on the graphene/Si (100) diode properties were explained by the competition between the effects of the different h-BN film compositions, thicknesses, and roughness on the one hand and the influence of the graphene structure and electronic properties.

1. Introduction

The - two-dimensional hexagonal carbon nanomaterial, graphene, has captured the attention of the scientific world owing to its unmatched mechanical, optical, and electronic properties [1–3]. In particular, their use as substitute for metal electrodes and transparent conductor layers in optoelectronic devices is promising. Most notably, replacing materials containing rare chemical elements, such as indium in indium tin oxide (ITO) [4], is crucial for maintaining a cost-effective approach in device fabrication while additionally increasing device performance [5–11]. For example, by acting as an effective charge extractor in perovskite solar cells, graphene increases the power conversion efficiency to 6.7% when produced in monolayer form, and to 11.5% when a multilayer film is used [12].

© 2025 The Author(s). Published by IOP Publishing Ltd

To ensure that such device fabrication retains scalability and performance, direct graphene fabrication appears to be a feasible route, compared to the readily available exfoliation and transfer of graphene grown by chemical vapor deposition on catalytic copper foil [13, 14]. Graphene can be synthesized directly on different semiconductors and dielectric substrates using various vapor phase-based deposition methods. 'Conventional' chemical vapor deposition can be applied for this purpose. The graphene synthesis temperature can be significantly reduced from 1000 °C–1400 °C [15–18] to 500 °C–700 °C using high-density plasma assistance [19–21]. However, directly synthesized graphene is usually nanocrystalline and contains many grain-boundary defects [22, 23]. This limits the performance of directly synthesized graphene-based semiconductor devices and sensors [21].

The densities of grain boundaries and other defects can be significantly reduced by selecting a suitable substrate for direct graphene synthesis. In particular, graphene and hexagonal boron nitride (h-BN) share very similar hexagonal crystal lattice parameters, enabling epitaxial growth of low-defect-density graphene on boron nitride [24–29]. However, exfoliated h-BN flakes or h-BN synthesized by chemical vapor deposition (CVD) on copper foil have been used in graphene epitaxial growth experiments.

There are very few studies on graphene synthesis using h-BN interlayers grown directly onto non-catalytic substrates such as silicon or SiO_2, and existing studies ([30]) have not succeeded in synthesizing graphene with low defect density nor investigated its functional device properties. Moreover, previous studies focused solely on structural and compositional analysis of graphene without exploring optoelectronic performance. In this study, we employed high-power impulse magnetron sputtering (HIPIMS) to grow h-BN interlayers directly onto silicon at a significantly reduced temperature (800 °C) compared to the 1000 °C typically required for chemical vapor deposition (CVD) [30]. Our approach also utilizes nitrogen gas instead of hazardous ammonia borane precursors, thus enhancing safety and purity and reducing contamination risks. Additionally, by applying plasma-enhanced CVD for subsequent graphene synthesis, we lowered the required graphene growth temperature to 700 °C, substantially below the 1000 °C used in [30]. This significant reduction in synthesis temperatures offers substantial practical advantages for device integration, scalability, substrate preservation, and industrial feasibility.

Crucially, this study provides the first systematic investigation of the effects of h-BN interlayer composition and thickness on structure, morphology, electrical, photovoltaic, and photoelectric properties specifically for graphene directly synthesized on h-BN interlayers grown onto non-catalytic substrates without transfer processes. We demonstrate that graphene self-doping effects can be partially controlled and that the insertion of an optimized h-BN interlayer significantly increases the photocurrent, short-circuit current, and open-circuit voltage of graphene/Si(100) photodiodes. Additionally, our results indicate that the dominant defect type in graphene directly grown on non-catalytic substrates can be influenced by adjusting the thickness of the underlying h-BN interlayer, offering a valuable approach for tailoring graphene properties in device applications.

2. Materials and methods

In this study, monocrystalline, double-side-polished, n-type Si(100) wafers were used as substrates. The silicon wafer resistivity was in the range 1–10 Ω·cm. Some graphene samples studied by contact-mode conductive atomic force microscopy were synthesized on the 300 nm thickness SiO_2 films grown by the thermal oxidation of Si(100) to avoid the possible influence of the semiconducting Si(100) substrate. The substrates were coated by hexagonal boron nitride (h-BN) interlayers. h-BN films were deposited by high-power impulse magnetron sputtering (HIPIMS) at 800 °C. The impulse parameters were as follows: $t_{on} = 17$ μs, $t_{of} = 150$ μs, impulse current of 1.2 A, average current constant during all processes and was about ~0.12 A, average voltage of ~930 V, and distance between the substrate and magnetron cathode of 15 cm. Other interlayer deposition conditions are listed in table 1. h-BN interlayer deposition conditions were selected based on our previous study [31].

Graphene was synthesized using a microwave plasma-enhanced chemical vapor deposition system (Cyrannus Innovative Plasma Systems (Iplas) GmbH, Germany). A special enclosure was used to prevent the excessive action of direct plasma on the substrate and growing graphene layer [20, 32, 33]. Before the growth of graphene, hydrogen plasma was ignited to clean the substrate surface. The plasma power was set at 1 kW, process temperature was 700 °C, hydrogen flow was 200 sccm, pressure was 10 mbar, and cleaning time was 10 min. Subsequently, methane gas was introduced and graphene synthesis was initiated. The graphene growth process conditions were as follows: plasma power 0.7 kW, hydrogen gas flow, 75 sccm; methane gas flow, 25 sccm; pressure, 10 mBar; substrate temperature, 700 °C; synthesis time, 60 min.

Graphene/Si (100) diodes were fabricated to investigate their electrical and photoelectric properties. First, a sample consisting of graphene grown on a Si(100) piece was cleaned. Cleaning consisted of boiling in dimethylformamide and acetone, etching in a 1:1:5 solution of $NH_4OH + H_2O_2 + H_2O$, impurity removal using

Table 1. H-BN interlayer deposition conditions.

Sample no.	Substrate	N_2 flow (sccm)	h-BN film Growth time (s)	h-BN film thickness (nm)
1	Si(100)	Reference sample (no h-BN interlayer)	—	—
2	SiO_2	Reference sample (no h-BN interlayer)	—	—
3	Si(100)	152	36	1
4	Si(100)	152	108	3
5	Si(100)	152	180	5
6	Si(100)	152	360	10
7	Si(100)	152	540	15
8	Si(100)	152	720	20
9	Si(100)	152	3600	100
10	Si(100)	152	10800	300
11	Si(100)	197	33	1
12	Si(100)	197	99	3
13	Si(100)	197	165	5
14	Si(100)	197	330	10
15	Si(100)	197	495	15
16	Si(100)	197	660	20
17	Si(100)	197	3600	110
18	Si(100)	197	10800	330

a 1:50 solution of $HF + H_2O$, and etching using a 1:1:6 solution of $HCl + H_2O_2 + H_2O$. The Al back contact was e-beam-evaporated on the uncoated side of the silicon. Cr/Cu electrodes were deposited on graphene through a mask with 500 μm circular holes. The thicknesses of the Cr interlayer and Cu layer were 20 nm and 200 nm, respectively. More information on the fabrication of graphene/Si(100) diodes can be found elsewhere [32, 33].

The boron nitride film thickness was determined using a laser ellipsometer Gaertner L-115 operating with a He–Ne laser ($\lambda = 632.8$ nm). The thickness of films thinner than 20 nm was evaluated by considering the deposition rate estimated for thicker films and the deposition time.

Raman scattering measurements were performed using a Raman scattering spectrometer InVia (Renishaw, Wotton-, UK). The excitation beam from a diode laser with a wavelength of 532 nm was focused on the sample using a 50× objective lens (NA = 0.75; Leica, Solms, Germany). The Raman spectra were measured at least three times at different sample locations and the average values were calculated. The D, G, D′, and 2D peaks were fitted using Lorentzian functions. The intensity ratio of the 2D and G peaks (I(2D)/I(G)) was used to estimate the number of graphene layers [34]. The I(2D)/I(G) ratio decreased with increasing number of graphene layers. The intensity ratio of the D to G peaks (I(D)/I(G)) was calculated to evaluate the defect density of the graphene [35, 36]. The I(D)/I(G) ratio increase with increased graphene's defects density. Since there are various defects present in graphene [37], the intensity ratios of the D and D′ peaks were analyzed to determine the prevailing defect type [38, 39]. Notably, the I(D)/I(D′) ratio 7 is typical for vacancies, the I(D)/I(D′) ratio 3.5 is typical for boundary defects, and the ratio 1.3 is typical for on-site defects. The positions of the G and 2D peaks (Pos(G) and Pos(2D)) were considered as parameters sensitive to graphene doping and stress [40, 41].

The surface morphology and current of the samples were investigated using atomic force microscopy (AFM, NanoWizard® 3, JPK Instruments, Bruker Nano GmbH, Berlin, Germany). Morphological images were acquired with an ACTA probe (Applied NanoStructures, Inc., Mountain View, CA, USA) operating in the tapping mode with a tip radius of curvature of 6 nm. The surface current, which serves as a measure of the electrical conductivity of the samples, was examined using contact-mode conductive atomic force microscopy (C-AFM) with a Pt/Ir-coated ANSCM-PT silicon tip probe (thickness: 25 ± 5 nm; App-Nano, Mountain View, CA, USA). Both the reflex and tip sides of the probe were coated. The spring constant of the ANSCM probe was 1.6 N m^{-1} with a tetrahedral tip shape, a radius of curvature (ROC) of 30 nm, a height of 14–16 μm, and a frequency of 61 kHz. Ag electrodes were fabricated on the graphene layer to investigate the surface contact current. The surface current was measured as a function of the applied bias voltage (−10 to 10 mV). All the measurements were performed at room temperature in ambient air with a slight noise of 55 fA at a current gain of 1×.

The current-voltage (I–V) characteristics were measured using a Keithley 6487 picoampermeter/voltage source. The measurements were performed at several points on the sample to evaluate the possible dispersion of the characteristics. The photovoltaic and photoelectric properties of the fabricated devices were investigated in three different regimes. These were the dark mode (I–V characteristic measured in the dark), UV mode (when the sample was illuminated by a 406 nm wavelength light-emitting diode (LED)), and IR mode (when the sample was illuminated by an 800 nm wavelength light-emitting diode). The currents supplied to the LEDs were selected to ensure the same optical power (5.2 mW) between different measurement modes. Diode behavior was studied by examining the reverse current (0.5 V) measured in the dark. The photovoltaic parameters (short-circuit

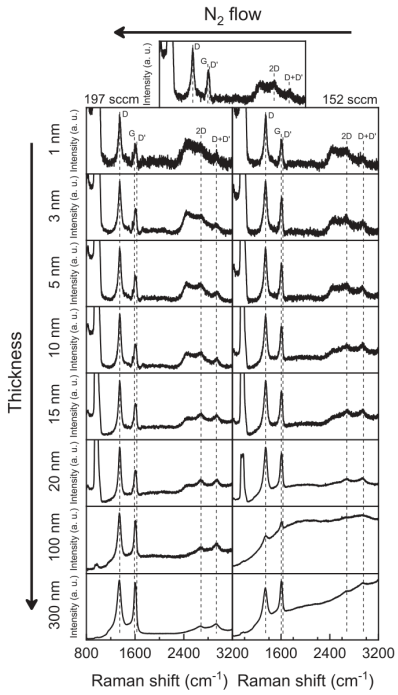


Figure 1. Typical Raman scattering spectra of the graphene synthesized on the h-BN interlayers of the different thickness. The reference spectra of the graphene synthesized directly on the Si(100) is on the top.

current (I_{SC}) and open-circuit voltage (U_{OC})) were estimated using the I-V characteristics measured under illumination. The photocurrent was calculated as the difference between the reverse current measured under illumination and that measured in the dark: In this case, the reverse measurement voltage was 0.5 V.

3. Results and discussion

The structures of the samples were investigated using Raman scattering spectroscopy. Typical spectra of h-BN interlayers are shown in figure S1. The Raman scattering spectra of graphene synthesized on different h-BN interlayers and the reference sample grown directly on Si(100) are presented in figure 1. G, 2D, D+D′, and D+D′ peaks were observed. A defect-related D peak was observed in all samples. The D peak was positioned at ~1347 cm^{-1} in the Raman spectrum of graphene synthesized on Si(100). The main h-BN Raman peak was observed at ~1370 cm^{-1} (see figure S1 [31]). It can be stated that an essential decrease in the graphene defect density and growth of the defect-free graphene was not achieved by using the HIPIMS-deposited h-BN interlayer. However, the h-BN interlayer provides other benefits, as explained later in this paper. It must be mentioned that for graphene directly synthesized on the h-BN interlayer grown by chemical vapor deposition on the SiO_2 film [30], the I(D)/I(G) ratio was similar to that in the present study. On the other hand, in present study, 2D peak was significantly more pronounced compared to the results reported in [30], where the 2D peak was almost invisible [30]. The defect-related D′ peak is presented as a G-peak shoulder. Luminescence background was observed in the Raman spectra of the samples deposited on thicker h-BN interlayers. This was

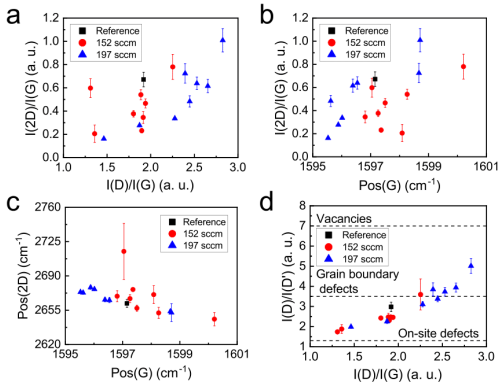


Figure 2. Interdependencies of Raman parameters. I(2D)/I(G) versus I(D)/I(G) (a); I(2D)/I(G) versus Pos(G) (b); Pos(2D) versus Pos (G) (c); I(D)/I(D′) versus I(D)/I(G) (d). Error bars show the dispersion of Raman parameters within the same sample.

more pronounced when h-BN interlayers were deposited using 152 sccm nitrogen gas flow. This is in good accordance with the peculiarities of the h-BN interlayer spectra—for h-BN films deposited using 152 sccm N_2 gas flow, significant luminescence background and luminescence lumps were observed (figure S2 and [31]) due to the formation of B–H and C–H bonds [31]. It should be mentioned that in the case of the graphene synthesized on the thicker h-BN interlayers, the 2D peak was less intensive than D+D′. This behavior is typical for hydrogenated graphene [42–45]. A similar luminescence background was observed previously in graphene directly synthesized on h-BN interlayers grown by CVD on SiO_2 substrates [30] and on catalytic copper foil [26], indicating common characteristics independent of substrate choice.

Subsequently, the Raman scattering spectra of the graphene samples were analyzed. As mentioned above, the I(2D)/I(G) ratio was proportional to the number of graphene layers [34]. Simultaneously, the presence of defects and doping can significantly reduce the I(2D)/I(G) ratio [35, 40, 46, 47]. In particular, the I(2D)/I(G) ratio decreases, and the G peak position shifts to higher wavenumbers (upshifted) because of doping [40, 47]. However, in our case, the I(2D)/I(G) ratio tended to increase with the I(D)/I(G) ratio and Pos(G) upshifting (figure 2). Thus, the I(2D)/I(G) ratio can be used to evaluate the number of graphene layers.

Pos(2D) was downshifted with Pos(G) upshift (figure 2). Some deviation from this tendency was only the Pos (2D) of the graphene synthesized on the 1 nm thickness h-BN interlayer deposited using a 152 sccm N_2 gas flow. The Pos(2D) downshift with Pos(G) is typical for n-type doped graphene [40, 41]. A similar behavior reported in our previous studies on graphene directly synthesized on Si(100) substrates was explained by the - substrate-induced self-doping of graphene [20, 32, 48]. It should be noted that graphene self-doping effects were also reported for graphene directly synthesized on the h-BN interlayer grown by chemical vapor deposition onto the SiO_2 film [30] and for h-BN and graphene layers grown by CVD on catalytic substrates and subsequently transferred onto SiO_2 [49].

A single deviation from these clear trends was observed for the graphene synthesized on the 100 nm thick h-BN interlayer deposited using a 152 sccm nitrogen flow, showing anomalously high Pos(2D) values (~2720 cm^{-1}) and significant dispersion. Such elevated Pos(2D) values may indicate accidental local p-type doping due to adsorbates or surface contamination, resulting in spatially varying doping characteristics and increased uncertainty within this particular sample [40, 41]. However, this isolated anomaly does not compromise the robustness or clarity of the overall trends across all other samples. Although repeating this isolated measurement was beyond the scope of the current work, future targeted studies could further clarify this minor deviation. Exact Raman parameter values of samples and their corresponding h-BN interlayer thicknesses can be seen in table S1.

It must be mentioned that exfoliated graphene placed on exfoliated h-BN exhibited reduced unintentional self-doping compared to graphene on SiO2 [50]. Now, one can see that graphene self-doping reduction can be achieved using the h-BN films deposited reactive magnetron sputtering, the technology compatible with large-

area industrial-scale deposition and direct graphene synthesis. Regarding the possible source of substrate-induced graphene self-doping, it should be mentioned that in the case of h-BN grown by CVD on catalytic Cu foil, the formation of surface defects (presence of amorphous BN or cubic BN clusters in the film) and presence of impurities (BxCyNz particles) have been reported, resulting in graphene self-doping [51]. In our case, a similar behavior was assumed. In addition, defects may be created because of the possible interactions between graphene and the h-BN interlayer during graphene synthesis [52]. The abovementioned defects and impurities can induce additional h-BN surface potentials and their local variations, resulting in self-doping of graphene.

The I(D)/I(D′) ratio increased with the I(D)/I(G) ratio. Thus, the I(D)/I(G) ratios of the samples with I(D)/I(D′) ratios close to those of graphene-containing on-site defects were the lowest. It should be mentioned that graphene on-site defects are usually associated with hydrogen bonding to graphene [39]. As pointed out above, the D + D′ peak was more intense than the 2D peak. This also supports the hypothesis of graphene hydrogenation [42–45]. No relationship between Pos(G) and I(D)/I(D′) was found, indicating that the - n-type graphene self-doping observed in this study was not related to graphene hydrogenation.

The effects of the h-BN interlayer on the structure and electronic properties of the synthesized graphene were investigated (figure 3). The defect density increased and the number of graphene layers decreased with the insertion of the boron nitride interlayer. An increase in the h-BN interlayer thickness resulted in a subsequent decrease in the I(D)/I(G) ratio and an increase in the number of graphene layers. With the insertion of the ultrathin h-BN interlayer, Pos(G) was upshifted and Pos(2D) was downshifted. Subsequently, Pos(G) downshifted and Pos(2D) upshifted with increasing boron nitride interlayer thickness.

One can see that Pos(G) and Pos(2D) shift towards the values typical for undoped and stress free graphene ($1581.6 \pm 0.2\ cm^{-1}$ and $2676.9 \pm 0.7\ cm^{-1}$, respectively [41]) with increased h BN film thickness when the h BN interlayer is thicker than 5 nm. This indicates reduced self-doping of graphene. However, self-doping has not yet been completely eliminated. The insertion of the h BN interlayer also affects the prevailing defect type in graphene, as can be seen in the I(D)/I(D′) versus h-BN interlayer thickness plot (figure 3(e)). In addition to the prevailing boundary defects typical of directly synthesized graphene, the 1 nm thick BN interlayer promoted the formation of vacancy defects. In the case of graphene grown on a 100 nm or thicker boron nitride interlayer, hydrogenation related to on-site defects and boundary defects dominated.

The structure of the grown graphene was investigated by AFM study of the surface morphology and conductivity of the samples to reveal the peculiarities of graphene growth on HIPIMS-deposited h-BN and graphene electronic properties. The Si/SiO_2 substrate was much smoother than the - h-BN film (figure 4). An aberrant grainy but smooth surface, with a root mean square roughness R_q of 0.64 nm, and grain sizes of 20 , 15 , and 3 nm in length, width, and height, respectively, was observed. After graphene deposition, the topography showed little to no change. However, the R_q value changed significantly to 1.68 nm. Similarly, the surface current signal increased to 3.77 pA (table S2). Both h-BN and graphene deposited on it showed a similar increase in R_q with increasing h-BN thickness. The graphene surface roughness clearly increased with the substrate surface roughness, and in all cases, the R_q of graphene was slightly larger than that h-BN interlayer R_q (figure S3). The h-BN thin film surface current readouts were similar to the background signal and did not exceed 1.5–2 pA. When the thickness of h-BN was increased to 110 nm, one can observe hexagonal structures with lengths, widths, and heights of 100 nm, 80 nm, and 15 nm were obtained. In this sample, there is an increase in R_q to 5.55 nm and the current value increase to 51.9 pA after graphene deposition, whereas the topography view seems indifferent. Further increasing the thickness of h-BN to 330 nm, a typical hexagonally shaped surface, with $R_q = 14.83$ nm and the size of the structural element 220 nm, 200 nm, and 40 nm in length, width, and height, can be observed. In this case, graphene deposition noticeably changed the surface morphology, increasing R_q to 18.86 nm. The grain sizes, in terms of length, width, and height, were 220, 60 , and 50 nm, respectively. For a given h-BN thickness of 330 nm, an increase in the average surface current signal (6.6 pA) was observed. The h-BN film composition was also important. The graphene synthesized on the 100 nm thickness h-BN film grown using different N_2 gas flows (152 sccm) was smoother, and its surface current was somewhat lower (32 pA compared to 52 pA). Hexagonally shaped structures were observed. From figure 5, it can be seen that, with an increase in R_q of graphene deposited on h-BN, the surface current signal increases and reaches a maximum value when $R_q = 5.55$ nm. The surface current signal decreases when a further increase in R_q is observed. The topographical parameters are listed in table S2. No relationship was observed between graphene surface conductivity and self-doping (figure S4). However, it should be noted that despite the h-BN films' surface roughness being much larger than the roughness of the SiO_2 film or Si(100) and despite the possible presence of B–H and C–H bonds in some h-BN films used in the present study (see [31] figure S1), reduced graphene self-doping was achieved, similar to the cases of exfoliated or transferred graphene and h-BN stacks[49, 50, 52].

In summary, we show that the synthesis of h-BN thin films on a Si/SiO_2 substrate using a N_2 gas flow of 197 sccm yields a hexagonal boron nitride surface with distinct 220 nm × 200 nm grains in length and width, respectively, with varying heights. Subsequently, the deposited graphene exhibits grain narrowing and

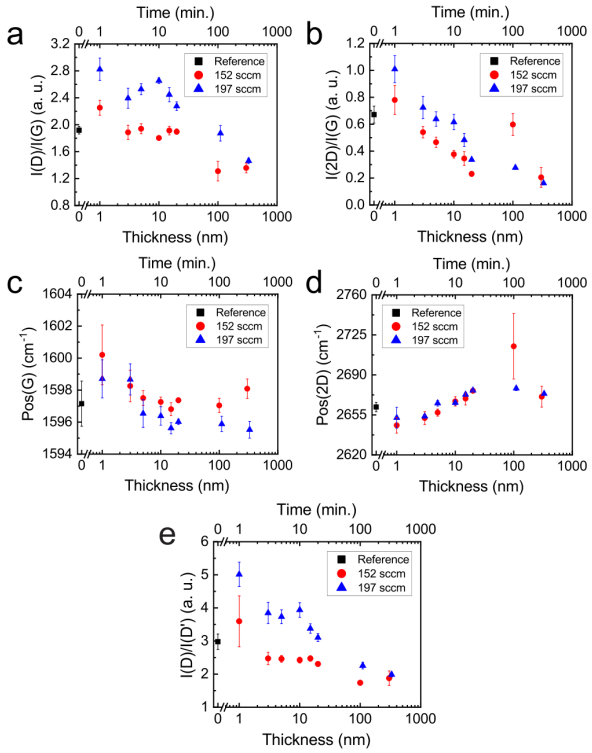


Figure 3. H-BN interlayer thickness effects on the I(D)/I(G) (a), I(2D)/I(G) (b), Pos(G) (c), Pos(2D) (d), I(D)/I(D′) (e). Error bars show the dispersion of Raman parameters within the same sample.

heightening. The average surface current signals increased because of the notable differences in the grain structure height. With high h-BN thickness, the surface current decreased. However, a relatively high surface current region was still observed in the sample.

Typical current-voltage (I–V) characteristics of the graphene/h-BN/Si(100) and graphene/Si(100) diodes are presented in figure 6 (I–V curves of individual samples are shown in figures S5–S17). In all the cases, the insertion of the h-BN interlayer resulted in an increased forward voltage. However, linear or quasi-linear reverse I-V characteristics, typical for directly synthesized graphene/Si(100) heterojunctions [32], were observed for nearly all samples. Thus, the primary reverse current charge transport mechanism is tunneling [32]. The insertion of the h-BN interlayer did not reduce the leakage current of the graphene/Si(100) heterojunction (figures 6, 7(a)). The leakage currents of the graphene/h-BN/Si(100) with an interlayer grown using 152 sccm nitrogen gas flow were higher than those of h-BN deposited using 197 sccm N_2 gas flow. This is likely related to the much higher carbon content in the films grown using a 152 sccm nitrogen gas flow (>15 at% versus ∼3 at% [31]). However, it can be seen in figures 7(b), (c) that the h-BN interlayer can be used to increase the diode photocurrent and short circuit current. The effect was much more pronounced when the interlayer was grown under a 152 sccm N_2 gas flow. It can be seen that the photocurrent and short-circuit current non-monotonically depended on the thickness; the lowest photocurrent and the smallest short-circuit current were observed for

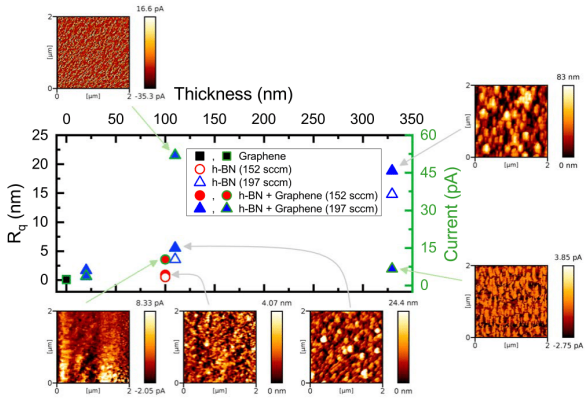


Figure 4. The dependence of the surface current (green axis and outline) and the root mean square roughness (R_q) (black axis) on the thickness of the h-BH thin film. Sample colors follow same style as in previous plots, where different N2 flows used during h-BN deposition are denoted with red circle (152 sccm) and blue triangle (197 sccm). Reference graphene sample is shown as black square. Sample points outlined with green color indicate a C-AFM value which can be deduced from green axis on the right side. AFM and C-AFM images show characteristic graphene/h-BN/Si(100) samples and corresponding points in the plot.

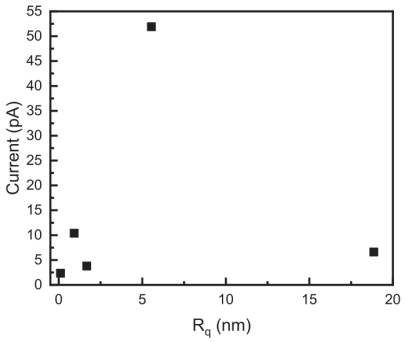


Figure 5. Graphene/h-BN/Si/SiO_2 surface current versus R_q.

samples fabricated using a 5–15 nm thick interlayer. The average open-circuit voltage of the graphene/h-BN/Si (100) diode was almost always higher than that of the graphene/Si diode. It should be mentioned that excitation by IR light for most samples resulted in a higher photocurrent, short-circuit current, and open-circuit voltage than UV light excitation. In our previous study, similar behavior was observed for the electrical and photovoltaic properties of graphene/Si(100) heterojunctions [32].

No clear dependence of the electrical and photoelectric properties of the samples on the Raman scattering spectral parameters was observed (figure S5). However, some weak expression tendencies were observed. The average reverse dark current decreased with an increase in the graphene defect density and number of layers. Thus, the graphene hydrogenation should be minimized to decrease the reverse dark current. The short-circuit current and photocurrent increased with Pos(G) upshift. The I_{SC} and photocurrent initially decreased and then

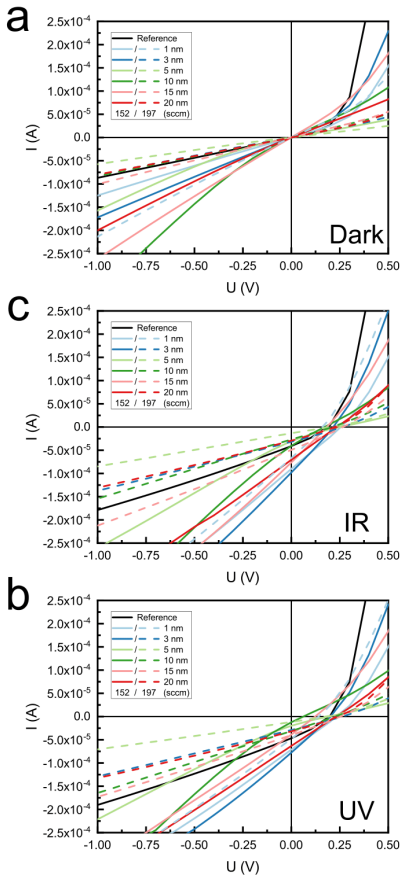


Figure 6. Graphene/h-BN/Si(100) I-V curves under no (a), IR (b) and UV (c) illumination.

increased with the Pos(2D) upshift. It can be assumed that graphene self-doping may be beneficial for increasing the photocurrent and the short-circuit current. The open-circuit voltage initially increased with defect density and subsequently decreased. However, no U_{OC} dependence on the I(D)/I(D′) ratio was observed, indicating that this behavior is not related to the prevailing defect type.

It should be mentioned that, in our previous study, the reverse current decreased with increasing graphene self-doping level for graphene/Si(100) diodes [32]. However, in the case of graphene/Si(100) heterojunctions, silicon surface pre-treatment significantly affected the electrical and photovoltaic properties of the fabricated diodes. Notably, in the case of the U_{OC}, surface pre-treatment is much more important than the graphene structure [32]. In that study, the I_{SC} tended to increase with reduced graphene self-doping. However, silicon surface pre-treatment conditions are also critical. It should be noted that there were more variables in this study. Notably, along with differences in the graphene's structure and electronic properties, there are factors of the

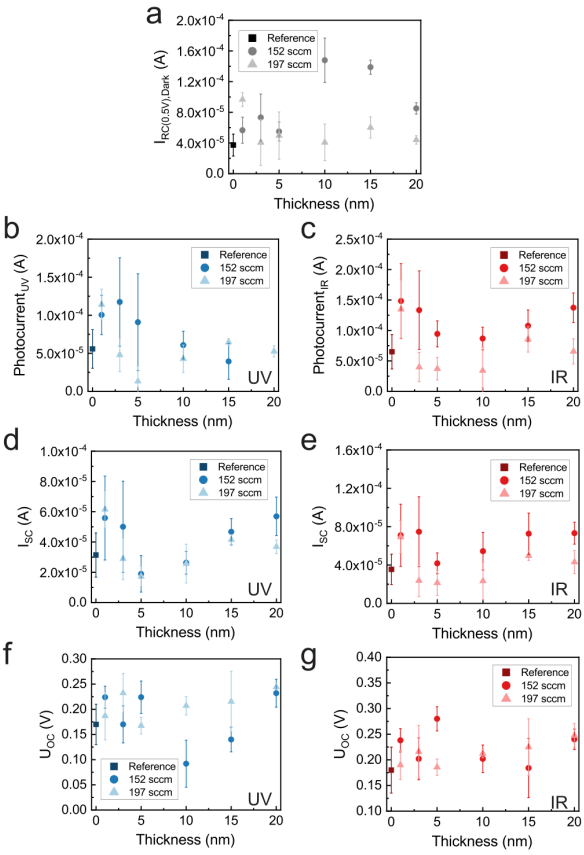


Figure 7. Graphene/h-BN/Si(100) diodes electrical and photoelectric properties dependence on the h-BN interlayer thickness: dark current (a), photocurrent (UV) (b), photocurrent (IR) (c), short circuit current (UV) (d), short circuit current (IR) (e), open circuit voltage (UV) (f), open circuit voltage (IR) (g). Error bars show the dispersion of the optoelectronic parameters within the same sample.

different h-BN film compositions or h-BN interlayer thicknesses, in addition to the variation in the film roughness. In addition, it can be assumed that in the case of the thinnest hexagonal boron nitride interlayer, the boron nitride film is - discontinuous. Competition between the abovementioned factors may hide the possible influence of the graphene structure, electronic properties, and h-BN interlayer on the electrical and photoelectric properties of graphene/h-BN/Si(100) diodes.

Notably, in the case of graphene/Si heterojunction solar cells fabricated using transferred graphene, the insertion of the h-BN interlayer significantly increased the open-circuit voltage and short-circuit current of the solar cell [10, 53–58]. In our case, a significant increase in the short-circuit current and open-circuit voltage was observed when magnetron sputter deposited h-BN films were used instead of transferred high-crystallinity h-BN flakes. In particular, the average short-circuit current and photocurrent nearly doubled, and the average

IR-light-excited open-circuit voltage increased by ~100 mV (figures 7 and S18). This improvement is comparable to the results reported for transferred graphene/Si solar cells enhanced by a transferred h-BN interlayer [10, 53, 58]. Thus, h-BN interlayers deposited by reactive high-power impulse magnetron sputtering can be effectively used to improve the photoelectric and photovoltaic properties of graphene/Si solar cells.

4. Conclusions

The effects of h-BN interlayer composition and thickness on the structure, morphology, and electrical properties of graphene and graphene-based devices were studied. Defect-free graphene was not grown using the HIPIMS-deposited h-BN interlayer. However, it was found that the graphene self-doping, attributed mainly to substrate-induced effects, could be partially controlled, and the graphene/Si(100) diode photocurrent, short-circuit current, and open-circuit voltage could be significantly increased by inserting an h-BN interlayer. The defect type of prevailing graphene can be changed by varying the boron interlayer thickness. The graphene layers grown on the boron nitride films were significantly rougher than those grown on the SiO_2 films. The surface current of graphene grown on h-BN was much higher than that of graphene synthesized on the SiO_2 film. No relationship was found between graphene surface conductivity and graphene self-doping. However, it must be mentioned that despite the h-BN film surface roughness being much larger than the roughness of the SiO_2 film or Si(100) and the possible presence of B–H and C–H bonds in some h-BN films, reduced graphene self-doping was achieved. Tunneling is the primary reverse current charge transfer mechanism, similar to graphene/Si(100) diodes, and h-BN interlayers cannot decrease the reverse dark current. Despite all the abovementioned circumstances, the insertion of the h-BN interlayer resulted in a photocurrent and a significant increase in the photocurrent, short circuit current, and open circuit voltage compared to the graphene/Si(100) heterojunction. Notably, the average short-circuit current and photocurrent nearly doubled, and the average IR-light-excited open-circuit voltage increased by ~100 mV. Thus, h-BN interlayers deposited by reactive high-power impulse magnetron sputtering can be effectively used to improve the photoelectric and photovoltaic properties of graphene/Si solar cells. The observed effects of the h-BN interlayer on the properties of the graphene/Si(100) diodes were explained by the competition between the influence of the graphene structure and electronic properties and the one hand and impact of different h-BN film compositions, thicknesses, and roughness.

Acknowledgments

This study was supported by the Research Council of Lithuania (Proposal No. P-MIP-22-235; Contract No S-MIP-22-67).

Conflicts of interest

The authors declare no conflict of interest.

Data availability statement

All data that support the findings of this study are included within the article (and any supplementary files).

Funding

This study was funded by the Research Council of Lithuania (Proposal No. P-MIP-22-235; Contract No S-MIP-22-67).

ORCID iDs

Šarūnas Meškinis https://orcid.org/0000-0001-9622-7573
Šarūnas Jankauskas https://orcid.org/0000-0001-6347-5167
Asta Guobienė https://orcid.org/0000-0002-1421-0012

References

[1] Lee C, Wei X, Kysar J W and Hone J 2008 Measurement of the elastic properties and intrinsic strength of monolayer graphene *Science (1979)* **321** 385–8
[2] Nair R R, Blake P, Grigorenko A N, Novoselov K S, Booth T J, Stauber T, Peres N M R and Geim A K 2008 Fine structure constant defines visual transparency of graphene *Science (1979)* **320** 1308
[3] Morozov S V, Novoselov K S, Katsnelson M I, Schedin F, Elias D C, Jaszczak J A and Geim A K 2008 Giant intrinsic carrier mobilities in graphene and its bilayer *Phys. Rev. Lett.* **100** 016602
[4] Lee J-Y, Connor S T, Cui Y and Peumans P 2008 Solution-processed metal nanowire mesh transparent electrodes *Nano Lett.* **8** 689–92
[5] Zhang Z, Du J, Zhang D, Sun H, Yin L, Ma L, Chen J, Ma D, Cheng H-M and Ren W 2017 Rosin-enabled ultraclean and damage-free transfer of graphene for large-area flexible organic light-emitting diodes *Nat. Commun.* **8** 14560
[6] Wu M, Wang Z, Wang X and Yu J 2018 High-performance organic light-emitting photodetector fabricated by separating photodetective center from emissive layer without luminance trade-off *Opt. Lett.* **43** 4502
[7] Lin X *et al* 2022 *In situ* growth of graphene on both sides of a Cu–Ni alloy electrode for perovskite solar cells with improved stability *Nat. Energy* **7** 520–7
[8] Mahalingam S, Manap A, Omar A, Low F W, Afandi N F, Chia C H and Rahim N A 2021 Functionalized graphene quantum dots for dye-sensitized solar cell: key challenges, recent developments and future prospects *Renew. Sustain. Energy Rev.* **144** 110999
[9] Nasir S, Johrin N, Low W, Moh P Y, Megat Hasnan M M I, bin, Ghosh B K and Chee F P 2024 Review—development of graphene-based photodiode device: synthesis, deposition, and characterization *ECS J. Solid State Sci. Technol.* **13** 121001
[10] Fallahazad P 2023 Rational and key strategies toward enhancing the performance of graphene/silicon solar cells *Mater Adv.* **4** 1876–99
[11] Sun M, Wang S, Liang Y, Wang C, Zhang Y, Liu H, Zhang Y and Han L 2025 Flexible graphene field-effect transistors and their application in flexible biomedical sensing *Nanomicro Lett.* **17** 34
[12] Yan K *et al* 2015 High-performance graphene-based hole conductor-free perovskite solar cells: schottky junction enhanced hole extraction and electron blocking *Small* **11** 2269–74
[13] Yi K, Liu D, Chen X, Yang J, Wei D, Liu Y and Wei D 2021 Plasma-enhanced chemical vapor deposition of two-dimensional materials for applications *Acc. Chem. Res.* **54** 1011–22
[14] Fang Y, Zhou K, Wei W, Zhang J and Sun J 2024 Recent advances in batch production of transfer-free graphene *Nanoscale* **16** 10522–32
[15] Chen Z *et al* 2021 Direct growth of wafer-scale highly oriented graphene on sapphire *Sci. Adv.* **7** 1–7
[16] Mishra N *et al* 2019 Wafer-scale synthesis of graphene on sapphire: toward fab-compatible graphene *Small* **15** 1904906
[17] Wang Y, Zhang M, Li P, Chen X, Xue Z, Wu X and Di Z 2022 Structural properties of grain boundary in graphene grown on germanium substrates with different orientations *Appl. Phys. Lett.* **121** 011901
[18] Wang H, Xue X, Jiang Q, Wang Y, Geng D, Cai L, Wang L, Xu Z and Yu G 2019 Primary nucleation-dominated chemical vapor deposition growth for uniform graphene monolayers on dielectric substrate *J. Am. Chem. Soc.* **141** 11004–8
[19] Shi Q *et al* 2020 Substrate developments for the chemical vapor deposition synthesis of graphene *Adv. Mater. Interfaces* **7** 1902024
[20] Meškinis Š, Vasiliauskas A, Guobienė A, Talaikis M, Niaura G and Gudaitis R 2022 The direct growth of planar and vertical graphene on Si(100) *via* microwave plasma chemical vapor deposition: synthesis conditions effects *RSC Adv.* **12** 18759–72
[21] Meškinis Š *et al* 2023 Biosensor based on graphene directly grown by MW-PECVD for detection of COVID-19 Spike (S) protein and its entry receptor ACE2 *Nanomaterials* **13** 2373
[22] Chugh S, Mehta R, Lu N, Dios F D, Kim M J and Chen Z 2015 Comparison of graphene growth on arbitrary non-catalytic substrates using low-temperature PECVD *Carbon N Y* **93** 393–9
[23] Khan A, Islam S M, Ahmed S, Kumar R R, Habib M R, Huang K, Hu M, Yu X and Yang D 2018 Direct CVD growth of graphene on technologically important dielectric and semiconducting substrates *Adv. Sci.* **5** 1800050
[24] Han Z, Li M, Li L, Jiao F, Wei Z, Geng D and Hu W 2021 When graphene meets white graphene—recent advances in the construction of graphene and *h*-BN heterostructures *Nanoscale* **13** 13174–94
[25] Yang W *et al* 2013 Epitaxial growth of single-domain graphene on hexagonal boron nitride *Nat. Mater.* **12** 792–7
[26] Wang M *et al* 2013 A platform for large-scale graphene electronics—CVD growth of single-layer graphene on CVD-grown hexagonal boron nitride *Adv. Mater.* **25** 2746–52
[27] Song X, Sun J, Qi Y, Gao T, Zhang Y and Liu Z 2016 Graphene/h-BN heterostructures: recent advances in controllable preparation and functional applications *Adv. Energy Mater.* **6** 1600541
[28] Huang M, Deng B, Dong F, Zhang L, Zhang Z and Chen P 2021 Substrate engineering for CVD growth of single crystal graphene *Small Methods* **5** 2001213
[29] Gao W, Zhi G, Zhou M and Niu T 2024 Growth of single crystalline 2D materials beyond graphene on non-metallic substrates *Small* **20** 2311317
[30] Entani S, Takizawa M, Li S, Naramoto H and Sakai S 2019 Growth of graphene on SiO2 with hexagonal boron nitride buffer layer *Appl. Surf. Sci.* **475** 6–11
[31] Stankus V, Vasiliauskas A, Guobienė A, Andrulevičius M and Meškinis Š 2024 Synthesis and characterization of boron nitride thin films deposited by high-power impulse reactive magnetron sputtering *Molecules* **29** 5247
[32] Jankauskas Š, Gudaitis R, Vasiliauskas A, Guobienė A and Meškinis Š 2022 The graphene structure's effects on the current-voltage and photovoltaic characteristics of directly synthesized graphene/n-Si(100) Diodes *Nanomaterials* **12** 1640
[33] Glemža J, Palenskis V, Gudaitis R, Jankauskas Š, Guobienė A, Vasiliauskas A, Meškinis Š, Pralgauskaitė S and Matukas J 2022 Low-frequency noise of directly synthesized graphene/Si(100) junction *Diam. Relat. Mater.* **127** 109207
[34] Hwang J-S *et al* 2013 Imaging layer number and stacking order through formulating Raman fingerprints obtained from hexagonal single crystals of few layer graphene *Nanotechnology* **24** 015702
[35] Childres I, Jauregui L A, Tian J and Chen Y P 2011 Effect of oxygen plasma etching on graphene studied using Raman spectroscopy and electronic transport measurements *New J. Phys.* **13** 025008
[36] Dresselhaus M S, Jorio A, Souza Filho A G and Saito R 2010 Defect characterization in graphene and carbon nanotubes using Raman spectroscopy *Philosophical Transactions of the Royal Society A: Mathematical, Physical and Engineering Sciences* **368** 5355–77
[37] Bhatt M, Kim H and Kim G 2022 Various defects in graphene: a review *RSC Adv.* **12** 21520–47
[38] Eckmann A, Felten A, Mishchenko A, Britnell L, Krupke R, Novoselov K S and Casiraghi C 2012 Probing the Nature of Defects in Graphene by Raman Spectroscopy *Nano Lett.* **12** 3925–30
[39] Venezuela P, Lazzeri M and Mauri F 2011 Theory of double-resonant Raman spectra in graphene: intensity and line shape of defect-induced and two-phonon bands *Phys. Rev. B* **84** 035433
[40] Casiraghi C 2009 Probing disorder and charged impurities in graphene by Raman spectroscopy *Rapid Research Letters* **3** 175–7

[41] Lee J E, Ahn G, Shim J, Lee Y S and Ryu S 2012 Optical separation of mechanical strain from charge doping in graphene *Nat. Commun.* **3** 1024
[42] Luo Z, Yu T, Kim K, Ni Z, You Y, Lim S, Shen Z, Wang S and Lin J 2009 Thickness-dependent reversible hydrogenation of graphene layers *ACS Nano* **3** 1781–8
[43] Elias D C *et al* 2009 Control of graphene's properties by reversible hydrogenation: evidence for graphane *Science (1979)* **323** 610–3
[44] Melios C, Spencer S, Shard A, Strupiński W, Silva S R P and Kazakova O 2016 Surface and interface structure of quasi-free standing graphene on SiC *2D Mater.* **3** 025023
[45] Shtepliuk I, Ivanov I G, Iakimov T, Yakimova R, Kakanakova-Georgieva A, Fiorenza P and Giannazzo F 2019 Raman probing of hydrogen-intercalated graphene on Si-face 4H-SiC *Mater. Sci. Semicond. Process.* **96** 145–52
[46] Clapa M and Gaj J 2021 Behavior of graphene under glow discharge plasma *Sens Actuators A Phys.* **332** 113069
[47] Casiraghi C, Pisana S, Novoselov K S, Geim A K and Ferrari A C 2007 Raman fingerprint of charged impurities in graphene *Appl. Phys. Lett.* **91** 233108
[48] Gudaitis R, Lazauskas A, Jankauskas Š and Meškinis Š 2020 Catalyst-less and transfer-less synthesis of graphene on Si(100) using direct microwave plasma enhanced chemical vapor deposition and protective enclosures *Materials* **13** 5630
[49] Fukamachi S, Solís-Fernández P, Kawahara K, Tanaka D, Otake T, Lin Y-C, Suenaga K and Ago H 2023 Large-area synthesis and transfer of multilayer hexagonal boron nitride for enhanced graphene device arrays *Nat. Electron.* **6** 126–36
[50] Dean C R *et al* 2010 Boron nitride substrates for high-quality graphene electronics *Nat. Nanotechnol.* **5** 722–6
[51] Kim S, Kim B, Park S, Chang W S, Kang H, Kim S, Lee H and Kim S 2023 Hysteretic behavior of all CVD h-BN/graphene/h-BN heterostructure field-effect transistors by interfacial charge trap *Surfaces and Interfaces* **36** 102615
[52] Xu H, Wu J, Chen Y, Zhang H and Zhang J 2013 Substrate engineering by hexagonal boron nitride/SiO_2 for Hysteresis-free graphene FETs and large-scale graphene p–n junctions *Chem. Asian J.* **8** 2446–52
[53] Behura S K, Wang C, Wen Y and Berry V 2019 Graphene–semiconductor heterojunction sheds light on emerging photovoltaics *Nat. Photonics* **13** 312–8
[54] Huang K, Yu X, Cong J and Yang D 2018 Progress of graphene–silicon heterojunction photovoltaic devices *Adv. Mater. Interfaces* **5** 1801520
[55] Bhopal M F, Lee D W, Rehman A ur and Lee S H 2017 Past and future of graphene/silicon heterojunction solar cells: a review *J. Mater. Chem. C* **5** 10701–14
[56] Kong X, Zhang L, Liu B, Gao H, Zhang Y, Yan H and Song X 2019 Graphene/Si schottky solar cells: a review of recent advances and prospects *RSC Adv.* **9** 863–77
[57] Song L, Yu X and Yang D 2019 A review on graphene-silicon schottky junction interface *J. Alloys Compd.* **806** 63–70
[58] Meng J-H, Liu X, Zhang X-W, Zhang Y, Wang H-L, Yin Z-G, Zhang Y-Z, Liu H, You J-B and Yan H 2016 Interface engineering for highly efficient graphene-on-silicon schottky junction solar cells by introducing a hexagonal boron nitride interlayer *Nano Energy* **28** 44–50

GYVENIMO, MOKSLINĖS IR KŪRYBINĖS VEIKLOS APRAŠYMAS (CV)

Šarūnas Jankauskas
sarunas.jankauskas@ktu.lt

Išsilavinimas:

2002–2012	**Pagrindinis** – Kauno Viktoro Kuprevičiaus pagrindinė mokykla
2012–2014	**Vidurinis** – Kauno „Varpo“ gimnazija
2014–2018	**Medžiagų technologijų bakalauras** – Kauno technologijos universitetas Studijos Suomijoje, Helsinkio universitete, pagal Erasmus+ mainų programą
2018–2020	**Fizinių mokslų magistras** – Kauno technologijos universitetas
2021–dabar	**Medžiagų technologijų doktorantūra** – Kauno technologijos universitetas

Profesinė patirtis:

2019–2025	**Projekto specialistas** – Kauno technologijos universitetas, Medžiagų mokslo institutas
2020–2025	**Projekto jaunesnysis mokslo darbuotojas** – Kauno technologijos universitetas, Medžiagų mokslo institutas
2025–dabar	**Projekto specialistas** – Kauno technologijos universitetas, Elektros ir elektronikos fakultetas
2026–dabar	**Lektorius** – Kauno technologijos universitetas, Elektros ir elektronikos fakultetas

Mokslinių interesų sritys:
Grafeno sintezė mikrobange plazma aktyvuotu cheminio nusodinimo iš garų fazės būdu, grafeno tyrimai Ramano sklaidos spektroskopijos, UV-Regimosios šviesos spektroskopijos metodais, programavimas MATLAB ir Python aplinkose. Medžiagų elektrinių savybių analizė, lustų pakavimas.

Dalyvavimas nacionaliniuose bei tarptautiniuose projektuose:

1. Projekto jaunesnysis mokslo darbuotojas „Grafeno ir susijusių 2D nanomedžiagų heterosandūros ir supergardelės fotovoltaikai“ (3D FOTOGRAF) projekte (2019 – 2021 m.). Vadovas: dr. Šarūnas Meškinis.
2. Projekto specialistas „Nerasojančios precizinės optinės liniuotės ir limbai“ (RASA) projekte (2020 – 2023 m.). Vadovas: dr. Šarūnas Meškinis.
3. Projekto jaunesnysis mokslo darbuotojas „Biojutiklis iš nanosluoksniuotų struktūrų SARS-COV2 nustatymui” projekte (2021 – 2023 m.). Vadovas: dr. Šarūnas Meškinis.
4. Projekto jaunesnysis mokslo darbuotojas „Hibridinės grafeno-lantano perovskitų struktūros megnetovaržinių jutiklių taikymams“ (Hybrid-MAGSENS) projekte (2022 – 2024 m.). Vadovas: dr. Asta Guobienė.
5. Projekto jaunesnysis mokslo darbuotojas „Heksagoninis boro nitridas grafeno/Si radialiniams saulės elementams“ (BONISOL) projekte (2022–2025 m.). Vadovas: dr. Šarūnas Meškinis.
6. Projekto specialistas Technologinių ir fizinių mokslų ekscelencijos centro (TiFEC) projekte (2026 m. – dabar). Vadovas: prof. Dr. Mindaugas Žilys.

MOKSLO STRAIPSNIŲ IR MOKSLO KONFERENCIJŲ SĄRAŠAS

Moksliniai straipsniai disertacijos tema:

1. JANKAUSKAS, Š.; R. GUDAITIS; A. VASILIAUSKAS; A. GUOBIENĖ ir Š. MEŠKINIS. The graphene structure's effects on the current-voltage and photovoltaic characteristics of directly synthesized graphene/n-Si(100) diodes. *Nanomaterials*. Basel: MDPI, 12, 2022, 10, 1640, 1–19. ISSN 2079-4991. Prieiga internetu: doi: 10.3390/nano12101640. 1-a kvartilė, citavimo indeksas: 5,3.
2. MEŠKINIS, Š.; R. GUDAITIS; A. VASILIAUSKAS; A. GUOBIENĖ; Š. JANKAUSKAS; V. STANKEVIČ; S. KERŠULIS; A. STIRKĖ; E. ANDRIUKONIS; W. MELO; V. VERTELIS ir N. ŽURAUSKIENĖ. Biosensor based on graphene directly grown by MW-PECVD for detection of COVID-19 spike (S) protein and its entry receptor ACE2. *Nanomaterials*. Basel : MDPI, 13, 2023, 16, 2373, 1–18. ISSN 2079-4991. Prieiga internetu: doi: 10.3390/nano13162373. 2-a kvartilė, citavimo indeksas: 4,4.
3. JANKAUSKAS, Š.; Š. MEŠKINIS; N. ŽURAUSKIENĖ ir A. GUOBIENĖ. Influence of synthesis parameters on structure and characteristics of the graphene grown using PECVD on sapphire Substrate. *Nanomaterials*. Basel : MDPI, 14, 2024, 20, 1635, 1–13. ISSN 2079-4991. Prieiga internetu: doi: 10.3390/nano14201635. 2-a kvartilė, citavimo indeksas: 4,4.
4. MEŠKINIS, Š.; A. LAZAUSKAS; Š. JANKAUSKAS; A. GUOBIENĖ ir R. GUDAITIS, Rimantas. Advancing graphene synthesis: low-temperature growth and hydrogenation mechanisms using plasma-enhanced chemical vapor deposition. *Molecules*. Basel: MDPI, 30, 2025, 1, 33, 1–16. ISSN 1420-3049. Prieiga internetu: doi: 10.3390/molecules30010033. 2-a kvartilė, citavimo indeksas: 4,2.
5. MEŠKINIS, Š.; Š. JANKAUSKAS; A. VASILIAUSKAS; V. STANKUS; A. GUOBIENĖ; K. LUKOŠEVIČIUS; A. JASUTIS ir R. GUDAITIS. Graphene direct growth by microwave PECVD on h-BN films deposited by reactive HIPIMS. Nano Express. Bristol : IOP, 6, 2025, 2, 025007, 1–13. Publishing. ISSN 2632-959X. Prieiga internetu: doi: 10.1088/2632-959X/add6bb. 2-a kvartilė, citavimo indeksas: 2,9.

Moksliniai straipsniai, nesusiję su disertacijos tema:

1. GLEMŽA, J.; V. PALENSKIS; R. GUDAITIS; Š. JANKAUSKAS; A. GUOBIENĖ; A. VASILIAUSKAS; Š. MEŠKINIS; S. PRALGAUSKAITĖ ir J. MATUKAS. Low-frequency noise of directly synthesized graphene/Si(100) junction. *Diamond and related materials*. Lausanne : Elsevier, 127, 2022109207, 1–8. ISSN 0925-9635. eISSN 1879-0062. Prieiga internetu: doi: 10.1016/j.diamond.2022.109207. 2-a kvartilė, citavimo indeksas: 4,1.
2. JANKAUSKAS, Š.; VASILIAUSKAS, A.; GUOBIENĖ, A.; ANDRULEVIČIUS, M.; ABAKEVIČIENĖ, B.; MEŠKINIS, Š. Study of the structure, composition and wettability of the DLC:N films. *Surface and coatings*

technology. Lausanne : Elsevier, 489, 2024, 131132, 1–9. ISSN 0257-8972. eISSN 1879-3347. Prieiga internetu: doi: 10.1016/j.surfcoat.2024.131132. 1-a kvartilė, citavimo indeksas: 6,1.

Mokslinės konferencijos:

1. JANKAUSKAS, Š.; R. GUDAITIS; A. LAZAUSKAS ir Š. MEŠKINIS. Catalyst-less and transfer-less synthesis of graphene on Si(100) using direct microwave plasma enhanced chemical vapor deposition and protective enclosures. Iš *Advanced materials and technologies: book of abstracts of 23rd international conference-school, 23–27 August 2021, Palanga, Lithuania*, p. 70. Kaunas: Kaunas University of Technology. 2021. ISSN 2669-1930. B-P40.
2. JANKAUSKAS, Š.; R. GUDAITIS; A. LAZAUSKAS ir Š. MEŠKINIS Catalyst-less and transfer-less synthesis of graphene on Si(100) using direct microwave plasma enhanced chemical vapor deposition and protective enclosures. Iš *Open readings 2022: 65th international conference for students of physics and natural sciences, March 15-18: abstract book* / Š. MICKUS, S. PŪKIENĖ, L. NAIMOVIČIUS (Eds), p. 174.Vilnius: Vilnius University press, 2022, P2-13. ISBN 9786090707227.
3. JANKAUSKAS, Š.; R. GUDAITIS; A. LAZAUSKAS ir Š. MEŠKINIS, Šarūns. Synthesis of graphene on Si(100) using direct mw-pecvd and protective enclosures. Iš *Joint international conference "Functional materials and nanotechnologies" and "Nanotechnology and innovation in the Baltic sea region", FM&NT – NIBS 2022, July 3–6, 2022 Riga, Latvia: book of abstracts*. L. GRĪNBERGA, A. ŠARAKOVSKIS, G. KUNAKOVA (Eds.). Riga: University of Latvia, 2022, Po-58. ISBN 9789934236457. p. 192.
4. JANKAUSKAS, Š.; R. GUDAITIS ir Š. MEŠKINIS, Šaūnas. Graphene/n-Si(100) diode, formed using transfer-less method, operation in different thermal conditions. Iš *Advanced materials and technologies: book of abstracts of 24th international conference-school, 22–26 August 2022, Palanga, Lithuania*. Kaunas: Kaunas University of Technology, 2022, A-P135, p. 176. ISSN 2669-1930.
5. JANKAUSKAS, Š.; A. VASILIAUSKAS; V. KOPUSTINSKAS; M. ANDRULEVIČIUS; A. GUOBIENĖ; B. ABAKEVIČIENĖ ir Š. MEŠKINIS. Deposition and study of the hydrophilic diamond-like carbon and diamond-like nanocomposite films. Iš *E-MRS Fall meeting 2022: 19–22 September, 2022, Warsaw, Poland*. Strasbourg: European materials research society, 2022, H.P.25, p. 1.
6. GUOBIENĖ, A.; M. KOLIADA; S. KERŠULIS; V. STANKEVIČ; V. VERTELIS, V.; V. PLAUŠINAITIENĖ, V.; Š. JANKAUSKAS, Š.; Š. MEŠKINIS ir N. ŽURAUSKIENĖ. Graphene-manganite structures for magnetic sensors applications Iš *E-MRS Spring meeting 2023: 40th anniversary: May 29 – June 2, 2023, Strasbourg, France*. Strasbourg: European materials research society, 2023, 00693, p. 1.
7. JANKAUSKAS, Š.; D. JUCIUS; V. GRIGALIŪNAS; M. JUODĖNAS; A. GUOBIENĖ; R. GUDAITIS; ir A. LAZAUSKAS. Transparent superhydrophilic

silicate glass surfaces for antifogging applications. Iš *IMAMPC 2023: 12th International meeting on atomic and molecular physics and chemistry, June 11-14, 2023, Innsbruck, Austria*: book of abstracts. Innsbruck: Institut für Ionenphysik und Angewandte Physik Universität Innsbruck, 2023, p. 69.

8. JANKAUSKAS, Š.; R. GUDAITIS, Rimatas; A. VASILIAUSKAS; A. GUOBIENĖ ir Š. MEŠKINIS. Impact of graphene structure on the electrical and photovoltaic performance of directly synthesized graphene/n Si(100) diodes. Iš *Advanced materials and technologies: book of abstracts of 25th international conference school, 21–25 August 2023, Palanga, Lithuania.* Kaunas: Kaunas university of technology, 2023, P101, p. 142. ISSN 2669-1930.
9. VASILIAUSKAS, A.; R. GUDAITIS; A. GUOBIENĖ; Š. JANKAUSKAS, Šarūns; M. ANDRULEVIČIUS; B. ABAKEVIČIENĖ ir Š. MEŠKINIS. Anti-fogging properties of the plasma nanotextured and diamond-like carbon coated optical grating scales. Iš *Advanced nanomaterials 2023 (ANM 23), 26–28 July 2023, Reitoria, University of Aveiro, Portugal*.
10. JANKAUSKAS, Š.; R. GUDAITIS; A. VASILIAUSKAS; A. GUOBIENĖ ir Š. MEŠKINIS. Mikrobangų plazma aktyvuoto cheminio nusodinimo iš garų fazės būdu suformuotų grafeno/n-tipo Si(100) prietaisų fotovoltinės savybės = Photovoltaic properties of directly synthesized graphene/n-Si(100) devices using microwave plasma-enhanced chemical vapor deposition technique. Iš *45-oji Lietuvos nacionalinė fizikos konferencija, 2023 m. spalio 25-27 d., Vilnius: programa ir pranešimų tezės*. Vilnius: Vilniaus universiteto leidykla, 2023, S2 - P10 p. 185. ISBN 9786090709818 (Vilnius University proceedings, ISSN 2669-0233; no. 38).

PADĖKA

Didžioji dalis disertacijoje pristatytų tyrimų atlikti Kauno technologijos universitete, Medžiagų mokslo institute. Visų pirma, autorius norėtų padėkoti visiems šio instituto kolegoms bei bendradarbiams už supratingumą, pagalbą ir geranoriškumą vykdant mokslinius tyrimus bei padedant administraciniais klausimais.

Autorius labiausiai dėkoja dr. Šarūnui Meškiniui, dr. Rimantui Gudaičiui, dr. Astai Guobienei bei dr. Brigitai Abakevičienei už patarimus, pagalbą vykdant tyrimus ir neįkainojamą patirtį, kuri prisidėjo prie mokslininko kompetencijų tobulinimo. Jie visuomet palaikė ir skatino siekti aukščiausių rezultatų, kartu išlaikė kantrumą ir supratingumą. Autorius jiems taip pat nori padėkoti už neformalias diskusijas, susijusias su tyrimais ir sprendžiant doktorantūros įsipareigojimų vykdymo klausimus.

Daug doktorantūros metu atliktų tyrimų nebuvo įtraukti į disertaciją, tačiau jie padėjo praplėsti supratimą fotonikos, medžiagų mokslo, anglies nanodarinių srityse. Už tai autorius dėkoja dr. Aušrinei Jurkevičiūtei už pagalbą tiriant plonų dangų tyrimus spektroskopine elipsometrija ir dr. Erikai Rajackaitei už suteiktas žinias bei medžiagas vieno, dviejų ir trijų sluoksnių grafeno plėvelių tyrimuose. Autorius taip pat dėkoja artimiems kolegoms dr. Tomui Klinavičiui, Gvidui Klyviui ir Klaudijui Midveriui, prisidėjusiems prie draugiškos, šmaikštumu bei įtraukiančiomis mokslinėmis diskusijomis paremtos darbo vietos kūrimo.

Galiausiai autorius nori padėkoti šeimos nariams už palaikymą ir skatinimą siekti užsibrėžtų tikslų.

UDK 546.26+544.174.5+53.082.9+539.2](043.3)

SL344. 20xx-xx-xx, xx leidyb. apsk. l. Tiražas 14 egz. Užsakymas xxx.
Išleido Kauno technologijos universitetas, K. Donelaičio g. 73, 44249 Kaunas
Spausdino leidyklos „Technologija“ spaustuvė, Studentų g. 54, 51424